A STUDY OF FOUR-JET EVENTS

AND SEARCH FOR DOUBLE PARTON INTERACTIONS

WITH THE COLLIDER DETECTOR AT FERMILAB

A Dissertation

by

LOUIS JOSEPH KEEBLE

Submitted to the Office of Graduate Studies of
Texas A&M University
in partial fulfillment of the requirements for the degree of

DOCTOR OF PHILOSOPHY
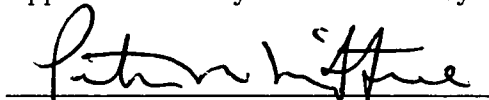
December 1992

Major Subject: Physics

A STUDY OF FOUR-JET EVENTS

AND SEARCH FOR DOUBLE PARTON INTERACTIONS

WITH THE COLLIDER DETECTOR AT FERMILAB
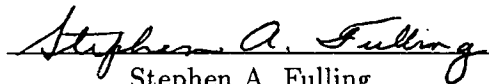
A Dissertation

by

LOUIS JOSEPH KEEBLE

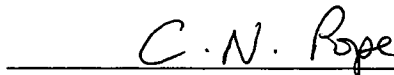Approved as to style and content by:

Peter M. McIntyre	Robert C. Webb
(Chair of Committee)	(Member)
Stephen A. Fulling	Christopher N. Pope
(Member)	(Member)
Richard L. Arnowitt	
(Head of Department)	

December 1992

ABSTRACT

A Study of Four-Jet Events and Search for Double Parton Interactions

With the Collider Detector at Fermilab. (December 1992)

Louis Joseph Keeble, B.Sc., Bristol University, Bristol, England;

M.S., Texas A&M University, College Station, Texas

Chair of Advisory Committee: Dr. Peter M. McIntyre

Kinematic properties of four-jet events in $p\bar{p}$ collisions at $\sqrt{s} = 1.8$ TeV are compared with the predictions of leading order quantum chromodynamics. Jets are clustered with a fixed cone algorithm using a cone size $R = 0.7$ where $R = \sqrt{\Delta\eta^2 + \Delta\phi^2}$. Pseudo-rapidity η is defined by the relation $\eta = -\ln\tan(\theta/2)$, where θ is the polar angle relative to the beam axis and ϕ is the azimuthal angle around this axis. A search for double parton interactions has resulted in an upper limit on the double parton scattering cross section of $\sigma_{DP} < 0.11$ μb (95% C.L.) for partons with transverse momenta greater than 18 GeV/c. Defining the effective cross section σ_{eff} through the equation $\sigma_{DP} = \sigma_{dijet}^2/2\sigma_{eff}$, the limits $\sigma_{eff} > 4.2$ mb (95% C.L.) and $\sigma_{eff} > 5.6$ mb (90% C.L.) have also been established, where σ_{dijet} is the cross section for two-jet events. The implications of these results for physics at $\sqrt{s} = 20$ TeV are discussed.

DEDICATION

To Donna

for her boundless love and support.

ACKNOWLEDGEMENTS

The last four years have been a lot of fun, and I have even learned some physics along the way. Having spent one summer in the United States prior to enrolling in graduate school, I knew that even if everything else failed I could always rely on the friendliness of Americans. While I am indebted to the country in general, there are many people whom I must thank on a more personal level.

First and foremost, I must thank my wife, Donna. From the day we met, life has just been getting better and better. My debt to her I may never be able to fully repay, but maybe finally getting a job so that *she* can go to graduate school will help (?).

Inevitably, along with a wife comes all the wife's family. .. Donna's parents, Bill and Nance, are two of the nicest people I have ever met. While they did occasionally refer to me as "the limey", I hold no grudges, and especially have to thank Bill for the hours he spent fixing the various cars/motorcycles that I bought (hey - I did get rid of that daughter of yours though, didn't I?). I thank Donna's brother Tim for teaching me the finer points of deer hunting ("point the gun away, Lou"), and Tim's wife Beth for getting us free tickets to see the White Sox and being a fun person. Cheryl and Vern, Donna's sister and brother-in-law, were always happy to see me, especially if I was going to help them move house (again). To the rest of the family, Tom and Dee, Pat and Judy, Tom and Marion Nagle and all the kids, I thank you for always making me feel welcome, and for introducing me to the pink stuff, whatever that is.

Meanwhile, on the other side of the Atlantic, I am ever so grateful to my mother. Over the years she has faithfully kept track of me on my various travels, and sent mail and a steady supply of McVitie's Jaffa Cakes which kept me from getting too homesick. She even allowed herself to be dragged 3,000 miles to be at my wedding, as did my brother Remi (who gave me my first and only near-death-experience while I was teaching him to drive in the U.S.) and his fiancé Kathy. I must also thank my very good friends from England, Shane Ahmet, Serge Barbe, Oscar Engles, Mick Gallagher, Paul Hickey, Roger Lewis, Trevor Merriden, Des Shannon, Jan Szczegolski and Jenny Tatham who have put up with my disappearing act and are still always ready to go off for a beer with me when I'm back home.

Both at Fermilab in Batavia, Illinois and at Texas A&M I have made many friends, all of whom have made graduate life easier and more fun. Bob Mattingly, Steve Moulding, Tom Baumann and Colin Jessop provided some great entertainment, as did Les Nakae, who seemed to get "hosed" by anything and everything on a regular basis. This made us all feel a little better about ourselves. Luckily, Dee Hahn always kept a steady supply of coffee going in B0, which was nice even though it either got rained on, snowed on or blown away on the short walk back to the trailers. John Cunningham and Baber Farhat are two great friends. I'll never forget the quote from John during the wild parades and throwing of beads at Mardi Gras "but what does it all mean?" - one thing's for sure, particle physics isn't going to explain that one!

Thanks also to Brenna Flaugher, who taught me a lot of jet physics and made me laugh while doing so, much to the distraction of those working around us, to whom I apologize! John Huth and Dave Brown are responsible for steering me in the

direction of QCD in the first place, and Marjorie Shapiro and Jim Mueller provided quite a bit of help at various sticky points of the analysis. Thanks to all of you. More generally, I thank the CDF collaboration for their hard work, and for making the 1988/89 run such a success. In addition, I acknowledge the kind hospitality of Bob Carlitz of the University of Pittsburgh, and thank him for his help with the analysis during my visit.

Back at Texas A&M, I thank Peter McIntyre my advisor for being so keen and enthusiastic when I first applied to the university, and for giving me the chance to go to Fermilab even before I began classes. He later trusted me with intellectual freedom, and as a result I have developed a sense of independence and self-reliance which will always be a valuable asset. Bob Webb of the high energy physics department was also very helpful both when I first arrived, and later on when I went through the various stages of qualifying exams, classes, research and preliminary exams. His support, both personal and financial, is very much appreciated. J.P. Done, Jim Lamecker, Tim Hessing, Ashutosh Sanzgiri, John Wahl and Shah Zaman are (or in some cases were) students in the high energy group who have become my friends and deserve my thanks. Also I thank Manuel Grau for being a good-humored landlord, and Rogélio Cansari, the "jungle-man" of Panama, for being such a bad influence! The kind friendship of Ann David, Nick Diaczenko and Teruki Kamon is also very much appreciated.

Finally, I thank the so-far unmentioned members of my committee, past and present, for their participation in the degree process, namely Stephen Fulling, Robert Hoskisson, Chris Pope, and Dimitri Nanopoulos who allowed me to sit in for his entertaining and enlightening particle physics class.

TABLE OF CONTENTS

CHAPTER   Page

LIST OF TABLES

LIST OF FIGURES

Figure Page

CHAPTER I

INTRODUCTION

A. Preliminary Overview : The Standard Model

Over the past fifty years, the field of particle physics has been rapidly evolving. The construction of large scale fixed-target and colliding-beam machines involving the collaboration of hundreds of experimentalists has been necessary. As higher center-of-mass energies are reached, one is able to look deeper into the nature of the various forces that govern the interaction of particles. This can be seen by considering the Heisenberg uncertainty relation $\Delta p \Delta x \sim \hbar$, which implies smaller de Broglie wavelengths at higher energies. We have learned from experiment that a picture of the universe comprised solely of protons, neutrons, electrons, neutrinos and photons is incomplete. Instead, additional particles may be created, provided that there is sufficient energy. The properties of all particles and the details of the interactions between them seem to be well described by the *Standard Model.*

The Standard Model has its roots in the relativistic description of spin 1/2 particles (or *fermions*) provided by the British physicist Paul Dirac in 1928,

$$(\gamma^\mu P_\mu - m)\psi = 0, \tag{1}$$

$$\bar{\psi}(\gamma^\mu P_\mu + m) = 0, \tag{2}$$

This dissertation follows the style of Physical Review D.

where γ^μ represents a set of four 4×4 matrices, P_μ is the momentum operator $-i\partial_\mu$, ψ is a four-component spinor and $\bar\psi = \psi^\dagger \gamma^\circ$. Natural units have been used ($\hbar = c = 1$). The corresponding Lagrangian is

$$\mathcal{L} = i\bar\psi\gamma_\mu\partial^\mu\psi - m\bar\psi\psi. \tag{3}$$

When second-quantized, the field operator ψ and its adjoint $\bar\psi$ may be expanded in terms of raising and lowering operators. These operators create and destroy particles and anti-particles, in direct analogy with the non-relativistic description of harmonic oscillator states in quantum mechanics. Equations 1 and 2 admit negative energy solutions, a situation previously considered to be an insurmountable problem in other theories of a similar nature. Dirac side-stepped this issue by proposing a filled *sea* of negative energy states. By invoking the Pauli exclusion principle, he argued that only positive energy states would generally be observed in nature. However, if enough energy were provided to create a hole in the sea, one would observe an anti-particle. In 1933, strong experimental evidence for the existence of anti-particles was seen for the first time [1]. The reinterpretation of anti-particles by Feynman as particles traveling backwards in time has since allowed a considerable conceptual simplification. Matrix elements may be written down in diagrammatic form with a set of specific rules (*Feynman diagrams*), facilitating the evaluation of scattering cross sections.

The invariance of the Lagrangian under symmetry transformations has profound implications. For example, we may require Equation 3 to be unaffected by the transformation $\psi \rightarrow e^{i\alpha}\psi$. In accordance with Noether's theorem [2] such a *global gauge invariance* leads to a conserved current density j^μ, defined as $j^\mu = -e\bar\psi\gamma^\mu\psi$.

The time-like component of this current, or the electric charge, is then also conserved in agreement with experimental observation. With the introduction of $U(1)$ *local* gauge invariance under a transformation of the four component fermion wave function $\psi \rightarrow e^{i\alpha(x)}\psi$, a firm theoretical connection between fermions and photons has been achieved. The dependence of the transformation variable α on the position four vector x necessitates the introduction of a vector field A^μ, which can be associated with the massless photon. The resulting theory is known as *quantum electrodynamics*, or QED. Although QED leads to transition matrix element integrals which are divergent, these divergences may be factorized into physically measurable parameters such as lepton charges and masses. This procedure is known as *renormalization*.

In addition to the electromagnetic force, a complete theory must be able to describe weak interaction processes such as neutron decay ($n \rightarrow p + e^- + \bar{\nu}_e$). In fact, both the weak and electromagnetic interactions were unified in the Weinberg-Salam $SU(2) \times U(1)$ *electroweak* model in 1967 [3]. In this model, leptons are treated as weak isospin doublets, such as (ν_e, e) and (ν_μ, μ), and the corresponding invariance parameter (previously $\alpha(x)$ for the $U(1)$ group) takes the form of a 2 × 2 matrix. In the same way that the field A^μ was required in the above example, four fields now become necessary to satisfy gauge invariance. One is simply the familiar photon field, but the other three describe new gauge bosons, $W^\pm$ and Z°. In 1971, the electroweak theory was shown to be renormalizable [4]. By invoking the Higgs mechanism of spontaneous symmetry breaking [5], Weinberg was able to explain mass generation for the heavy vector bosons. In addition, this mechanism inevitably leads to the introduction of a scalar particle known as the Higgs (H°). In 1983, the electroweak

model was confirmed by the observation of the three new gauge bosons at the CERN $p\bar{p}$ collider [6, 7, 8, 9], with $M_{W\pm} = 80.6$ GeV/c^2 and $M_{Z^0} = 91.2$ GeV/c^2. Many other predictions of the theory have since been confirmed by experiment, though so far the Higgs particle remains unobserved.

The gauge bosons of the electroweak theory ($W^{\pm}, Z^0, \gamma$) also couple to quarks, the spin-1/2 constituents of hadronic matter. Once again, the coupling exhibits a doublet symmetry, though now there is mixing between the various quark *flavors*. The quark doublets of the standard model are the up and down (u,d), charm and strange (c,s) and top and bottom (t,b) quarks. Quark mixing was originally proposed by Cabibbo in 1963 [10], and extended by Glashow, Iliopoulos, and Maiani [11] who successfully predicted the existence of the charm quark. All quarks except for the top have been experimentally observed. The current lower limit on the mass of the top quark, set by the CDF collaboration, is $M_{top} > 91$ GeV/c^2 [12].

The final piece needed to complete the Standard Model is a description of strong interactions. These interactions are responsible for binding protons and neutrons to form nuclei, and in turn for binding quarks, forming baryons and mesons. Following the group-theoretical approach, the strong interaction can be described in terms of an $SU(3)$ local gauge symmetric theory, with the introduction of the color quantum number and 8 gauge bosons known as gluons. This theory is known as *quantum chromodynamics* (QCD). The features of QCD will be examined more fully in the following section, since its predictions are specifically tested in the analysis described in this dissertation.

Table I. Particles described by the Standard Model, with corresponding charge, couplings and mediating bosons.

	Particle	Charge ($|Q|$)	Strong	El-Mag	Weak
quarks	u c t	$+\frac{2}{3}$	✓	✓	✓
	d s b	$-\frac{1}{3}$	✓	✓	✓
leptons	ν_e ν_μ ν_τ	0	–	–	✓
	e μ τ	-1	–	✓	✓
	Mediating Bosons $\rightarrow$	8 gluons	γ	$W^{\pm} Z^0 H^0$	

In Table I, a summary of the known constituents of matter as described by the Standard Model is given. The quarks and leptons are separated into three distinct generations in accordance with their symmetry under weak interactions. The number of generations has been constrained experimentally to be three at the 98% confidence level by experiments at the Large Electron Positron collider (LEP) [13, 14, 15, 16].

Dirac once wrote [17] "*The only object of theoretical physics is to calculate results that can be compared with experiment,* and it is quite unnecessary that any satisfying description of the whole course of the phenomena should be given". While the predictions of the Standard Model are presently consistent with all confirmed experimental results, there are a number of reasons to believe that it offers an incomplete picture. For example, there are more than twenty free parameters that are needed from experiment. A complete theory should be able to provide these quantities. Also, the reason why there are exactly three generations is not explained by the Standard Model. In addition, the weakest inter-particle force, gravity, has been

omitted. For these reasons, some high energy physics theorists are looking to higher symmetry groups, such as $SU(5)$, as a possible route to a *grand-unification* of the four forces of nature. Meanwhile, experimentalists are performing experiments designed to look for new physics, and are testing the existing theory at ever more stringent levels in the hope that they will see a deviation from predictions that would be a signal of physics beyond the Standard Model.

B. Quantum Chromodynamics and Jets

Quantum chromodynamics is a *non-abelian* $SU(3)$ gauge invariant theory. The 8 gluons which mediate the strong force can self-couple, a feature that is not possessed by the photons arising in QED. Quarks are assigned a color quantum number from the three possibilities, red (R), green (G) or blue (B). The introduction of this additional quantum number was originally proposed [18] to provide an explanation for the fact that the Δ^{++} particle had been observed, though it should be forbidden by the Pauli exclusion principle and the Fermi spin statistics theorem. The Δ^{++} is a state made from three u quarks, in the spin configuration $(u \uparrow u \uparrow u \uparrow)$. By assigning each quark a different color quantum number, the Pauli exclusion principle is no longer violated. Moreover, by requiring that the quarks be arranged to have a color anti-symmetric wave function, the overall wave function of the Δ^{++} can be made anti-symmetric. All observed particles are postulated to be color singlets (net color zero), since otherwise the color interaction would be observable in nature, which does not seem to be the case. The color wave function for a baryon is taken to be

$$(qqq)_{\text{singlet}} = \sqrt{\frac{1}{6}}(RGB - RBG + BRG - BGR + GBR - GRB). \qquad (4)$$

The introduction of color also leads to expressions for hadronic decay cross sections that are in agreement with experiment. For example, the decay rate of $\pi^\circ \to 2\gamma$ is predicted to be proportional to the square of the number of colors N_c. Experiment yields $N_c = 2.98 \pm 0.11$. Also the observed ratio

$$R = \frac{\sigma(e^+e^- \to \text{hadrons})}{\sigma(e^+e^- \to \mu^+\mu^-)} \tag{5}$$

is consistent with the existence of three color quantum numbers.

1. The Parton Model

The term *parton* was first coined by Feynman and collectively refers to quarks and gluons, the fundamental constituents of hadronic matter. The proton is a complex mixture of quarks, gluons, and virtual quark-antiquark pairs that exist for very short periods of time in accordance with the uncertainty principle. At energies of a few MeV (i.e. energies at which typical experiments in nuclear physics are conducted) the strong force can reasonably be described in the context of virtual π-meson exchange. This indicates that individual partons are not quite being resolved. At center-of-mass energies of a few GeV, hard parton scatterings are observed experimentally in the form of collimated sprays of particles, or *jets*. For two-body processes, these jets are produced more or less back-to-back, as required by momentum conservation.

The lowest order $2 \to 2$ parton scattering processes are listed in Table II, along with the corresponding matrix elements squared and the relative probability of each term at an angle in the center-of-mass system $\hat{\theta} = 90°$ [19]. Lowest order Feynman diagrams are shown in Figure 1. The sub-process cross sections are of the form

$$\frac{d\hat{\sigma}}{d\hat{t}}(ab \to cd) = \frac{|\mathcal{M}|^2}{16\pi\hat{s}^2}, \tag{6}$$

Table II. QCD $2 \to 2$ process matrix elements squared, spin and color-averaged. q and q' represent distinct quark flavors, $g_s^2 = 4\pi\alpha_s$ is the coupling squared.

Subprocess	$\| \mathcal{M} \|^2 / g_s^4$	$\| \mathcal{M}(90^\circ) \|^2 / g_s^4$
$qq' \to qq'$	$\frac{4}{9}\frac{\hat{s}^2+\hat{u}^2}{\hat{t}^2}$	2.2
$q\bar{q}' \to q\bar{q}'$	$\frac{4}{9}\frac{\hat{s}^2+\hat{u}^2}{\hat{t}^2}$	2.2
$qq \to qq$	$\frac{4}{9}\left(\frac{\hat{s}^2+\hat{u}^2}{\hat{t}^2} + \frac{\hat{s}^2+\hat{t}^2}{\hat{u}^2}\right) - \frac{8}{27}\frac{\hat{s}^2}{\hat{u}\hat{t}}$	3.3
$q\bar{q} \to q'\bar{q}'$	$\frac{4}{9}\frac{\hat{t}^2+\hat{u}^2}{\hat{s}^2}$	0.2
$q\bar{q} \to q\bar{q}$	$\frac{4}{9}\left(\frac{\hat{s}^2+\hat{u}^2}{\hat{t}^2} + \frac{\hat{t}^2+\hat{u}^2}{\hat{s}^2}\right) - \frac{8}{27}\frac{\hat{u}^2}{\hat{s}\hat{t}}$	2.6
$q\bar{q} \to gg$	$\frac{32}{27}\frac{\hat{u}^2+\hat{t}^2}{\hat{u}\hat{t}} - \frac{8}{3}\frac{\hat{u}^2+\hat{t}^2}{\hat{s}^2}$	1.0
$gg \to q\bar{q}$	$\frac{1}{6}\frac{\hat{u}^2+\hat{t}^2}{\hat{u}\hat{t}} - \frac{3}{8}\frac{\hat{u}^2+\hat{t}^2}{\hat{s}^2}$	0.1
$qg \to qg$	$\frac{\hat{s}^2+\hat{u}^2}{\hat{t}^2} - \frac{4}{9}\frac{\hat{s}^2+\hat{u}^2}{\hat{u}\hat{s}}$	6.1
$gg \to gg$	$\frac{9}{4}\left(\frac{\hat{s}^2+\hat{u}^2}{\hat{t}^2} + \frac{\hat{s}^2+\hat{t}^2}{\hat{u}^2} + \frac{\hat{u}^2+\hat{t}^2}{\hat{s}^2} + 3\right)$	30.4

where $\hat{s} = (P_a^\mu + P_b^\mu)^2$ is the sub-process invariant mass squared, $\hat{t} = (P_a^\mu - P_c^\mu)^2$ and $\hat{u} = (P_a^\mu - P_d^\mu)^2$. Quarks are assumed to have zero mass.

In a proton-antiproton collision, the invariant mass for the sub-process ($\sqrt{\hat{s}}$) is related to the total invariant mass ($\sqrt{s}$) by the relation $\hat{s} = x_a x_b s$, where x_a and x_b are the momentum fractions carried by partons a and b respectively. The lowest order QCD cross section for two-jet production is given by

$$\frac{d\hat{\sigma}}{dP_t^2}(AB \to 2 \text{ jets}) = \sum_{abcd} \int\int dx_A\, dx_B\, f_{a/A}(x_A)f_{b/B}(x_B)\frac{d\hat{\sigma}}{dP_t^2}(ab \to cd), \quad (7)$$

where ab and cd are the initial and final partons respectively, and integrations run from $x_A x_B \geq 4P_t^2/s$ to $x_A = x_B = 1$. The quantity $f_{a/A}$ represents the parton *structure function*, which is the probability of finding a parton of type a with momentum
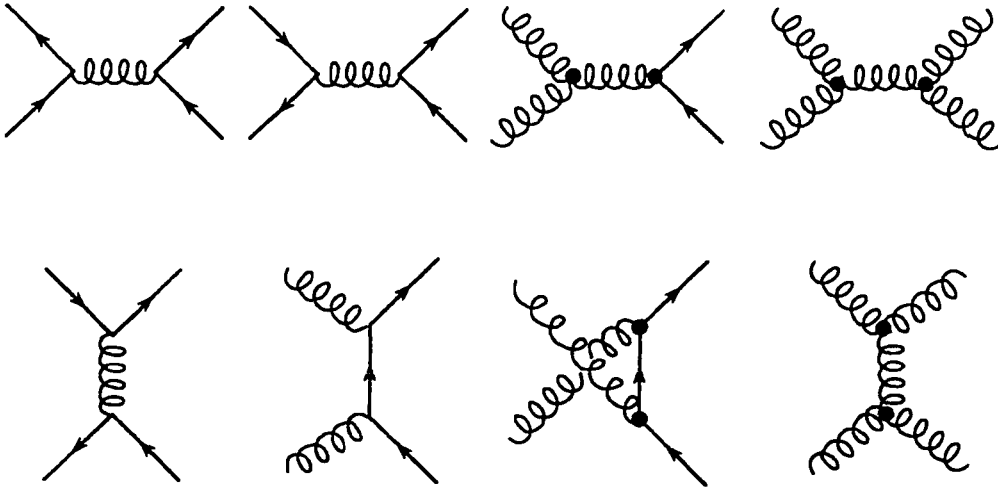
Figure 1. Lowest order Feynman diagrams for $2 \rightarrow 2$ parton scattering.

fraction x in hadron A. The transverse momentum of a parton is denoted by P_t. Since $E^2 = P^2 + m^2$, transverse momentum closely approximates transverse energy E_t, assuming the mass of the parton (m) is much smaller than its energy. At hadron colliders, cross sections are typically evaluated in terms of transverse quantities such as E_t and P_t. Such quantities are independent of fragmentation products which exit down the beam line.

Cross sections for jet production increase rapidly with available center-of-mass energy, $\sqrt{s}$. In each hadron the momentum fraction x required to produce a jet of a given energy gets smaller with increasing $\sqrt{s}$, and the number of partons with this x increases. The Tevatron at Fermilab produces $p\bar{p}$ collisions at a center-of-mass energy of 1.8 TeV, and in this energy régime QCD jet production dominates. Since quarks and gluons carry typically 30% or less of the parent hadron momentum, one
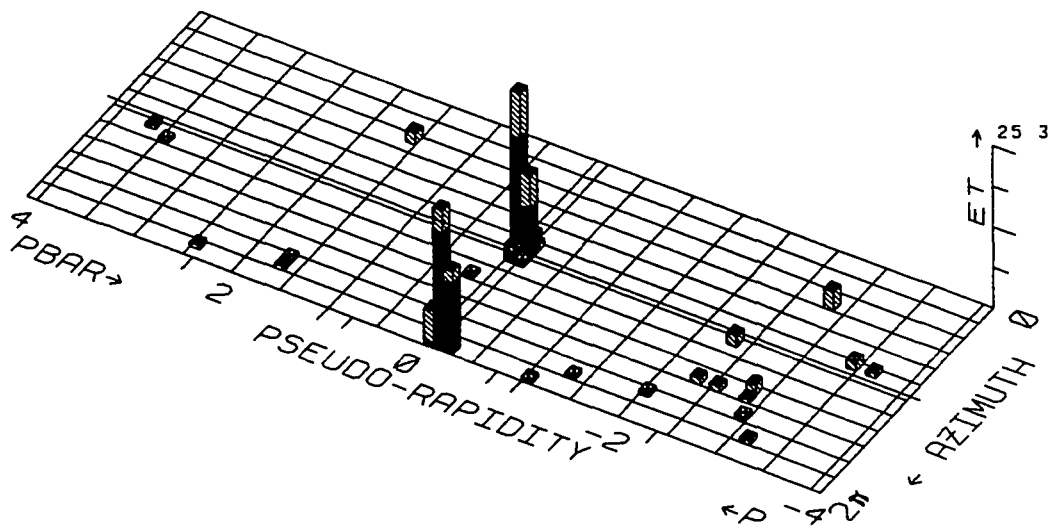
Figure 2. A typical dijet event taken during the 1988/89 run of the Tevatron. The plot shows energy deposited in a cylindrical region surrounding the beam line, the cylinder having been cut and laid flat.

does not expect many jets above a few hundred GeV/c in transverse momentum. A typical dijet event observed during the 1988/89 collider run of the Tevatron is shown in Figure 2. Both jets have a P_t of approximately 50 GeV/c.

2. Structure Functions and Deep Inelastic Scattering

In calculating cross sections using Equation 7 the parton structure functions, $f_{a/A}$, must be known. In practice, these are measured using deep inelastic scattering of electrons, neutrinos and photons at low momentum transfer relative to Λ_{QCD} ($\Lambda_{QCD} \sim 0.2 - -0.4$ GeV/c, see next section for more details). The valence quark content of the proton is (u, u, d), but in addition there is a cloud of virtual $q\bar{q}$ pairs. Experimentally, the available momentum of the proton cannot be completely accounted

for by valence and sea quarks alone. The remainder is postulated to be due to the presence of gluons. The gluon structure function can be experimentally determined [19] using the process

$$\gamma N \rightarrow \psi + \text{ anything,} \qquad (8)$$

where ψ is a charm-anticharm $(c\bar{c})$ bound state. Predictions of the parton model indicate that the structure functions depend only on the momentum fraction, a phenomenon known as *Bjorken scaling*. However, this model makes the assumption that quarks and gluons behave like point particles. In the framework of QCD, the inclusion of gluon radiation from a quark that has been struck by a lepton probe leads to an explicit non-scaling Q^2 dependence. The result is the *QCD-improved* parton model. A procedure for evolving the structure functions as a function of Q^2 is provided in the Altarelli-Parisi equations [20].

There currently exists a proliferation of structure function parameterizations. The differences are small in the regions where there is fitted data, arising mainly from small inconsistencies between the results of electron and neutrino experiments. However, in untested regions where data must be extrapolated there can be a much more significant variation. In Figure 3 the Q^2 behaviour of the Duke and Owens set 1 [21] structure function is shown. In QCD analyses, structure function uncertainty is typically taken into account by using several different parameterizations in order to
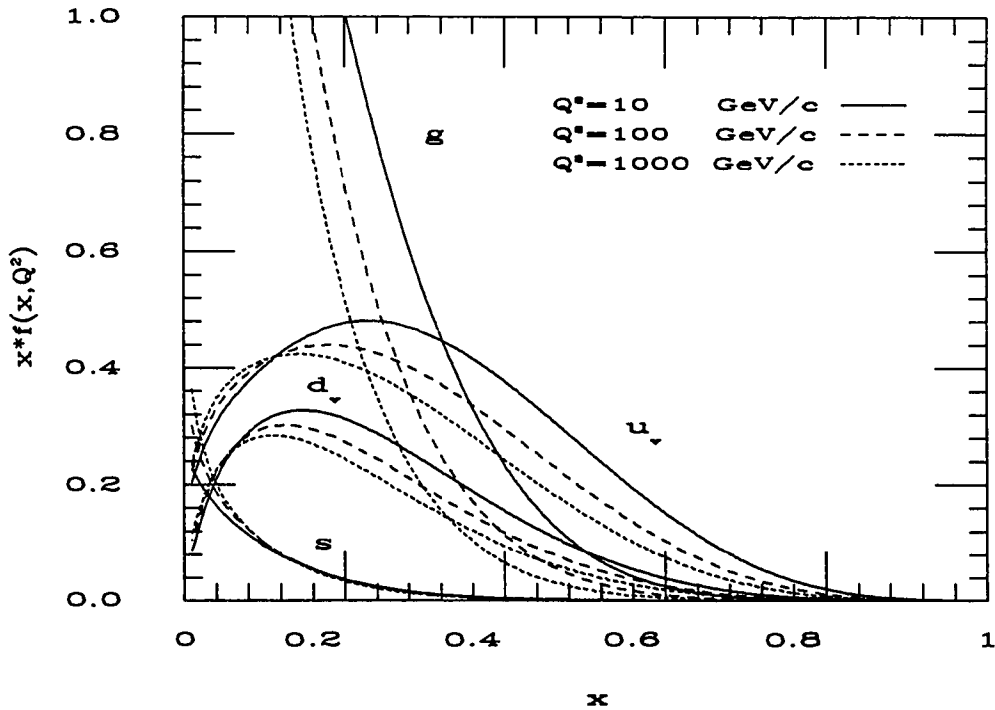
Figure 3. Q^2 evolution of structure functions for Duke and Owens set 1.

see the variation in results obtained.

3. The Running of α_s

Due to the common feature of local gauge invariance, there is a good analogy between QED and QCD higher order processes. In the case of QED, after the renormalization procedure the scattered leptons can be regarded as having a Q^2-dependent charge [22]

$$e(Q^2) = e \left[1 - \frac{\alpha}{15\pi} \frac{Q^2}{m^2} + \cdots \right]^{1/2}, \tag{9}$$

where m is the lepton mass. In terms of the fine-structure constant α, at large Q^2 a logarithmic dependence is obtained [23]

$$\alpha(Q^2) = \alpha \left[1 + \frac{\alpha}{3\pi} \ln \left(\frac{Q^2}{m^2} \right) + \cdots \right]^{1/2}. \tag{10}$$

Therefore the effective coupling strength $\alpha(Q^2)$ increases at large $\mid Q^2 \mid$. In the limit $\mid Q^2 \mid >> m^2$, the dominant contributions (or *leading logarithms*) in Equation 10 can be isolated and summed in perturbation theory. The result is

$$\alpha(Q^2) = \frac{\alpha}{1 - (\alpha/3\pi)\ln(Q^2/M^2)}, \tag{11}$$

where M^2 is a cut-off parameter, representing an upper bound on the fermion loop momentum [24]. In order to eliminate the dependence of $\alpha(Q^2)$ on the cutoff M, a reference (or renormalization) momentum μ is chosen. We then find

$$\alpha(Q^2) = \frac{\alpha(\mu^2)}{1 - (\alpha(\mu^2)/3\pi)\ln(Q^2/\mu^2)} \tag{12}$$

for large Q^2.

By analogy, the strong structure constant $\alpha_s = \alpha_s(Q^2)$ can be postulated. Again, an arbitrary parameter μ^2 with dimensions of [mass]^2 is introduced so that the reference value of α_s is $\alpha_s(\mu^2)$. The variation of α_s with Q^2 can be obtained through the use of perturbation theory as with QED, but now there are additional Feynman diagrams to consider since the gluon carries color charge. First order loop corrections
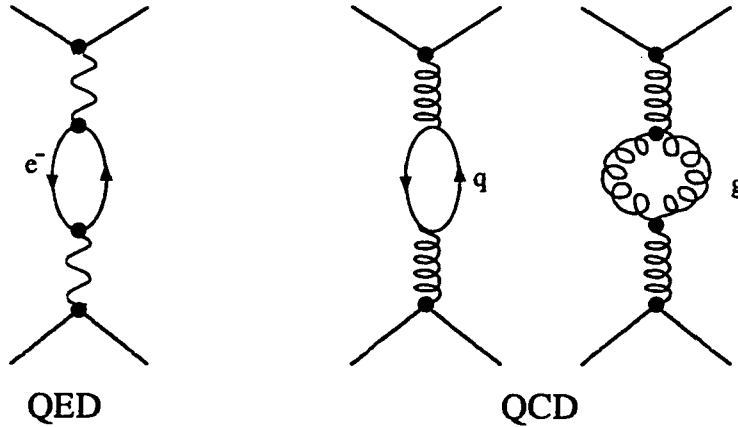
Figure 4.   First order loop correction for QED (left) and two first order loop correc-
tions for QCD (right), including the gluon self-coupling term.

for QED and QCD are shown in Figure 4.   The resulting QCD dependence is [25,
26]

$$\alpha_s(Q^2) = \frac{\alpha_s(\mu^2)}{1 + (\alpha_s(\mu^2)/12\pi)(33 - 2f)\ln(Q^2/\mu^2)}. \tag{13}$$

The quark loop gives the factor $-2f$, where f is the number of quark flavors. The
term arising from the gluons has the opposite sign, and it causes $\alpha_s(Q^2)$ to *decrease* at
large Q^2 if $f \leq 16$. In fact $\alpha_s(Q^2) \to 0$ as $Q^2 \to \infty$, a property known as *asymptotic
freedom*.

Equation 13 may be simplified by introducing the parameter Λ_{QCD} in the fol-
lowing way

$$\ln \Lambda_{QCD}^2 = \ln \mu^2 - \frac{12\pi}{(33 - 2f)\alpha_s(\mu^2)}, \tag{14}$$

which then yields

$$\alpha_s(Q^2) = \frac{12\pi}{(33 - 2f)\ln(Q^2/\Lambda_{QCD}^2)}. \tag{15}$$
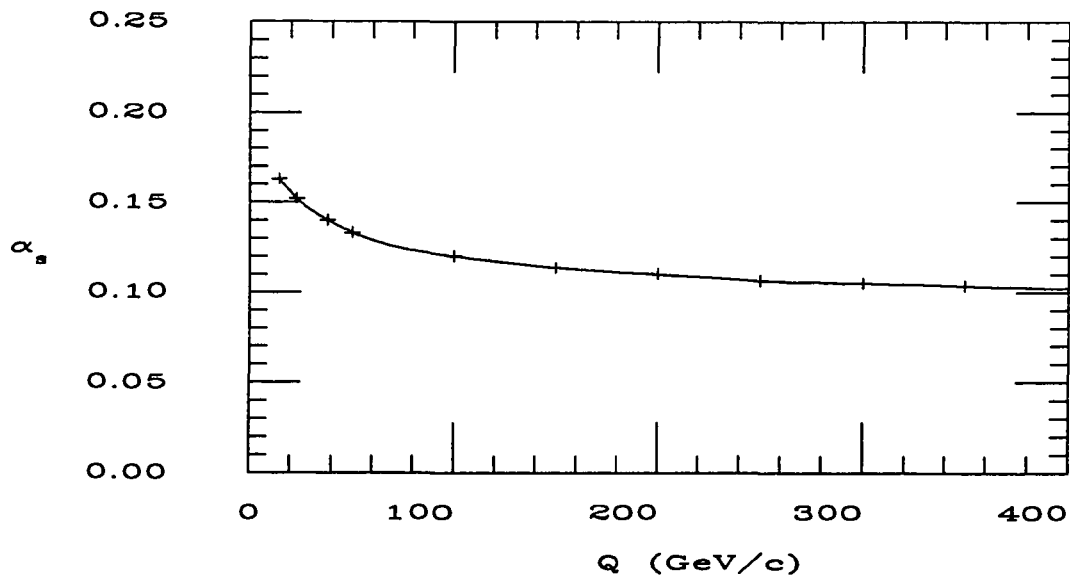
Figure 5.   The dependence of α_s on Q, with $\Lambda_{QCD} = 0.2$ GeV/c.

Thus α_s depends only on one parameter, Λ_{QCD}, which is found by experiment to be typically in the range 0.2–0.4 GeV/c. This can be thought of as the energy scale at which the confining forces of the strong interaction start to take effect. Note that the magnitude of α_s restricts the applicability of perturbation theory to processes with sufficiently high values of momentum transfer. Figure 5 shows the Q^2 dependence of α_s obtained with a leading-log calculation.

4.   The Fragmentation Process

Although partons are postulated to take part in hard scattering processes, they have never been directly observed. Instead, colorless hadrons emerge, having been pulled from the vacuum by color lines of force in the *fragmentation* process. At high energies, these hadrons are produced in well collimated jets around the initial parton

direction. The exact mechanism of fragmentation is currently unknown since the process involves interactions at low Q^2 and therefore defies calculation by methods of perturbative QCD. However, there exist models that provide a successful description of the global features of fragmentation. Two such examples are the string model, developed primarily by the Lund group of Sweden [27, 28, 29, 30] and the Feynman-Field independent fragmentation model [31].

The model used in this analysis is the Feynman-Field model. The concept used is that of a moving quark producing a chain of lighter mesons which carry off part of the momentum fraction. The initial quark q_1 creates a color field in which a new light pair $q_2\bar{q}_2$ is produced, q_1 then combines with $\bar{q}_2$ leaving q_2 to continue the reaction, and so on. The momentum fraction z is considered the only relevant variable. Defining $D(z)$ as the probability density for producing any meson with momentum fraction z, then D satisfies the equation,

$$D(z) = f(z) + \int_z^1 f(1 - z')D(z/z')dz'/z'. \tag{16}$$

This equation can be interpreted as describing a meson which is either the first in the chain with probability $f(z)$, or is part of a similar chain started by q_2 with probability $f(1 - z')$. The original Feynman-Field parameterization used the relation

$$f(z) = 1 - a + 3a(1 - z)^2, \tag{17}$$

with $a = 0.77$. The observed transverse spreading of jets was included by giving quarks a Gaussian P_t distribution relative to the initial parton direction, with

$\sigma = 0.35$ GeV/c. This process conserves momentum but not energy, which necessitates a final rescaling of momenta after fragmentation. The model assumes each parton evolves independently.

5. Underlying Event

So far we have been concerned mainly with the scattering of partons inside composite hadrons. However, we must also consider the remainder of the hadron. This remnant also fragments, producing a fairly uniform radiation of relatively low energy particles, known as the *underlying event*. The total underlying event energy is, to a good approximation, independent of the details of the hard scattering. Therefore the identification of jets at high enough energies is not significantly impaired. Since the process occurs at low Q^2 it cannot be calculated perturbatively and hence is not well understood. Typically, phenomenological models are used to model its effects.

C. Experimental Jet Production

1. The Observation of Jets at e^+e^- Colliders

The first experimental observation of jets was made in 1977 at SPEAR, an e^+e^- storage ring at SLAC (Stanford Linear Accelerator Center) [32]. Hadrons were observed to be loosely clustered about an axis. Assuming this axis to be the quark direction, the resulting distributions were found to be in agreement with QCD predictions for the process $e^+e^- \rightarrow q\bar{q}$. This indicated for the first time that the behaviour of individual quarks could be studied. The center-of-mass energy of SPEAR was fairly low and therefore the hard scattering momentum transfer (Q =6–8 GeV/c) was

not very far above that of the fragmentation process. The resulting low particle multiplicities for jets made their identification difficult. For this reason, a host of global event parameters (e.g. acoplanarity, spherocity) were introduced in an attempt to quantify the amount of jet activity in an event.

When PEP and PETRA energies were reached (Q =30–40 GeV/c), the production of back-to-back pairs of jets (or *dijets*) was the main process leading to hadron production. In addition, there were events where three jets could be clearly seen. These three-jet events provided the first experimental evidence for gluon emission in the process $e^+e^- \rightarrow q\bar{q}g$. Since gluons carry color charge, they are able to couple to either initial or final parton legs with coupling strength α_s. With this data, a value for α_s [33] was determined for the first time. The result was $\alpha_s(Q) = 0.115 \pm 0.005$. Also, by studying the angular jet distribution the gluon was determined experimentally to have spin 1 [34]. More recently, using e^+e^- collisions at a center-of-mass energy of 50–57 GeV combined with results from experiments operating at lower energies, the AMY collaboration has demonstrated that α_s decreases with Q^2, consistent with the predictions of QCD [35].

With higher energies available, jets become more clearly defined. This reflects the fact that fragmentation effects are less important relative to the hard scattering process. This prompted a shift from a description of jets using global event parameters to quantities obtained using clustering techniques.

2. Jets in Hadron Colliders

The development of hadron colliders was inspired by the desire to observe particle interactions at ever higher energies. Since the proton is approximately 2000 times

heavier than the electron, it emits far less synchrotron radiation when travelling along a circular path ($E_{\text{synchrotron}} \propto (E/M)^4$). Thus protons can be accelerated to much higher energies than electrons before the process becomes limited by synchrotron loss. The first hadron collider was the ISR (Intersecting Storage Ring) at CERN, which became operational in 1971 and produced pp collisions at $E_{CM} = 63$ GeV. The composite nature of protons, however, resulted in parton scattering far below this energy. The development of the technology of anti-proton ($\bar{p}$) storage and cooling [36] in conjunction with advances in accelerator physics soon prompted physicists to propose building a very high energy $p\bar{p}$ collider [37]. By 1981, the CERN Super Proton Synchrotron (SPS) had successfully produced $p\bar{p}$ collisions at $E_{CM} = 540$ GeV. The following year, the UA2 collaboration published a paper claiming the observation of large P_t jets in their detector [38].

The Tevatron, at Fermilab in Batavia, Illinois is the highest center-of-mass $p\bar{p}$ collider currently in existence. The first run with the CDF (Collider Detector at Fermilab) in place collected an integrated luminosity of 30 nb^{-1}. The occurrence of large isolated P_t clusters in the event displays indicated immediately that jets were being produced. Subsequent analyses of jet events provided strong confirmation of QCD and the parton model [39, 40]. The most recent run of the Tevatron in 1988/89 has also led to interesting jet physics, including a sensitive test of quark compositeness using the inclusive jet cross section in the central region of the detector [41]. Also, a study of the topology of three-jet events produced via gluon emission (or *bremsstrahlung*) has been performed [42], showing good agreement between data and the predictions of QCD.

3. Outline of Analysis

This dissertation is concerned with the analysis of four-jet events using data collected with a special trigger installed during the 1988/89 run. The mechanism for four-jet production assuming a single hard parton scatter is the simultaneous emission of two gluons (or *double gluon bremsstrahlung*). The four-jet data provides a means with which to test the predictions of QCD, as leading order calculations for this process have been performed and are available.

In the context of the parton model, there is another possible scenario for four-jet production, namely the simultaneous scattering of two pairs of partons within the same $p\bar{p}$ interaction. Such a double parton scattering process, if observable, will provide valuable information on parton correlations within the proton. Double parton scattering is also a potential background to processes involving the production of W or Z pairs such as Higgs decay or gluino decay through unstable supersymmetric particles [43].

The rate of double parton scattering is expected to increase quite dramatically with center-of-mass energy [44]. Currently, both the United States and Europe are in the process of building hadron colliders capable of achieving center-of-mass energies an order of magnitude higher than the Tevatron. These are the Superconducting Super Collider (SSC) in Waxahachie, Texas, and the Large Hadron Collider (LHC) in Geneva, Switzerland. Currently the Tevatron collider most closely reproduces the experimental environment of these higher energy machines. A study of double parton scattering at the Tevatron is therefore important in order to get a glimpse of what one might expect to see when these machines become operational.

CHAPTER II

FOUR-JET PRODUCTION

A. Double Gluon Bremsstrahlung

In a two-body parton interaction, gluons may be emitted from either the initial or final parton legs. The process involving the emission of *two* gluons is referred to as double gluon bremsstrahlung and is shown schematically in Figure 6a). A few of the contributing Feynman diagrams can be seen in Figure 6b). Under the right circumstances, this process may result in the production of four separate jets in the detector. For this to occur, the partons must be sufficiently energetic and well-separated. A typical example of a four-jet event taken during the 1988/89 run is shown in Figure 7. The energy clusters all cover several calorimeter towers, contain both hadronic and electromagnetic energy, and have an energy deposition pattern that decreases fairly monotonically from the center of the cluster. The precise relation between these clusters and theoretical partons is discussed fully in Chapter IV. The availability of such clean jet events demands an experimental check of the existing theoretical predictions for this process.

In the calculation of multi-parton amplitudes in QCD, one finds that the number of contributing Feynman diagrams increases very rapidly as a function of the number of final state partons. In Table III, the number of diagrams involved in the gluon scattering process $gg \rightarrow n\text{-}g$ is listed for a few values of n. The leading order (or *tree-level*) calculation of the four-jet matrix element took a team of theoretical
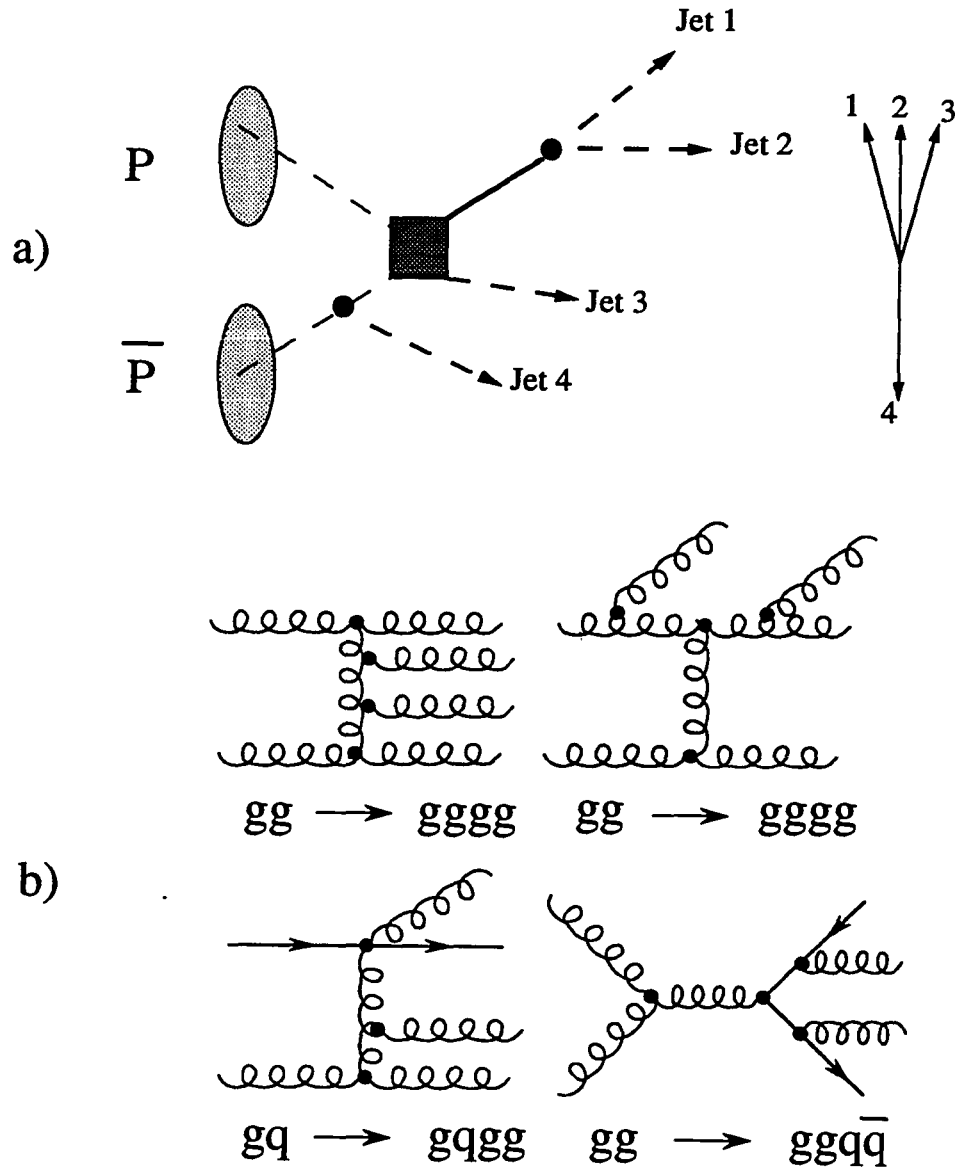
Figure 6. a) Schematic diagram of the double gluon bremsstrahlung process, b) a few examples of Feynman diagrams which contribute to the 2 → 4 parton scattering matrix element. The stick figure shows a typical final state parton configuration in the transverse xy plane.
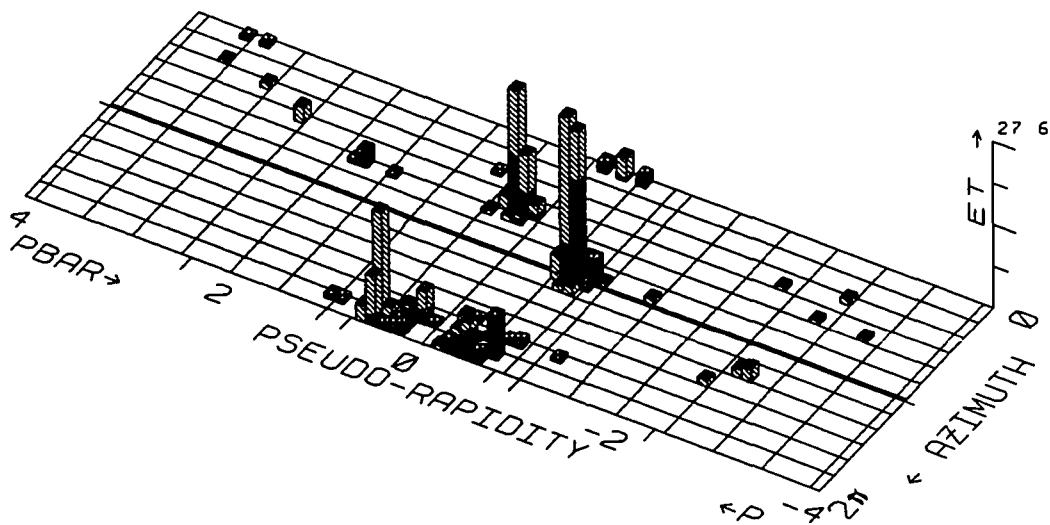
Figure 7. A typical four-jet event taken during the 1988/89 run.

Table III. The number of Feynman diagrams contributing to the process $gg \rightarrow$ n-gluons.

n	2	3	4	5	6
diagrams	4	25	220	2485	34300

physicists several years to complete [45]. Some of the terms in the calculation can be represented in a relatively simple manner, such as the $gg \rightarrow gggg$ matrix element which in a compact notation can be written [46],

$$| \mathcal{M}_4(g_1,\ldots,g_6) |^2 = 2g_s^8 N^4(N^2 - 1) \left(\sum_{i>j} s_{ij}^4 \right) \sum \frac{1}{s_{12}s_{23}\cdots s_{61}} + \mathcal{O}(N^{-2}). \quad (18)$$

Here N is the number of colors and s_{ij} is the product of parton four-momenta for partons i and j. Other terms are not as simple; for example the matrix element for the sub-process $gq \to gqgg$ involves over 1000 separate s_{ij} terms.

Due to the complexity of the complete solution, a considerable amount of work has been invested into producing approximations so that computer simulations can be performed in a reasonable amount of time. The approximation used primarily in this analysis is that of Kunszt and Stirling [47]. This contains the exact $gg \to gggg$ matrix element but models processes involving quarks with the $gg \to gggg$ functional form scaled by a factor of 4/9 for each quark replacing a gluon. The value of this factor was tuned in order to bring the approximation into good agreement with the exact calculation. An alternative approximation which is due to Maxwell [48] uses the technique of *gluon reduction* [49] to model quark sub-processes.

The denominator in Equation 18 may go to zero if two gluons are collinear, or if a parton has zero momentum (the latter case is sometimes referred to as the *infra-red* divergence). This problem may also occur for the matrix elements involving quarks instead of gluons, since quarks are approximated as being massless. Such infinities in the cross section may be avoided by simply requiring a minimum parton momentum and angular separation when modelling events using a QCD Monte Carlo program.

B.   Double Parton Scattering

The possibility of the simultaneous hard scattering of parton pairs has recently been discussed by several authors [50, 51, 52]. The mechanism is shown schematically in Figure 8a), and a few of the contributing Feynman diagrams can be seen in

Figure 8b). To leading order in α_s, the result of this scattering will be a pair of back-to-back dijets.

The double parton cross section may be expressed in the following form [53]:

$$\frac{d\sigma^{(4)}}{d^2q_{1_\perp}d^2q_{2_\perp}dy_1dy_2dy_3dy_4} = \sum_{q/g}\frac{1}{s^2}\int \Gamma(x_1,x_2;b_\perp)\Gamma(x_3,x_4;b_\perp)d^2b_\perp\frac{\hat{s}_1}{\pi}\frac{d\sigma}{d\hat{t}_1}\frac{\hat{s}_2}{\pi}\frac{d\sigma}{d\hat{t}_2}. \quad (19)$$

In Equation 19, y_i and $q_{i_\perp}$ are respectively the outgoing parton rapidities (see Appendix A) and transverse momenta; $\hat{s}_i$, $\hat{t}_i$ and $\hat{u}_i$ are the sub-process Mandelstam variables defined in Chapter I Section 1, with cross sections $d\sigma$ (see Table II); finally $\Gamma(x_1,x_2;b_\perp)$ represents the two-parton structure function with fractional momenta x_1, x_2 and transverse relative distance within the hadron $b_\perp$. Although not explicitly written, the distribution functions also depend on the Q^2 of the process. The form of Equation 19 suggests that the double parton cross section is of order $1/E_t^2R^2$ with respect to the double bremsstrahlung cross section, where R represents the hadron dimension (approximately 1 fm). The dependence on $1/R^2$ comes from the dimensions of the double structure functions and from integration over the parton transverse distance $b_\perp$.

In the kinematical region of interest, namely E_t small with respect to $\sqrt{s}$, the typical fractional momenta involved in parton collisions are rather small. Consequently we do not expect parton correlations to be important. Therefore a factorized form may be taken for the double structure functions,

$$\Gamma(x_1,x_2;b_\perp) = G(x_1)G(x_2)(1-x_1-x_2)F(b_\perp), \quad (20)$$
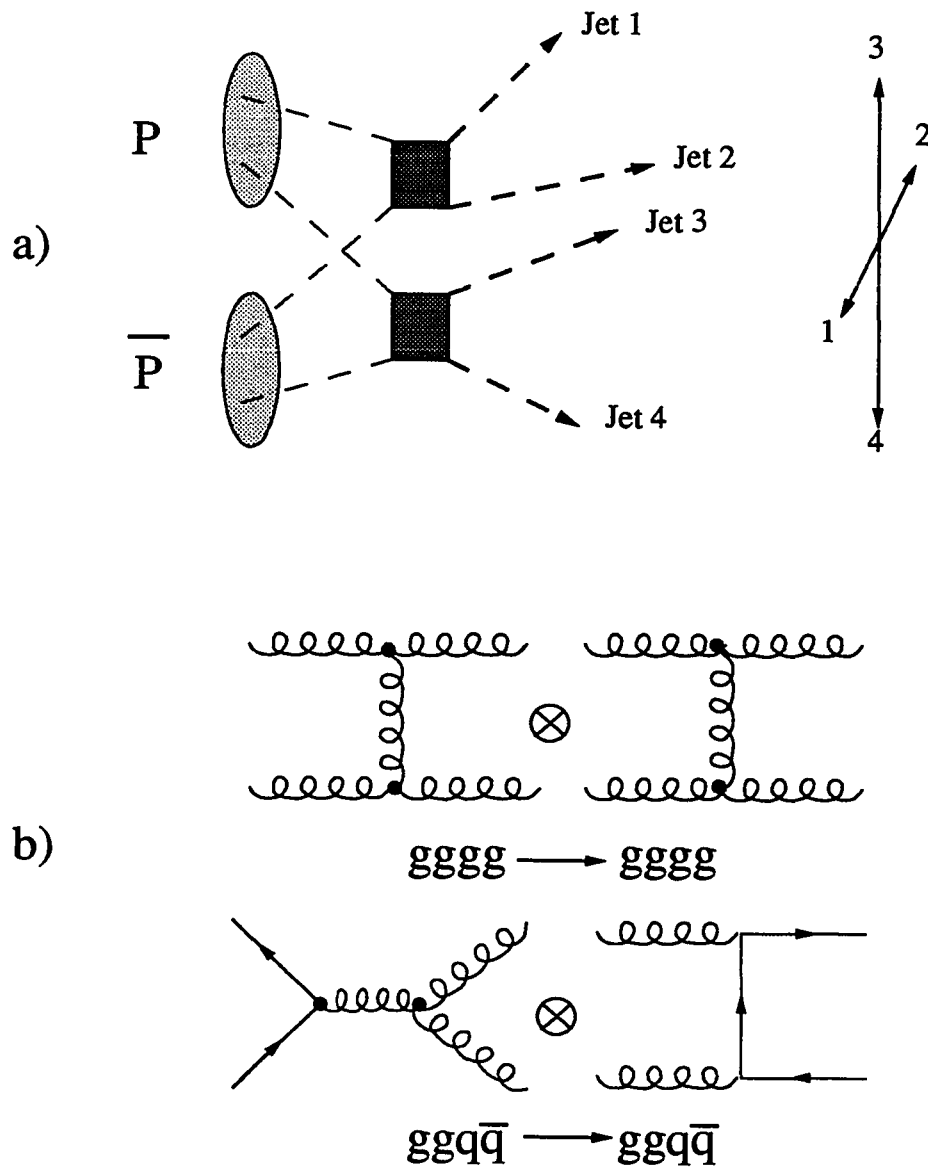
Figure 8. a) A schematic illustration of the double parton scattering process, b) a few of the relevant Feynman diagrams. The stick figure shows the balanced topology typical of double parton jets in the transverse xy plane.

where $G(x)$ refers to the usual single parton structure function. This factorization allows a re-expression of Equation 19 as follows:

$$\frac{d\sigma^{(4)}}{d^2q_{1\perp}d^2q_{2\perp}dy_1dy_2dy_3dy_4} = \frac{1}{2\pi R^2}\sum_{q/g}\frac{1}{s^2}G(x_1)G(x_2)G(x_3)G(x_4)\frac{\hat{s}_1}{\pi}\frac{d\sigma}{d\hat{t}_1}\frac{\hat{s}_2}{\pi}\frac{d\sigma}{d\hat{t}_2}, \quad (21)$$

where the dependence on $b_\perp$ has been included using the function

$$F(b_\perp) = \frac{1}{\pi R^2}\exp(-b^2/R^2). \quad (22)$$

The factorized double parton cross section of Equation 21 may be written in simplified form as,

$$\sigma_{DP} = \frac{\sigma_{dijet}^2}{2\cdot\sigma_{eff}}, \quad (23)$$

where σ_{dijet} is the $2\to2$ body cross section, and σ_{eff} is the so-called *effective* cross section. The factor of 2 is a consequence of Poisson statistics and is included merely by convention.

The physical significance of the effective cross section can be seen by considering a single $p\bar{p}$ interaction of integrated luminosity $\mathcal{L}$. Using Equation 23, the number of double parton interactions is then given by

$$N_{DP} = \mathcal{L}\cdot\sigma_{DP} = (\mathcal{L}\cdot\sigma_{dijet})\left[\left(\frac{1}{2\sigma_{eff}}\right)\cdot\sigma_{dijet}\right]. \quad (24)$$

The first term represents the number of dijet events, and the second term corresponds to the number of additional dijet interactions. Therefore we may associate the term $1/2\sigma_{eff}$ with an *effective luminosity*. Now, in producing the original dijet interaction a $p\bar{p}$ collision must have occurred. If we assume that the partonic remnants interact inelastically, then $2\sigma_{eff}$ can be associated naïvely with the total inelastic cross section

of approximately 40 mb. However, since the first interaction preferentially selects small impact parameters, the effective luminosity is increased by roughly a factor of 2.3 [54]. This suggests that a value $2\sigma_{\text{eff}} = 17.3$ mb, or $\sigma_{\text{eff}} = 8.7$ mb may be used in a preliminary estimation of the double parton cross section.

In order to get a quantitative measure of the relative double parton to double bremsstrahlung cross section at $\sqrt{s} = 1.8$ TeV, a parton-level Monte Carlo model has been constructed by merging together consecutive dijet events, with a corresponding cross section scaled by $1/2\sigma_{\text{eff}}$, with $\sigma_{\text{eff}} = 8.7$ mb. The model is described in more detail in Chapter VI, Section A. Figure 9a) shows the cross sections for both processes as a function of the P_t of the smallest parton. The double parton cross section falls off significantly faster than the double bremsstrahlung cross section. As expected, the ratio of cross sections closely obeys the relation

$$\frac{\sigma_{\text{DP}}}{\sigma_{\text{DB}}} \sim \frac{1}{P_t^2}. \tag{25}$$

In Figure 9b) both cross sections are plotted as a function of the scalar $\sum P_t$ of all four partons generated. These figures indicate that the double parton cross section will be outstripped by the double bremsstrahlung cross section at all practical P_t thresholds available to CDF (jet $P_t > 15$ GeV/c). The search for double parton scattering will greatly benefit from the inclusion of low P_t jets if possible. In practice, this must be weighed against the fact that uncertainties on jet resolution and energy scale increase

significantly at low P_t.

Having examined the behaviour of the double parton and double bremsstrahlung relative cross sections as a function of P_t, we now turn to their dependence on center-of-mass energy, E_{CM}. The rate of double parton scattering depends strongly on the number of partons in each colliding hadron, $N(x, Q^2)$. In the simplest approximation,

$$\sigma_{DP} \propto [N(\xi, Q^2)]^2, \tag{26}$$

where σ_{DP} represents the double parton scattering cross section. The corresponding dependence on N for the double bremsstrahlung cross section σ_{DB} is linear:

$$\sigma_{DB} \propto N(\xi, Q^2). \tag{27}$$

If the number of partons is large enough, then the double parton process will dominate. Using simple considerations [55] the number of partons with a given momentum fraction x at momentum transfer Q^2 can be approximated by

$$\ln N(x, Q^2) \sim \sqrt{2\zeta y}, \tag{28}$$

where

$$\zeta = \ln \ln Q^2, \tag{29}$$

and

$$y = \ln \frac{1}{x}. \tag{30}$$

Thus, for a given Q^2, parton densities increase with decreasing x. Since lower values of x are probed by experiments operating at higher center-of-mass energies, such experiments will produce *significantly more* double parton events. Note that the
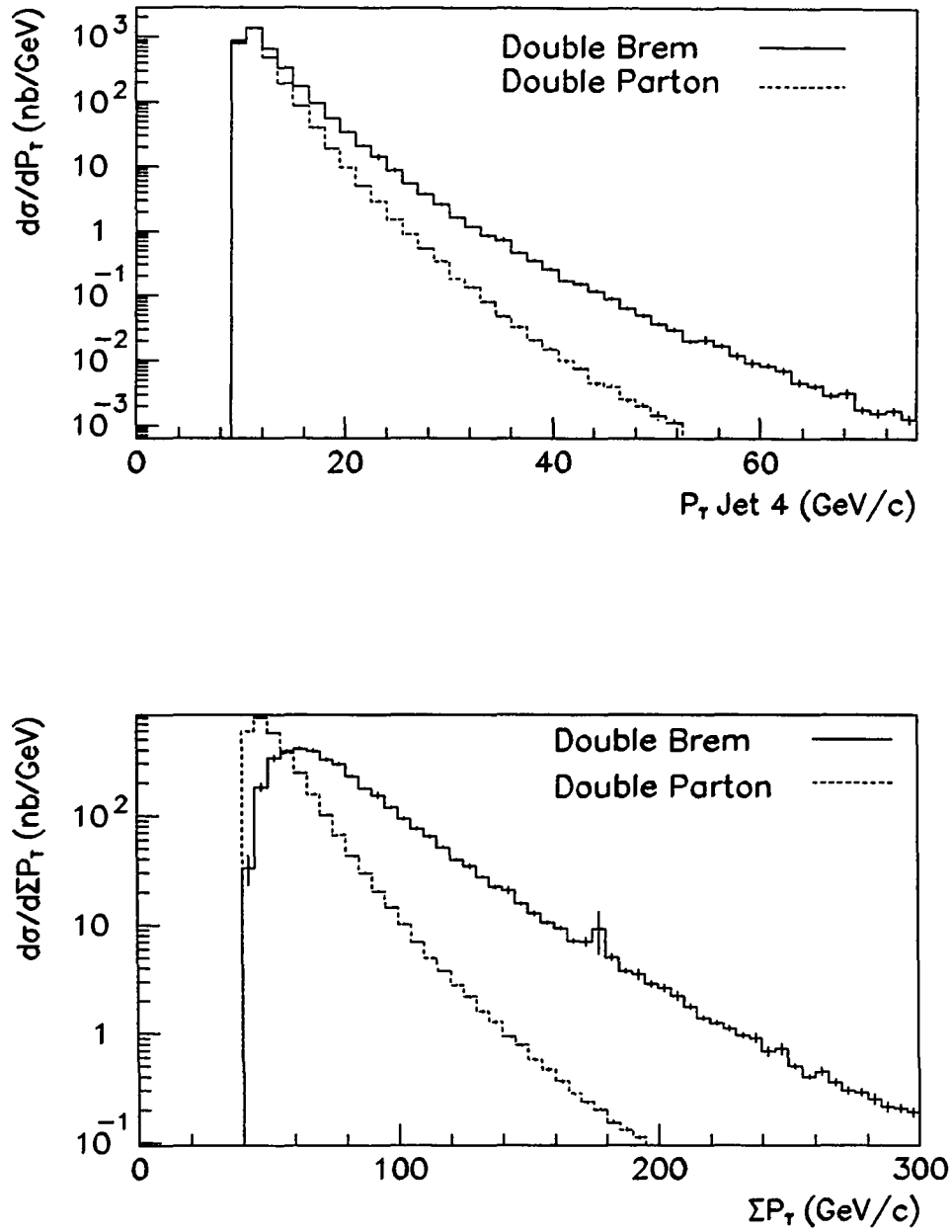
Figure 9. The double parton and double bremsstrahlung cross sections as a function of a) the P_t of the smallest parton generated and b) the scalar $\sum P_t$ of all four partons generated. A value of $\sigma_{\text{eff}} = 8.7$ mb has been used, with structure function set EHLQ1 and $Q = \langle P_t \rangle$.

approximations used do not hold as $x \to 0$, since eventually partons will overlap in their transverse direction. At energies of order 10 TeV or below, however, such overlap is negligible [56, 57].

Table IV shows the results of a calculation by Humpert and Odorico [51] giving estimations of integrated cross sections for both double parton and double bremsstrahlung scattering. The form taken for the double parton cross section is:

$$d\sigma_{\rm DP} = \sum_{q/g} \frac{d\hat{\sigma}_{12} d\hat{\sigma}_{34}}{\pi R^2} V(x_1, x_3) \cdot \bar{V}(x_2, x_4). \tag{31}$$

Here the factor πR^2 is the total inelastic cross section, which can be interpreted as the hadron size. The terms $V(x_k, x_l)$ are two-parton distributions, assumed to be the product of two single-parton distributions multiplied by a momentum-conserving phase space factor. The two-parton cross sections are denoted $d\sigma_{ij}$ and a value of $\pi R^2 = 40$ mb has been used (N.B. this number is subject to fairly large errors). As expected, the table indicates that the double parton cross section increases substantially faster than the double bremsstrahlung cross section as a function of E_{CM}. Therefore higher center-of-mass energies the four-jet double parton signal will be *less obscured* by background due to simultaneous gluon emission. Studies have also indicated that differences between topological variables formed with double parton and double bremsstrahlung events become more pronounced as a function of E_{CM} [51].

It should be noted that Table IV shows rates for both processes for partons with $P_t = 15$ GeV/c at $E_{CM} = 2$ TeV as being similar. However, experiment has recently shown [54] that in fact double bremsstrahlung strongly dominates. Although

Table IV. Estimated values of the total double parton (DP) and double gluon emission (DB) cross sections for a range of center-of-mass energies and minimum P_t cutoffs. These numbers have been taken from reference [51].

E_{CM} [TeV]	P_T [GeV/c]	σ_{DB} [cm²]	σ_{DP} [cm²]
0.62	10	2.5×10^{-31}	1.3×10^{-30}
	15	1.3×10^{-32}	1.7×10^{-32}
	20	1.5×10^{-33}	6.4×10^{-34}
2	10	5.6×10^{-30}	1.1×10^{-28}
	15	6.0×10^{-31}	3.6×10^{-30}
	30	7.3×10^{-33}	5.4×10^{-33}
20	10	2.0×10^{-28}	1.1×10^{-26}
	15	3.4×10^{-29}	9.2×10^{-28}
	30	1.2×10^{-30}	8.6×10^{-30}

the magnitude of both cross sections are inaccurate, their *relative* behaviour should be reliable.

C. Topological Differences

By making use of topological differences, a search for double parton scattering can be performed even with a large background resulting from the double bremsstrahlung process. The two main features that provide discrimination are P_t-balancing, and angular correlations. Double parton scattering tends to produce two pairs of dijets. These pairs should approximately balance in $\vec{P_t}$, which is not the case for jets produced by double bremsstrahlung. Also, gluons are preferentially emitted at small angle. Therefore there should be strong angular correlations between jets in events

produced by double gluon bremsstrahlung. Conversely, the dijet pairs produced by double parton scattering should be uncorrelated. Using this information, topological variables may be constructed which have significantly different shapes for the two processes. These variables can then be used to statistically extract the fraction of double parton events contained in the data. This procedure is described in detail in Chapter VI, Sections B and C.

D. Other Backgrounds

The most significant background to the double parton process at Tevatron energies is the production of four jets by the double bremsstrahlung mechanism. However, as discussed in the previous section, there is a marked difference in the topology of these two types of event which should in principle allow them to be separated. Conversely, there are other processes which lead to pairs of back-to-back jets, and which are therefore indistinguishable from double parton events.

1. Double Interactions

At the Tevatron, colliding protons and anti-protons are bunched together in finite sized packets, each containing approximately 10^{11} particles. Consequently more than one $p\bar{p}$ interaction can occur within the same bunch crossing. This raises the concern that both interactions could result in dijet events, and thus fake a double parton signal. This background may be estimated from simple considerations.

The expected number of double dijet events from double interactions in a given data sample (N_{dd}) is given by

$$N_{dd} = \mathcal{L}\sigma_{dijet} \cdot \mathcal{L}_1\sigma_{dijet},$$ (32)

where $\mathcal{L}$ is the total integrated luminosity of the data and $\mathcal{L}_1$ is the integrated luminosity for one bunch crossing. Now defining τ as the time between bunch crossings and $\mathcal{L}_{\text{inst}}$ as the instantaneous luminosity, we can write

$$\mathcal{L}_1 = \mathcal{L}_{\text{inst}} \cdot \tau. \tag{33}$$

Inserting numbers where possible, this allows us to express N_{dd} in terms of a constant times $\mathcal{L} \cdot \sigma^2_{\text{dijet}}$. We have,

$$\mathcal{L}_{\text{inst}} \sim 1 \times 10^{-30} \text{ cm}^{-2} \text{ s}^{-1}, \tag{34}$$

and for 6-on-6 bunch operation,

$$\tau = \frac{\text{Circumference of Tevatron ring}}{\text{Number of bunches} \cdot c} \sim \frac{6.5 \times 10^3}{6 \cdot 3 \times 10^8} = 3.6 \ \mu \text{ sec.} \tag{35}$$

Therefore, we obtain,

$$N_{\text{dd}} = 3.6 \text{ b}^{-1}(\mathcal{L} \cdot \sigma^2_{\text{dijet}}), \tag{36}$$

noting that $1b = 1 \times 10^{-24}$ cm^2. For the double parton process, using Equation 23 with $\sigma_{\text{eff}} = 8.7$ mb we find

$$N_{\text{DP}} = 58 \text{ b}^{-1}(\mathcal{L} \cdot \sigma^2_{\text{dijet}}). \tag{37}$$

Therefore double parton events are expected to dominate dijet pairs produced in double interactions by a factor of 15. Additional background rejection is provided by the CDF vertex detector, which has the ability to resolve secondary vertices to within approximately 7 cm. This gives a further factor of 8 rejection, pushing the background due to double interactions below the 1% level.

2. Standard Model Processes

Examples of Standard Model processes which could produce four jets apart from double bremsstrahlung are WW production and $W + 2$ jet production. However, such processes produce event rates which are entirely negligible in comparison with the number of events expected from double parton scattering [58].

E. Previous Experimental Work

The first experimental four-jet analysis was published by the Axial Field Spectrometer group (AFS) in 1987 [59]. Collisions of protons on protons were studied using the CERN ISR at $\sqrt{s} = 63$ GeV. A minimum jet transverse momentum of 4 GeV/c was required for the four jets in their data sample. The AFS group reports a large fraction of double parton events, and measures $\sigma_{eff} = 5$ mb. Since this work was performed before the exact leading order four-jet matrix element calculation had been completed, the ISAJET Monte Carlo program was used to simulate four-jet production. This program includes initial and final state gluon radiation through the leading logarithm approximation of the parton cascade. Figure 10 shows two examples of four-jet events observed in the AFS detector. The variable used in their search for double parton scattering is defined as

$$\mathcal{J} = \frac{1}{2}(\vec{P}_{t_1}^{\,2} + \vec{P}_{t_2}^{\,2}). \tag{38}$$

Where $\vec{P}_{t_i}$ is the resultant vector sum for jet pair i. The $\mathcal{J}$ variable is minimized over the three possible pairing combinations.

By contrast, the very recent study completed by the UA2 collaboration finds no evidence for double parton scattering, and sets the limit $\sigma_{\text{eff}} > 8.3$ mb at the 95% confidence level [60]. The center-of-mass energy available to the UA2 group is $\sqrt{s} = 630$ GeV, a factor of 10 higher than the AFS case. They also impose the requirement $P_t > 15$ GeV/c on all jets. As a consequence, the UA2 jets are cleaner than those used by the AFS collaboration. Figure 11 shows the UA2 data overlaid on the predictions of a leading order double bremsstrahlung calculation and a double parton simulation for one (P_t-balancing) variable. Clearly the data points are well described by double gluon bremsstrahlung alone.

The CDF collaboration has also carried out a previous search for double parton scattering [54]. This search was performed using data from the 1987 run. No clear evidence for double parton scattering was found, and a limit of $\sigma_{\text{eff}} > 2.5$ mb was set, though never published. A summary of the experimental results and conditions to date is given in Table V.

F. Motivation and Overview

Towards the end of the 1988/89 CDF run, a special jet trigger was installed. The purpose of this trigger was solely to collect a large sample of four-jet events. With this sample, a high statistics test of the QCD double bremsstrahlung process can be performed at the highest center-of-mass energy currently available. Because of the exceptionally broad coverage of the CDF calorimeters (see Chapter III) a nearly
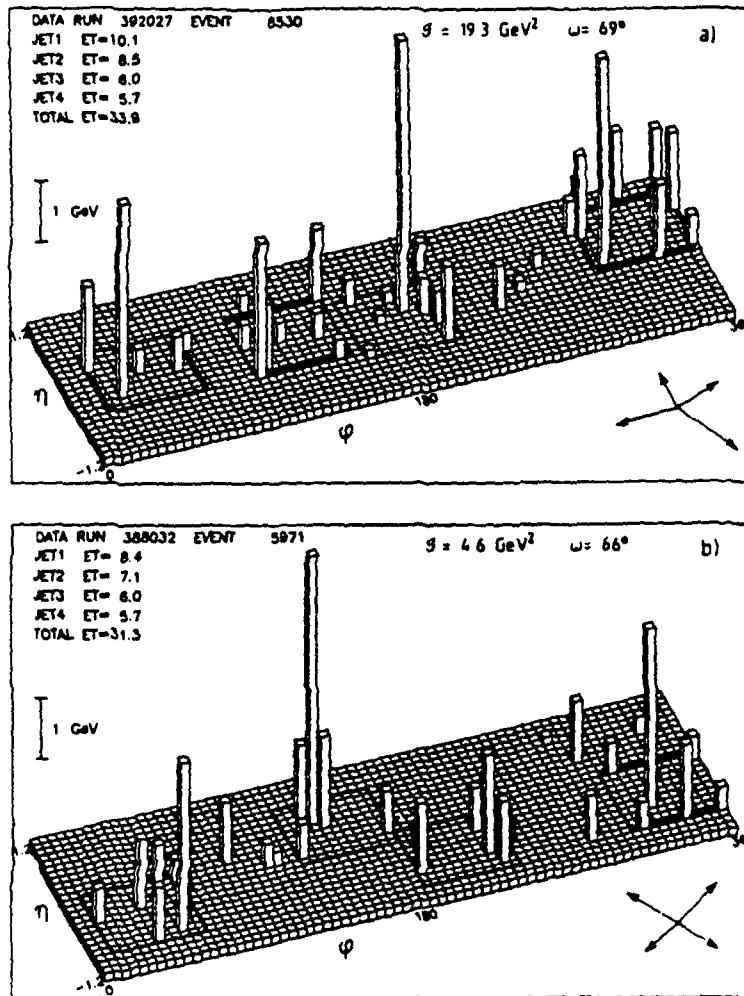
Figure 10. Two examples of four-jet events collected by the AFS collaboration. The event on top is consistent with the topology expected of an event produced by the double bremsstrahlung mechanism, while the lower event is a double parton scattering candidate.
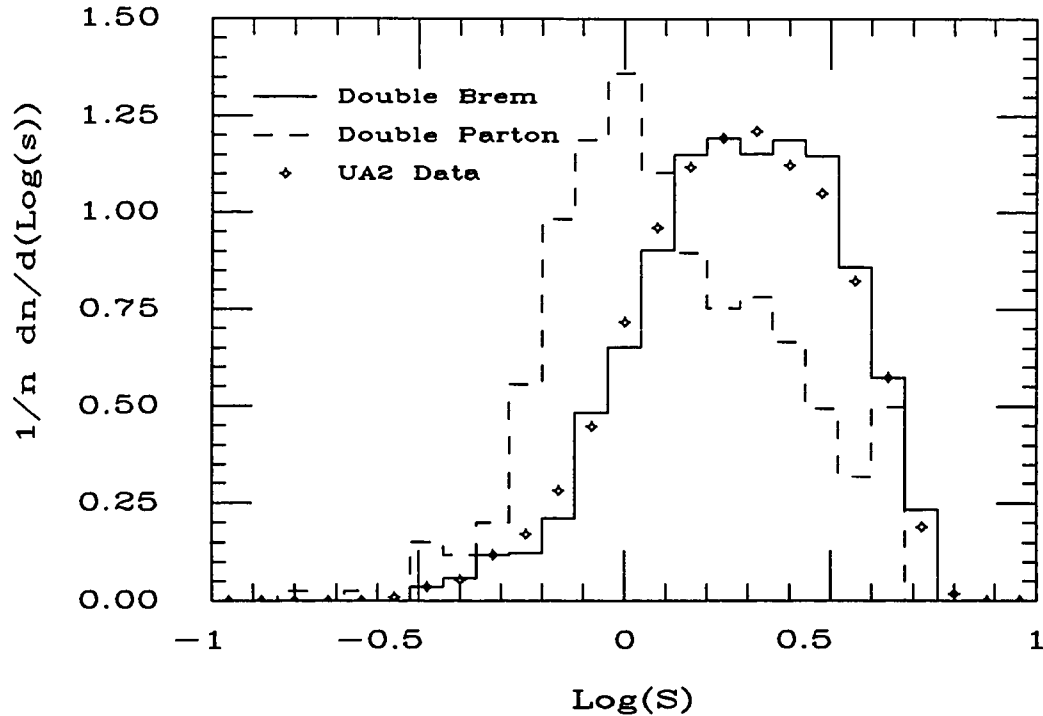
Figure 11. Data from the UA2 four-jet analysis overlaid on predictions from leading
order QCD four-jet production, and those of the PYTHIA Monte Carlo
simulation modified to produce double parton scattering.

complete range of topological freedom is available for jets in these events. This

implies a more stringent test of QCD than that previously performed by the UA2

collaboration.

In addition, a search for double parton scattering with this data set will extend

our understanding of the process to a new energy régime, complementing the studies

that have been performed by the AFS and UA2 collaborations. This work is expected

to be of particular relevance to the next generation of hadron colliders.

Table V. A summary of some of the relevant experimental parameters and cuts used in previous searches for double parton scattering. Pseudo-rapidity is defined as $\eta = -\ln\tan(\theta/2)$, where θ is the polar angle measured from the beam line.

	$\sqrt{s}$ (GeV)	$P_t^{\min}$ (GeV/c)	η-range	N_{events}	Result
AFS	63	4	$-1 < \eta < 1$	~ 1000	$\sigma_{\text{eff}} = 5$ mb
UA2	630	15	$-2 < \eta < 2$	~ 10000	$\sigma_{\text{eff}} > 8.3$ mb
CDF	1800	15	$-3.5 < \eta < 3.5$	~ 1000	$\sigma_{\text{eff}} > 2.5$ mb

The accurate measurement of jet properties is crucial to both the study of the double bremsstrahlung process and the double parton search. The clustering of jets and their correction for detector and other effects is described in detail in Chapter IV. The procedure used to tune the phenomenological model of jet fragmentation is also discussed. In Chapter V a description of the data set is given, including details of event cuts aimed at removing bias introduced by the trigger. Chapter V also contains details of event simulation at the parton level, and the two detector simulations used. Finally the results of a kinematic comparison between data and QCD is presented.

Chapter VI is concerned with the search for double parton scattering. Topological variables are introduced, and their relative signal-finding effectiveness is determined. The data points are then fitted to an admixture of signal and background shapes, and the number of double parton events is extracted. Effects such as additional clusters due to the underlying event and fifth jets are also considered. Since the double parton signal is small, limits are set on both the double parton cross section

σ_{DP} and the effective cross section parameter σ_{eff}. The method used in setting these

limits, and the associated systematic errors are explained in detail in Chapter VII.

Conclusions from this work are presented in Chapter VIII.

CHAPTER III

EXPERIMENTAL DESCRIPTION

The Tevatron collider located in Batavia, Illinios provides a high luminosity environment with which to study the physics of $p\bar{p}$ interactions at $E_{CM} = 1.8$ TeV. A schematic view of the collider is shown in Figure 12a). Initially, H^- ions are generated by a Cockroft-Walton accelerator, and are then stripped of their electrons and injected into a linear accelerator (LINAC). From the LINAC the protons pass through to the *booster*, where they are accelerated to 8 GeV before being injected into the *main ring*. The main ring serves the dual purposes of accelerating protons to 150 GeV and producing anti-protons via proton collisions with a tungsten target. The protons are directly fed into the Tevatron, while the anti-protons are stochastically cooled in an accumulator ring. Once their divergence and longitudinal momentum spread has been reduced, the anti-protons are also injected into the Tevatron where they circulate in the opposite direction to the protons. The Tevatron ring accelerates the bunches of protons and anti-protons to 900 GeV, and the two beams are focussed by quadrupole magnets at the desired interaction region in the center of the Collider Detector at Fermilab (CDF).

In order to explain this analysis, an overview of the CDF detector will be provided, together with a more detailed description of the components used to make jet measurements. Full details of the detector can be found elsewhere [61].

The orientation of the CDF co-ordinate system is shown in Figure 12b). Relevant parameters are the polar angle θ, the azimuthal angle ϕ and the pseudo-rapidity
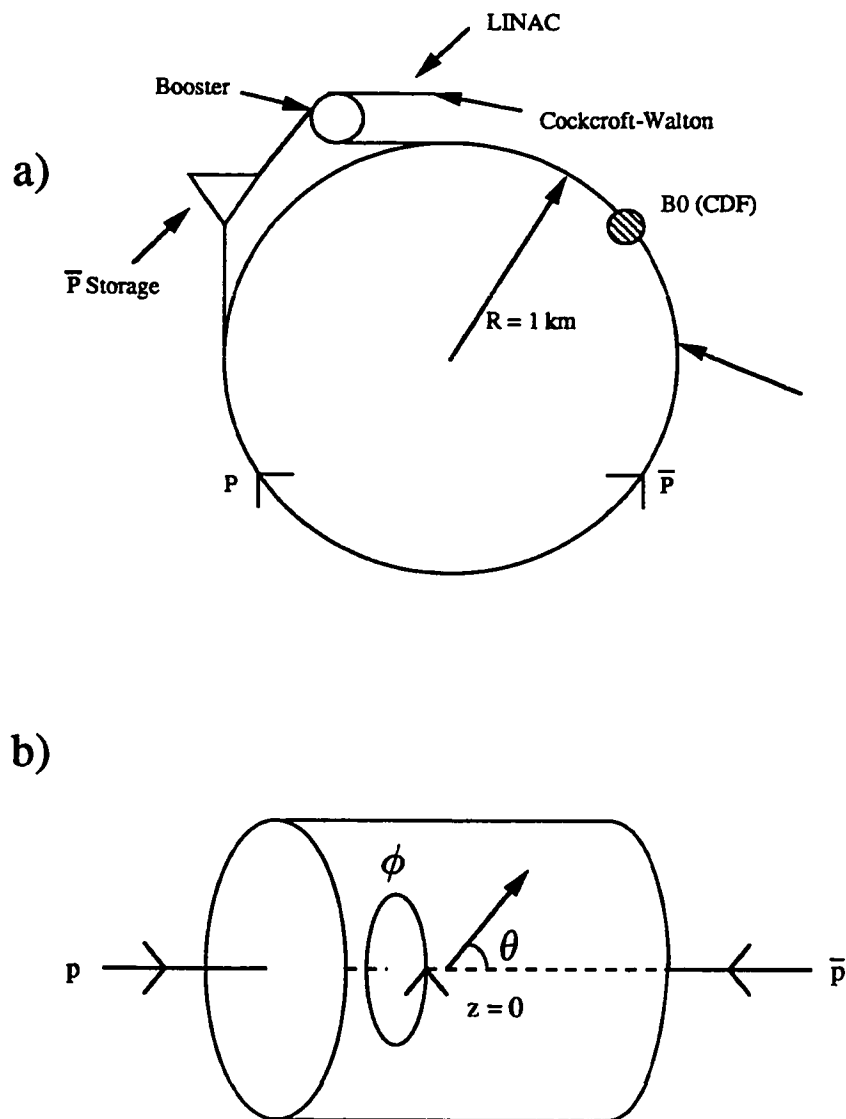
Figure 12.   a) Schematic view of the Tevatron collider at the Fermi National Accelerator Laboratory, b) orientation of the CDF co-ordinate system.

η, defined as $\eta = -\ln \tan(\theta/2)$. Pseudo-rapidity is closely related to the rapidity y [62] which changes by a constant when a Lorentz boost is performed along the beam (or z) direction (see Appendix A). Figure 13 shows two views of the Collider Detector. The interaction point, indicated by an arrow on the right hand side of Figure 13a), is surrounded by many different components in order to measure the energy, momentum and position of a variety of different particles over as large a solid angle as is practical. The central, forward and backward regions of the detector are shown in perspective in Figure 13b).

A. Calorimetry

The energy and position of a particle may be measured by inducing its cascade into a shower of other particles and measuring the shower energy. For electrons, passage through a high Z material such as lead will encourage photon bremsstrahlung followed by e^+e^- pair production in a chain reaction. The corresponding shower-producing process for hadrons is inelastic nuclear scattering.

The CDF calorimeters are multi-layer sandwiches of iron (hadronic) or lead (electromagnetic) interleaved with an active medium in which the energy of the shower products is sampled. There are various calorimeters, corresponding to three different η regions known as the central ($| \eta | < 1.1$), plug ($1.1 < | \eta | < 2.2$) and forward ($2.2 < | \eta | < 4.2$). Each region has a calorimeter designed to measure electromagnetic and hadronic showers.

The read-out of the calorimeters is divided into *towers* in η-ϕ space. These towers collectively form a projective conical grid whose apex is at $\eta = 0$ and $z = 0$, the
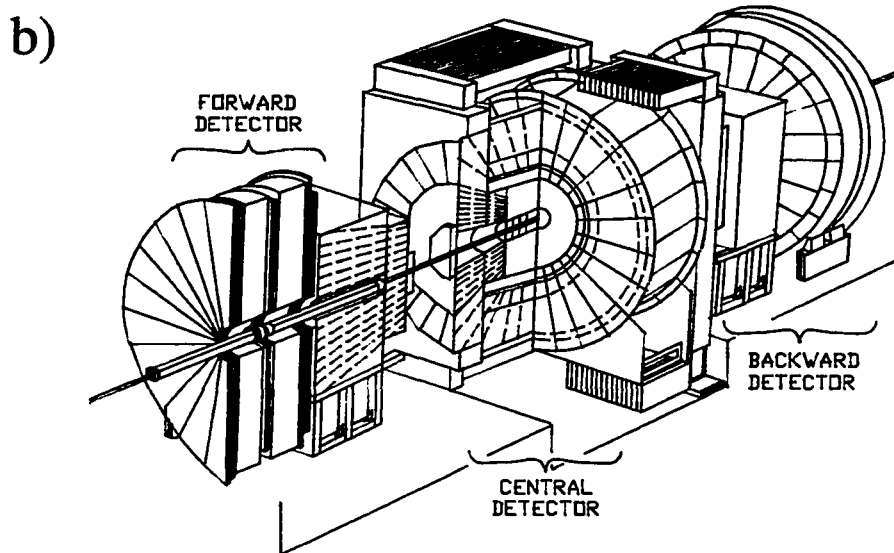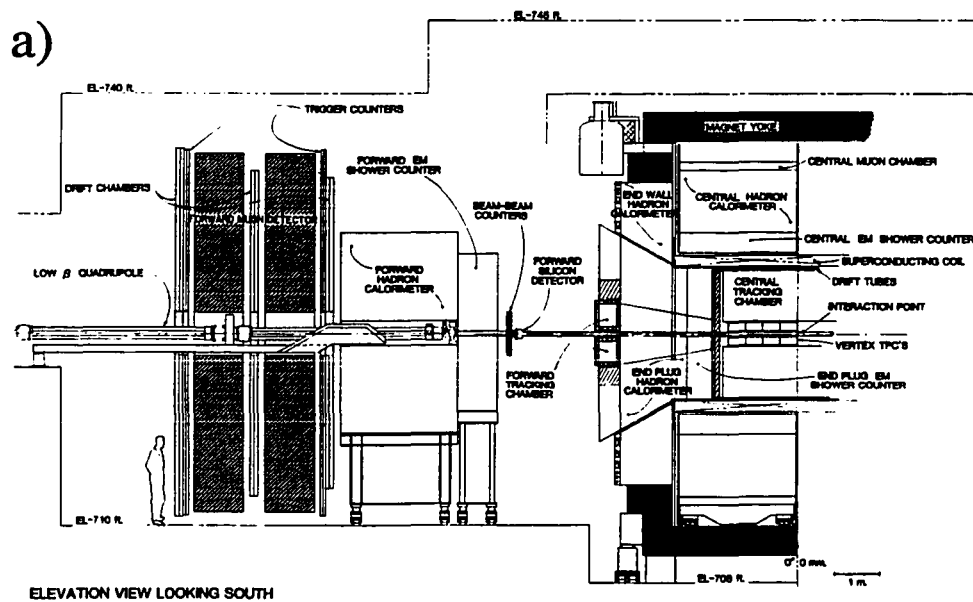
Figure 13. Two schematic views of the Collider Detector at Fermilab. a) A side-on view; the detector is symmetric about a vertical plane through the interaction point, indicated by an arrow on the right hand side. b) A perspective view of the detector, showing the three main sections, the central region and the forward and backward regions.

nominal interaction point. This configuration has been chosen primarily to facilitate the measurement and clustering of jets. In Figure 13b) the projective geometry is indicated by dashed lines. The total calorimeter coverage in η is $\mid \eta \mid < 4.2$, which is equivalent to $2.0° < \theta < 178°$. Complete azimuthal coverage is provided.

1. Central Electromagnetic Calorimeter

The central calorimeters are mounted in 4 C-shaped arches surrounding the Central Tracking Chamber (CTC). Each arch supports 12 individual *wedges* containing chambers for monitoring electromagnetic and hadronic showers. The arches join together in pairs to provide complete azimuthal coverage. The Central Electromagnetic Calorimeter (CEM) covers the angular region $\mid \eta \mid < 1.1$ (approximately $39° < \theta < 141°$) [63]. One CEM wedge is shown schematically in Figure 14.   In this figure the projective geometry of the 10 CEM towers can be seen, along with the layout of the light-gathering system. The measurement of electromagnetic showers is performed using 31 layers of lead interleaved with 31 layers of 5 mm thick SCSN-38 polystyrene. The blue light from the scintillator is first green wave-shifted before being fed into Hamamatsu R580 photomultiplier tubes. These tubes have a gain of approximately 10^5 at 1000 V. The energy resolution for electrons centered in towers is given by $\sigma/E_t = 13.5\%/\sqrt{E_t} \oplus 2\%$, where the symbol $\oplus$ signifies that the constant term is added in quadrature in the resolution.

The CEM is a hybrid detector, since it incorporates a strip chamber near shower maximum to determine shower position and transverse development. The strips are copper-backed 1/16 inch PC boards. High voltage wires are strung orthogonally to
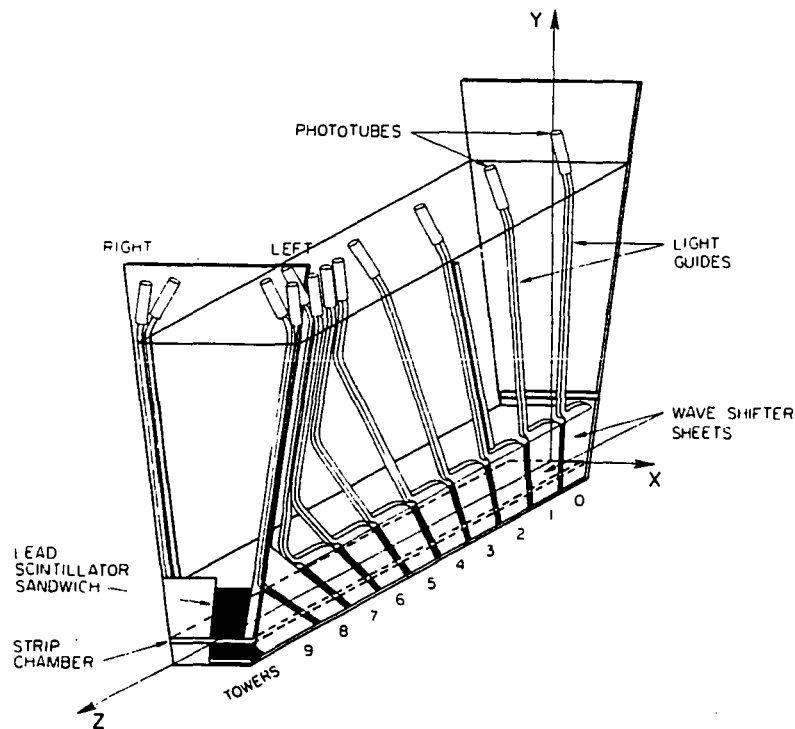
Figure 14. Schematic of one CEM wedge, showing light-gathering system.

these strips. Since the strip chamber measurement depends on the position of shower

maximum, the response is nonlinear. All calorimeter modules have been calibrated in

a 50 GeV electron test beam. In this way the position resolution has been determined

to be 2 mm, reproducible at the 1% level.

2. Central Hadron and Endwall Calorimeters

A side view of the geometry of the Central Hadron Calorimeter (CHA) and the

Endwall Calorimeter (WHA) is shown in Figure 15. Also included is the Plug Hadron
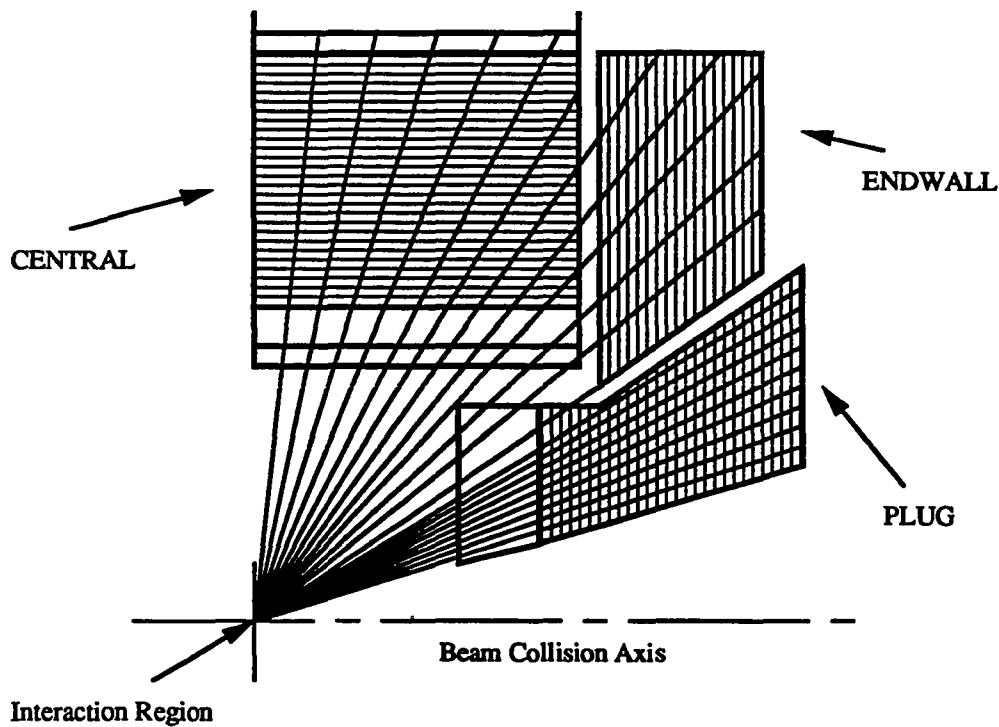
Figure 15.   Side view of the geometric coverage of one quadrant of the CHA, WHA and PHA.

Calorimeter (PHA). This diagram shows a clear gap between the WHA and the PHA at approximately 30°. This gap and similar gaps elsewhere in the calorimeters will be the subject of further discussion in Chapter IV.

The CHA provides the measurement of hadronic showers in the region $| \eta | < 0.9$, or $45° < \theta < 135°$ [64]. A total of 48 steel-scintillator sampling calorimeters are mounted on the arches outside of the CEM. There are 11 towers, each covering 0.1 unit of η and 15° in azimuth. There are 32 layers of 2.5 cm thick steel and 1 cm thick scintillator. The scintillating plastic is PMMA-based with additives. Light is

wave-shifted by UVA PMMA strips, doped with laser dye #481 which has an emission peak at approximately 490 nm. Thorn-EMI 9954 phototubes are used to collect the light and are operated at a gain of approximately 10^5. The longitudinal response of the CHA is uniform to better than 10%. Calibration maintenance is performed using a pulsed laser system, and aging effects can be detected by comparing the results of the laser tests with those of a separate calibration check performed with a ^{137}Cs source. The resolution of the CHA is $\sigma/E_t = 75\%/\sqrt{E_t} \oplus 3\%$.

The Endwall Hadron Calorimeter (WHA) covers the region $30° < \theta < 45°$ and $135° < \theta < 150°$, or in terms of pseudo-rapidity, $0.7 < | \eta | < 1.3$. Financial and installation constraints resulted in a 5 cm steel sampling size (a factor of 2 more than for the CHA). This reduces the resolution of the WHA with respect to the CHA. However, for a given transverse energy, the total energy in the WHA is on average a factor $\sqrt{2}$ larger than in the CHA, since it is further out in η. In other respects, the two calorimeters are very similar.

3. Gas Calorimetry

The central calorimeters use scintillator for good energy resolution and adequate radiation hardness. In the more forward, higher $| \eta |$ regions of the detector, resolution becomes less critical and the radiation exposure becomes greater. In addition, finer transverse segmentation is needed to achieve the same position resolution available in the central calorimeter. At the time of design and construction, this segmentation was envisaged as being difficult to achieve using a scintillator-based calorimeter. As a result, all calorimeters in the region $1.1 < | \eta | < 4.2$ use gas (50/50 Argon/Ethane with a small percentage of alcohol) as an active medium.

Gas calorimeters have historically been of great use in the field of high energy physics. The principle of operation is based on the ionization and subsequent measurement of electrons in a gas. A wire at high potential attracts electrons in a short period, resulting in quick response. By making use of the image charge induced in a segmented, instrumented metal plane close to a network of these wires, reasonable position and energy resolution is achieved. In practice, a semi-conducting layer must be inserted between the high voltage wires and cathode pads to achieve the desired image charge.

While the technology is well understood, there are drawbacks. The main problem is that the response of the gas-type detectors at CDF to a particle of fixed energy changes with ambient pressure and temperature. This effect is monitored using many proportional wire tubes mounted in gas lines around the detectors. These tubes measure the response of the gas passing through the calorimeters, and the results are used to correct the data online. The hardware and software used to make this correction are collectively known as the *gas gain* system.

4. Plug Electromagnetic Calorimeter

The Plug Electromagnetic Calorimeter (PEM) covers the region $1.2 <| \eta |< 2.4$, or $10° < \theta < 36°$ and $144° < \theta < 170°$ [65]. This calorimeter is cylindrical in shape, has 34 sampling layers, and is located at either end of the CTC. As is the case with all the gas calorimeters at CDF, the most precise energy and position measurement is provided by an etched copper circuit board, segmented in η-ϕ into *cathode pads*. A ribbon cable wire is soldered to each pad for read-out. The high voltage wires are also used to provide additional information. The PEM is somewhat unique in that it makes

use of etched strip boards. There are two kinds, having strips either in the radial or transverse direction. The segmentation used is $\Delta\phi = 1°$ and $\Delta\eta = 0.02$. Strip boards are inserted alternately from layers 6 to 15. The η-ϕ segmentation of the PEM pad readout is $\Delta\phi = 5°$ and $\Delta\eta = 0.1$. In the ϕ direction, three PEM pads match up with one central calorimeter pad (recall that $\Delta\phi = 15°$ for the CEM, CHA and WHA). The energy resolution of the PEM can be expressed as $\sigma/E = 28\%/\sqrt{E} \oplus 2\%$. The angular resolutions measured by the strips are $0.04°$ to $0.06°$ in the θ direction, and approximately $0.1°$ in the ϕ direction. Using a test beam, a rejection factor of 500 to 1000 was obtained for 100 GeV π-mesons with 60-80% efficiency for electrons.

5. Plug Hadron Calorimeter

The Plug Hadron Calorimeter (PHA) covers the region $1.1 <| \eta |< 2.2$ or $10° < \theta < 30°$ and $150° < \theta < 170°$ [66]. Hadronic showers are produced in 21 steel plates each 5 cm thick, corresponding to a total of 6.5 interaction lengths. Gas proportional chambers are placed between the plates. Each chamber has 72 cathode pads, arranged to project back to the interaction region. The 50 μm gold plated tungsten anode wires are centered in resistive plastic tubes. The PHA is divided up into twelve sectors (or *stacks*) of 30° in azimuthal angle ϕ. All anode wires in a single chamber are ganged and read out, giving longitudinal information from each plane in each stack. The resolution of the PHA is given approximately by $\sigma/E = 90\%/\sqrt{E} \oplus 4\%$.

6. Forward Electromagnetic Calorimeter

The Forward Electromagnetic Calorimeter (FEM) provides coverage over the region $2.2 <| \eta |< 4.2$, or $2° < \theta < 10°$ and $170° < \theta < 178°$ [67]. This is the

largest coverage in η-ϕ space of the three electromagnetic calorimeters. The FEM is located approximately 6.5 meters from the interaction point, and consists of 30 layers of lead interleaved with gas sampling chambers. The lead sheets are each 0.8 radiation lengths thick. The projective geometry is extended from the plug region in a grid of approximately 0.1 unit in η and 5° in ϕ. The pads are ganged at constant η into two 15 layer regions. In each chamber 124 anode wires are arranged vertically and are ganged together in five sectors for readout. The signals from the wires are useful for diagnostics and also provide a longitudinal shower profile. Each wire is strung inside a tube made from a repeated array of extruded Aluminum "T"-shaped channels mounted on the cathode pad panel as shown in Figure 16. The wires are 50μm in diameter and are nickel flashed for a reliable solder connection. The cathode pad array is made from an etched layer of copper.

Using data obtained with a test beam, the resolution of the FEM is found to be $\sigma/E = 25\%/\sqrt{E} \oplus 2\%$. At the nominal operating voltage of approximately 2000 V, the response of the FEM doubles in response to an increase in voltage of 75 V. The measured energy response is linear up to 160 GeV, and the position resolution varies between 1 and 4 mm depending on location in the calorimeter. The ability of the FEM to discriminate between electrons and π-mesons is good. The π-meson misidentification probability is below 0.5%, and the electron identification efficiency is greater than 90%.

7. Forward Hadron Calorimeter

The Forward Hadron calorimeter (FHA) was built by the experimental group at Texas A&M University [68]. Coverage is provided in the pseudo-rapidity range
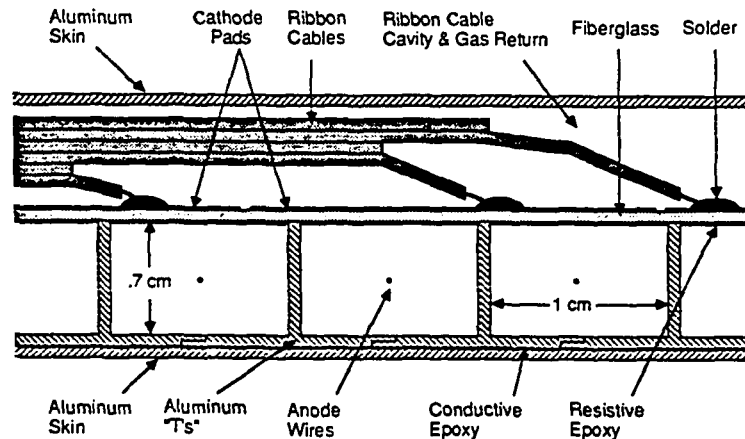
Figure 16. Cross section of an FEM chamber, with appropriate dimensions.

$2.2 <| \eta |< 4.2$, or $2° < \theta < 10°$ and $170° < \theta < 178°$. The chamber design is almost identical to that of the FEM. There are 27 layers of 5 cm thick steel interleaved with the chambers in each of the eight quadrants. Hadronic shower maximum occurs for 227 GeV π-mesons at approximately layer 9. Calorimeter resolution for the FHA is given by $\sigma/E = 130\%/\sqrt{E} \oplus 4\%$. In each chamber the anode wires are segmented into six regions for read-out, and cathode pad signals are summed in towers of constant η and ϕ.

B. Tracking

The momentum of a charged particle in a magnetic field can be inferred from the radius of curvature of its trajectory. In the past, high speed photography was used

to freeze-frame particle tracks left in large bubble chambers. More recently, electronic versions of the old bubble chambers have allowed a more efficient rate of data analysis and more precise measurements of momenta. In addition, modern tracking chambers allow individual tracks to be resolved even with the high particle multiplicities that are present at the Tevatron.

1. Central Tracking Chamber

At CDF, the Central Tracking Chamber (CTC) tracks charged particles in a 1.4 Tesla magnetic field [69]. The CTC makes it possible to measure high P_t particles in jet cores, identify energy directed at cracks in the calorimeters, identify second vertices due to stable particles and measure track parameters at angles below 30° with respect to the beam direction. Three dimensional track extrapolation is performed with a resolution of the order of a few millimeters.

The CTC is made up of large cylindrical drift cells arranged in 9 *superlayers*, containing a total of 84 layers of sense wires. There is an alternating wire orientation, 12 wire layers in the axial direction for the outermost superlayer, followed by 6 layers canted at 3° (for a stereo effect) and so on. The ionization medium is a mixture of argon/ethane/ethanol (49.6%/49.6%/0.8%). Drift cells are tilted at an angle of 45° to the radial direction to provide compensation for the Lorentz angle of the electron drift direction in the electric and magnetic fields. The large number of sense wires in each cell guarantees that every radial track must pass close to at least one sense wire in every superlayer, allowing fast triggering and good pattern recognition.

2. Vertex Time Projection Chamber

The Vertex Time Projection Chamber (VTPC) system consists of eight projection chambers mounted in sequence close to the beam-line covering the angular region $3.5° < \theta < 176.5°$ [70]. This component serves many useful purposes, such as the determination of the interaction z-position, the identification of multiple interactions and intermediate angle tracking, which complements the measurements made by the CTC.

The vertex z-position (z_{vertex}) is not always zero, since the bunches of protons and anti-protons that collide to produce interactions have a finite length. As can be seen in Figure 17, the distribution of the vertex position found with the VTPC is Gaussian in shape, with mean close to zero and standard deviation of approximately 30 cm. The z-position is an important variable used in the determination of transverse momentum. Also, if the event originates too far from the nominal interaction point, there will be distortion of the projective tower geometry of the calorimeters. These two factors alone make accurate vertex measurement essential. Further, the decay of a long-lived particle may give rise to two discernable vertices, and measurement of the vertex separation will then yield the lifetime of this particle.

Each VTPC module contains a central high voltage grid that divides it into two 15.25 cm long drift regions. This length ensures that the maximum drift time is less than 3.5 μs at typical operating conditions (gas of 50/50 Argon/Ethane, E = 320 V/cm). At the end of each module are two end caps, divided into octants, with 24 sense wires and 24 cathode pads in each. The arrival times of the electrons at the
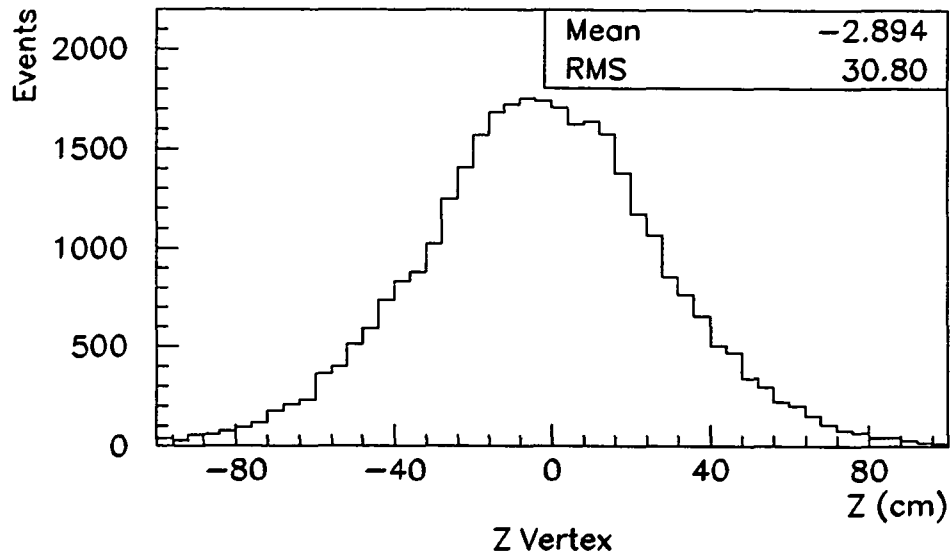
Figure 17.   Distribution of event vertices along the beam axis for a typical CDF run.

sense wires provide an event picture in the r-z plane. Adjacent modules have a relative rotation angle about the beam axis. This eliminates inefficiencies near boundaries, and provides ϕ information from small angle stereo. The position resolution near the sense wires is about 200 μm, while the resolution for the longest drift times is about 550 μm.

Both the wire and the pad information are enough to provide independent two-dimensional tracking. By combining the r-z data from the wires with the ϕ data from the pads, a three-dimensional track can be accurately reconstructed. The material for the VTPC was carefully chosen to minimize particle energy loss, since photon conversions in this detector can lead to track mismeasurement in the other tracking detectors and degradation of electron identification capability.

C. Lepton Measurement

Leptons have been used extensively in the past to test the electroweak sector of the Standard Model, and they will probably be the key to the long awaited discovery of the top quark. At CDF, charged leptons generally leave a clear track in the CTC. Electrons also typically shower in the electromagnetic calorimeters and can be found by looking for clumps of energy that match a track of the appropriate charge and P_t in the CTC. Since muons are approximately 200 times more massive than electrons, they travel at lower velocities. Therefore they are able to pass through the calorimeters without producing an electromagnetic shower through photon radiation. This is a strong signature in itself, but there also exist two dedicated muon detectors in the central [71], and forward/backward regions [72]. Neutral leptons (neutrinos) generally do not interact with the detector, and thus can be found by looking for significant missing E_t in the calorimeters.

D. Trigger Counters and Luminosity Monitoring

A plane of scintillation counters in front of the FEM provides a *minimum bias* trigger. At least one counter in each plane is required to fire within a 15 ns time window centered on the beam crossing time. These counters are known as the beam-beam counters (BBC) and are also used to monitor luminosity.

E. Data Acquisition System

The approximately 100,000 individual channels of information available from the detector are mainly read out using the RABBIT (Redundant Analogue Bus-Based Information Transfer) system. This system was developed at Fermilab [73] in

response to the request for an inexpensive CDF front-end system capable of reading many calorimeter channels within 1-2 ms. The full scale signal to calibration ratio is approximately 1000:1, required to be accurate to 1%. This implies a dynamic range of 100,000:1, necessitating 16-bit digitization. As well as meeting the above requirements, the system also has the benefits of compact packaging, redundancy and the ability to perform operational diagnostics and calibrations remotely. The last two features are particularly important, since the detector needs to run for extended periods of time with minimal interruption. In order to reduce noise pick-up from cables, signal digitization is performed near the detector. The only analog signals transported to the control room are those needed for triggering.

The components of the RABBIT system include the crates, the system modules, the front end instrumentation modules inside the crate and the processors which direct readout. The crates have slot positions for 25 electronic RABBIT cards. Three of the 25 slots are used for system operations. There are two EWE's (Event Write Encoder) and one BAT (Before After Timer). The two EWE modules perform signal digitization and make full use of the system's dual bus capability. Very fast parallel crate readout is possible when both of the EWE modules are in operation, however the system can still function with one EWE if necessary. The BAT module generates various gate timing signals which are transmitted across the crate backplane and are available at each slot position. Signals from the detector come directly through pins in the backplane of the RABBIT cards, leaving the front edge of the cards free for trigger output connectors. Each EWE is controlled by an MX scanner-processor. The MX communicates to FASTBUS through a Multiple Event Port, and the signals are
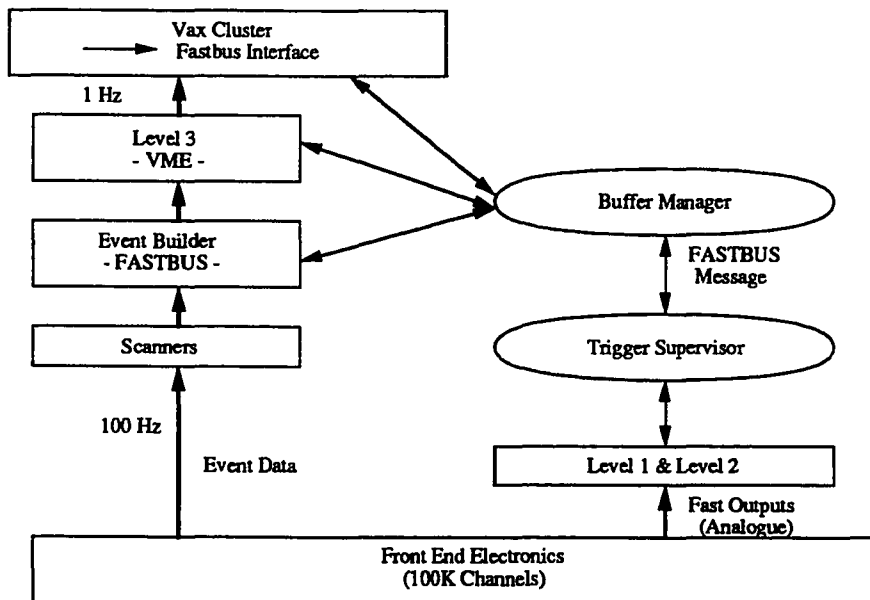
Figure 18. A schematic view of the CDF trigger and data acquisition system.

then fed into a VAX computer for processing. The tracking information is read out

exclusively using FASTBUS, through a scanner called an SSP [74].

F. Trigger

The trigger and data acquisition system are shown schematically in Figure 18.

The objective of the multi-level trigger system is to reduce the high raw event rates

of 50–75 kHz down to the level of 100 Hz before reading out the entire detector.

Of course, the surviving events should only be those with the potential to contain

interesting physics. There are three main levels to the system. Levels 1 and 2 are

hardware triggers based on FASTBUS modules, using ECL logic for speed, and Level 3

is a software trigger [75].

A Level 1 decision is made in less than the 3.5 μs between bunch crossings, and

consequently this trigger incurs no dead time. The Level 1 trigger has only global

information at its disposal such as calorimeter energy, transverse energy imbalance,

and the existence of stiff tracks and muon candidates in the central and forward muon

chambers. The trigger passes events through to Level 2 at the rate of a few kHz. The

Level 2 trigger performs a crude clustering of energy above a tower threshold of 1 GeV.

The tower size for this clustering is $\Delta\eta = 0.2$ and $\Delta\phi = 15°$. This trigger is able to

calculate many cluster parameters such as position and E_t, and also can determine

if there exists a high P_t track pointing at a cluster. Therefore the Level 2 trigger

is able to differentiate crudely between events containing jets, electrons and muons.

As an example, the Level 2 stage of the trigger used in the collection of data for

this analysis looked for at least two calorimeter energy clusters and required that the

total transverse energy in the event be above 80 GeV. A Level 2 decision is made in

approximately 20 μs.

The Level 3 trigger uses a farm of 60 Motorola 68020 processors to clean data

of noise and reconstruct physics quantities before making the decision to write the

event to tape [76, 77]. The farm was developed by the Fermilab Advanced Computer

Program. The final rate of writing data to tape is one event per second, which is

compatible with the rate at which the CDF collaboration is able to analyze the data

offline.

The data acquisition and triggering systems are tied together by the trigger supervisor and the buffer manager. The trigger supervisor sends a signal to the buffer manager when the data has been read by the MX and SSP scanners. The buffer manager then signals the event builder to read and reformat the data from a specified buffer. When this process is complete, a signal will be sent back to the trigger supervisor to allow triggering on the next event.

Events accepted by the Level 3 trigger may be examined online during data-taking for diagnostic purposes. In addition there are *consumer processes* running during data-taking which provide real-time detector diagnostics. For example, the Alarms and Limits program provides information on high voltage trips, and the GASDAQ program performs a continuous check of the gas gain system.

G.   Noise Filtering and Event Reconstruction

Data from the calorimeters are initially read out in the form of digitized ADC counts. Offline, this data is subjected to a number of corrections and noise filtering algorithms. The first of these corrections is the so-called *pedestal shift*. The normal operation of the ADC's requires the subtraction of a constant pedestal count before the application of a multiplicative ADC-to-GeV scaling factor. This constant is observed to drift during data-taking for some channels. Such channels are found using minimum bias data and the corresponding mean signal is subtracted. Minimum bias data is also used to tag channels which consistently register a large signal. These *hot channels* are then suppressed.

All the calorimeters were afflicted with electronic noise and spurious signal generation during the 1988/89 run. The central calorimeters registered spikes due to high voltage discharges at phototube bases and the showering of particles in light guides or wave shifters. The gas calorimeters exhibited a phenomenon called *Texas towers*, visible as an anomalously large energy deposition in only one sampling layer. The likely explanation is energy-dumping by low energy neutrons. These neutrons range out in one layer, as their scattering cross section with Hydrogen is far larger than that with lead or steel. This is not the case for π-mesons, where the energy deposited in the gas is tiny compared to that deposited in the metal. Since the calorimeters are designed to measure electrons or π-mesons, *not* neutrons, they employ large scaling factors to correct sampled energy to particle energy. A neutron which *preferentially* reacts with the chamber gas thus produces an enormous signal. In all cases, signal spikes are easily identifiable, making offline filtering efficient.

The scale factors which convert ADC counts to GeV are determined using data taken with a test beam of known momentum [78]. For the gas calorimeters, a reference point is taken at which to measure the gas gain, and the variation of calorimeter response to gas gain (and therefore gas density) is also determined. In practice, the calorimeter energy scales found using a test beam sometimes did not compare well with the energy scales measured *in situ* during the 1988/89 run. This was especially true of the FHA, which was estimated to have an error of approximately 30% in its scale factor [79]. Such errors are corrected offline using the technique of *dijet-balancing*, discussed in the following chapter.

CHAPTER IV

THE MEASUREMENT OF JETS AT CDF

Jets in the calorimeters are visible as clumps of energy produced by particles having small transverse momentum with respect to the initial parton direction. As can be seen in the event pictures of Figures 2 and 7, these clusters are distinctive and generally easily identifiable. Unfortunately, the calorimeters use a wide variety of technologies, and consequently have their own particular characteristics. This lack of uniformity is perhaps the biggest barrier to accurate jet measurements over the entire detector. Many CDF jet analyses in the past have exclusively used the central region, resulting in more reliable measurements at the expense of reduced acceptance. For the four-jet process, the kinematics often result in one or more jets being produced in the plug and forward regions; approximately half of the events in the four-jet data sample contain at least one jet in the pseudo-rapidity range $| \eta | > 2.0$. Therefore the loss of acceptance incurred by not using the jets in these regions is great. In order to use these events and have confidence in the results, the energy scale and resolution for jets in the non-central region must be well understood. This chapter describes those aspects of jet measurement and correction that are relevant to the four-jet analysis, with particular emphasis on the high η region.

A. Jet Clustering

While jet identification is simple conceptually, there arise situations where a jet clustering algorithm may make mistakes. One such example is the case where several

jets are in close proximity. The procedure adopted by the CDF collaboration uses a fixed cone algorithm and has shown itself to be robust in its treatment of these potential problems [80]. The routine used to perform clustering is called JETCLU. The algorithm takes advantage of the fact that jets are approximately circular in the η-ϕ metric (see appendix A).

Figure 19 shows the calorimeter tower geometry as it appears in flat η-ϕ space. Before clustering, the gas calorimeter towers are merged in groups of 3 to give a coarser 15° ϕ segmentation matching that of the central calorimeters. Clustering is performed in transverse energy E_t defined by

$$E_t = E \cdot \sin\theta. \tag{39}$$

Towers having E_t greater than 1 GeV are identified as cluster seeds, and are used as the foundations for *pre-clusters*. Pre-clusters are connected towers that have at least 100 MeV in energy and monotonically decrease in magnitude as the distance from the seed tower increases. Once pre-clustering is complete a circle in η-ϕ space is constructed, centered on the E_t weighted center-of-mass of each pre-cluster. The circle defines a cone containing the jet candidate. The cone size R is defined by

$$R = \sqrt{(\Delta\eta)^2 + (\Delta\phi)^2}. \tag{40}$$
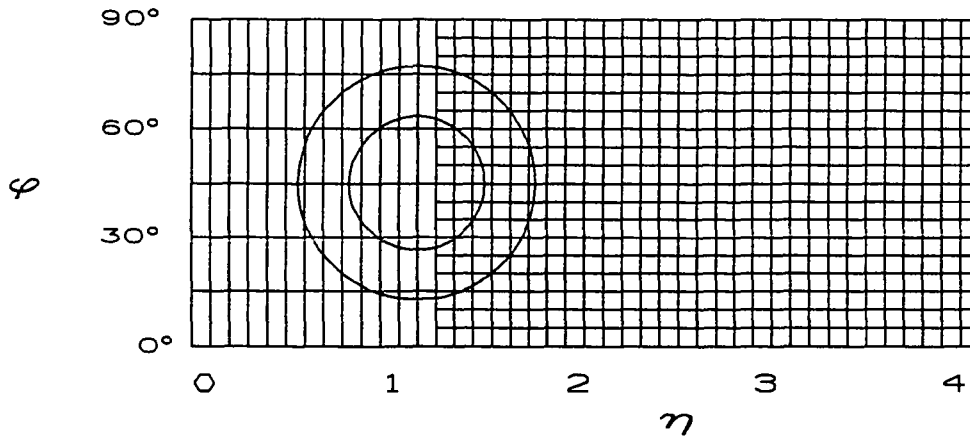
Figure 19. Schematic diagram of one quadrant of the CDF calorimeters unrolled in η-ϕ space, with circles defining cone sizes of 0.4 and 0.7.

Cones of sizes R =0.4 and 0.7 can be seen in Figure 19. A cone size of $R = 0.7$ η-ϕ radians is used in this analysis. Experience has shown that a cone size in the range 0.4–1.0 includes a major fraction of jet energy and hence is suitable for jet clustering.

Once a circle has been formed, JETCLU constructs a list of towers with E_t above 100 MeV whose centers fall within the circle and the new E_t weighted center-of-mass is evaluated. This point is then used as the center of a new circle, and the procedure is repeated until the list of towers is stable. The original pre-cluster is always included in the tower list to prevent excessive drifting of the jet center. The process is typically stable after approximately 3 iterations.

Once all the clusters in the event have been located, a search is made for over-lapping clusters. If one cluster is completely contained within another, the smaller

cluster is merged into the larger cluster. Otherwise, the overlap variable f_o is computed, defined as

$$f_o = \frac{\Sigma E_t(\text{Common towers})}{\Sigma E_t(\text{Towers in smallest } E_t \text{ cluster})}.\qquad(41)$$

If f_o is greater than 0.75, the two clusters are combined. If not, common towers are uniquely assigned to the cluster with the nearest centroid. This necessitates a further evaluation of the cluster centroids and the procedure is again iterated until a stable configuration is reached.

Raw jet energy (both electromagnetic and hadronic components) and jet position in terms of ϕ and η are determined from the calorimeters. The z-vertex information from the VTPC is necessary in order to obtain η in event co-ordinates rather than detector co-ordinates. The variable η_d, or the *detector* η is defined as the value of η assuming $z_{\text{vertex}} = 0$. The jet shower maximum position in the calorimeters is used in conjunction with z_{vertex} to perform the conversion between η_d and η. Shower maximum is taken as 10 radiation lengths for the electromagnetic calorimeters and 3 nuclear interaction lengths for the hadronic calorimeters.

The properties of clustered jets are obtained from both electromagnetic and hadronic calorimeters by forming vector sums in the following way:

$$P_x = \sum_i (E^i_{em} \sin \theta^i_{em} + E^i_{had} \sin \theta^i_{had}) \cos \phi^i, \qquad(42)$$

$$P_y = \sum_i (E^i_{em} \sin \theta^i_{em} + E^i_{had} \sin \theta^i_{had}) \sin \phi^i, \qquad(43)$$

$$P_z = \sum_i (E^i_{em} \cos \theta^i_{em} + E^i_{had} \cos \theta^i_{had}), \qquad(44)$$

$$E = \sum_i (E^i_{em} + E^i_{had}), \qquad(45)$$

$$P_t = \sqrt{P_x^2 + P_y^2}, \tag{46}$$

$$E_t = E\left(\frac{P_t}{|\vec{P}|}\right), \tag{47}$$

where the sums are performed over all towers passing the 100 MeV minimum E_t requirement.

B. Jet Corrections

There are several detector effects which must be taken into consideration when trying to make jet comparisons between theory and data. The non-uniform nature of the calorimetry leads to a significant variation in jet response as a function of η. Also, the response of the Central Hadron calorimeter (CHA) is not linear, resulting in a fragmentation-dependent jet measurement. Finally, underlying event particles add a variable amount of energy to jets, and particles from a parton may be emitted at wide angle and not be included in the jet cone. In order to correct for these effects, a comprehensive jet correction routine has been written.

The two main stages of this routine are the *relative* and *absolute* jet energy scale corrections. The relative jet energy scale measures calorimeter response in the non-central regions of the detector relative to the central region. The absolute jet energy scale is a measure of the most likely $|\sum \vec{P_t}|$ of the particles which produced an observed cluster in the central calorimeters. The jet correction procedure is applied in two steps. Firstly, the relative correction is used to transform the P_t of a given jet into the P_t that would have been recorded had that jet landed in the central region. Then the absolute jet correction is applied, yielding the corresponding particle

$| \sum P_t |$. Both corrections are described in detail in the following two sections. Also, the effects of underlying event particles and particles emitted outside the jet clustering cone are considered.

1. Relative Jet Correction

The technique of dijet balancing is the key to performing the relative jet energy scale correction [81, 82]. Since dijets balance approximately back-to-back in P_t, the energy of one area of the calorimeter relative to the other will be related to the missing $\vec{P_t}$ between two jets of a dijet pair, where one jet lands in each area. Since the central calorimeters are the best understood and calibrated, all jets are corrected relative to this region. The η_d interval chosen to define the central region is $0.2 < | \eta_d | < 0.7$. This avoids the gaps in the calorimetry that occur at $\eta_d \sim 0$ and $| \eta_d | \sim 1.1$. These gaps are due to breaks between the major calorimeter components, specifically the boundary between the two halves of the central calorimeter ($\eta_d = 0$) and between the central and plug calorimeters ($\eta_d \sim 1.1$). Another gap exists between the plug and forward calorimeters at $\eta_d \sim 2.2$. Jet energy is often under-measured as a result of particles being lost down these cracks.

The data used for the relative jet correction was collected with single jet triggers during the 1988/89 run [41]. Most of the events are dijet events, and they span the entire detector and a wide range of jet P_t. There were three separate single jet triggers in place, their Level 2 single jet E_t thresholds were 20, 40 and 60 GeV, and they were denoted by the names JET_20, JET_40 and JET_60 respectively. To remove bias due to trigger effects, a cut on the $\sum P_t$ of each event is made. The required minimum $\sum P_t$ is significantly higher than twice the single jet trigger P_t for each trigger. If this

Table VI. Number of events in each of the five $\sum P_t$ ranges used for the relative jet scale correction.

Trigger	$\sum P_t$ (GeV/c)	Events
JET20	50–100	13926
JET40	100–130	5306
JET60	130–170	35012
JET60	170–200	7453
JET60	> 200	5272

were not the case, then the largest P_t jet would tend to be preferentially located in the central region [83]. In addition to the cut on $\sum P_t$, the following cuts are imposed:

1. At least one jet in the range $0.2 <| \eta_d |< 0.7$.

2. Two (and only two) jets with $P_t > 15$ GeV/c.

3. $| z_{\text{vertex}} |< 60$ cm.

4. No second z-vertex (i.e. no secondary interactions).

5. $| \phi_1 - \phi_2 |> 2.5$ radians.

The data is divided up into five separate $\sum P_t$ ranges; the number of events in each range is shown in Table VI. The choice of 5 bins in P_t is made to ensure adequate statistics in each bin, especially at high η_d. For ease of reference, the central jet is termed the *trigger* jet, and the remaining jet is called the *probe* jet. If both jets happen to fall in the central region a random number is thrown in order to decide which is the trigger and which is the probe.

Studies have shown that the relative jet scale can be determined more accurately from missing E_t ($\vec{\not{E}_t}$) than from missing P_t [81]. This is because $\not{E}_t$ is a sum over all calorimeter towers and is therefore not dependent on the jet clustering procedure. The missing E_t is defined by,

$$\vec{\not{E}_t} = -\sum_i E_t^i \hat{n}_i, \quad i = \text{calorimeter tower number with } |\eta| < 3.6 \tag{48}$$

where $\hat{n}_i$ is a unit vector perpendicular to the beam axis and pointing at the ith calorimeter tower. The missing E_t projection fraction (MPF) is defined by

$$MPF = \frac{2 \cdot \vec{\not{E}_t} \cdot \widehat{P}_t^{\text{Probe}}}{P_t^{\text{Trigger}} + P_t^{\text{Probe}}}, \tag{49}$$

where the factor of 2 comes from dividing by $average\ P_t$. The missing E_t is projected along the probe jet axis to minimize the effect of any transverse boost due to gluon emission. On average then, we have

$$\vec{\not{E}_t} \cdot \widehat{P}_t^{\text{Probe}} = P_t^{\text{Trigger}} - P_t^{\text{Probe}} \tag{50}$$

giving

$$MPF = \frac{2 \cdot (P_t^{\text{Trigger}} - P_t^{\text{Probe}})}{P_t^{\text{Trigger}} + P_t^{\text{Probe}}}. \tag{51}$$

Now we can define the relative jet scale as

$$\beta = \frac{P_t^{\text{Trigger}}}{P_t^{\text{Probe}}}, \tag{52}$$

and obtain

$$\beta = \frac{2 + MPF}{2 - MPF}. \tag{53}$$

We are thus able to determine the relative jet energy scale β as a function of MPF.

The missing E_t projection fraction is shown for the five selected $\sum P_t$ ranges in Figures 20, 21 and 22. In these figures, the cracks in the calorimeter coverage can clearly be seen. Even in some regions not dominated by cracks, MPF is not zero. This reflects the fact that the energy scales of the plug and forward calorimeters are not the same as that of the central.

The final relative correction must be a continuous function of P_t and η_d. This is achieved by fitting the β versus η_d distributions for each $\sum P_t$ bin with a cubic spline and then parameterizing the P_t dependence with a linear fit. A set of 37 η_d points is chosen to represent the variation of MPF for each $\sum P_t$ range; most of these points are clustered around the crack regions. Due to poor statistics in the forward region, an averaging is performed over the high η_d bins. This results in a flatter correction function, consistent with uniform calorimeter coverage in the range $2.4 < \eta_d < 3.5$. A summary of this averaging procedure is given in Table VII.

For the selected η_d bins a straight line is fitted to β versus average P_t for each of the 5 $\sum P_t$ ranges. This yields two parameters for each η_d bin, a slope and an intercept. The parameters are varied using the MINUIT fitting package and a smooth cubic spline fit made to β versus η_d for each $\sum P_t$ range. The best fit parameters are extracted iteratively by minimizing the χ^2 of the fit to the data. The results of this procedure are shown in Figure 23 for a cone size of $R = 0.7$. As previously mentioned, there are 37 η_d points used in the evaluation of the χ^2; one point is positioned at $\eta_d = 0$ and 18 points are placed symmetrically on either side of this point. Since both a slope and an intercept are computed for each η_d point, the entire
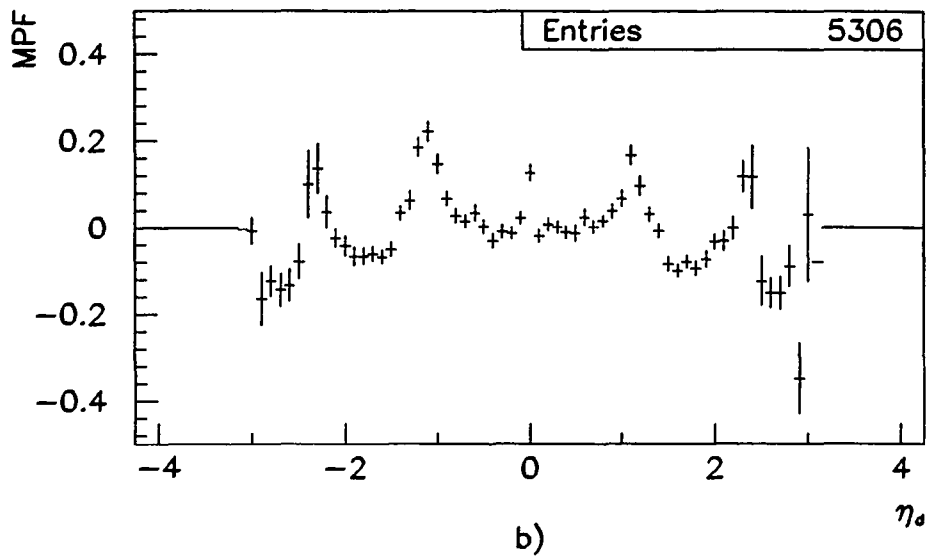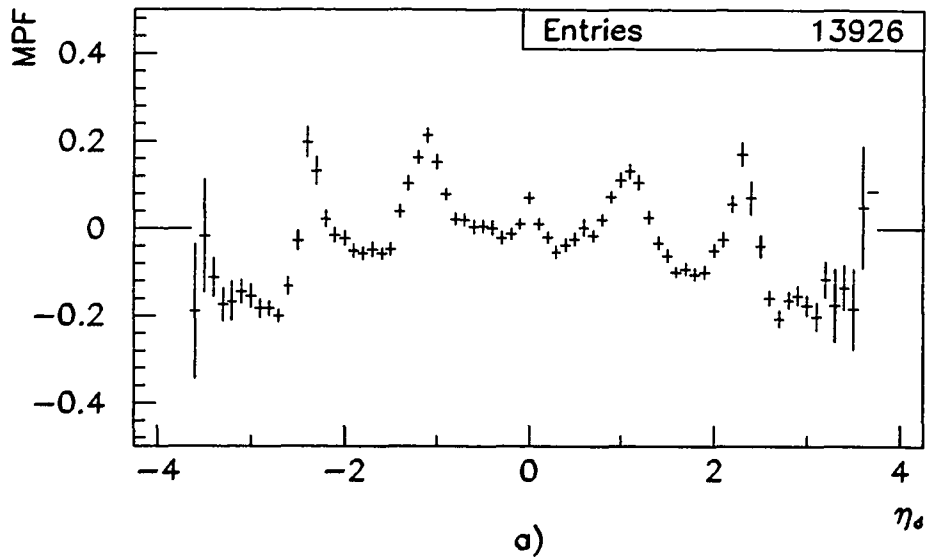
Figure 20. The missing E_t projection fraction as a function of η_d measured with dijet data in the ranges a) $50 < \sum P_t < 100$ GeV/c, and b) $100 < \sum P_t < 130$ GeV/c.
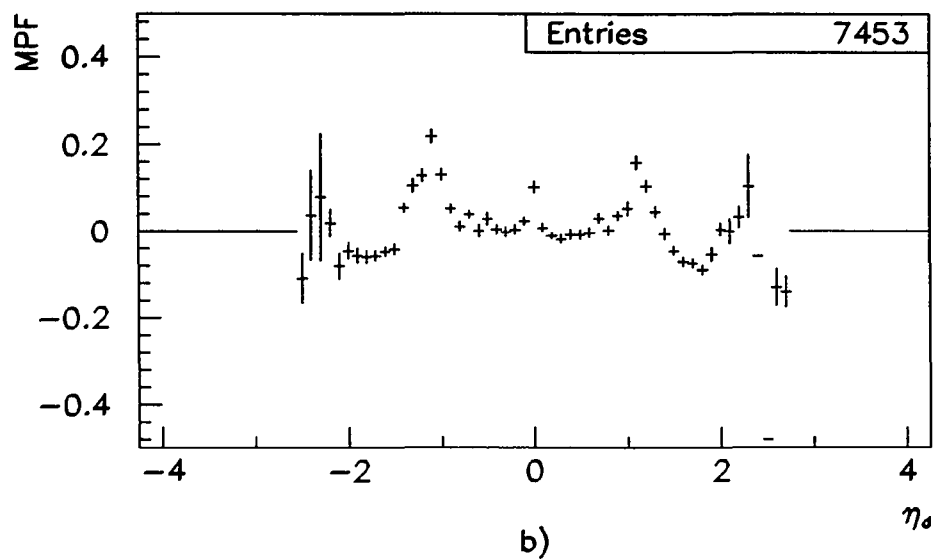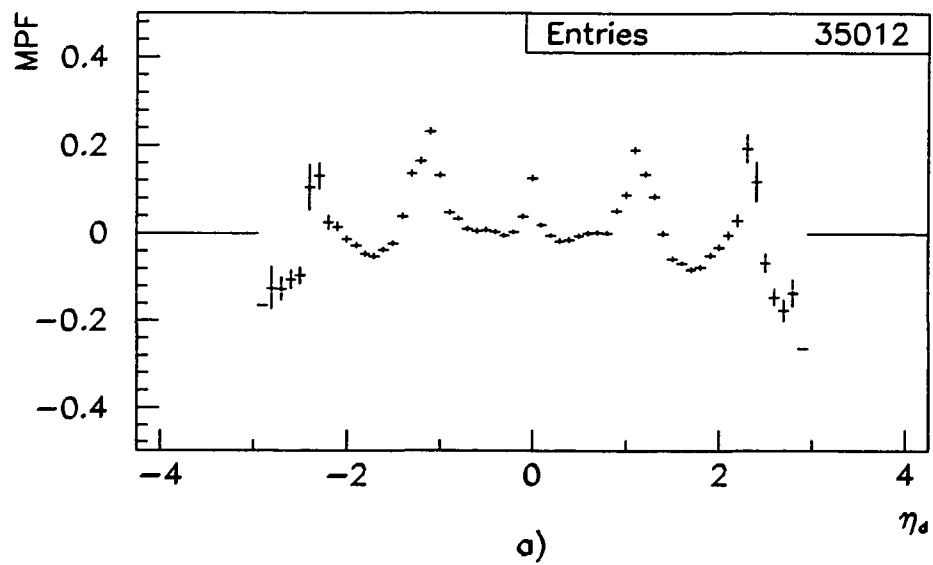
Figure 21. The missing E_t projection fraction as a function of η_d measured with dijet data in the ranges a) $130 < \sum P_t < 170$ GeV/c, and b) $170 < \sum P_t < 200$ GeV/c.
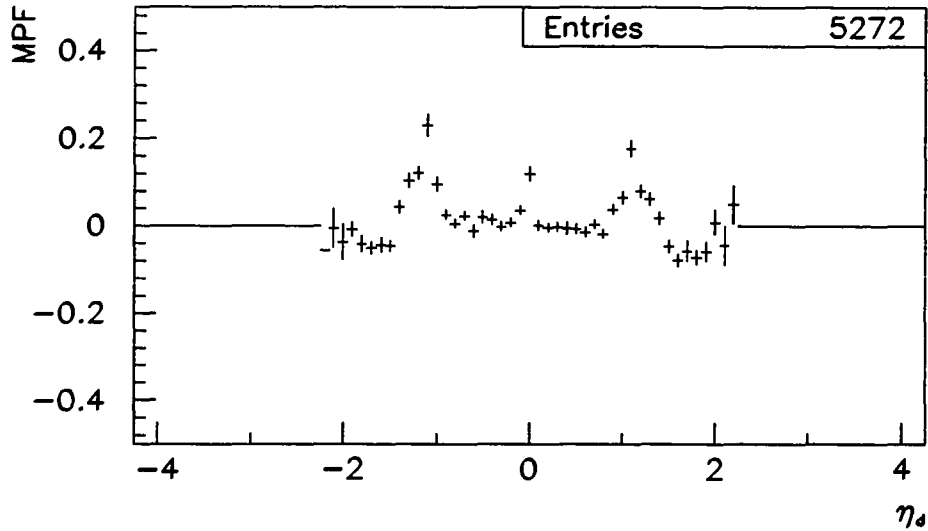
Figure 22. The missing E_t projection fraction as a function of η_d measured with dijet data in the range $\sum P_t > 200$ GeV/c.

Table VII. Details of the η_d ranges used in averaging the MPF, and the η_d ranges that have been fixed.

P_t range	η for average	η range fixed	η range used
50–100	$2.95 <\| \eta \|< 3.55$	$3.05 <\| \eta \|< 3.55$	$-3.5 < \eta < 3.5$
100–130	$2.55 <\| \eta \|< 3.2$	$2.75 <\| \eta \|< 3.55$	$-3.5 < \eta < 3.5$
130–170	$2.55 <\| \eta \|< 3.2$	$2.65 <\| \eta \|< 3.55$	$-3.5 < \eta < 3.5$
170–200	–	–	$-2.0 < \eta < 2.0$
> 200	–	–	$-2.0 < \eta < 2.0$
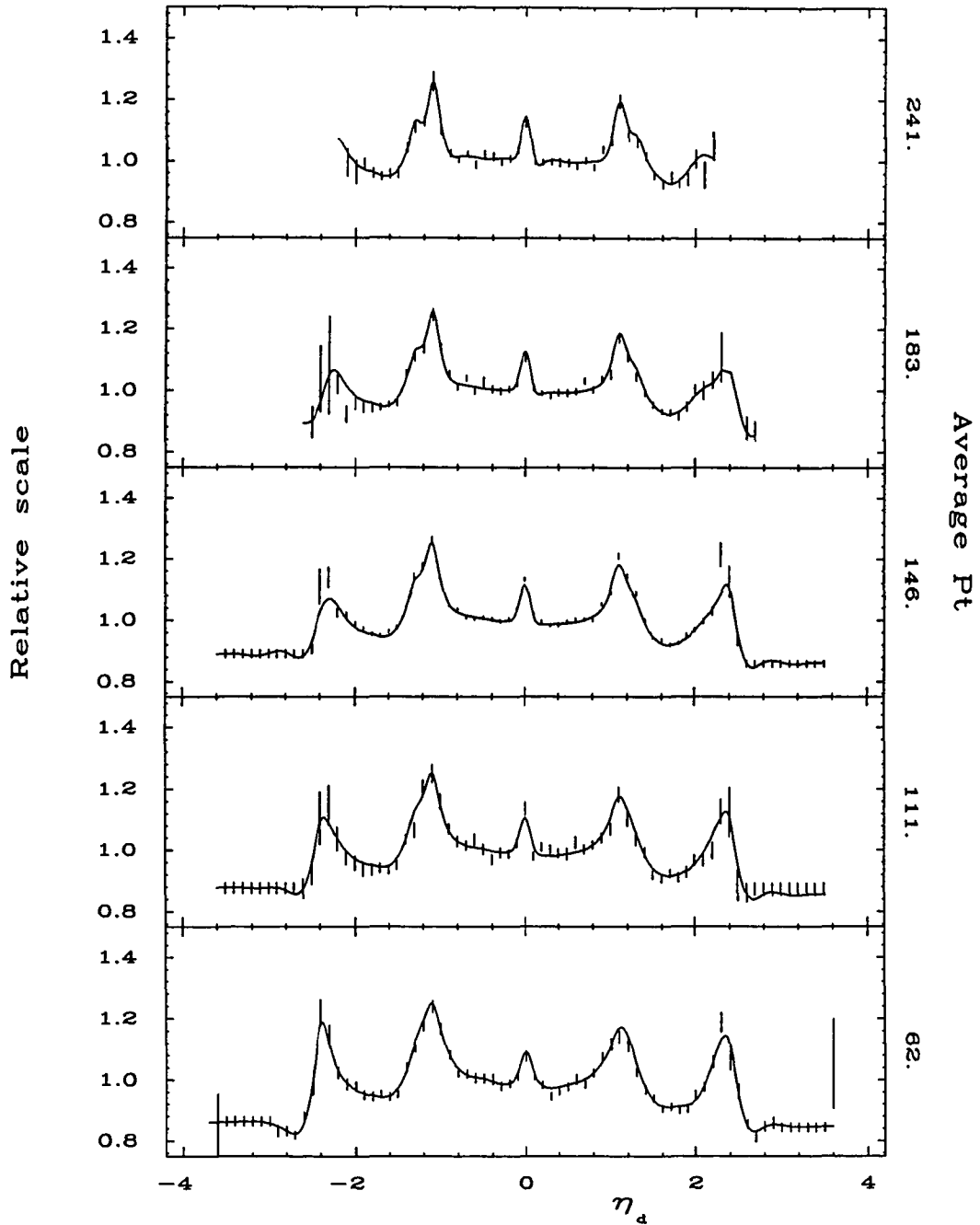
Figure 23. The relative jet energy scale (β) as a function of η_d for the 5 chosen $\sum P_t$ ranges for a cone size $R = 0.7$.

relative jet energy scale is thus reduced to a set of 74 parameters. This allows an interpolation of β for any given P_t and η_d, as desired.

As a self-consistency check, the dijet balancing was performed again, this time using the new correction function to correct each jet. Each jet P_t was multiplied by β (as defined in Equation 52). The difference in P_t was used to adjust the total E_t so that the MPF variable would reflect the correction. The results of the balancing can be seen in Figures 24, 25 and 26. After the correction, MPF is almost completely flat as a function of η_d, indicating that the correction is very effective.

2. Absolute Jet Correction

An absolute jet energy correction is required because the processes of fragmentation, showering and clustering all serve to blur the distinction between parton P_t and clustered jet P_t. To be able to correct for these effects and get as close as possible to parton P_t given a jet we need to be equipped with several tools. Firstly, we need to have an accurate model of the fragmentation process. Secondly, we need a reliable measurement of the (non-linear) response of the CHA to π-mesons. Finally, we need a detector simulation that will reproduce the geometry and response of the central calorimeters. The absolute jet energy scale concerns the central calorimeters only, since η_d-dependent differences in response can be corrected out with the relative correction just described.

a. Fragmentation Tuning

The Feynman-Field fragmentation model used for this analysis was adapted from the ISAJET Monte Carlo program [84]. The resulting routine is called SETPRT,
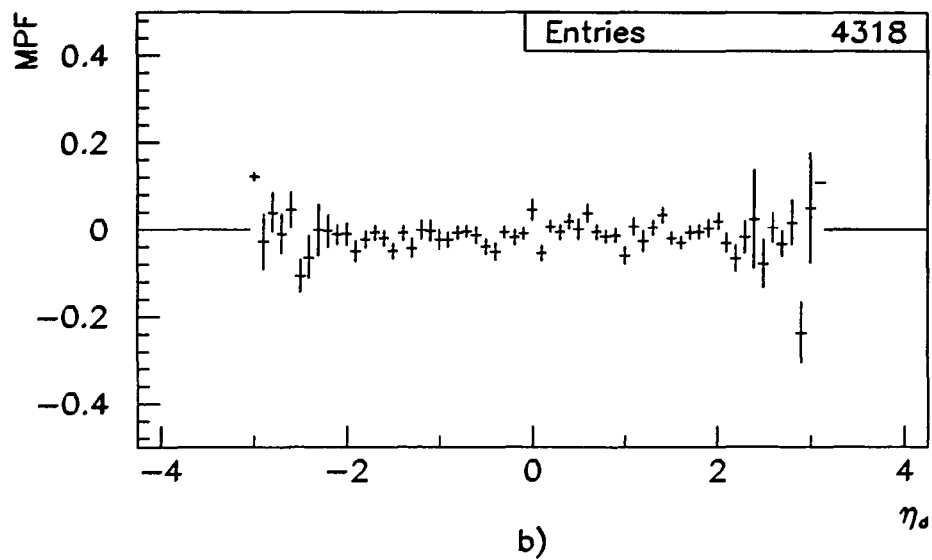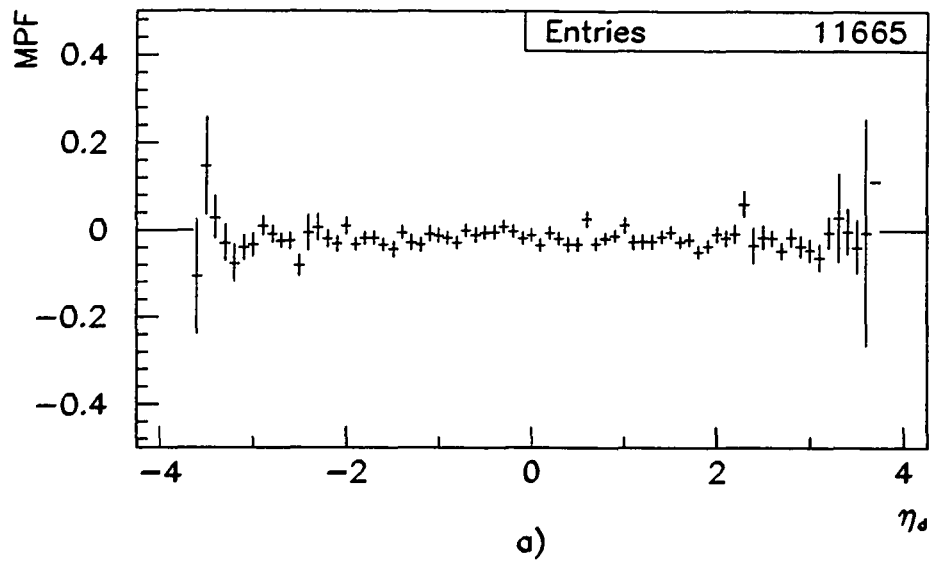
Figure 24. The missing E_t projection fraction as a function of η_d, after correction, for dijet data in the range a) $50 < \sum P_t < 100$ Gev/c, and b) $100 < \sum P_t < 130$ GeV/c.
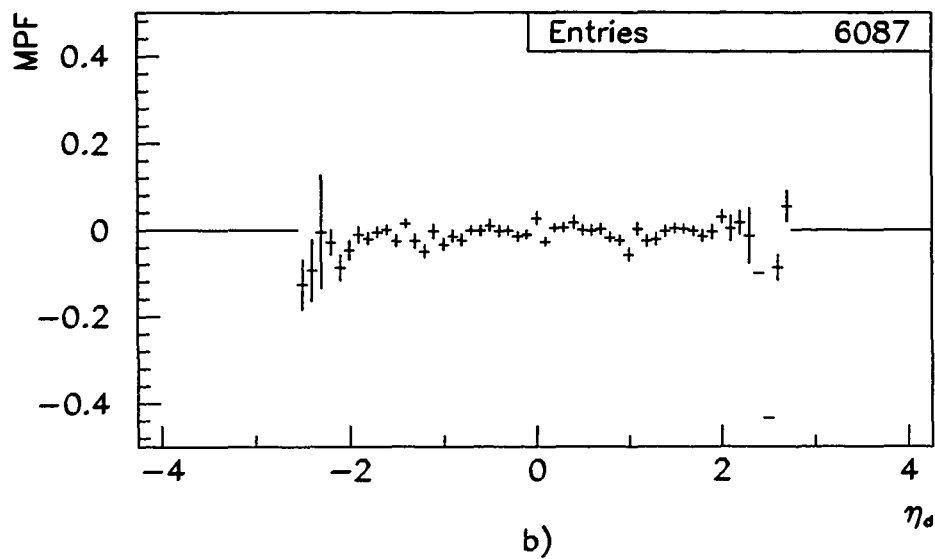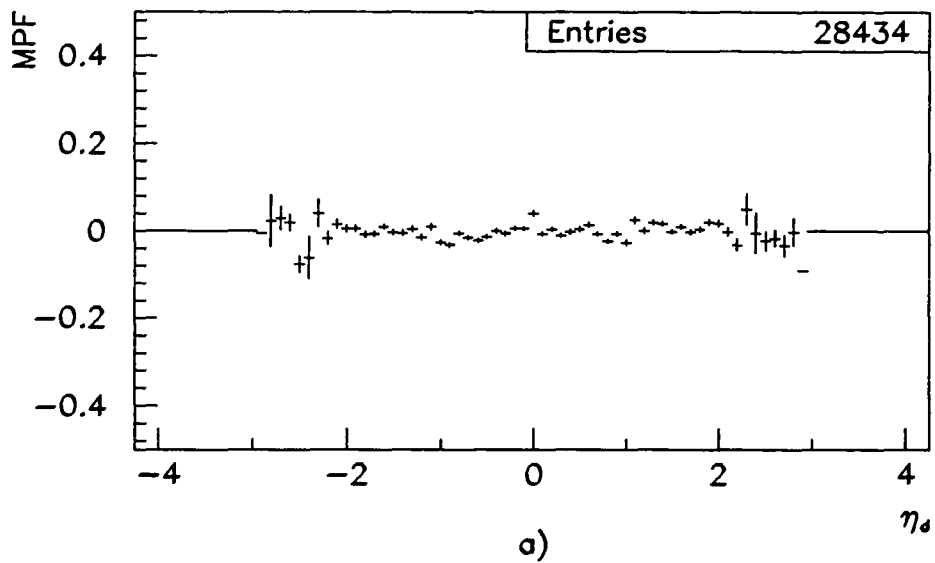
Figure 25. The missing E_t projection fraction as a function of η_d, after correction, for dijet data in the range a) $130 < \sum P_t < 170$ Gev/c, and b) $170 < \sum P_t < 200$ GeV/c.
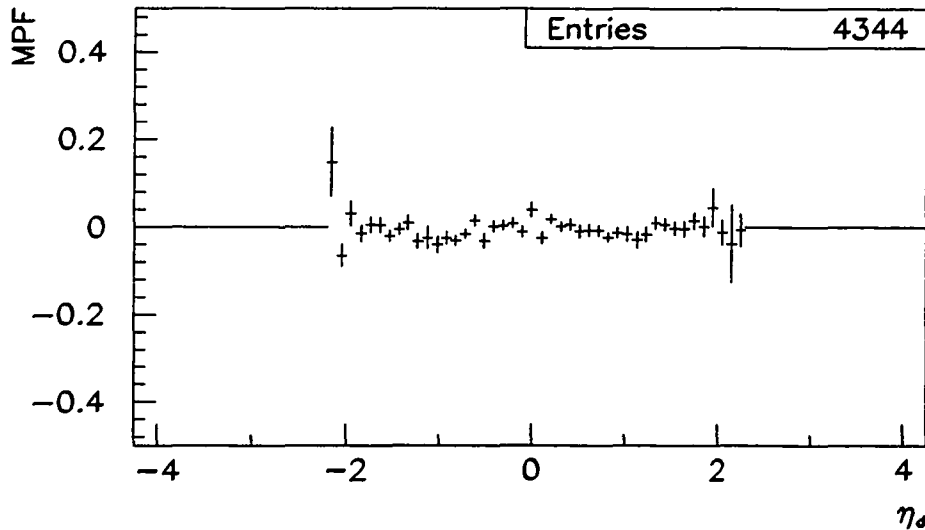
Figure 26. The missing E_t projection fraction as a function of η_d, after correction, for dijet data in the range $\sum P_t > 200$ GeV/c.

and uses the following parameterization:

$$F(Z) = 1 - XGEN(1) + XGEN(1) \times (XGEN(2) + 1) \times (1 - Z)^{XGEN(2)}, \quad (54)$$

where $F(Z)$ represents the probability that a meson carries off momentum fraction Z, and $XGEN(1)$ and $XGEN(2)$ are constants which describe the normalization and slope of the fragmentation function respectively. The main change from ISAJET fragmentation is that gluon radiation has been turned off, and this makes it necessary to separately tune the transverse fragmentation [85]. The variables $SIGQT0$ and $SIGQT$ are used to define the P_t of tracks in the underlying event and jets

respectively, and $CON2$ represents the transverse fragmentation power through the following relation,

$$P_t = N \cdot SIG \cdot \sqrt{R^{-1/CON2} - 1}. \tag{55}$$

Here the variable SIG is used to denote the use of either $SIGQT0$ or $SIGQT$ depending on whether the equation describes the underlying event or the jet particle P_t. The fragmentation variables are tuned by comparing fragmentation distributions extracted from the data to those obtained with a combination of SETPRT and full detector simulation [86]. The detector simulation also incorporates the tracking efficiency of the CTC for tracks inside jets. A few of the distributions used in the tuning procedure are:

1. The fragmentation distribution (Z) defined by

$$Z(T) = P_{//}(Track)/ \sum_{in\ cone} (P(Track)), \tag{56}$$

where $P_{//}$ is the momentum of the track parallel to the jet axis.

2. The number of tracks in the cone of the jet.

3. The number of tracks in a cone 90° away in ϕ from the jet (underlying event track multiplicity).

4. The momentum of tracks in the jet cone transverse to the jet direction, $P_\perp$.

The final tuned values for the SETPRT parameters are shown in Table VIII. A comparison of the final tuned Monte Carlo distributions with data is shown in Figures 27,

Table VIII.   Final tuned values of the fragmentation parameters used in the SETPRT
             program.

Variable	Tuned Value
XGEN(1)	0.950
XGEN(2)	7.500
SIGQT	0.250
SIGQT0	0.370
CON2	1.200

28, 29 and 30.

b.   Central Hadron Calorimeter Pion Response

The response of the CHA to charged π-mesons has been studied using a com-
bination of test beam and collider data [87]. For the test beam studies, several
beams of known momenta in a range 7–227 GeV/c were directed onto a wedge of
the central calorimeter. A comparison of beam and calorimeter energies indicates a
significant non-linearity at particle momenta below 100 GeV/c. The measurements
were extended lower in energy using events containing isolated π-mesons collected
while running with the minimum bias trigger in collider mode. The results from the
measurements (including estimated systematic errors) are shown in Figure 31. This
curve has been incorporated into the full detector simulation.

c.   Full Detector Simulation (QFL)

The detector simulation mentioned in the previous two sections is called QFL.
This program allows a complete simulation of fragmented particles in both the CTC
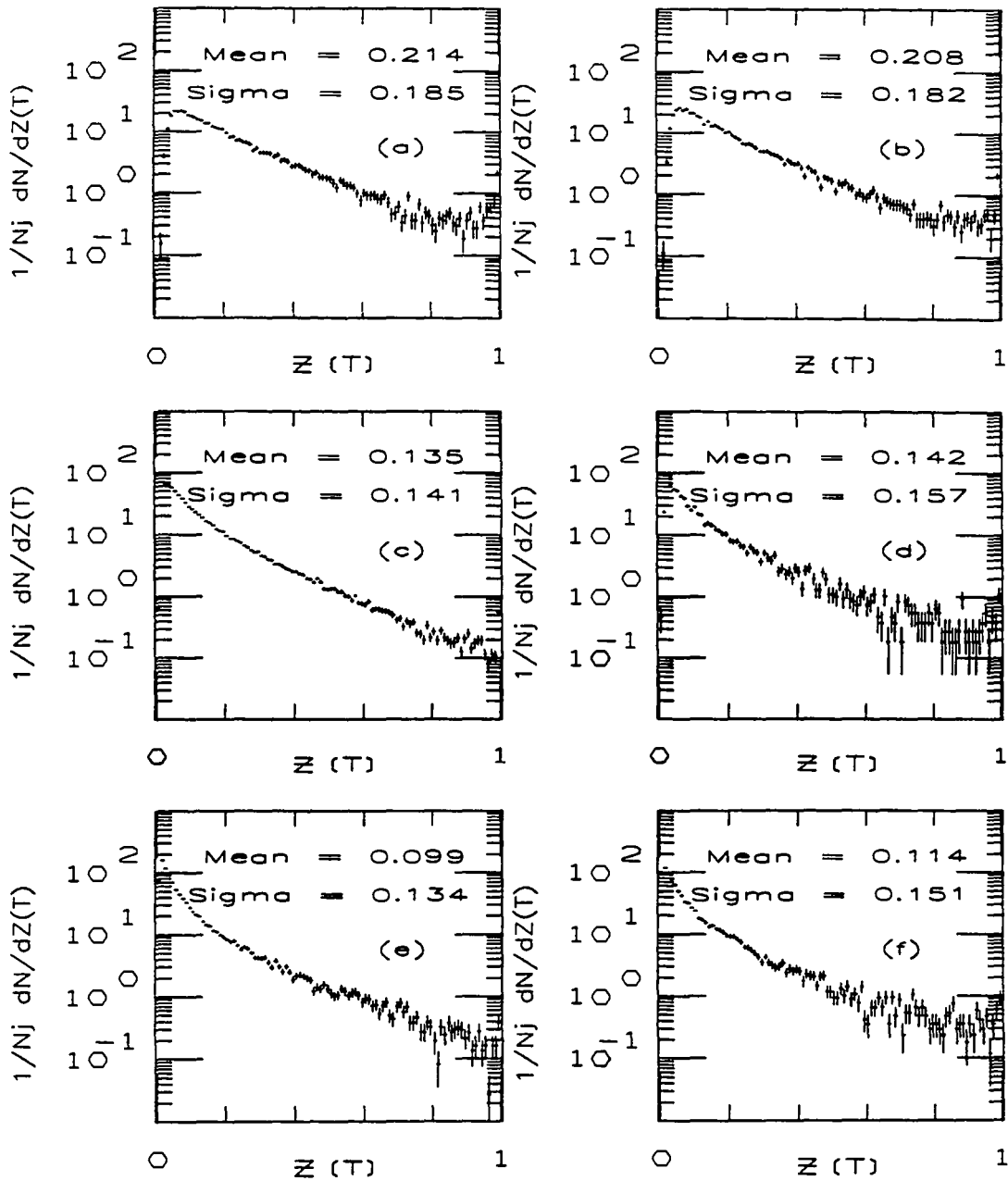
Figure 27. The distribution of $Z(T)$ (see text for definition) in jets with a cone size of 0.7. Shown are a) data and b) simulation in the E_t range 10–20 GeV, c) data and d) simulation in the E_t range 30–60 GeV, e) data and f) simulation in the E_t range 120–150 GeV.
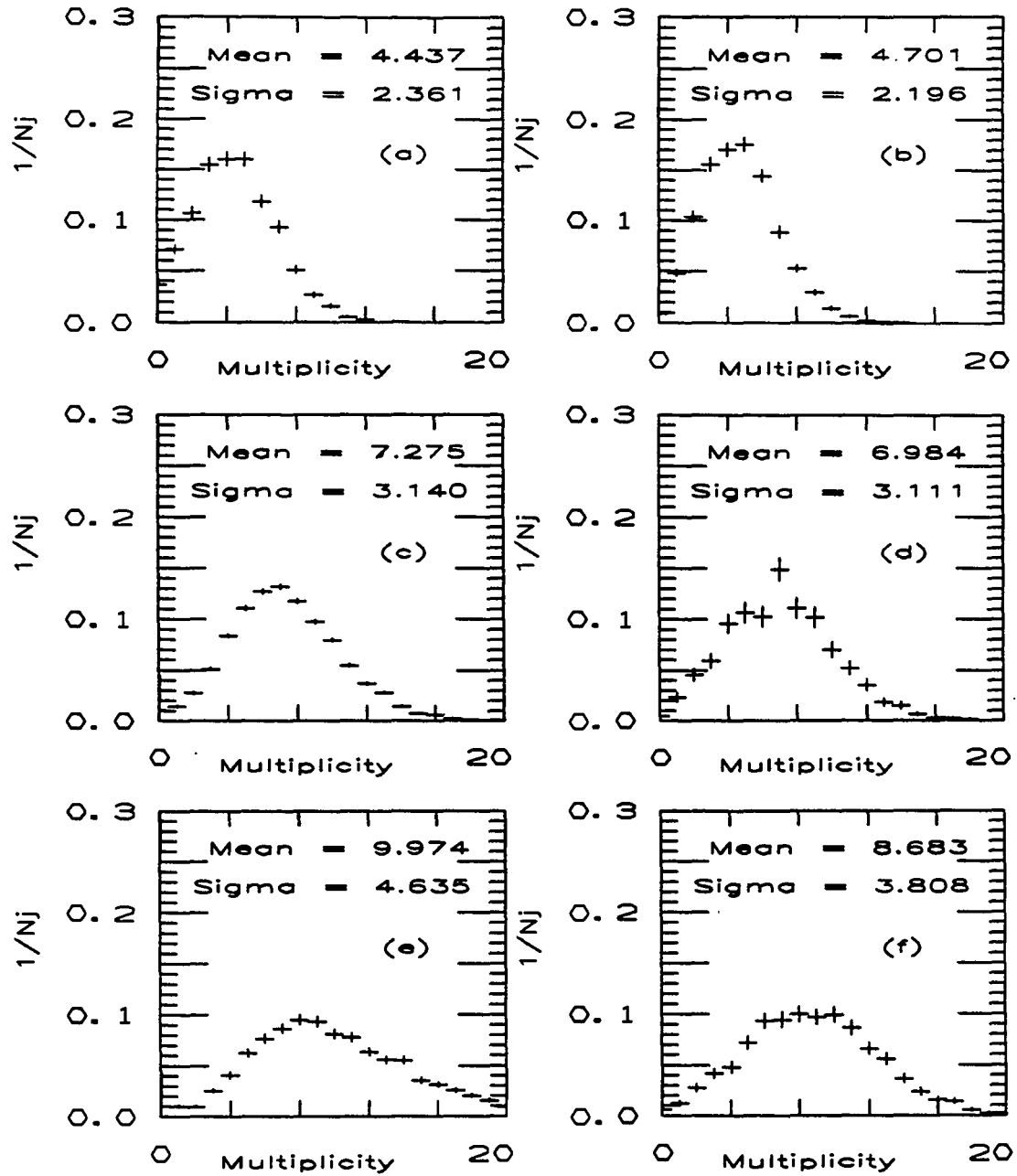
Figure 28. Jet track multiplicity in jets with a cone size of 0.7. Shown are a) data and b) simulation in the E_t range 10–20 GeV, c) data and d) simulation in the E_t range 30–60 GeV, e) data and f) simulation in the E_t range 120–150 GeV.
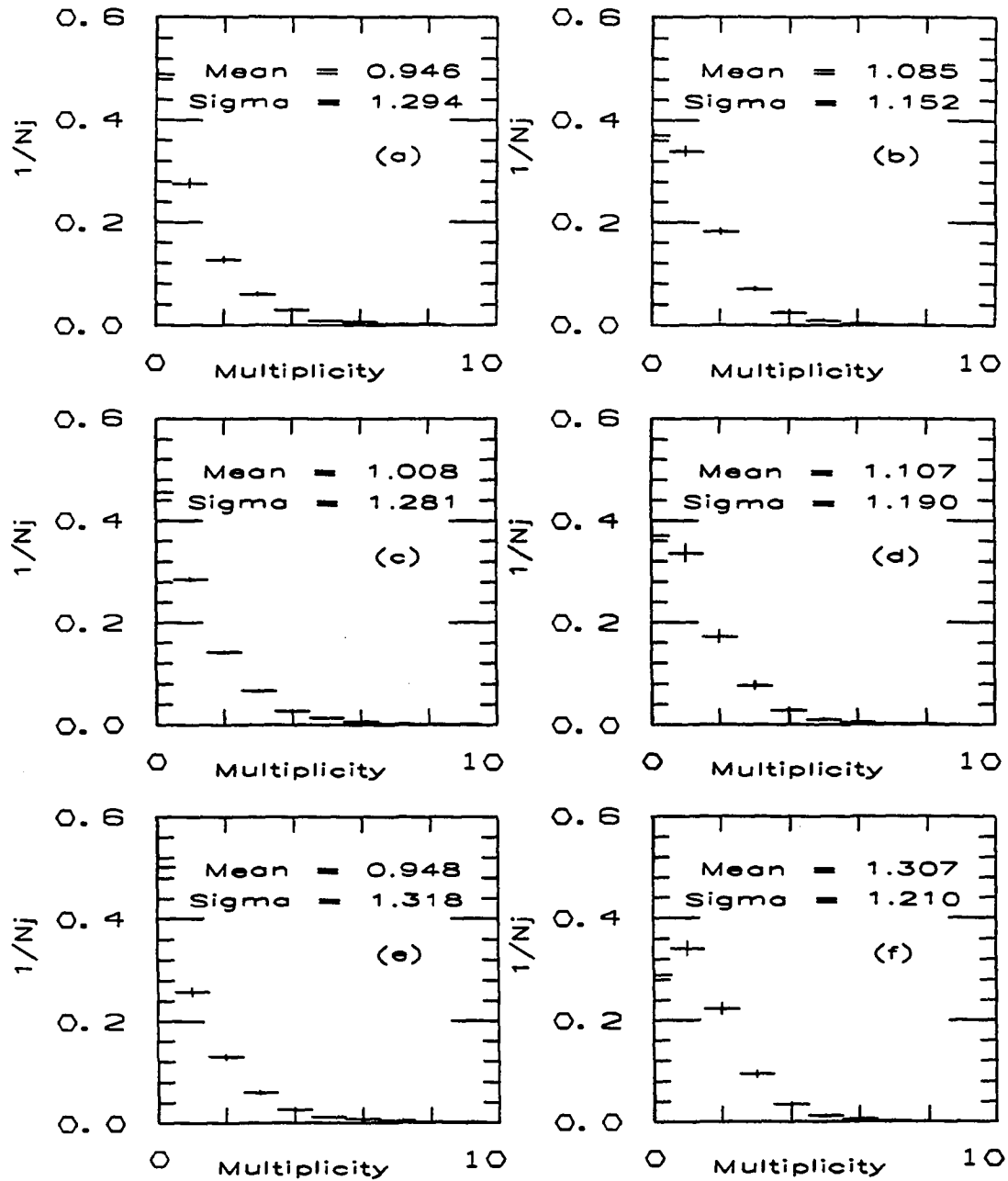
Figure 29. The underlying event track multiplicity in jets with a cone size of 0.7. Shown are a) data and b) simulation in the E_t range 10–20 GeV, c) data and d) simulation in the E_t range 30–60 GeV, e) data and f) simulation in the E_t range 120–150 GeV.
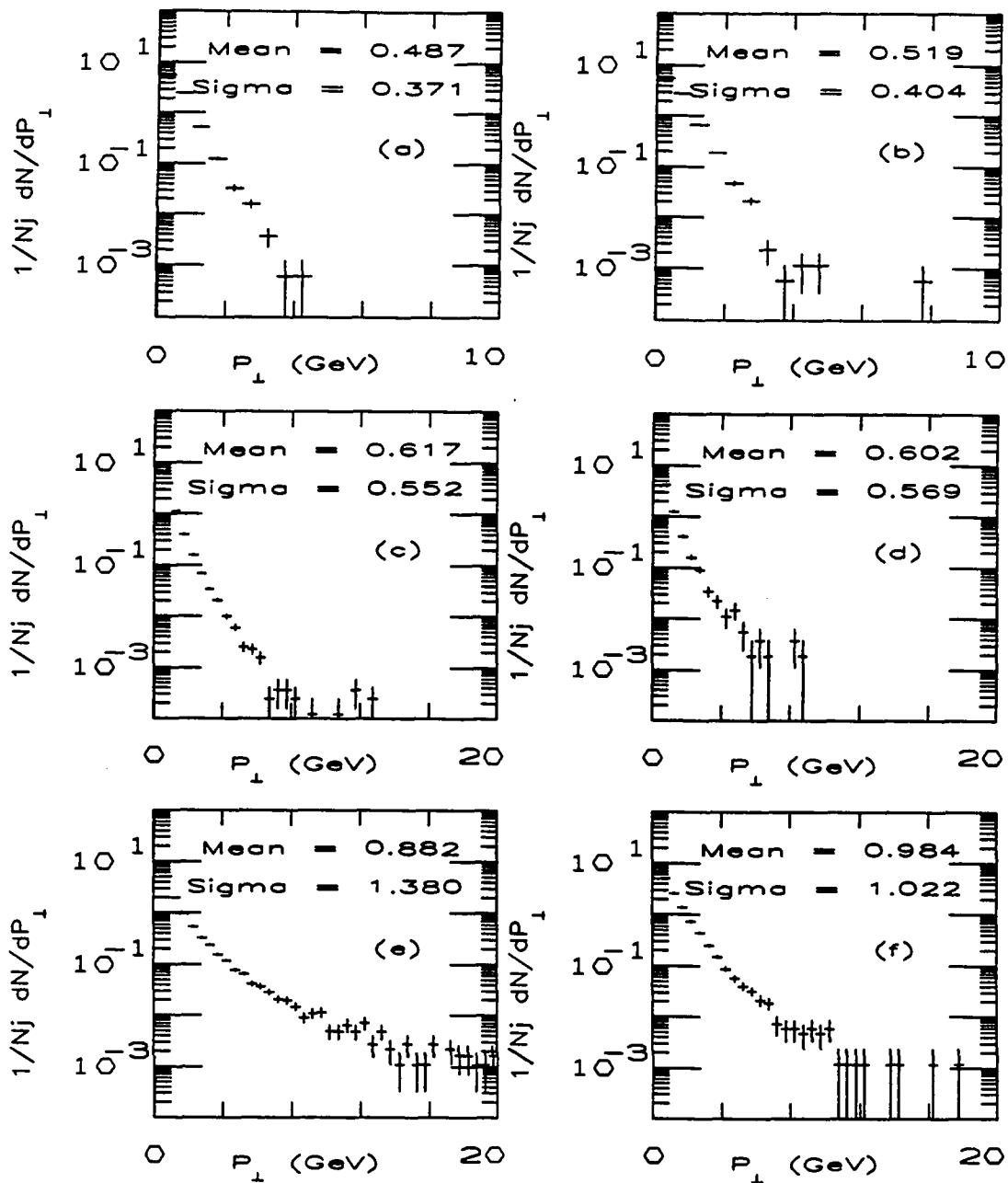
Figure 30. The distribution of $P_\perp$ (see text for definition) in jets with a cone size of 0.7. Shown are a) data and b) simulation in the E_t range 10–20 GeV, c) data and d) simulation in the E_t range 30–60 Gev, e) data and f) simulation in the E_t range 120–150 GeV.
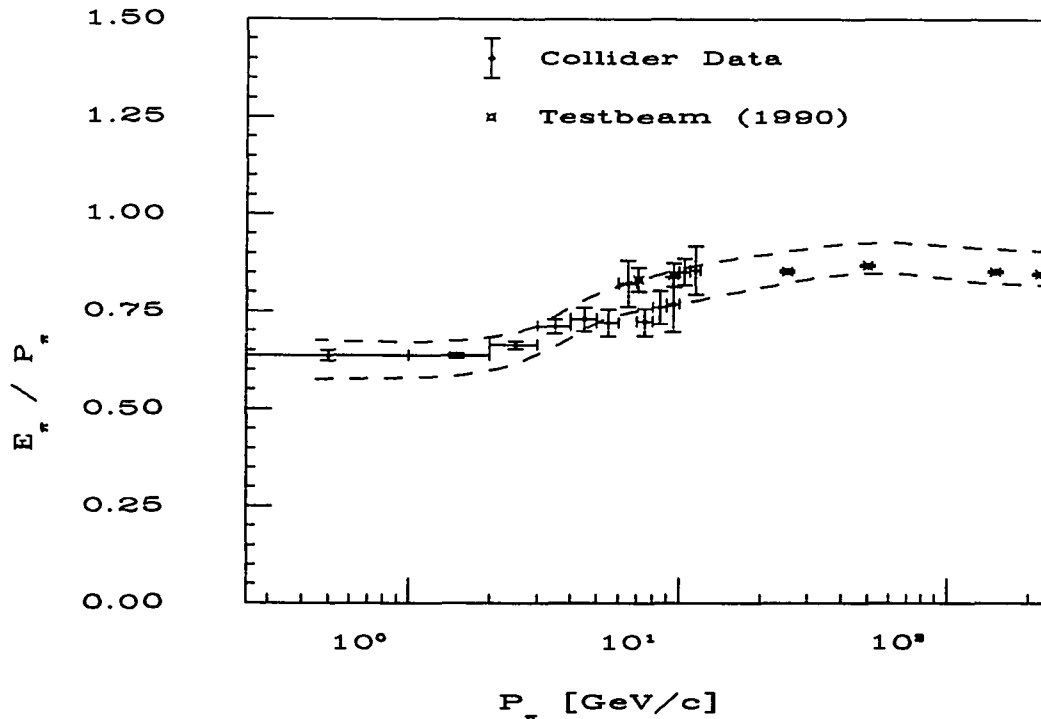
Figure 31. The response of the Central Hadron Calorimeter to charged π-mesons of various momenta. Estimated systematic errors are indicated by dashed lines.

and the calorimeters. The calorimeters are modelled with uniform density, finite sampling thickness being ignored. Despite this, tests have shown [88] that jet properties are reproduced well by QFL in the range $|\eta_d| < 2.0$. The simulation has not been finely tuned at high η_d. The non-linearities of the PHA and FHA are assumed to be identical to that measured in the CHA. This assumption does not affect the four-jet analysis, as the full detector simulation is primarily used to model the central region of the detector.

d. Method of Correction

The analysis path used for the absolute jet energy scale determination is as follows:

1. SIMJET : Generates pairs of massless partons in the range $2 < P_t < 700$ GeV/c and $\mid \eta \mid < 1.2$. A flat P_t spectrum is used to obtain good statistics over a large P_t range. A transverse momentum kick is generated to simulate the effects of gluon emission, along with an underlying event.

2. SETPRT : Performs fragmentation.

3. QFL : Full detector simulation.

4. JETCLU : Clusters jets with a cone size of 0.7.

All events were required to pass the following cuts:

1. $\mid z_{\text{vertex}} \mid < 60$ cm.

2. Jet $P_t > 5$ GeV/c.

3. $0.2 < \mid \eta_d \mid < 0.7$

Partons are associated with a clustered jet using the matching criterion

$$\sqrt{(\eta_{\text{Parton}} - \eta_{\text{Jet}})^2 + (\phi_{\text{Parton}} - \phi_{\text{Jet}})^2} < 0.5. \tag{57}$$

The quantity $\mid \sum \vec{P_t} \mid$ is then formed, where the sum is taken over all simulated particles having their *initial* $\widehat{P_t}$ direction inside the jet cone. Hereafter, this quantity is denoted by P_t^{Cone}. The theoretical uncertainty in the fragmentation process leads to a correction based on P_t^{Cone} rather than the actual P_t of the parton. The absolute energy scale is then defined by

$$\alpha(P_t^{\text{Jet}}) = \left\langle \frac{P_t^{\text{Cone}}}{P_t^{\text{Jet}}} \right\rangle, \tag{58}$$

where the brackets denote an average value over many events. In practice, the quantity α is determined as a function of P_t^{Jet} in 60 bins of 10 GeV/c each in the range 0–600 GeV/c. Jet P_t is taken at the center of each bin, and a Gaussian fit is used to determine α for each of the bins. The relation

$$P_t^{\text{Cone}} = \alpha \cdot P_t^{\text{Jet}} \qquad (59)$$

is used to construct a monotonic plot of averaged values of P_t^{Cone} versus P_t^{Jet}. The final plot is fitted to a double quadratic function, with breakpoint at $P_t^{\text{Jet}} = 100$ GeV/c. At this value there is a transition between highly non-linear and approximately linear behaviour. Figure 32 shows the variation of the ratio $P_t^{\text{Jet}}/P_t^{\text{Cone}}$ with jet P_t. This Monte Carlo data has been used to extract the absolute jet energy scale for cone size $R = 0.7$. The distribution of $P_t^{\text{Cone}}/P_t^{\text{Jet}}$ is shown in Figure 33 for various bins of jet P_t, and the final response curve can be seen in Figure 34. Also shown are the deviations between the Monte Carlo data and the corresponding fit. For the four-jet data sample, most of the jets have $P_t < 100$ GeV. This region is particularly well fitted by the quadratic form.

3. Underlying Event and Out-of-Cone Energy

The cone that is constructed around a cluster does not necessarily contain *all* the particles that were emitted by its associated parton. Also, additional particles may enter the cone from the soft underlying event. A schematic picture of these two effects can be seen in Figure 35. Such a counting error propagates directly into the measurement of parton P_t.
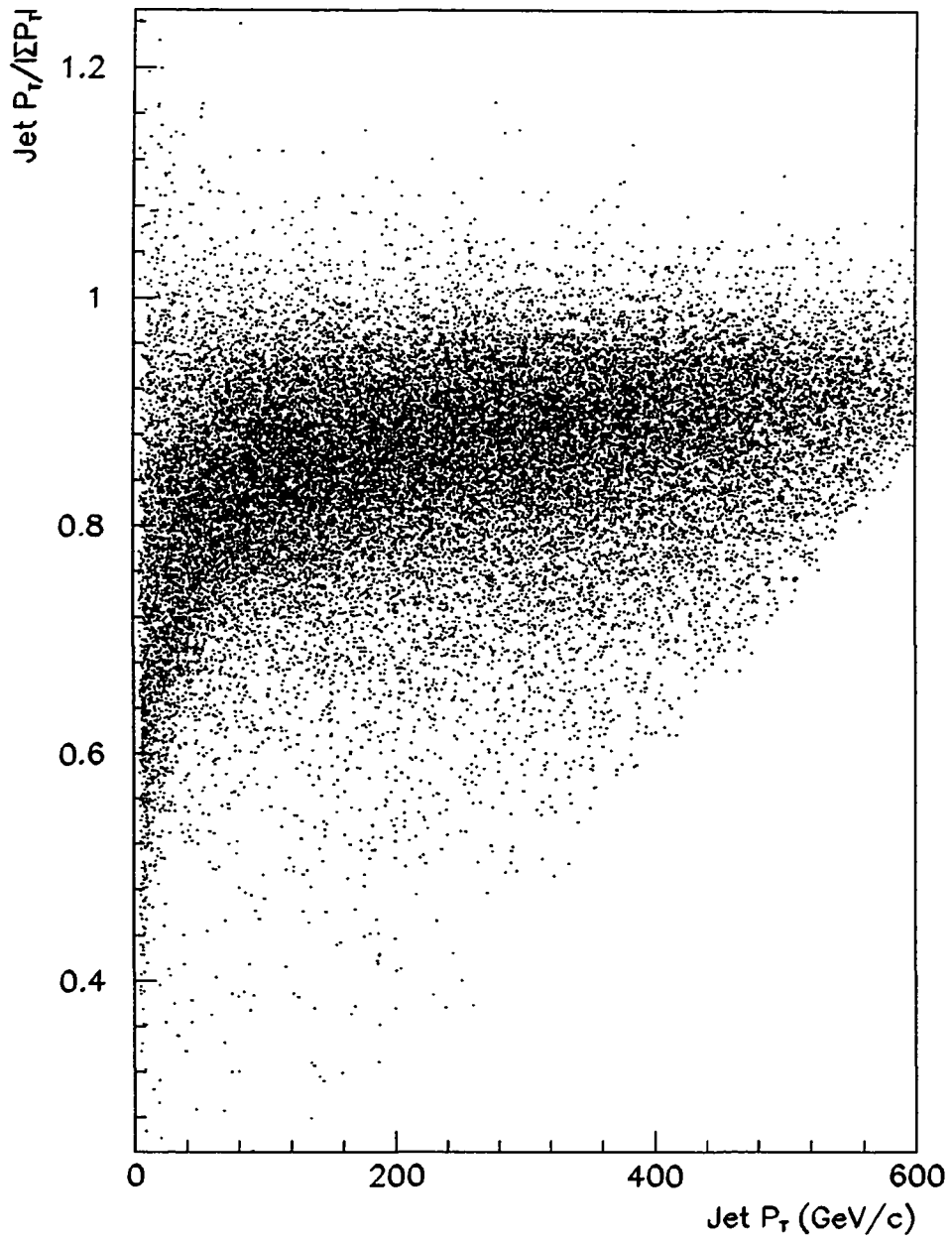
Figure 32. Monte Carlo data showing $P_t^{\text{Jet}}/P_t^{\text{Cone}}$ versus P_t^{Jet}.
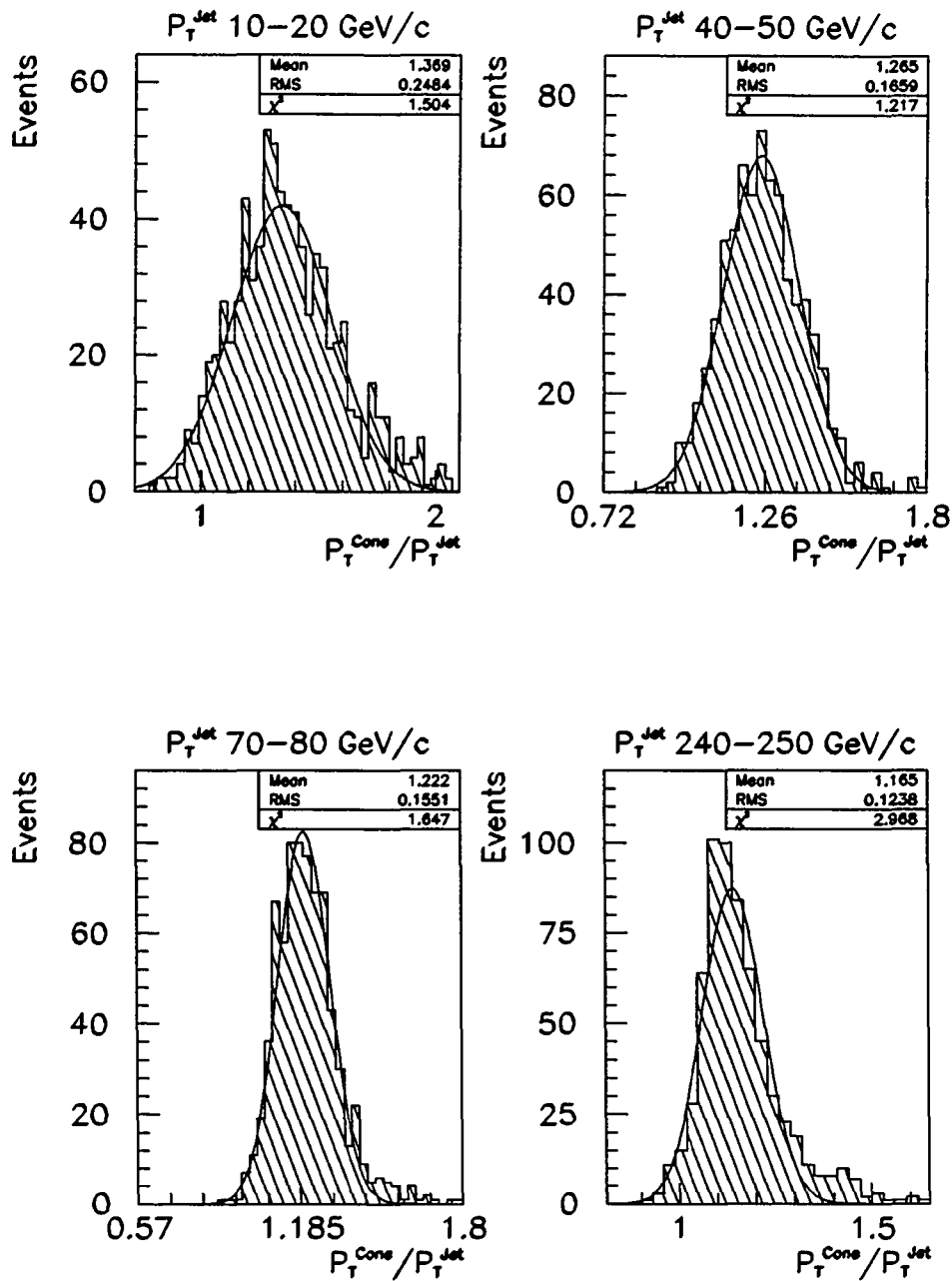
Figure 33. Distributions of $P_t^{\mathrm{Cone}}/P_t^{\mathrm{Jet}}$ for various P_t^{Jet} ranges. Shown are 10–20, 40–50, 70–80 and 240–250 GeV/c.
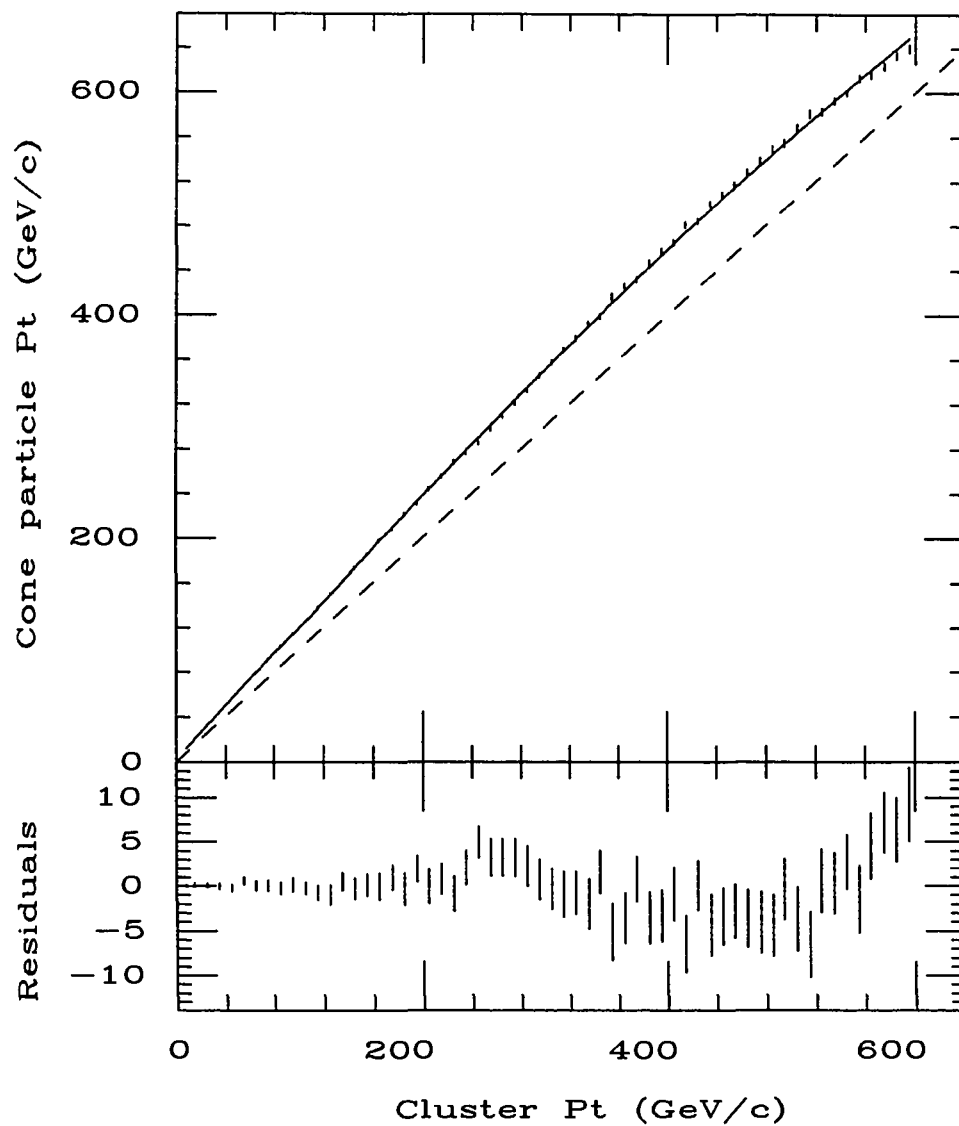
Figure 34.   Particle P_t^{Cone} versus P_t^{Jet} with fit to a double quadratic. A cone size of 0.7 has been used. The break point for the fitted function is at $P_t^{\text{Jet}} = 100$ GeV/c.
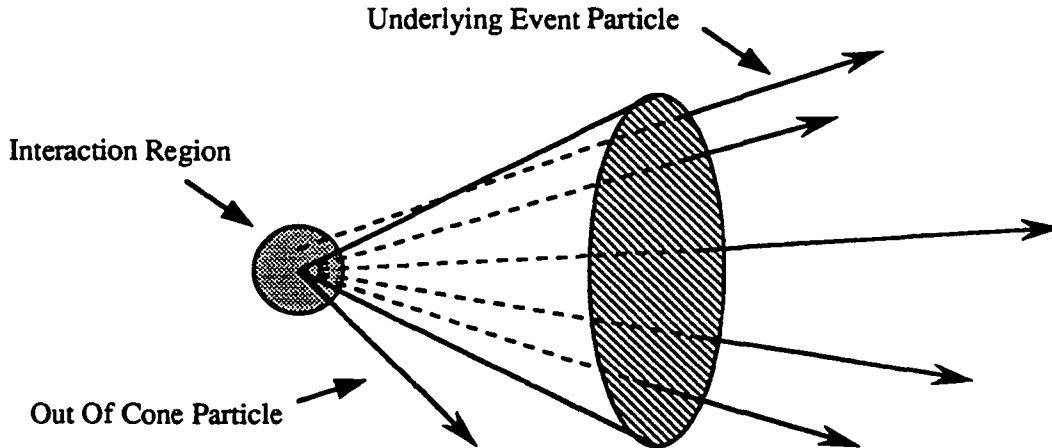
Figure 35. Schematic picture of underlying event and out-of-cone particles.

An estimate of the underlying event energy has been made using data taken with the minimum bias trigger [89]. The average E_t summed over calorimeter towers in the region $-1.0 < \eta_d < 1.0$ has been measured as 5.78 GeV. Dividing by the angular area of this region (4π) and multiplying by a factor of 1.6 for particle mismeasurement yields an underlying event particle E_t density of 0.46 GeV/η-ϕ radian. Since underlying event energy deposition is approximately uniform in η-ϕ space, the total underlying event E_t for a given jet cone size can now be obtained. For a cone of size $R = 0.7$ an E_t of 1.13 GeV on average will be contributed from the underlying event.

The P_t of particles that fall outside the clustering cone is measured using the same simulation used to determine the absolute jet energy scale. The correction for

a given jet is defined as:

$$\text{OUTCONE} = | \sum \vec{P_t}(\text{All particles}) - \sum \vec{P_t}(\text{Particles in cone}) |, \qquad (60)$$

where the particles in question have been emitted from the parton that has been paired up with its corresponding jet using the criterion of Equation 57.

The out-of-cone P_t is found to increase monotonically with jet P_t. In constructing a correction function, the median Monte Carlo value of OUTCONE was plotted against jet P_t in six bins of 100 GeV/c, from 0–600 GeV/c. A fit was then performed, using the functional form

$$\text{OUTCONE} = a(1 - be^{-cP_t}). \qquad (61)$$

This form was found to fit the results very well. Figure 36 shows the distribution of the OUTCONE variable for various bins of jet P_t, and Figure 37 shows the resulting data points together with the fitted curve. Both figures have been constructed using a cone size of $R = 0.7$. The fragmentation at wide angles relative to the cone center is a subject of considerable uncertainty, and the results obtained here are model dependent. Consequently in the four-jet analysis the out-of-cone energy correction is applied only for the purpose of estimating systematic errors (see Chapter VII). The underlying event energy correction is treated in the same manner, since the correction derived from minimum bias data does not necessarily apply to the four-jet process. The partial cancellation of the two corrections means that applying both separately should yield a conservative measure of their combined systematic error.
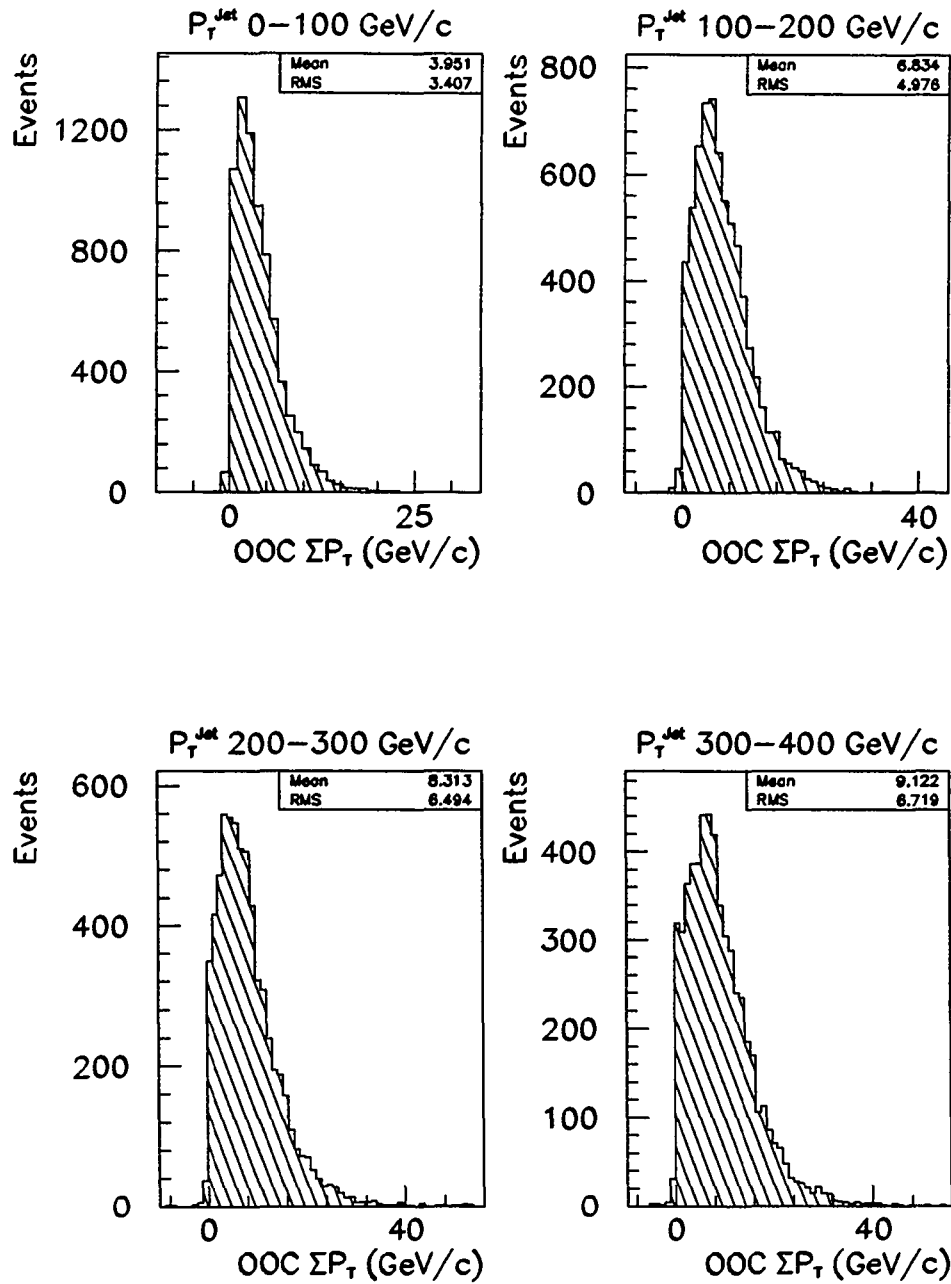
Figure 36. The out-of-cone correction for various ranges of jet P_t for a cone size of 0.7. The P_t ranges shown are 0-100, 100-200, 200-300 and 300-400 GeV/c.
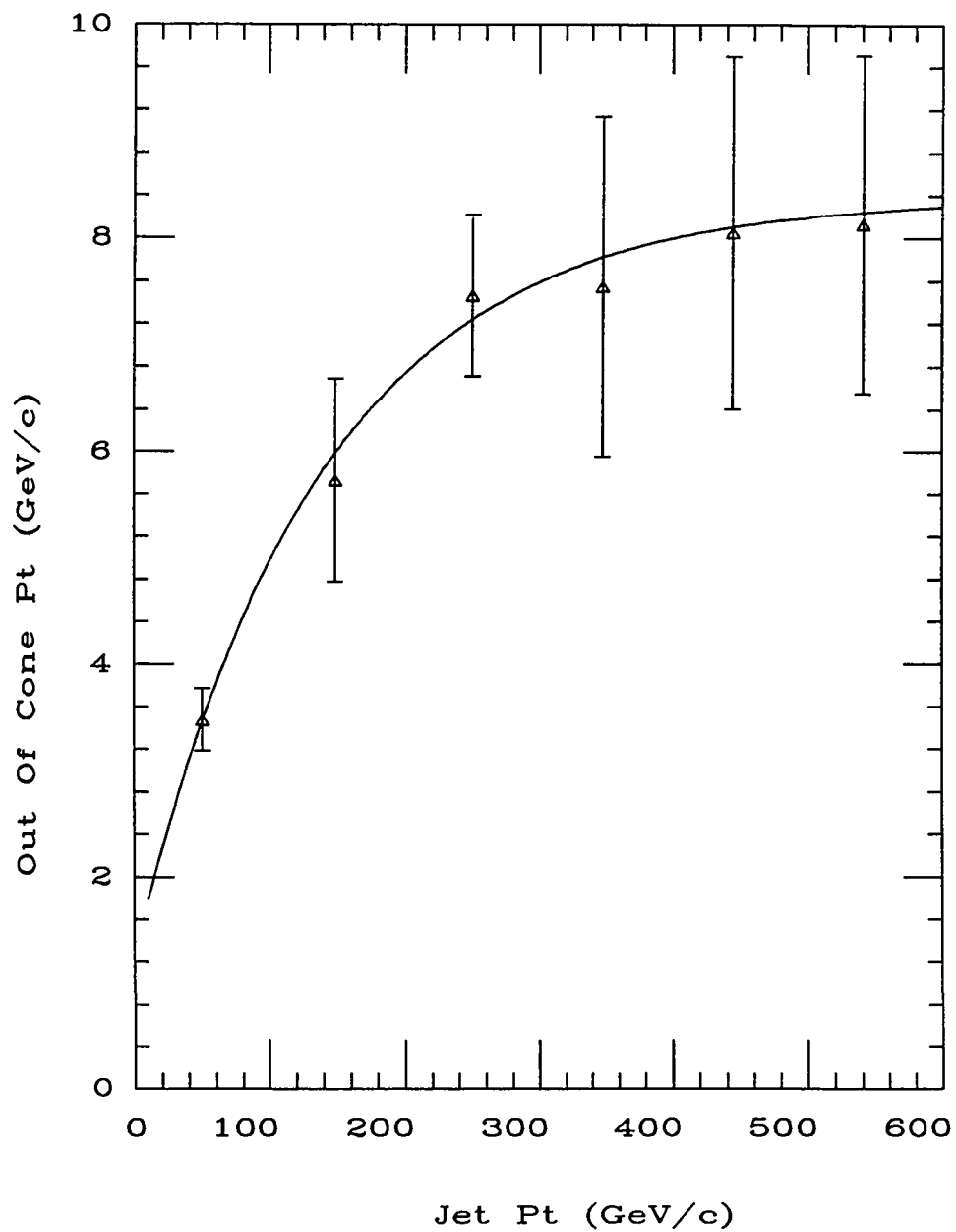
Figure 37. The out-of-cone correction plotted as a function of jet P_t with fit for cone size $R = 0.7$.

CHAPTER V

FOUR-JET KINEMATIC ANALYSIS

In making a comparison between data and QCD we must ensure that both data and Monte Carlo simulations are well understood. The main concern with the data used in this analysis is the possibility of problems introduced by the fairly complicated trigger. This has been studied in detail and cuts have been placed on reconstructed jet quantities in order to ensure that bias due to the trigger is minimal. This first part of this chapter is concerned with the placing of these cuts. A fast Monte Carlo program used in the simulation of jet properties is then discussed in detail, and its ability to reproduce the observed jet resolution is examined. Finally a comparison of kinematical quantities is made between the four-jet data and a leading order calculation of the QCD double bremsstrahlung process. Note that this data is expected to be mainly comprised of double bremsstrahlung events (see Figure 9).

A. Data Set

The data set used in this analysis was accumulated using a dedicated trigger known as the *multijet* trigger. The requirements were:

1. Level 1 : $\sum E_t > 18$ GeV, over all calorimeter towers.

2. Level 2 : At least two calorimeter energy clusters, with E_t denoted by E_{t_1} and E_{t_2} where 1 and 2 refer to the highest and next highest E_t cluster respectively.

3. Level 2 : $\sum E_t - E_{t_1} - E_{t_2} > 40$ GeV. This requirement is henceforth known as the ξ cut.

4. Level 3 : At least 4 clusters with $P_t > 15$ GeV/c. Offline reconstruction is applied but no jet corrections are performed. Also, the z-vertex is assumed to be at 0 cm.

The Level 3 requirement is fairly stringent. The sole object of this trigger is to collect a large sample of four-jet events. The total integrated luminosity of this data set has been determined as [90, 91],

$$\mathcal{L} = 324.9 \pm 6.8\% \text{ nb}^{-1}. \tag{62}$$

The luminosity falls far short of the integrated 1988/89 run luminosity (approximately 4 pb^{-1}). One reason for this is that the trigger was only in place for a few months near the end of the run. In addition, the trigger was found to have a large cross section, and was therefore inserted into the special low luminosity trigger table.

The following data quality cuts are placed on the events used in this analysis:

1. $\mid z_{\text{vertex}} \mid < 60$ cm.

2. Jet $\mid \eta_d \mid < 3.5$.

3. $\Delta R > 1.0$ where ΔR is the minimum jet separation angle in η-ϕ space, defined by $\Delta R = \sqrt{(\eta_i - \eta_j)^2 + (\phi_i - \phi_j)^2}$, minimized over all possible jet pairings.

4. No secondary z-vertex observed with the VTPC.

All jets are clustered with a cone size of $R = 0.7$. This cone size was also used by the Level 3 trigger during data-taking. The jet multiplicity obtained using these cuts for jets having $P_t > 25$ GeV/c (corrected) is shown in Figure 38. The relative depletion
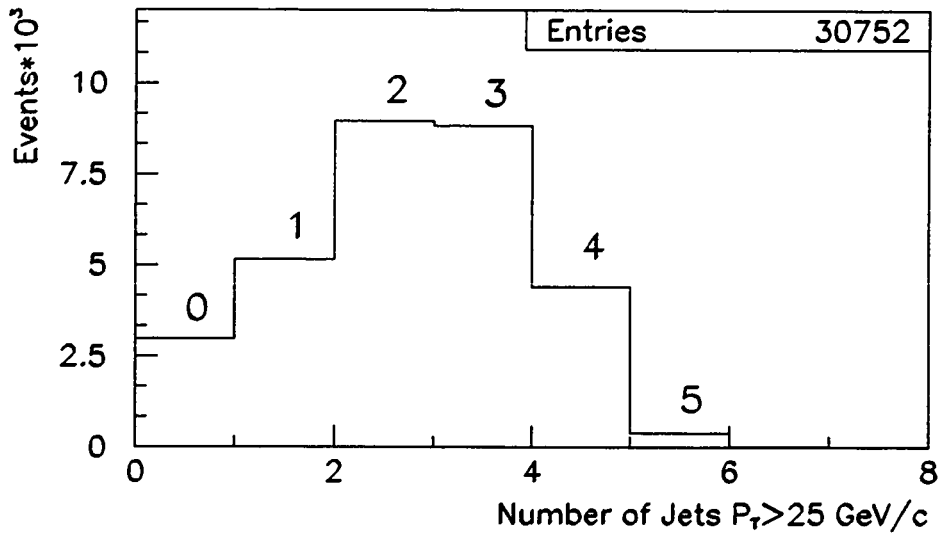
Figure 38.   The number of jets having $P_t > 25$ Gev/c (corrected) obtained with the standard data quality cuts.

of dijet events relative to three-jet and four-jet events is a consequence of the Level 2 and 3 triggers.

B.   Cuts to Remove Trigger Bias

Further offline cuts are imposed with the aim of removing the effects of trigger bias while still retaining adequate statistics. Specifically, cuts are imposed on single jet P_t and on the scalar $\sum P_t$ of the largest 4 jets.

1.   Single Jet P_t Cut

The single jet P_t cut is aimed at reducing bias caused by the Level 3 trigger requirement of 4 jets with $P_t > 15$ GeV/c. These jets are uncorrected for detector

mismeasurement and smearing of the z-vertex. Consequently there will be a predominance of jets in areas where the energy response of the calorimeters is high and a depletion in the crack regions. The approach adopted is to ensure that the Level 3 trigger is fully efficient for events passing the cut over the entire range of η_d. In other words the events that remain are *unbiased* by the Level 3 trigger. The penalty for this is a reduction in statistics.

To study the single jet P_t cut, approximately 1500 events were generated using the following path:

PAPAGENO SETPRT QFL JETCLU JETCL3 MULTI

The Monte Carlo event generator PAPAGENO [92] produces parton four-vectors using the Kunszt-Stirling approximate four-jet matrix element [47]. The tuned fragmentation program SETPRT is used to transform partons into particles which can then be propagated through the detector simulation QFL. Two clustering algorithms are then run on the resulting calorimeter data. JETCLU is the regular jet clustering algorithm. The routine JETCL3 also performs clustering, but now the jets are not corrected for z-vertex smearing. Instead, the z-vertex position is assumed to be 0 cm. This clustering routine therefore produces jets that are equivalent to those used by the Level 3 trigger during the run. The final routine MULTI performs corrections on the jets clustered by JETCLU and is used to place a cut on the resulting jet P_t. The cut was imposed on *corrected* P_t so as not to further bias the data.

The corrected P_t distribution of the smallest jet versus its simulated Level 3 P_t can be seen in Figure 39a). The dashed line shows the Level 3 trigger threshold of

15 GeV/c, where an offline jet P_t cut of 25 GeV/c has been applied. This figure shows that nearly all these events would have been passed by the Level 3 trigger and are therefore unbiased. The efficiency of this cut is found to be 98.7% by event counting. This study is entirely based on simulated data. However, Figure 39b) shows that there is good agreement between data and simulated four-jet double bremsstrahlung events for the smallest jet P_t spectrum. This indicates that the cut will work equally well with real data.

2. Cut on $\sum P_t$

A cut on the $\sum P_t$ of the four largest jets was necessary in order to remove bias introduced by the Level 2 trigger. One of the requirements of this trigger was that $\sum E_t > 80$ GeV over all the calorimeters. This requirement again resulted in an excess of jets in regions of high calorimeter response. An offline cut on $\sum P_t$ was made to ensure that the remaining events had uniform jet acceptance.

The $\sum P_t$ cut has been placed by carefully simulating the trigger and using these results in conjunction with information obtained from data. The analysis path used was similar to that described in the previous section with the addition of the CDF trigger simulation package, TRGSIM. This program uses the output of QFL to construct simulated Level 2 quantities. Figure 40 shows a scatter plot of corrected jet $\sum P_t$ plotted against the Level 2 $\sum E_t$, for both data and Monte Carlo four-jet events. The dashed lines show the online 80 GeV requirement and the offline cut which is chosen to be 140 GeV/c. Although there are less events in the case of the simulation, both plots are very similar, indicating that the simulation is reliable. With the cut in
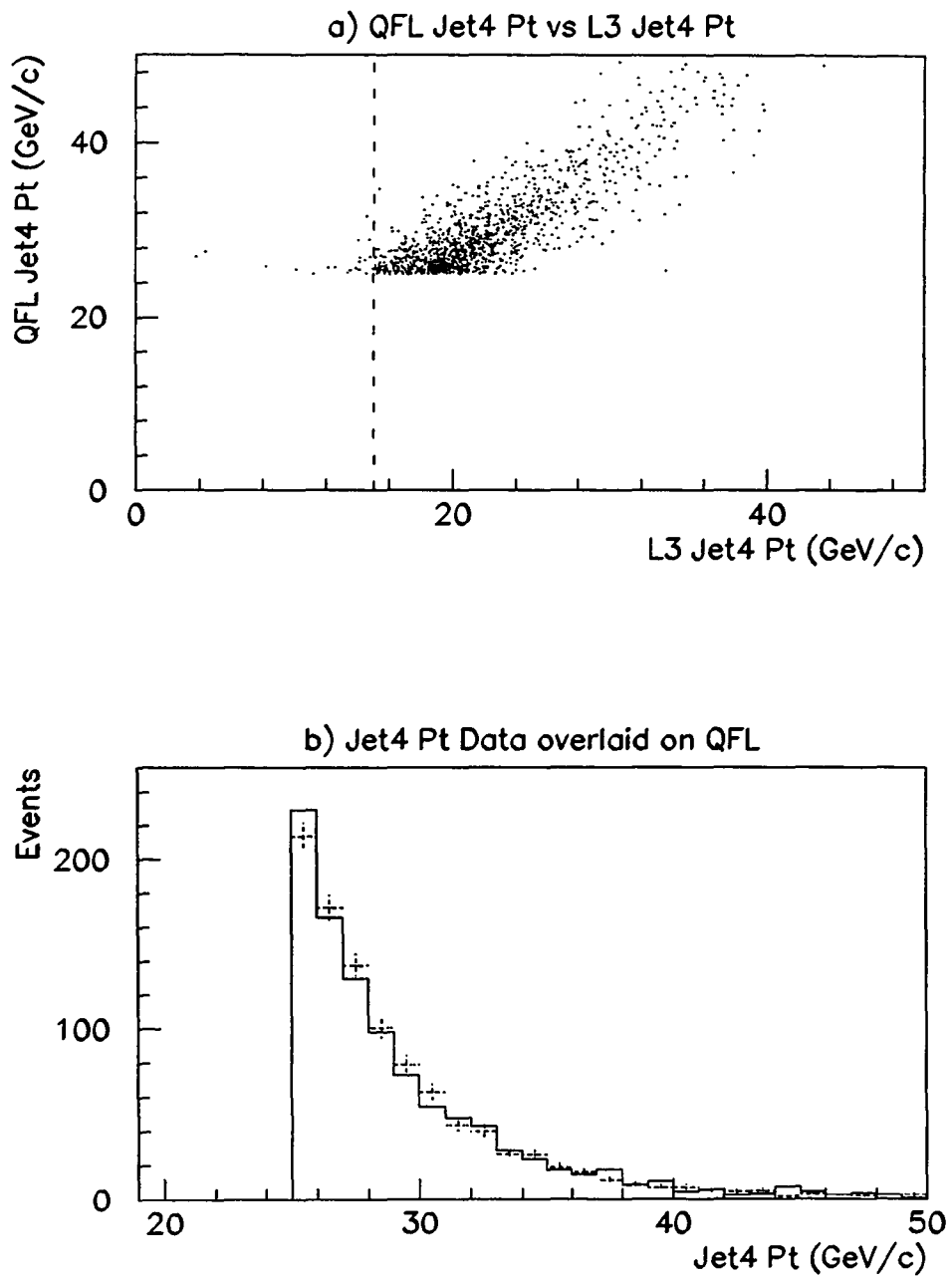
Figure 39. Monte Carlo (QFL) Level 3 study. a) Corrected offline P_t of the smallest
jet versus the corresponding Level 3 P_t. b) A comparison of the smallest
jet P_t between data and Monte Carlo, with $P_t > 25$ GeV/c.

place, the efficiency of the Level 2 $\sum E_t$ trigger is found to be 100%. The distribution of the Level 2 simulated $\sum E_t$ before and after the cut on corrected four-jet events of $\sum P_t > 140$ GeV/c is shown in Figure 41. To further demonstrate the reliability of the Level 2 simulation, Figure 42 shows a comparison of the Level 2 $\sum E_t$ obtained with the data and simulation after the offline cut.

After the cuts on jet P_t and $\sum P_t$ there remains a well understood data sample of 2213 events. This number of events is large enough to allow a rigorous check of QCD. In principle, the fairly severe offline cuts could be avoided by including the effects of trigger cuts in the simulated events. The benefit would be an improved double parton signal to double bremsstrahlung background. However, this would involve using many PAPAGENO + QFL events in conjunction with the full Level 2 and 3 simulations. Unfortunately, the computing power required to produce a sufficient number of events for smooth simulated distributions is too great to be practical at the present time. In addition, this technique implies a greater reliance on the trigger simulation, and hence a worsening of systematic errors.

3. The Level 2 ξ Cut

The ξ cut was implemented in Level 2. By imposing the requirement $\xi = \sum E_t - E_{t_1} - E_{t_2} > 40$ GeV many of the dijet events that had been selected by the $\sum E_t > 80$ GeV cut were rejected. The effects of this trigger are not treated with an offline cut, since doing so effectively reduces the event sample to an insignificant level. Fortunately, the correlation between offline (corrected) ξ and Level 2 ξ is very weak, as shown in Figure 43. Offline ξ is defined analogously to Level 2 ξ by the relation

a) Data Offline ΣPt vs L2 ΣEt

b) QFL Offline ΣPt vs L2 ΣEt
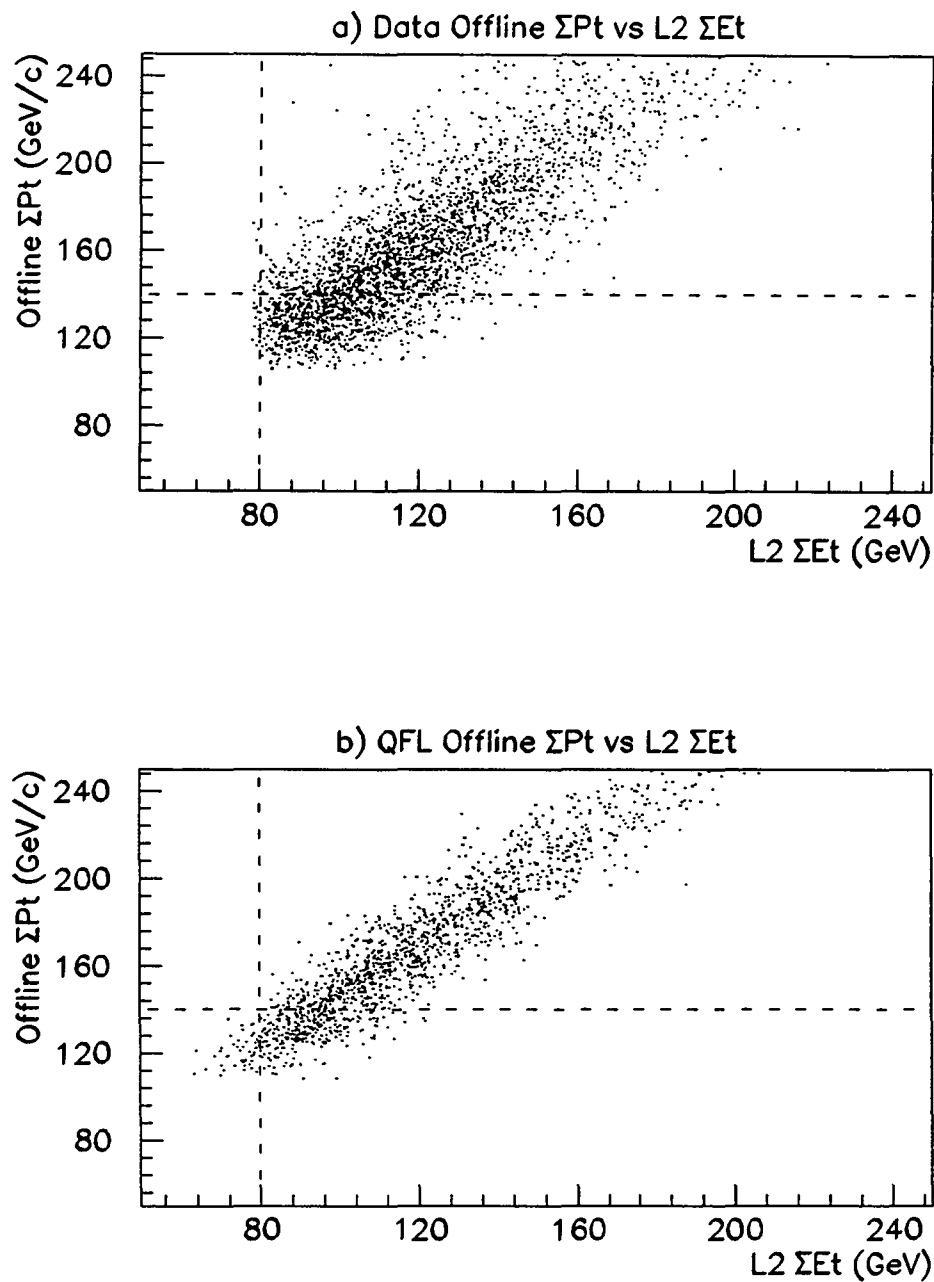
Figure 40. Offline $\sum P_t$ versus Level 2 $\sum E_t$. Shown are a) data and b) simulation using double bremsstrahlung events and the full detector simulation. The online cut $\sum E_t > 80$ GeV and offline cut $\sum P_t > 140$ GeV/c are indicated by dashed lines.
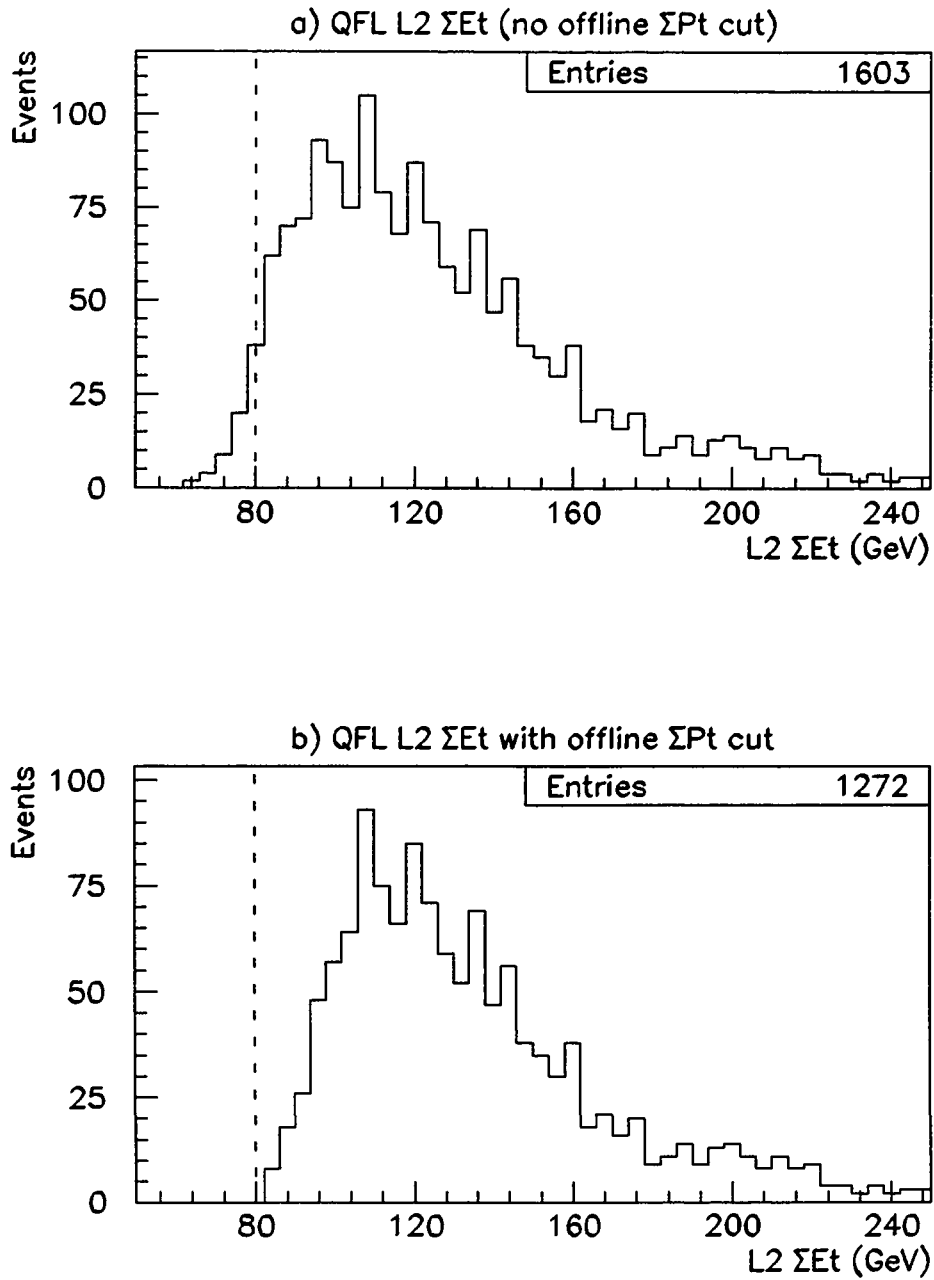
Figure 41. Simulated Level 2 $\sum E_t$ before and after the offline cut $\sum P_t > 140$ GeV/c. Shown are the distributions a) before the cut and b) after the cut using double bremsstrahlung events with full detector simulation.
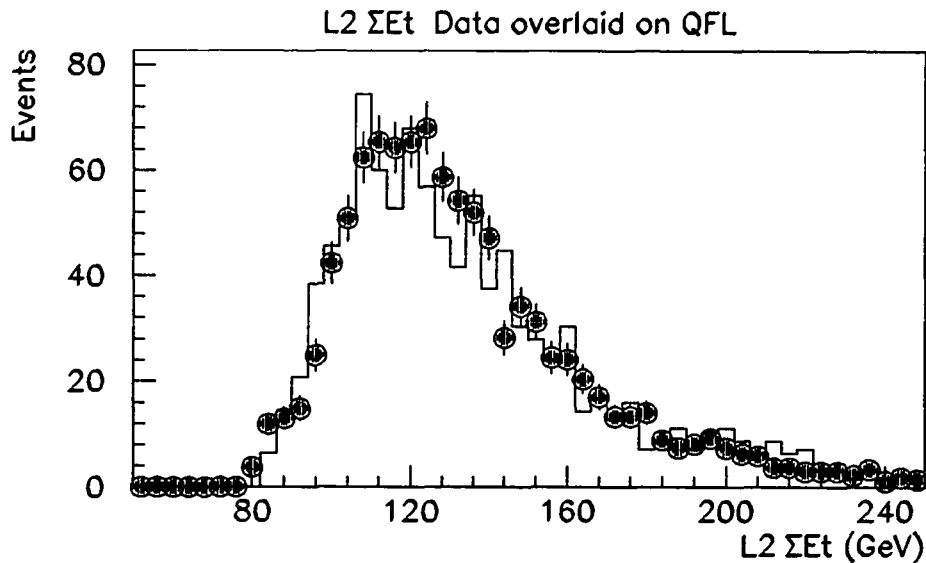
Figure 42.   A comparison of data and Monte Carlo Level 2 $\sum E_t$. The cuts $P_t >$ 25 GeV/c (for all jets) and $\sum P_t > 140$ GeV/c have been applied.

$\xi = \sum P_t - P_{t_1} - P_{t_2}$, where $\sum P_t$ is taken over the four leading P_t jets. This lack of correlation implies that the Level 2 ξ cut does not bias the data to any appreciable degree. An explicit check of this is performed in Chapter VI.

C.   The Fast Jet Simulation

The PAPAGENO event generator produces parton four-vectors which may then be fragmented by other routines. The events generated are assigned weights according to their probability of occurrence according to the matrix element used. The sum of all weights is equal to the cross section for the process generated. For the four-jet process the weights fluctuate over a wide range, and a large number of events must be generated in order to obtain smooth distributions. To produce a smooth
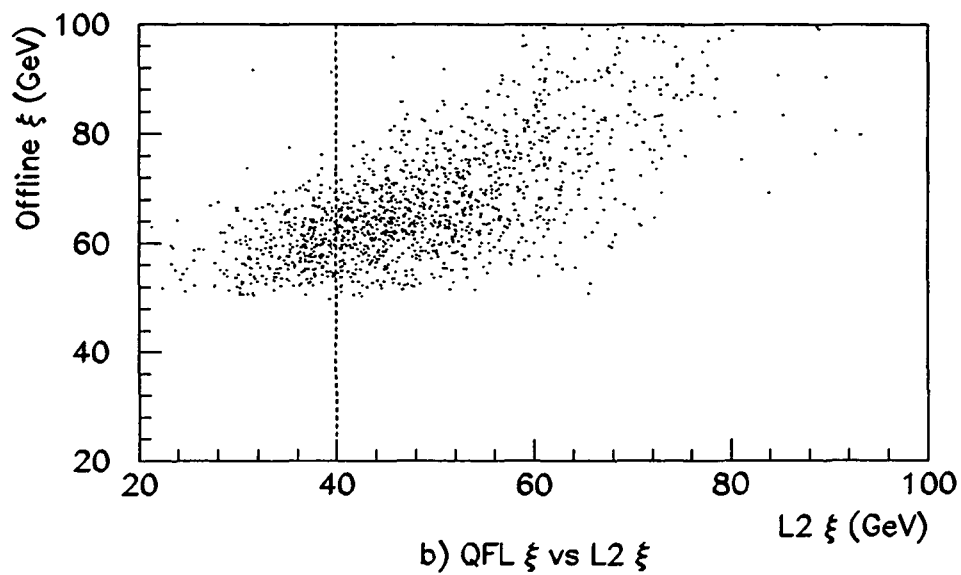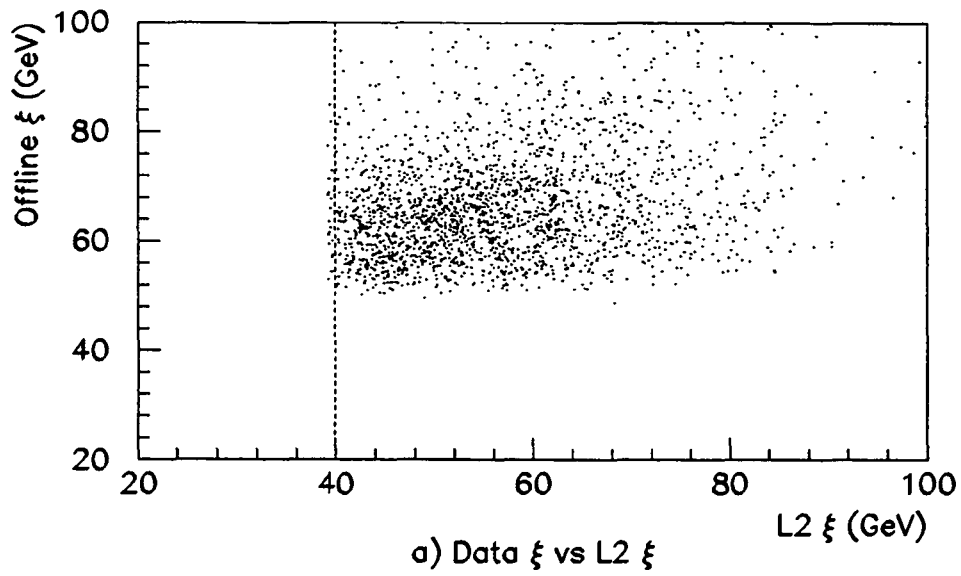
Figure 43. A comparison of ξ (see text for definition) for corrected jets and Level 2 clusters. Shown are a) data (note the cut at 40 GeV) and b) simulation using QFL + TRGSIM with PAPAGENO double bremsstrahlung events.

1-dimensional histogram containing 50 bins, approximately one million events are needed. The generation process is inefficient since generation thresholds must be low enough to include all kinematic possibilities that may occur in the data. An unfortunate consequence of this is that many events are generated in areas of low detector acceptance. Consequently, to produce one million final events passing all cuts requires the generation of one hundred million parton-level events. Passing all these events through the full detector simulation is impractical, so a fast simulation program has been written that can transform partons to jets very quickly. This program is called QDJTMC [93] and will be henceforth be referred to as the *fast jet simulation*. For the trigger simulation studies using QFL, the PAPAGENO events were statistically unweighted before being used. This is a painstaking procedure, approximately half a *billion* events were generated in order to obtain an unweighted sample of 1,500 events passing all cuts. This was achieved by running 10 Vaxstation 3100-M76 processors in parallel. Since multiple data sets must be created to study systematic errors in the analysis, the use of the fast jet simulation is preferable. In addition, the fast jet simulation may be easily tuned to reproduce the observed jet energy scale and resolution. This gives the fast simulation an important advantage. Neither the fragmentation routine SETPRT nor the full detector simulation QFL have been finely tuned to reproduce the observed jet response and resolution at high η_d.

The fast jet simulation uses results obtained from data to transform a zero mass parton four-vector into a massive jet four-vector. The process of mass generation is modelled using the obesity variable, $\Omega = M^2/2P_t$ [94]. This variable depends only

weakly on jet P_t. Obesity has been measured with CDF jet data and the distribution obtained is used as the basis for the Monte Carlo simulation. Having generated a mass for the parton, the resulting four-vector is rescaled by a constant factor to conserve energy. The next step is to simulate the effects of initial state gluon radiation. This is achieved by Lorentz-boosting the jet system transverse to the beam direction. This so-called K_t *kick* has been tuned to agree with dijet data, and is modelled using a Gaussian distribution with zero mean and σ chosen using a random number r as follows:

$$\sigma = \begin{cases} 9.5 & \text{GeV/c} & \text{if } r > 0.75 \\ 4.0 & \text{GeV/c} & \text{otherwise} \end{cases} \tag{63}$$

where $r \in [0,1]$. Another random number is used as input to the Gaussian distribution, and this determines the magnitude of the kick. The resulting four-vector is then transformed using the inverse of the jet correction function to obtain the most likely clustered jet four-vector. Both relative and absolute jet corrections have been inverted for this purpose. The ratio $P_t^{\text{Jet}}/P_t^{\text{parton}}$ determined using this function for various values of jet P_t is shown in Figure 44 for the full range of η_d.

So far, the properties of the *average* clustered jet have been inferred from the initial parton four-vector. However, smearing in jet P_t, η and ϕ must also be added in accordance with the observed detector resolution. For the purposes of kinematic comparison, correctly simulating the jet resolution is of particular importance. Thus a careful tuning of the fast jet simulation has been necessary, involving a separate evaluation of the jet resolution measured in each different calorimeter region [95].
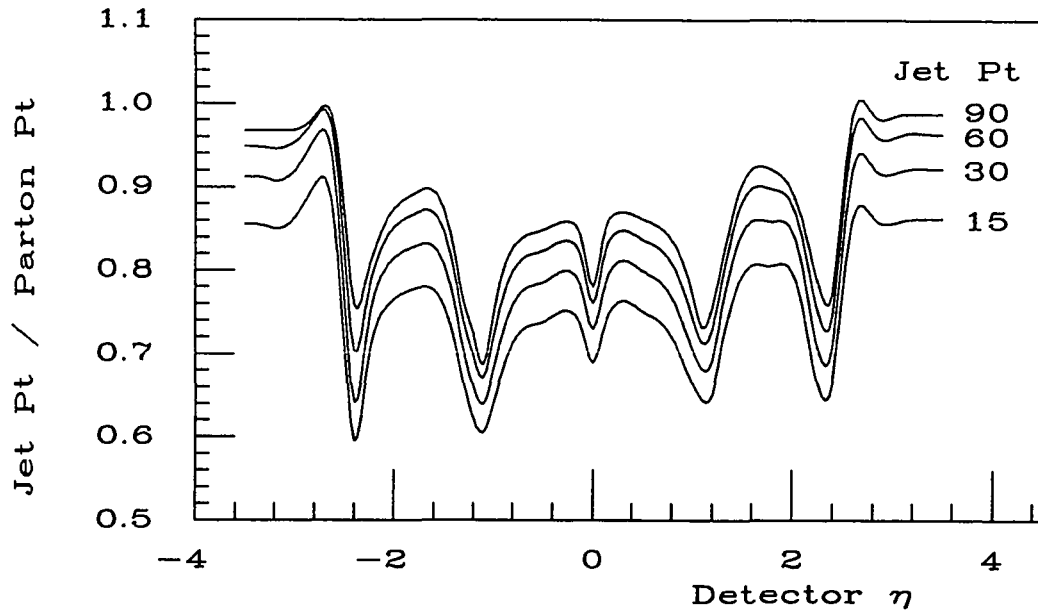
Figure 44.   The ratio of jet P_t to parton P_t for various choices of jet P_t as a function of η_d, using the fast jet simulation.

The fast jet simulation uses Gaussian distributions to produce jet P_t smearing. In order to tune the simulation, the detector was divided up into 6 regions in $\mid \eta_d \mid$ as shown in Table IX. The resolution for the central region has been determined [41] as

$$\sigma(P_t) = 0.1 \cdot P_t + 1.0 \quad \text{GeV/c}. \tag{64}$$

This general form is assumed to hold true for most of the other regions, to within an overall normalization factor $\mathcal{F}(\eta_d)$. The factors were determined with dijet events, using the technique of P_t-balancing. After the jet corrections are applied, any P_t imbalance is primarily due to detector resolution effects, with a small contribution from initial state radiation. Such contributions may be minimized by projecting the

Table IX. Definition of the $\mid \eta_d \mid$ regions used in tuning the fast jet simulation. Also shown are the resolution normalization factors $\mathcal{F}$ relative to the central region.

Region	$\mid \eta_d \mid$ Coverage	$\mathcal{F}(\eta_d)$
Central Crack	0.0–0.1	-
Central	0.20–0.70	1.00
Central-Plug Crack	0.95–1.25	1.10
Plug	1.55–1.85	1.03
Plug-Forward Crack	2.25–2.45	1.10
Forward	2.85–3.5	1.6

missing P_t vector along the transverse dijet axis. The variable used in practice is defined as

$$P_t^{\mathbf{Long}} = (P_t^{\mathrm{Jet1}} - P_t^{\mathrm{Jet2}}) \cdot \sin \left(\frac{\Delta\phi}{2} \right), \tag{65}$$

where $\Delta\phi$ is the inter-jet angle in the transverse plane.

The data sample used for tuning was the same sample used to construct the relative jet correction (JET_20, JET_40 and JET_60 data). For comparison, the Monte Carlo program PAPAGENO was used to generate dijet events which were then passed to the fast jet simulation. The factors found to produce results consistent with data are shown in Table IX for all regions except that of the central crack. In the central crack region, the normalization factor

$$\mathcal{F}(0.0 - 0.1) = 0.0014 \cdot P_t + 0.95. \tag{66}$$

was found to reproduce the data well. Comparisons of the P_t^{Long} variable between data and the tuned fast jet simulation can be seen in Figures 45, 46 and 47.

There is clearly good agreement between data and simulation. A quantitative measure of the differences between the two is given by the percent residuals R_p, defined as

$$R_p = \frac{\text{RMS}_{\text{Data}} - \text{RMS}_{\text{Sim}}}{\text{RMS}_{\text{Data}}} \cdot 100\%, \tag{67}$$

where RMS denotes the root-mean-square deviation of the Gaussian-shaped distributions. Table X shows the percent residuals for all detector regions. The final column of this table shows the largest value of R_p obtained, rounded up to the nearest integer. These values can be regarded as a conservative estimate of the error involved in using the fast simulation to estimate the experimental jet resolution. This information is used in the evaluation of systematic errors in Chapter VII.

Smearing of jets in η-ϕ space is also included in the fast jet simulation. Jet η is smeared by varying jet P_z and E while keeping P_t constant [93]. The jet η resolution has been measured with data, and is found to improve with increasing jet P_t. Accordingly, the width of the Gaussian function used to model this resolution falls with P_t, as shown in Figure 48a). The jet ϕ resolution is modelled with a rotation transverse to the beam line. The magnitude of this rotation is also based on a Gaussian, the width of which is shown in Figure 48b). The improvement in jet position resolution with increasing P_t stems from the fact that jets become narrower at higher P_t. In addition, they become less susceptible to the effects of small energy depositions due to electronic noise or the underlying event.
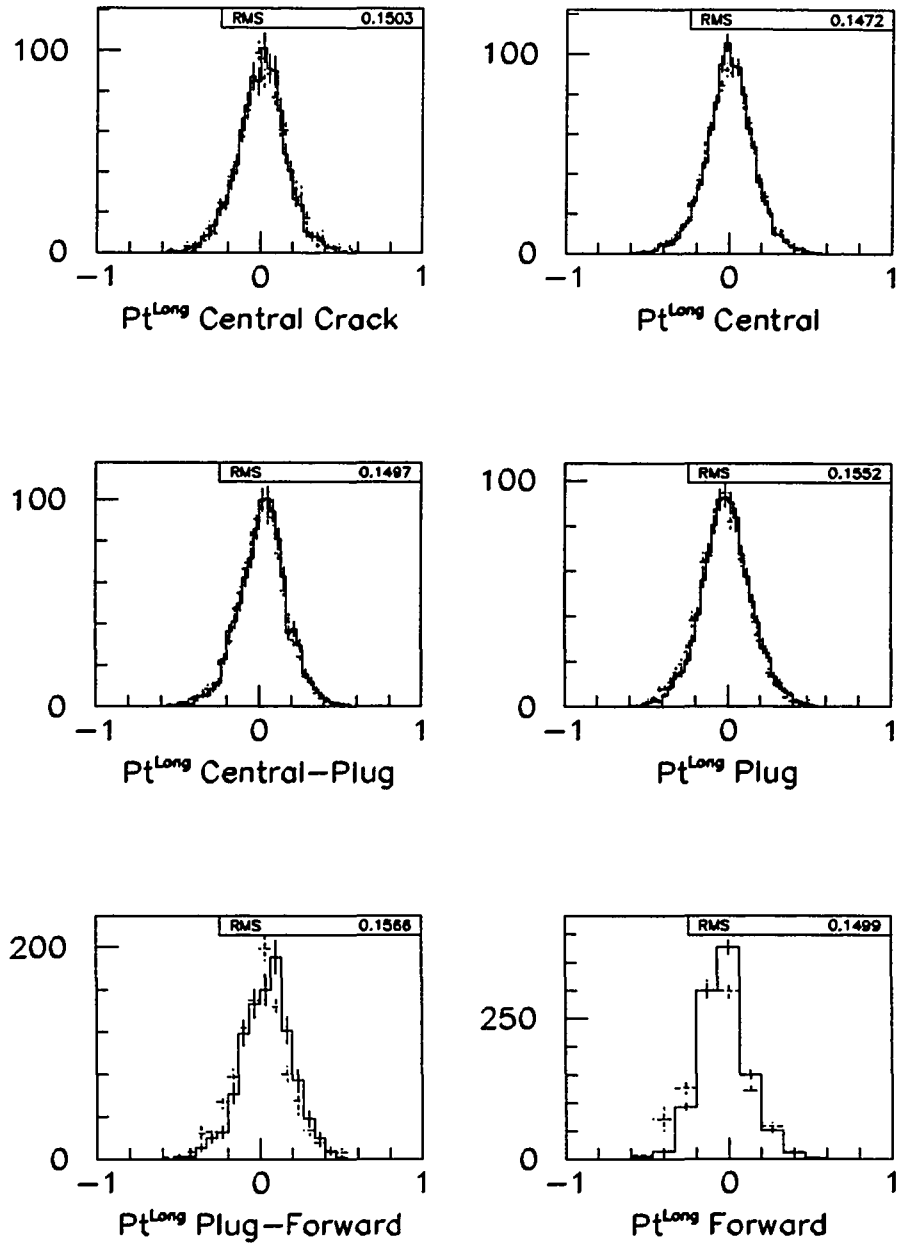
Figure 45. Distribution of the P_t^{Long} variable (see text for definition) in data taken with the JET_20 trigger overlaid on the results obtained using the fast jet simulation. The six $|\,\eta_d\,|$ regions are defined in Table IX

JET_40 Study
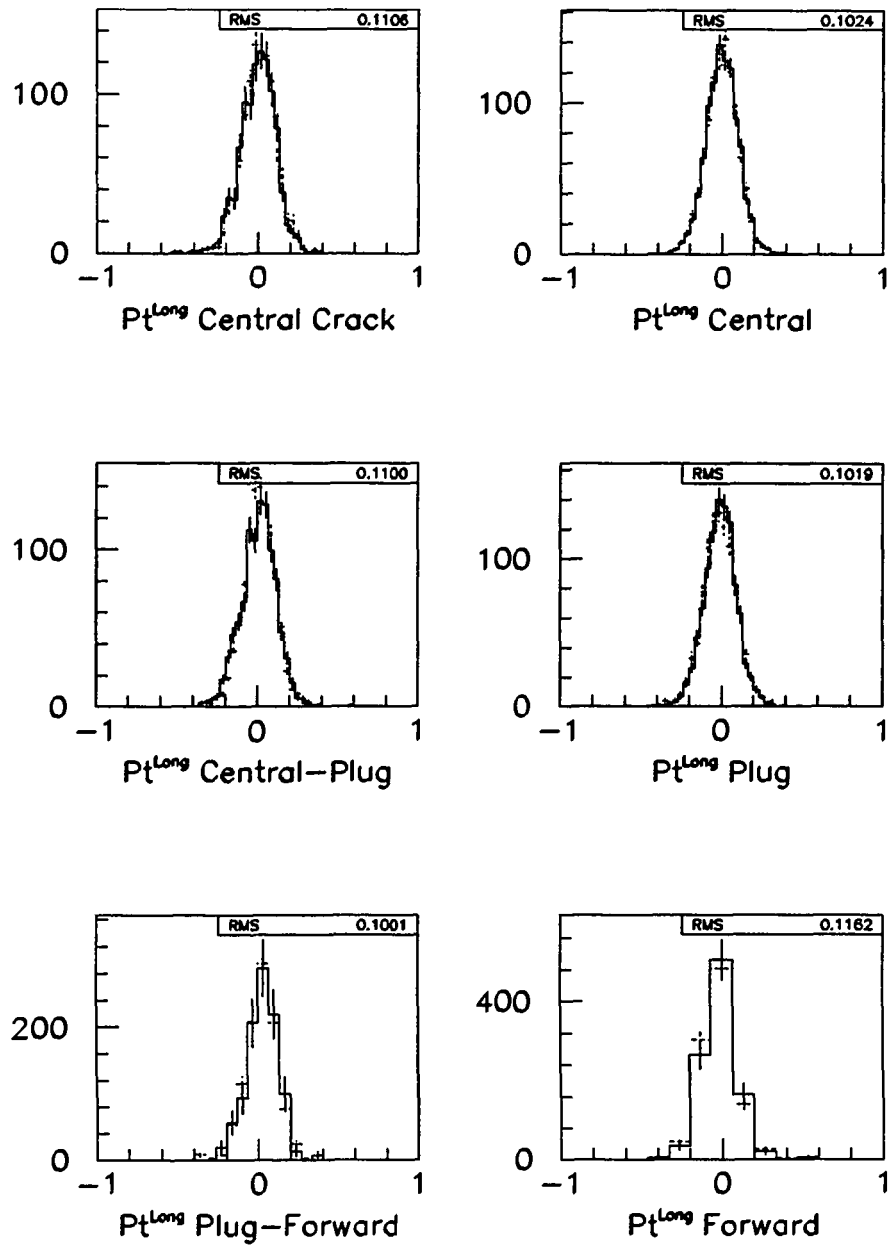
Figure 46. Distribution of the P_t^{Long} variable (see text for definition) in data taken with the JET_40 trigger overlaid on the results obtained using the fast jet simulation. The six $|\eta_d|$ regions are defined in Table IX

JET_60 Study
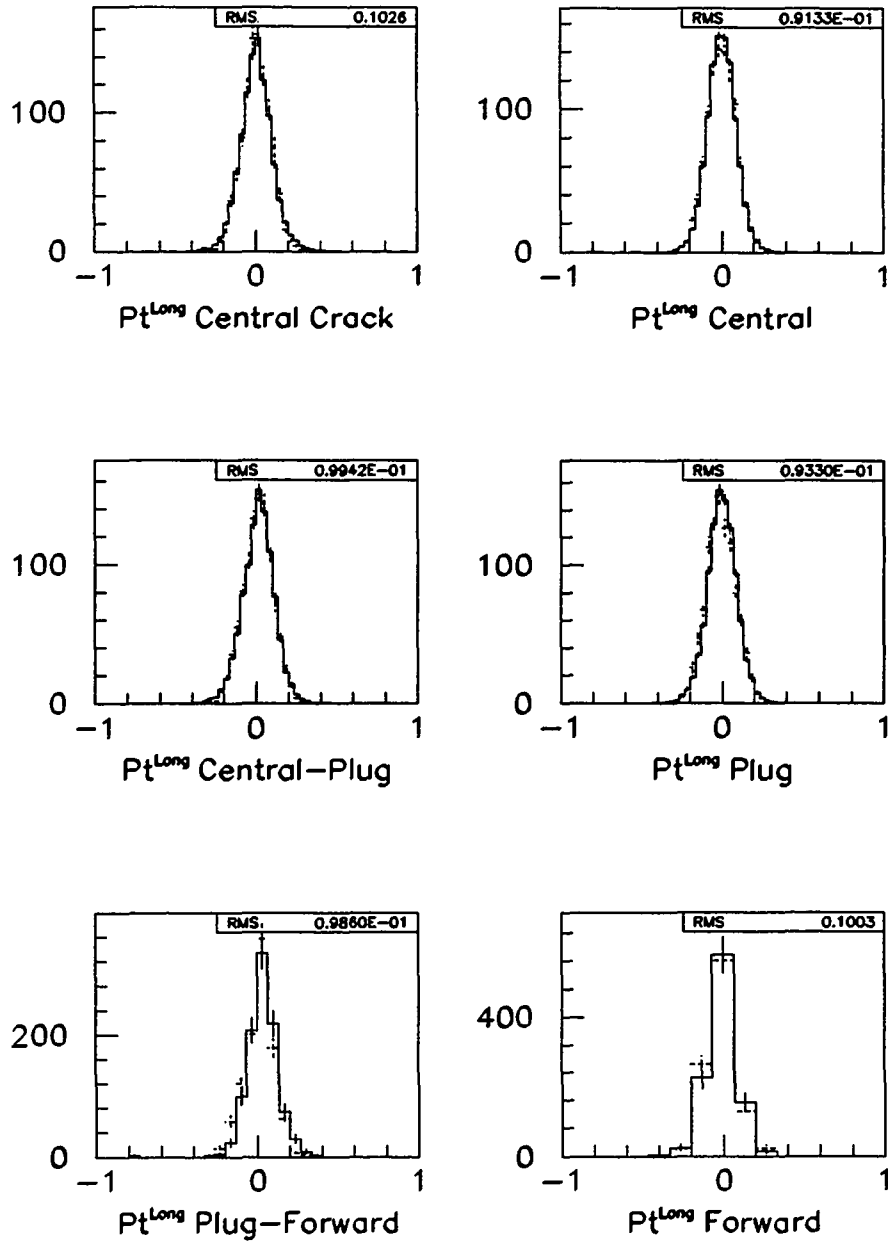
Figure 47. Distribution of the P_t^{Long} variable (see text for definition) in data taken with the JET_60 trigger overlaid on the results obtained using the fast jet simulation. The six $|\eta_d|$ regions are defined in Table IX

Table X. Percent jet resolution deviations between data and the fast jet simulation. The final column shows the highest deviation rounded up to the nearest integer.

Region	JET_20	JET_40	JET_60	Upper Bound
Central Crack	-2.58	5.96	13.53	14
Central	-3.31	1.31	-0.80	4
Central-Plug Crack	0.27	11.55	6.84	12
Plug	-2.08	-1.75	-0.17	3
Plug-Forward Crack	-8.05	-1.59	7.60	9
Forward	-19.22	3.41	0.82	20

D. Generation Cuts for Double Bremsstrahlung Events

The fast jet simulation reliably models the global features of jet production and measurement in the detector. A full simulation of QCD double bremsstrahlung events, including detector effects, now becomes possible. The cuts used in the generation of PAPAGENO four-jet double bremsstrahlung events are as follows:

1. $P_t^{Parton} > 13$ GeV/c

2. $\Delta R > 0.8$ where ΔR is the jet separation in $\eta - \phi$ space.

3. $| \eta_d | < 4.0$

Using the fast jet simulation, these cuts have been carefully tuned for maximum efficiency, while ensuring that no possible kinematical region is omitted from the final sample. Figure 49a) shows the P_t spectrum for the lowest P_t parton, after all event cuts have been applied. The offline minimum P_t cut of 25 GeV/c ensures that no partons below 13 GeV/c produce jets that contribute to the final sample. Figure 49b)
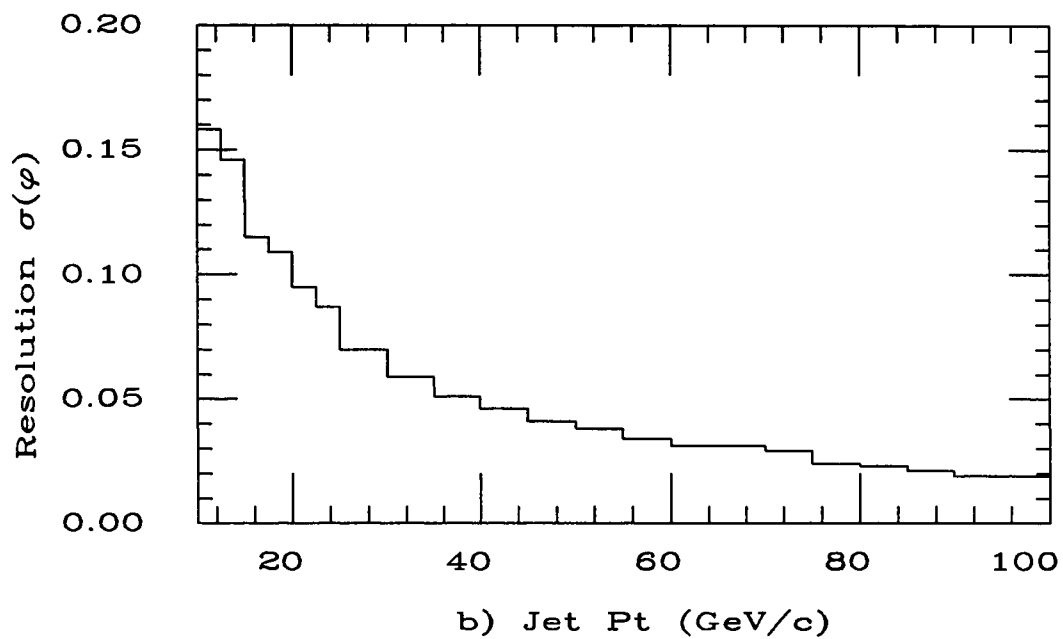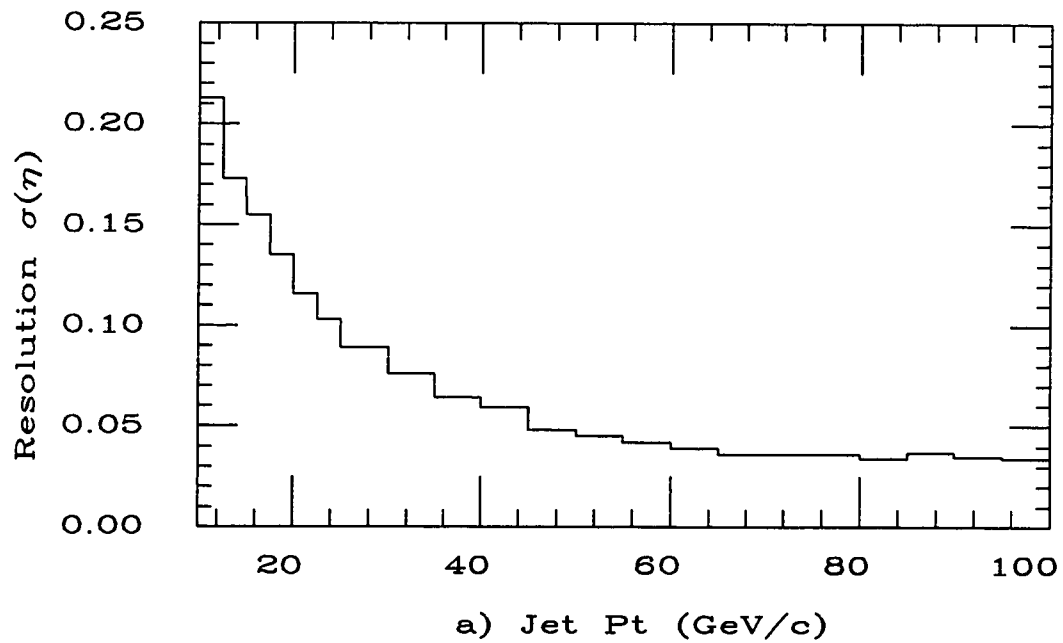
Figure 48. The position resolution of the fast jet simulation as a function of jet P_t. Shown are the resolutions in a) η-space and b) ϕ-space.

shows the minimum parton separation obtained after all offline cuts, and indicates that the cut of $\Delta R > 0.8$ is fully efficient. Figure 50 shows the η distributions obtained for all four generated partons, again after all offline cuts. The distributions approach zero as $\mid \eta \mid \rightarrow 4.0$.

E. Comparison of Data and QCD

For the kinematic comparisons between data and QCD, the EHLQ set 1 structure function is used, with $Q = \langle P_t \rangle$. The distributions obtained using the double bremsstrahlung matrix element do not vary significantly with choice of structure function and Q^2 parameterization.

To summarize, the *offline* cuts for both data and Monte Carlo are:

1. $\mid z_{\text{vertex}} \mid < 60$ cm.

2. $\mid \eta_d \mid < 3.5$.

3. No secondary vertices observed in the VTPC.

4. Exactly 4 jets.

5. $\Delta R > 1.0$

6. Jet $P_t > 25$ GeV/c, corrected.

7. Jet $\sum P_t > 140$ GeV/c, where the sum is taken over the 4 jets.

After correction, jets are arranged in order of descending P_t; jet 1 has the highest P_t, jet 2 the next highest and so on. Figure 51 shows a comparison between data and QCD prediction of the P_t spectrum for each of the four jets. In Figure 52 the P_t for all jets has been added, yielding the jet $\sum P_t$ for comparison. While the agreement between data and theoretical predictions is very good, the P_t distributions shown are
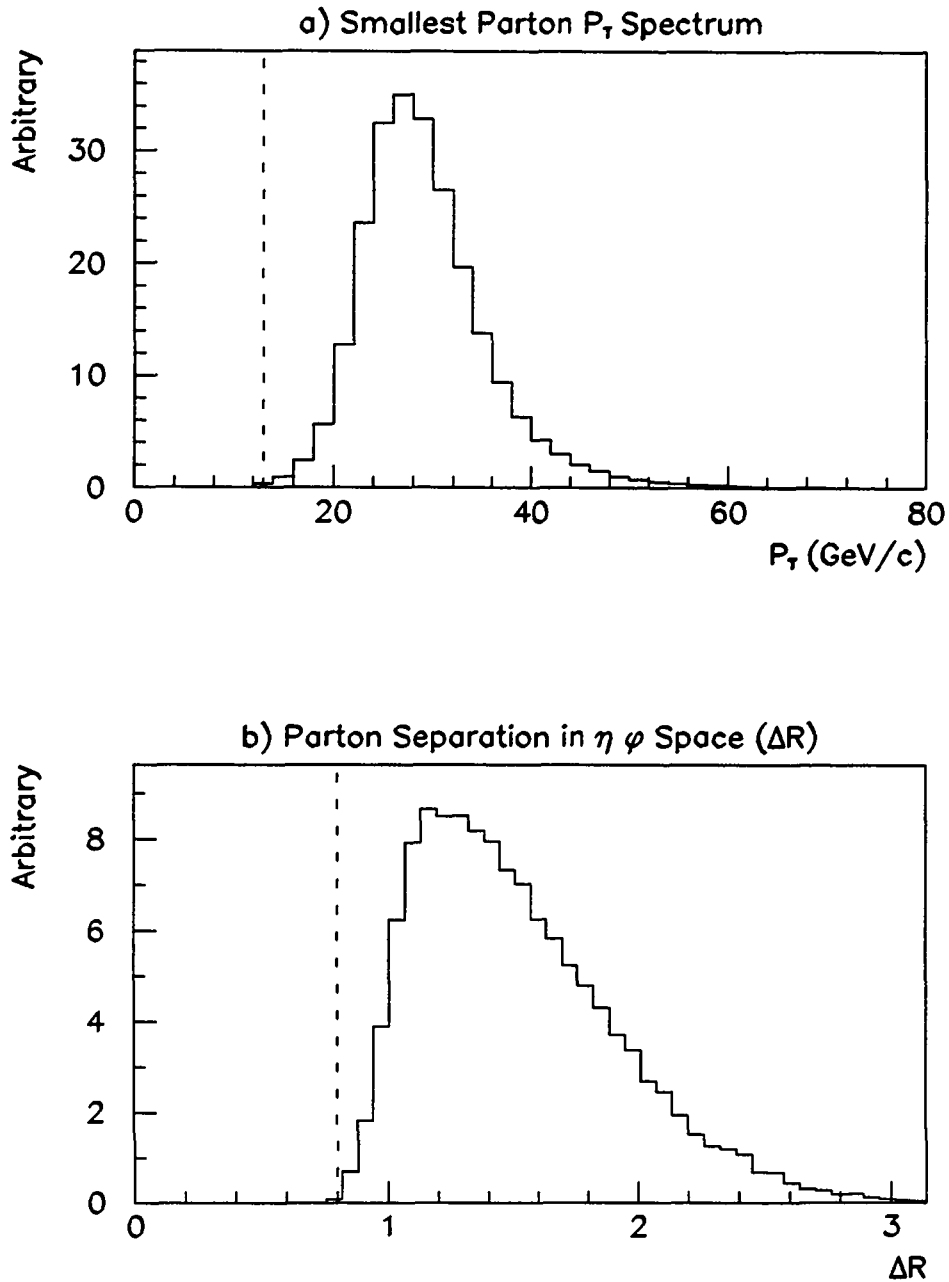
Figure 49. A check of the double bremsstrahlung Monte Carlo generation cuts using PAPAGENO and the fast jet simulation. a) The P_t spectrum of the smallest parton after all offline cuts. b) The smallest separation in η-ϕ space between any two partons, ΔR. Generation cuts are indicated by dashed lines.
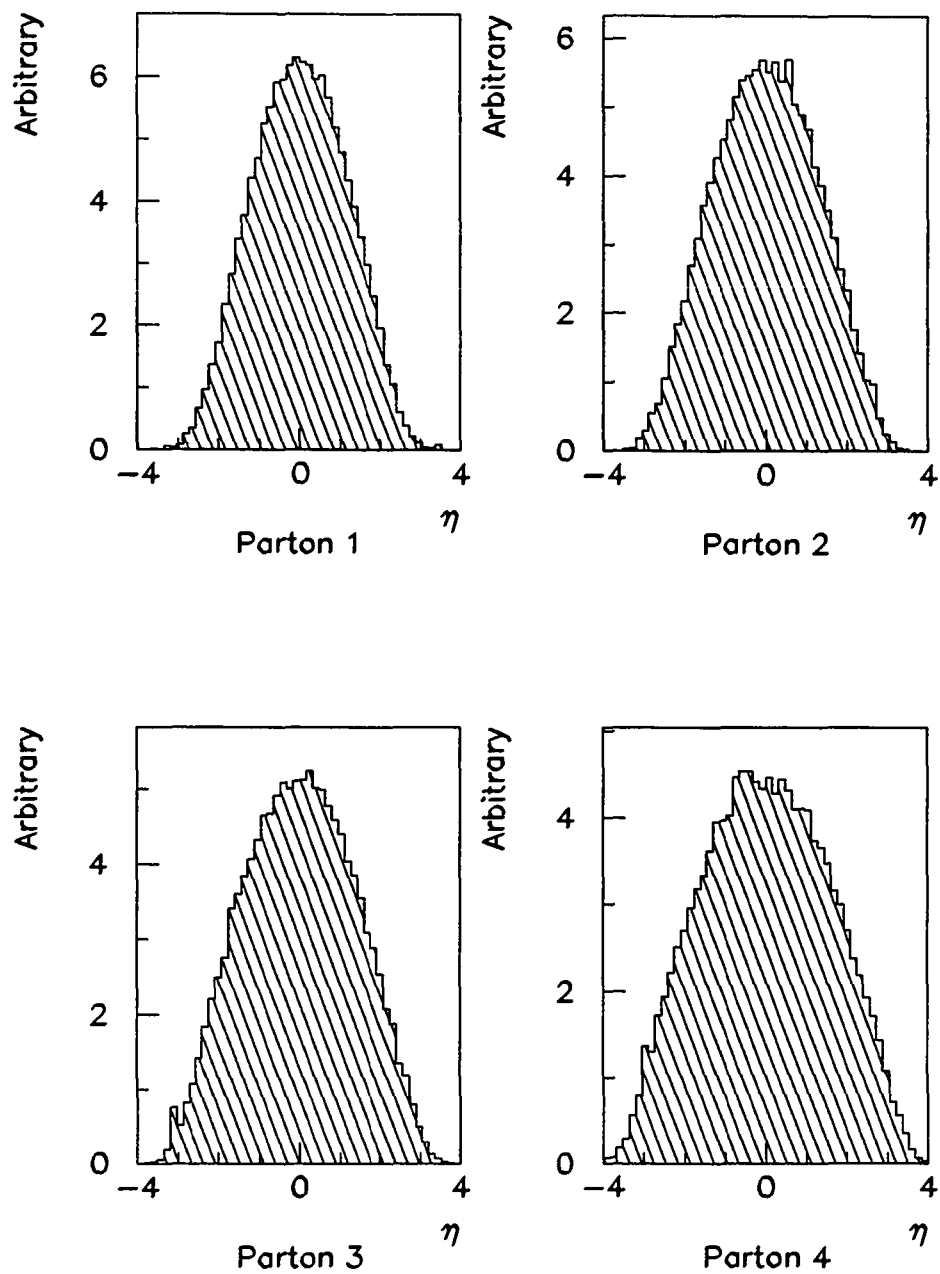
Figure 50. The η distribution of the four generated partons after all offline cuts, using PAPAGENO and the fast jet simulation.

not the most sensitive to the subtleties of QCD. In fact, the distributions obtained with a phase space Monte Carlo (where the matrix element is essentially unity) are very similar. A more stringent test is provided by examining *angular* distributions.

The angular distribution of the four-jet system has been analyzed in terms of inter-jet angles in the center-of-mass reference frame. The variable Ω_{ij} is defined as the angle between jets i and j in this frame. The internal configuration of the four jets may then be completely described by the six quantities $\cos \Omega_{ij}$, where $i \neq j$. These quantities are interrelated by the invariant mass of the four-jet system. The distributions obtained for both data and QCD are shown in Figures 53 and 54. Also shown are the corresponding distributions obtained where the approximate four-jet matrix element has been replaced by phase space. This time, the predictions of QCD and phase space are significantly different. In all six cases, the agreement between data and QCD is extremely good. The four-jet data sample is clearly dominated by double bremsstrahlung events, as expected.

It is worthwhile to re-emphasize the fact that comparisons have been made between data and an exclusive *leading order* theoretical calculation. No additional jets are generated in the simulation process; such effects are modelled using a small transverse K_t kick. Nonetheless, the agreement is particularly striking. This indicates that higher order corrections to the four-jet QCD calculation should produce little change in the resulting kinematics.
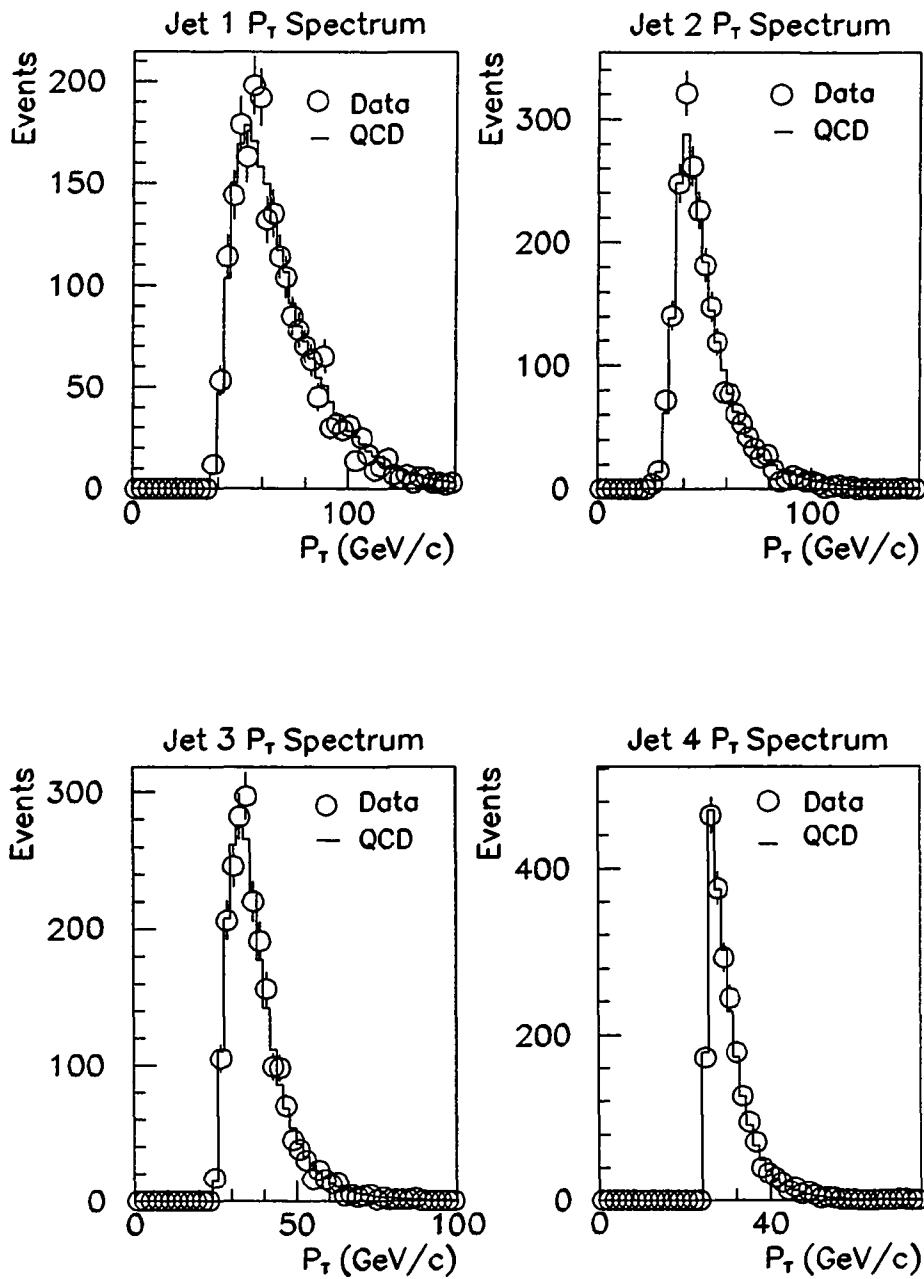
Figure 51. The P_t spectra of all four jets; data points are overlaid on the predictions of leading order QCD.
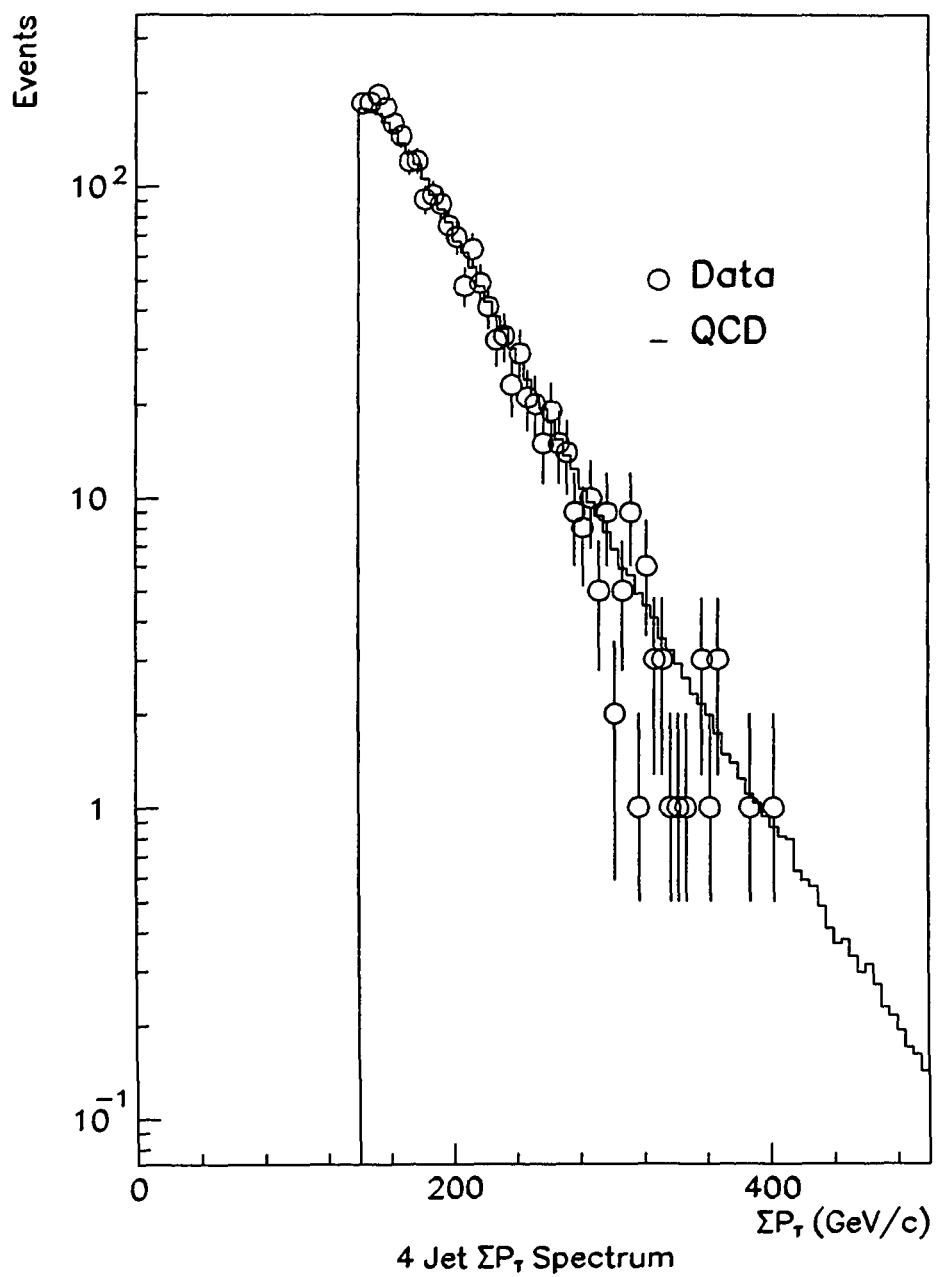
Figure 52. The $\sum P_t$ spectrum for four-jet events; data points are overlaid on the predictions of leading order QCD.
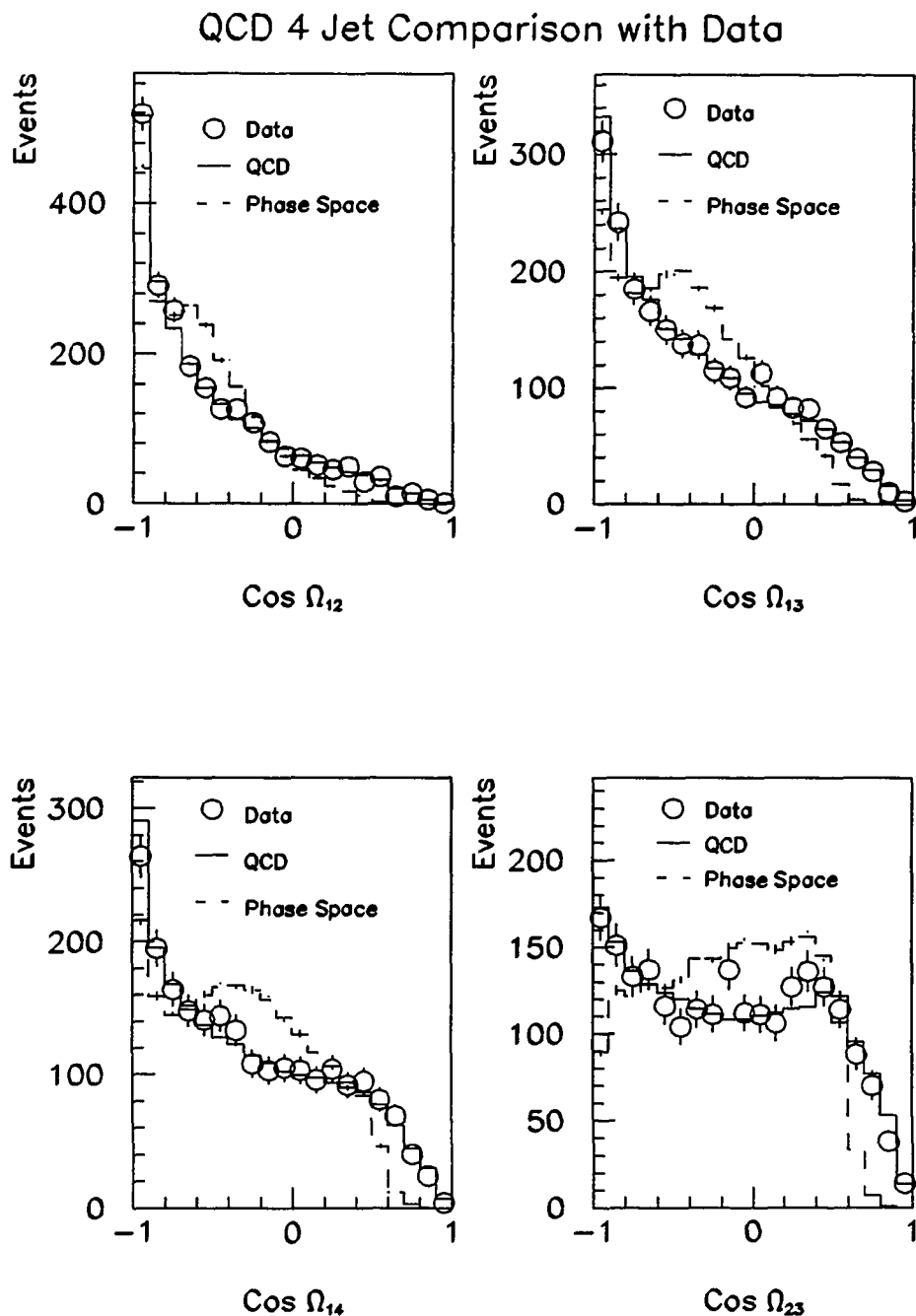
Figure 53. Data overlaid on the predictions of an approximate leading order QCD four-jet calculation for the angular variables Ω_{12}, Ω_{13}, Ω_{14} and Ω_{23}. Also shown are the corresponding distributions where the double bremsstrahlung matrix element has been replaced by phase space.
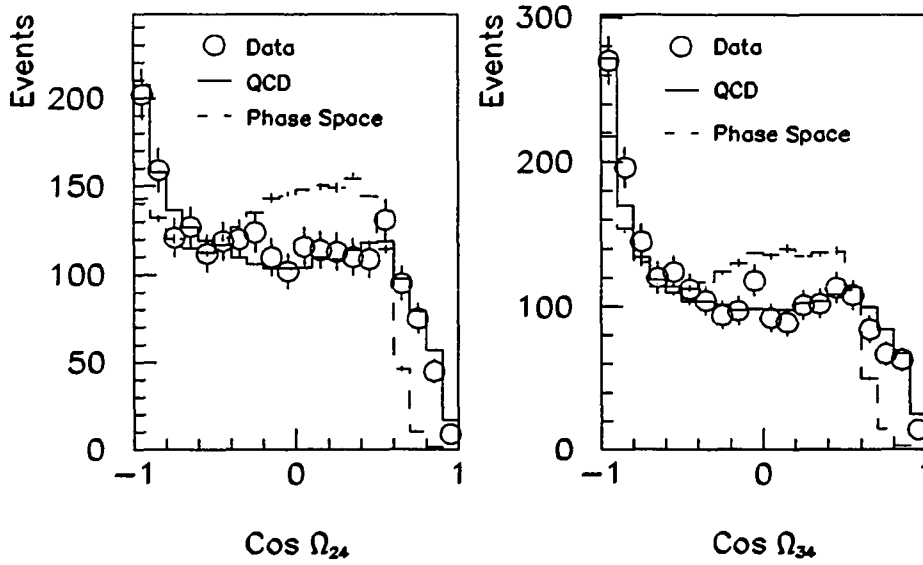
Figure 54. Data overlaid on the predictions of an approximate leading order QCD four-jet calculation for the angular variables Ω_{24}, and Ω_{34}. Also shown are the corresponding distributions where the double bremsstrahlung matrix element has been replaced by phase space.

CHAPTER VI

DOUBLE PARTON ANALYSIS

The kinematic comparisons presented in Chapter V demonstrate impressive agreement between the predictions of leading order QCD and the data for the four-jet process. However, this agreement does not rule out the existence of a contribution from double parton scattering. The similarities between the processes of double bremsstrahlung and double parton scattering cause many of the kinematic distributions to be nearly identical. The construction of variables that have significantly different shapes for the two processes is therefore necessary before a rigorous search may be performed. The first step in this procedure is the development of a sufficiently realistic Monte Carlo model of the double parton process. In this chapter, the model used is described, and the differences between events formed by double parton scattering and double gluon emission are exploited in the construction of suitable topological variables. The sensitivity of these variables to a possible double parton signal is tested using a special Monte Carlo data sample.

Significant differences in the amount of signal found by the different variables has prompted a detailed study of the more subtle effects present in the data. The factors studied (and the relevant sections) are:

1. Events containing two $p\bar{p}$ interactions (Section D).

2. Additional clusters caused by underlying event fragmentation (Section E).

3. The effect of the Level 2 ξ cut $\sum E_t - E_{t_1} - E_{t_2} > 40$ GeV (Section F).

4. Additional clusters (fifth jets) produced through gluon emission, but which do

not pass the cut $P_t > 25$ GeV/c (Section G).

The main cause of the differences is found to be item 4, namely fifth jets. These

additional clusters are not correctly modelled by the exclusive four-jet Monte Carlo

programs. By cutting out these jets from the data, an accurate determination of

the double parton content of the data becomes possible. Note that the data set and

event quality cuts used in this chapter are identical to those used in the kinematical

comparison described in Chapter V, Section E.

A. Double Parton Monte Carlo Program

The double parton Monte Carlo program used in this analysis has been created

by merging two PAPAGENO dijet events at the parton level. Both pairs of partons

are given a separate K_t kick to simulate the effect of gluon radiation, and are ran-

domly rotated in the ϕ direction. The partons are then passed to the fast simulation

for transformation into jets as described in Chapter V, Section C. This prescription

results in the production of two pairs of uncorrelated dijet events. The only restric-

tion placed in generation is that energy conservation is not violated. This occurs very

rarely, and these events are not used.

Since PAPAGENO events are weighted, some care must be taken in the merging

procedure. In practice, the product of the weights for both merged dijet events is

used as the weight for the resulting double parton event. If the dijet events are first

statistically unweighted, then this procedure is not necessary since the frequency of

particular event configurations will then correspond to their relative cross sections.

The double parton Monte Carlo program facilitates a search for variables which might be sensitive to a possible double parton signal. Figure 55 shows distributions of four of the inter-jet angular variables Ω_{ij} obtained with simulations of both signal (double parton) and background (double bremsstrahlung). There is a strong similarity, making signal separation difficult. As discussed in Chapter II, Section C, the most powerful variables will be those which exploit the natural differences between the two processes.

B. Signal Finding Variables

The *significance*, or S variable makes use of pair-wise P_t-balancing between dijet pairs of a double parton event. This variable is defined as

$$S(1+2, 3+4) \equiv \sqrt{\left[\left(\frac{|\vec{P}_{t_1} + \vec{P}_{t_2}|}{\sqrt{P_{t_1} + P_{t_2}}}\right)^2 + \left(\frac{|\vec{P}_{t_3} + \vec{P}_{t_4}|}{\sqrt{P_{t_3} + P_{t_4}}}\right)^2\right] / 2}. \tag{68}$$

The S variable is computed for each of the three different combinations of pairings ([12,34], [13,24], [14,23]) and the minimum is taken. The jets have been ordered in P_t, so that 1 refers to the highest P_t jet, 2 the next highest and so on. For a dijet event, the corresponding significance variable may be expressed as

$$S_{\text{dijet}} = \frac{|\vec{P}_{t_1} + \vec{P}_{t_2}|}{\sqrt{P_{t_1} + P_{t_2}}}. \tag{69}$$

The numerator on the right of this equation is similar to the single jet resolution. The variation of particle resolution with energy is given by $\sigma_E \sim \sqrt{E}$. Therefore the behaviour of the jet resolution should be similar, and dividing the jet resolution by $\sqrt{P_t}$ should yield a quantity which is approximately independent of jet P_t. This
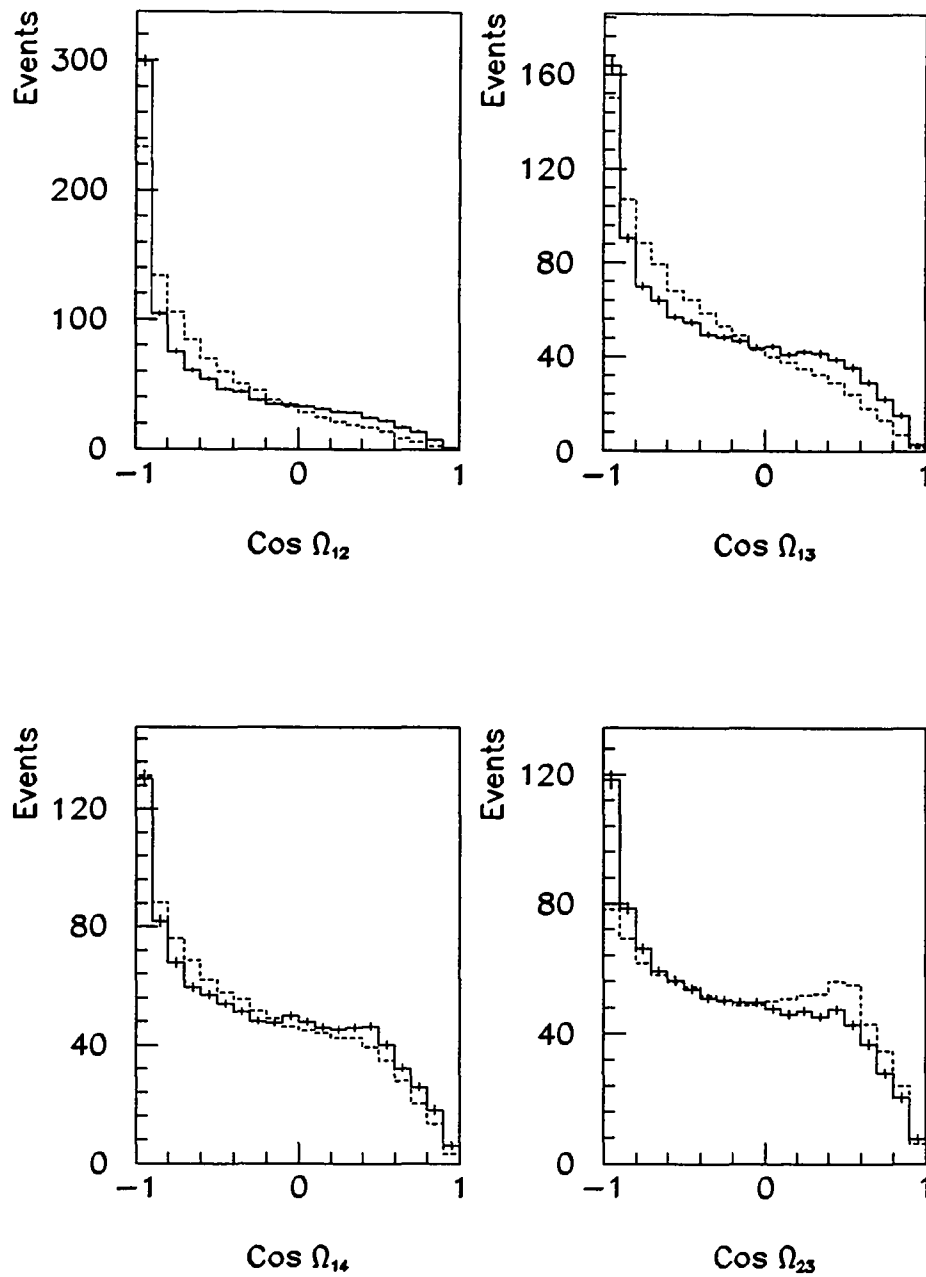
Figure 55.   The Monte Carlo distributions of the angular variables Ω_{12}, Ω_{13}, Ω_{14} and Ω_{23} for both double parton (solid) and double bremsstrahlung (dashed) processes.

reasoning provides the basis for Equation 68. If the event is a double parton event, then the quadratic average of the two dijet significance variables is taken. This quantity should be equal to the single dijet significance. On the other hand, for a double bremsstrahlung event S will be far larger, as there will no longer be pair-wise P_t-balancing.

At the parton level, S for double parton events will always be zero. However, detector resolution effects smear out the S distribution for real jets. The shapes for simulated double parton and double bremsstrahlung events after applying the fast detector simulation are shown in Figure 56a). For the double parton process most events lie within the range $0 < S < 2.5$, and consequently any excess of events in the data in this region may indicate a double parton signal.

Having paired off jets in order to minimize S, a different variable may now be defined using the *angular* properties of both pairs. The ϕ direction is chosen for this purpose rather than η, since the differences between signal and background are far more pronounced in the transverse direction. The ϕ_S variable is defined as the azimuthal angle between the largest P_t jets of each matched pair, in the range $0 < \phi_S < \pi$. For double parton events, the distribution of ϕ_S is expected to be flat, with a slight depletion near 0 and π due to the offline separation cut of $\Delta R > 1.0$. This reflects the fact that the dijet pairs are uncorrelated. Conversely, events produced by double gluon emission will exhibit some degree of correlation. Also, since momentum transverse to the beam line (i.e. in the xy plane) is conserved, the leading jets in each matched pair will tend to be opposite in azimuth. This will result in a strong peaking near $\phi_S = \pi$ for these events. The distribution of ϕ_S for both processes is

shown in Figure 56b). For the ϕ_S variable, a double parton signal will result in an excess of events in the relatively clean background region near $\phi_S = 0$.

Another variable has been constructed which takes advantage of angular correlations. The technique this time has been to use the *resultant* transverse direction of the matched pairs. Assuming that the S variable minimization procedure has resulted in the pairing [ij,kl], the variables κ_1 and κ_2 are defined as:

$$\kappa_1 = \phi(\vec{P_{ti}} - \vec{P_{tj}}), \tag{70}$$

$$\kappa_2 = \phi(\vec{P_{tk}} - \vec{P_{tl}}), \tag{71}$$

where $\phi(\vec{r})$ denotes the azimuthal angle of the vector $\vec{r}$. We then take the difference,

$$\Delta_S = \kappa_1 - \kappa_2. \tag{72}$$

The motivation for this definition can be seen by considering Figure 57a), which shows a scatter plot of κ_1 versus κ_2 for double bremsstrahlung events. The equivalent plot for double parton events is uniform. The broad diagonal bands in this figure show that the double bremsstrahlung system prefers to be in the configuration where $\kappa_1 - \kappa_2 = \pm \pi$ radians, again caused by overall momentum conservation. Now, projecting this plot along the diagonal line $\kappa_1 + \kappa_2 = 2\pi$ as shown results in a distribution which is peaked at $\Delta_S \simeq \pm \pi$ radians, and depleted at $\Delta_S \simeq 0$ radians. The corresponding double parton projection is peaked at $\Delta_S = 0$. This combination of maximum signal and minimum background results in powerful signal discrimination. Figure 57b) shows the relative Δ_S shapes for both processes.
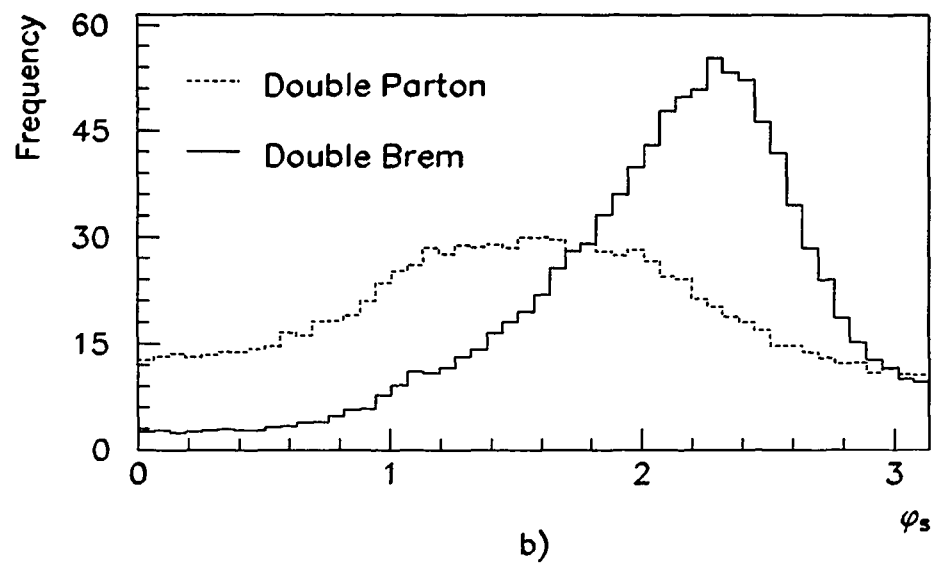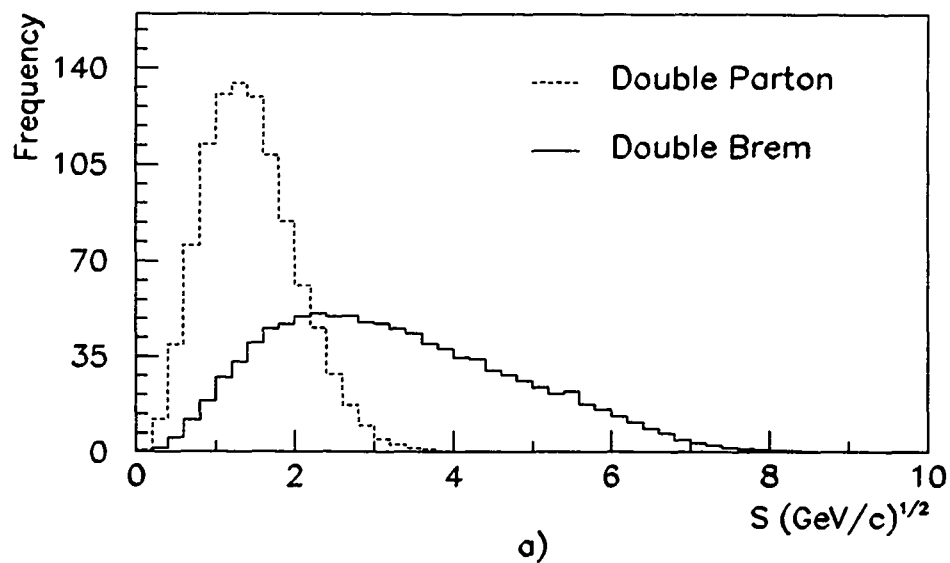
Figure 56. a) The significance variable S and b) ϕ_S obtained with simulated double parton (dashed) and double bremsstrahlung (solid) events. The events have been generated using PAPAGENO and the fast jet simulation.
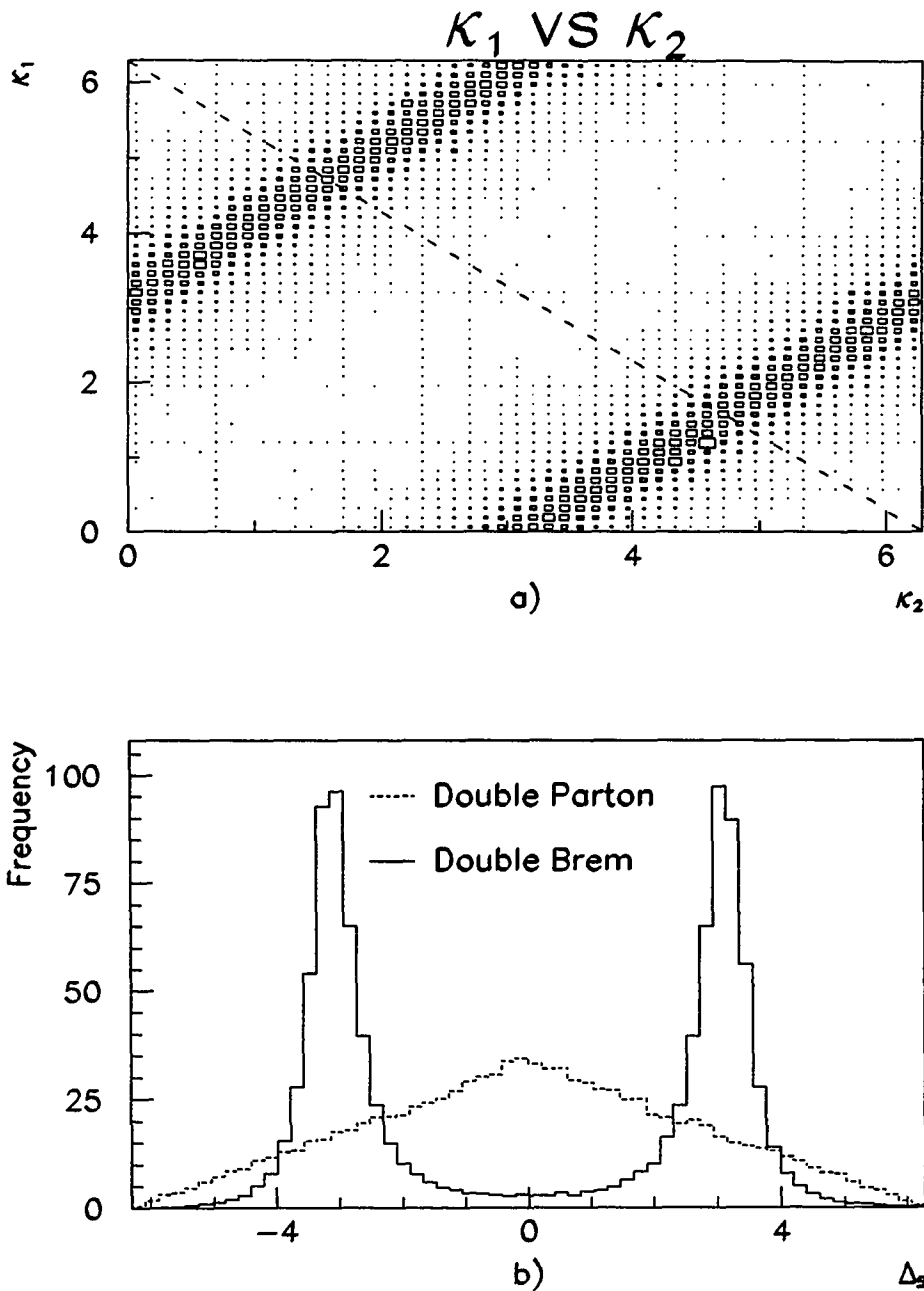
Figure 57. a) Angular variables κ_1 versus κ_2 for simulated double bremsstrahlung events, b) the Δ_S variable obtained with simulated double parton and double bremsstrahlung events. The events have been generated using PAPAGENO and the fast jet simulation.

The signal-finding ability of each of the three variables discussed so far has been tested using the relative distributions for double parton and double bremsstrahlung scattering. Taking each variable in turn, a new histogram is formed from 10% double parton and 90% double bremsstrahlung shapes. This histogram is fitted to an admixture of signal and background, and the relative admixture of each is varied in order to observe the resulting change in the fit. The goodness of fit is measured using the log-likelihood χ^2 parameter (see Appendix B for a detailed explanation). The variation of χ^2 with the percentage of signal is shown in Figure 58. The steepness of variation provides a measure of the ability of each variable to pick out a double parton signal from a background comprised of double bremsstrahlung events. The best signal-finding variable has the steepest variation. Figure 58 shows that Δ_S has the best signal finding resolution, followed by S and ϕ_S. This is consistent with naïve expectations based on the variable shapes for both processes.

C. Signal Extraction

The double parton content of the data is extracted using a similar technique to that used in the fitting study just described. We define the variable $\mathcal{R}$ as

$$\mathcal{R} = \frac{\text{Number of Double Parton Events}}{\text{Number of Double Bremsstrahlung Events}}. \tag{73}$$

The data points are then fitted to a normalized admixture of simulated signal and background shapes, adjusting $\mathcal{R}$ until the log-likelihood χ^2 has been minimized. Using the fast jet simulation, enough events have been generated to produce smooth theory distributions for fitting. The results of the fit are shown graphically for the
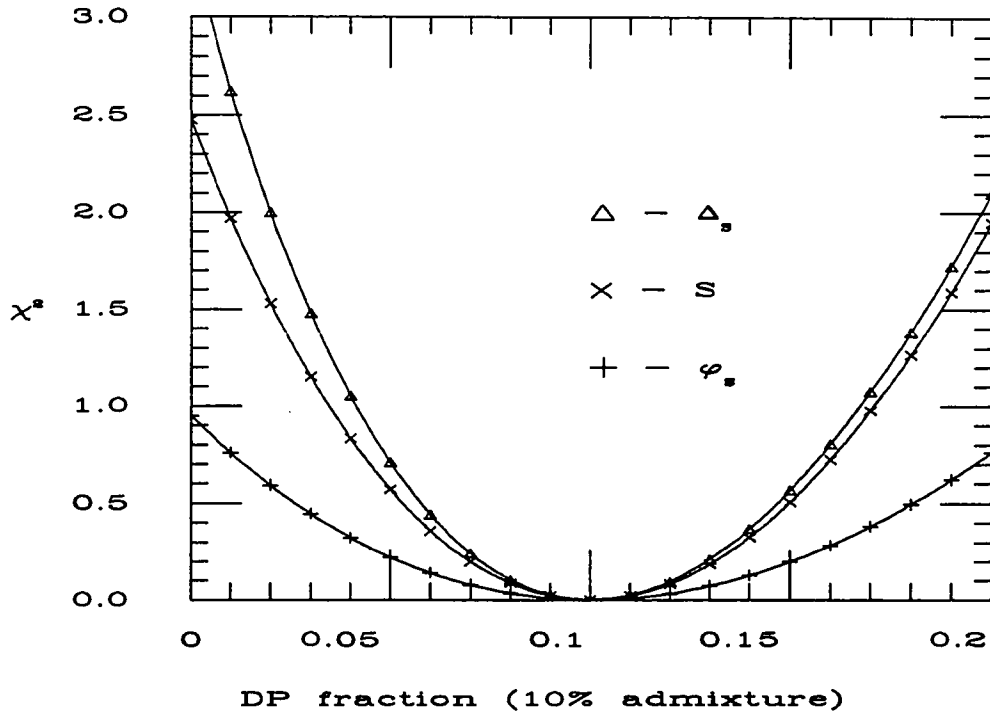
Figure 58. Results of the Monte Carlo variable fitting study. Shown is the χ^2 per degree of freedom as a function of the fraction of double parton events for a sample of 90% double bremsstrahlung and 10% double parton shapes.

three chosen topological variables in Figures 59a), 59b) and 60. There is substantial variation in the value of $\mathcal{R}$ for the different variables, ranging from 2% for S to 17% for Δ_S. This indicates that there may be aspects of the four-jet production that are being inadequately modelled by the exclusive four-jet Monte Carlo simulation. In the following sections, various factors are examined in order to understand this apparent

discrepancy.

D. Double Interactions

Double interactions in the event sample have been discussed in Chapter II, Section D1. The tentative conclusion reached was that events of this type are unlikely to produce a significant number of events having a pair of dijet events. Using the VTPC, this hypothesis has also been tested experimentally.

The VTPC is able to resolve the majority of secondary vertices due to multiple interactions. Figure 61 shows the distribution $z_{vertex}(1) - z_{vertex}(2)$ in events collected with the multijet trigger, where 1 and 2 refer to the primary and secondary vertices respectively. The dashed lines at ± 7 cm indicate the boundary of resolving power; at smaller vertex separations the VTPC sees only one interaction. The central bounded region corresponds to approximately 12.5% of all events. Therefore, even though events containing visible double interactions are rejected in the final four-jet sample, there still remain events where a double interaction has been missed. Before the cut on double interactions, there are 2807 events in the sample. After the cut there are 2213, and so approximately 20% of the events initially contain a secondary interaction. With a rejection efficiency of 87.5%, this implies a 3% double interaction contamination in the final sample.

Using CTC data, the $| \sum \vec{P_t} |$ of tracks originating from each of the two vertices has been determined. If both interactions result in the production of dijet pairs, then high P_t tracks originating from *both* vertices should be visible. Figure 62a) shows the distribution of track $| \sum \vec{P_t} |$ from each vertex for four-jet events having two
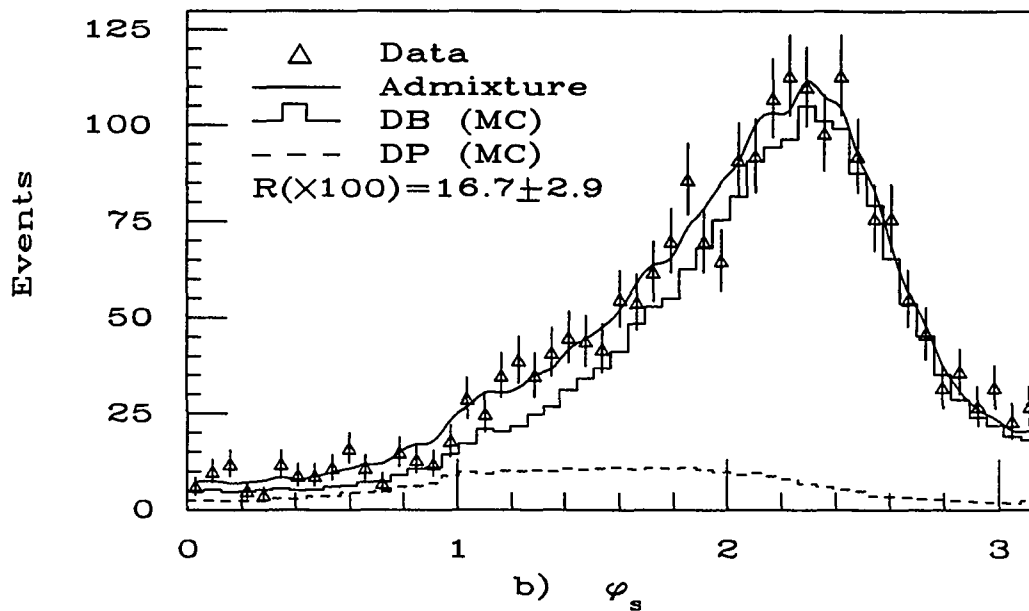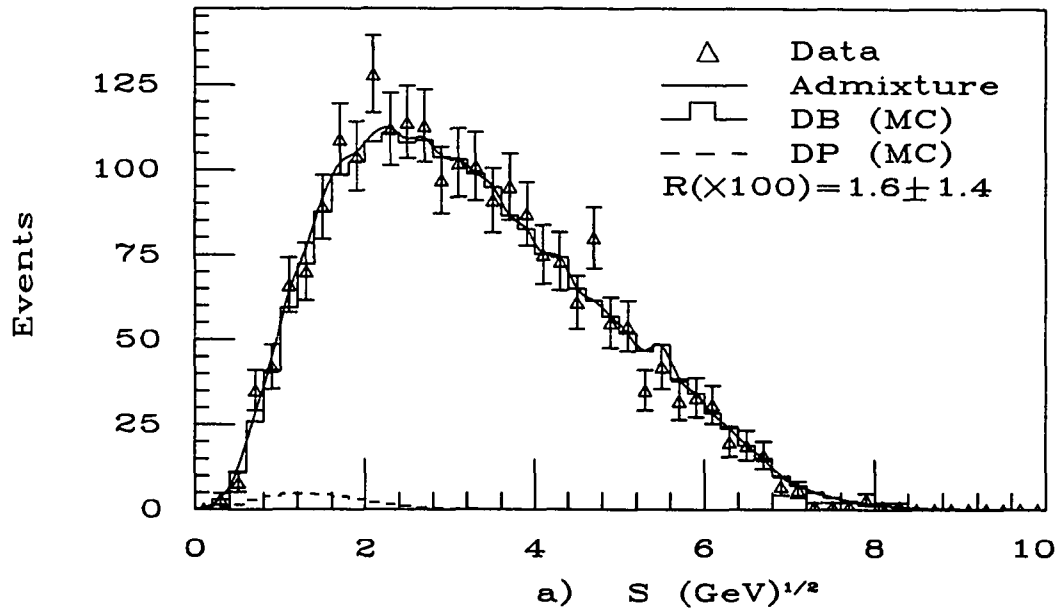
Figure 59. Data fitted to an admixture of signal and background for a) S and b) ϕ_S. Also shown is the fraction of double parton events found from the best fit, $\mathcal{R}$.
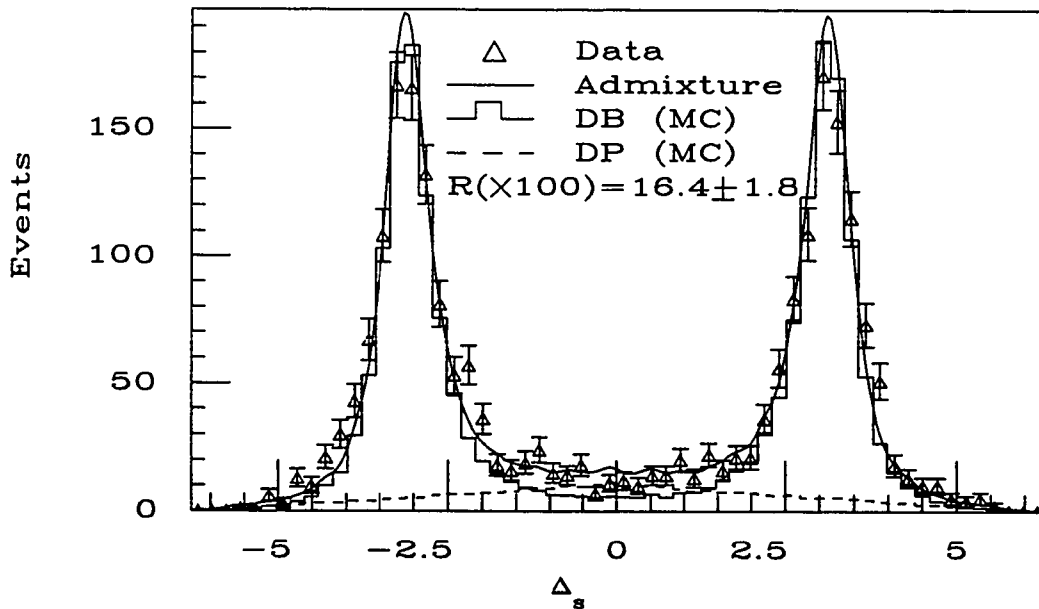
Figure 60. Data fitted to an admixture of signal and background for Δ_S. Also shown is the fraction of double parton events found from the best fit, $\mathcal{R}$.

discernable interactions. This figure shows that nearly all of the high P_t tracks originate from the primary vertex. This is consistent with an event composition of one double bremsstrahlung and one minimum bias event, rather than two dijet events. Figure 62b) shows the S variable obtained with events having two z-vertices with $z_{vertex}(1) - z_{vertex}(2) < 15$ cm, overlaid on the distribution for S with simulated double bremsstrahlung events. Within statistics the two are in agreement, indicating that these double vertex events are similar to events produced by QCD double gluon emission. If there had been a significant contribution from double dijet events produced in events containing two interactions, an excess would be visible at low values of S. Note that the properties of all jets in an event are reconstructed using the
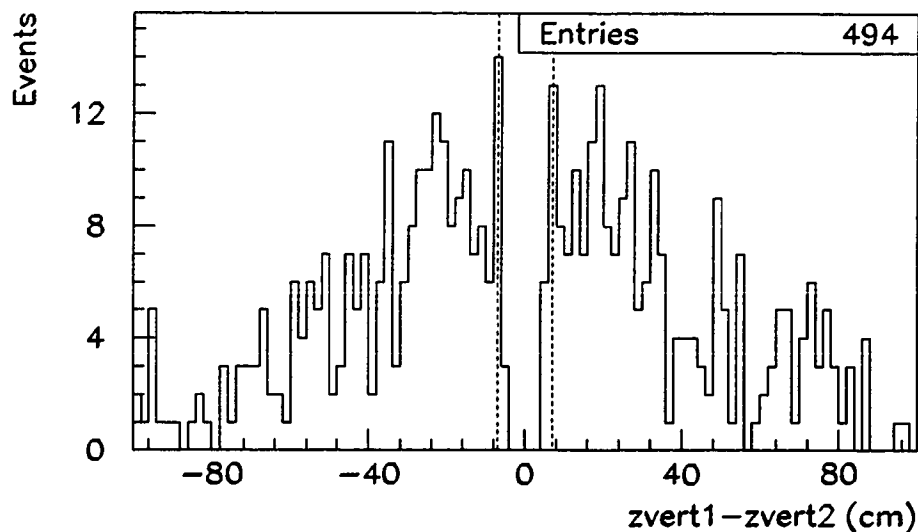
Figure 61. The distribution $z_{vertex}(1) - z_{vertex}(2)$ for the four-jet sample, showing the limited resolving power of the VTPC.

primary z-vertex position. This means that jets originating at the secondary z-vertex are incorrectly reconstructed. The z-vertex separation cut of 15 cm has been required to keep this effect small, while still retaining a reasonable number of events.

Based on this information from the four-jet data, double interactions are neglected as a significant source of background to double parton interactions. Such events also cannot explain the discrepancy between the double parton signals found by the S, ϕ_S and Δ_S variables.

E. Underlying Event

The effect of underlying event clusters on the three topological distributions has been investigated using a simple Monte Carlo technique. There are two cases which
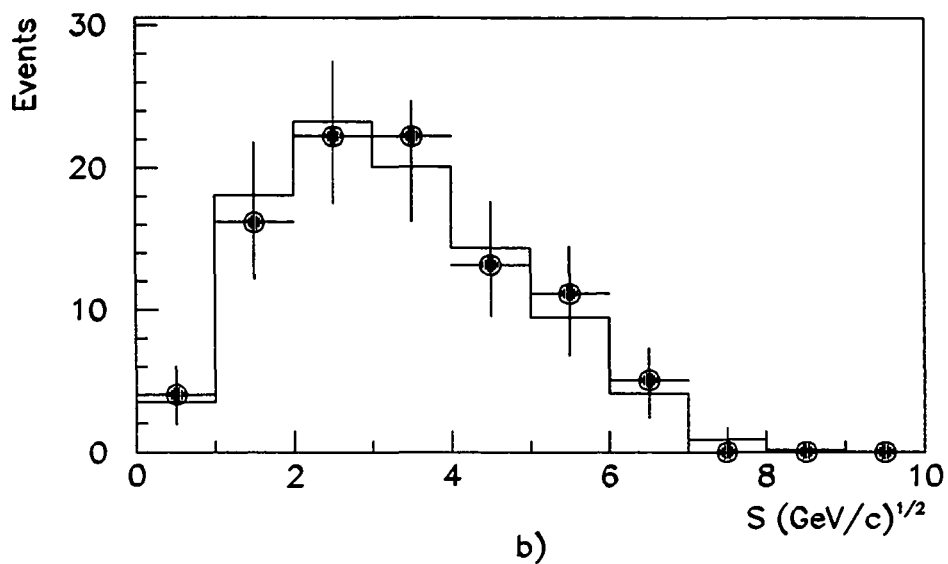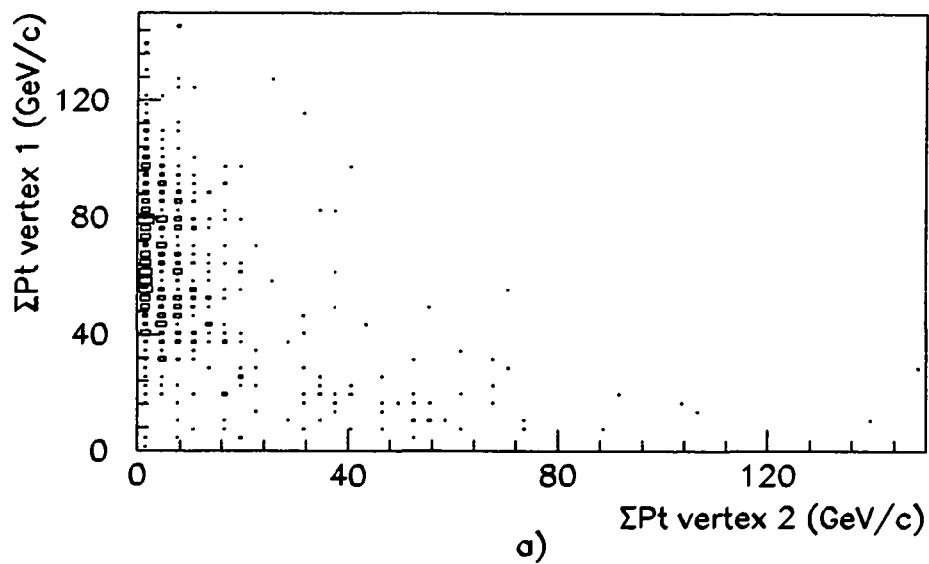
Figure 62. a) The $| \sum \vec{P_t} |$ of particles from the primary vertex versus that from the secondary vertex, b) the S variable for events containing two interactions overlaid on the distribution obtained with double bremsstrahlung simulated events.

are relevant, namely dijet events with two underlying event clusters, and three-jet events with one extra cluster. In both cases four jets are produced, so these two types of events may be present in significant numbers in the four-jet sample.

To simulate underlying event clusters, two-jet and three-jet events are generated, and additional clusters are produced at random ϕ and η. The P_t of these clusters is determined by the P_t of the smallest existing jet, smeared by a Gaussian of width $\sigma = 5$ GeV/c. While this is a somewhat ad-hoc procedure, the purpose is solely to investigate the general topological effect of fake clusters on the chosen signal finding variables. The random positioning of the simulated clusters is motivated by experimental observation [89]. The P_t of the simulated cluster is based on the smallest P_t of existing jets to ensure a large fake rate at low P_t.

Figures 63 and 64 show the distributions obtained using the above method for two-jet and three-jet events with two and one fake jets respectively. The shapes for double bremsstrahlung events are also shown for reference. Both figures demonstrate a marked difference in behaviour between events with underlying event clusters and those produced by QCD double gluon emission. Interestingly, underlying event clusters cause a depletion of events in the signal region relative to the double bremsstrahlung process for the S variable and an excess for the ϕ_S and Δ_S variables. This would lead to different values of $\mathcal{R}$ being measured for the three topological variables, consistent with observations. However, the general shapes are so different that any significant underlying event contribution would presumably also lead to an obvious

disagreement between the data and the double bremsstrahlung distributions. This level of disagreement is not observed.

A further check of the underlying event can be performed by looking at the P_t distribution of underlying event jets in the unweighted Monte Carlo simulation of the double bremsstrahlung process. The routines SETPRT and QFL (full detector simulation) are used to generate the events for this study. The underlying event fragmentation in the routine SETPRT has been compared to data and found to be in reasonable agreement [86]. In the simulated data, 5th jets are assumed to be due to the underlying event, as only four jets were originally generated. Figure 65 shows the resulting P_t spectrum. The distribution peaks at a corrected P_t of approximately 8 GeV/c and then falls rapidly, which again indicates that events containing underlying event clusters do not form a significant fraction of the four-jet data set.

F. The Effect of the Level 2 ξ Cut

The effects of the Level 2 ξ cut are not completely removed by the offline cuts on P_t and $\sum P_t$. Therefore a study of the influence of this cut on the topological variables has been performed. Using the sample of Monte Carlo data generated using the full detector and trigger simulations, the three variables S, ϕ_S and Δ_S have been plotted with and without the ξ cut in order to check whether any bias is introduced. Figure 66 shows a direct comparison between results obtained before and after the cut. No systematic variation is seen. As a further check, the difference between the three distributions with and without the cut has been taken and is plotted in Figure 67.
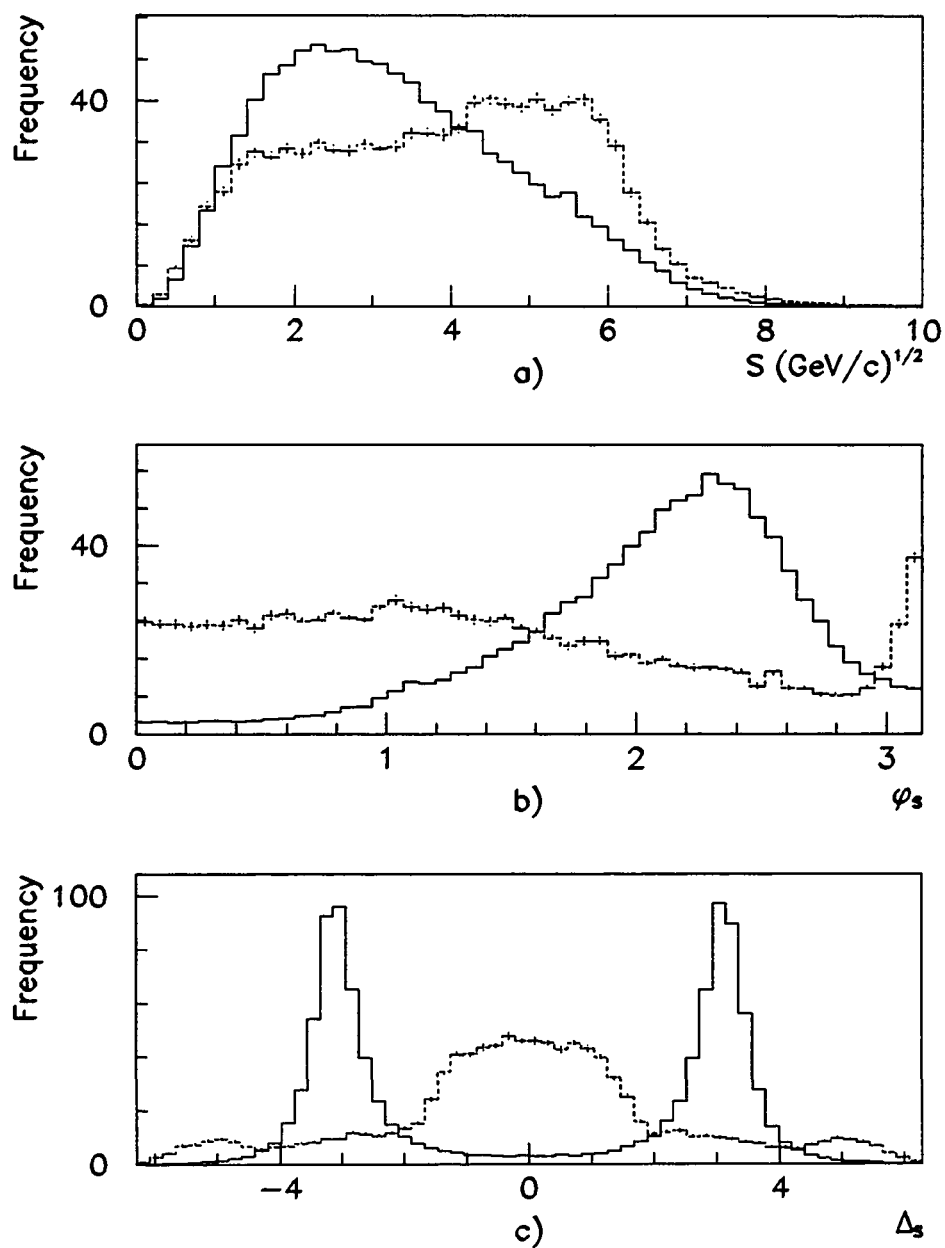
Figure 63.   Distributions of a) S, b) ϕ_S and c) Δ_S for dijet events with two fake jets (dashed) and for four-jet double bremsstrahlung events (solid).
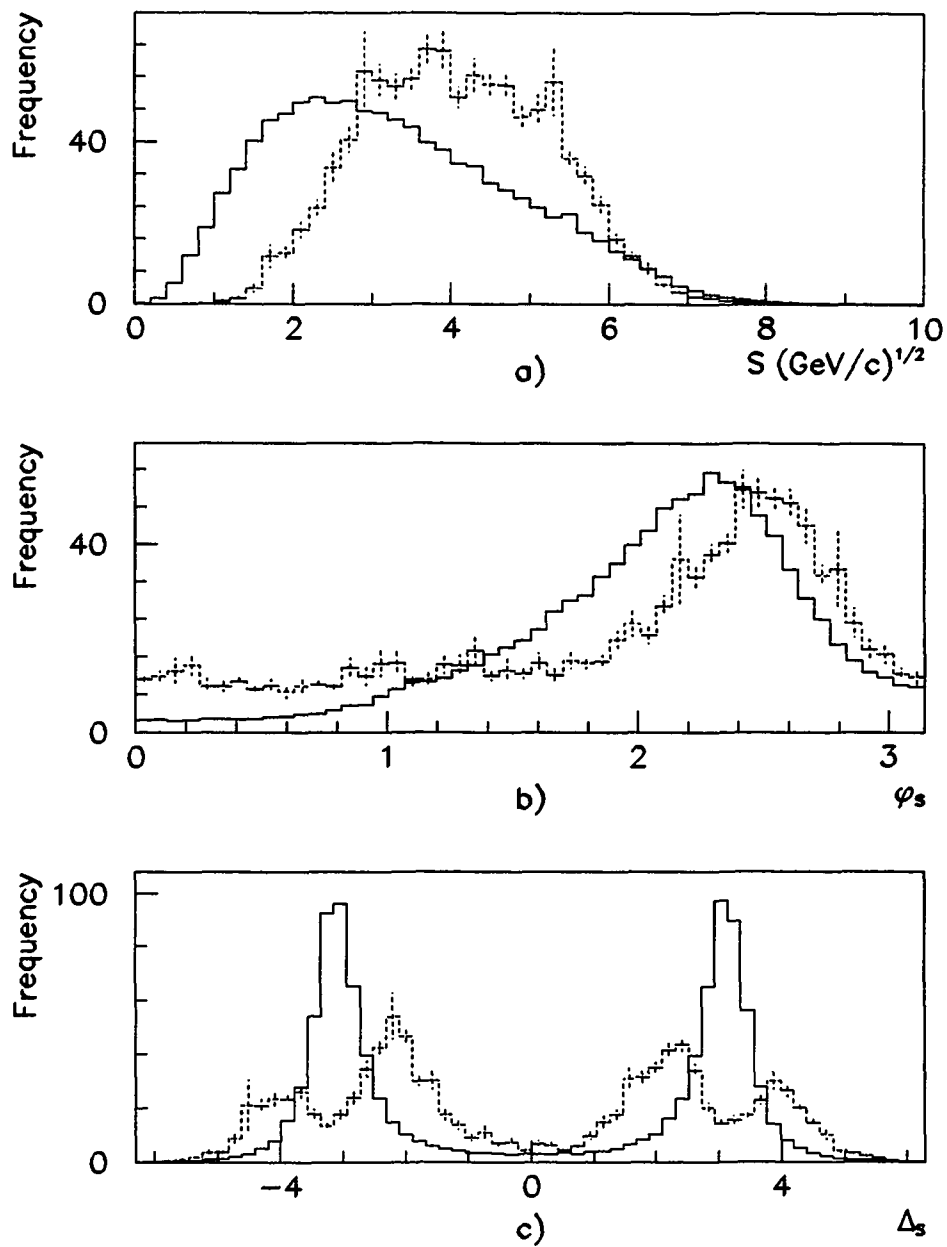
Figure 64. Distributions of a) S, b) ϕ_S and c) Δ_S for three-jet events with one fake jet (dashed) and for four-jet double bremsstrahlung events (solid).

QFL 5th jet Pt (UE) 4 jet events
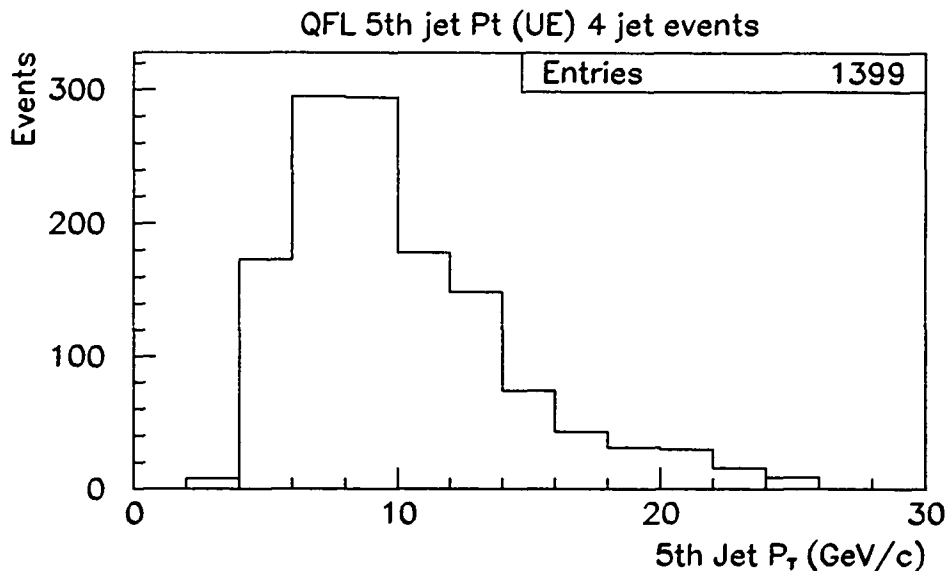
Figure 65. The P_t spectrum of Monte Carlo underlying event jets with full detector simulation.

The fluctuations are of a random nature and no significant excess or depletion is observed in the respective signal areas of each distribution.

G. The Effect of Fifth Jets

All jets in the final four-jet sample pass the cut $P_t > 25$ GeV/c. No specific cut is made on smaller fifth jets, the only requirement being that they are *less* than 25 GeV/c by default. In the four-jet double bremsstrahlung simulation, four jets are generated exclusively. While additional gluon radiation is simulated using a K_t kick, there are no additional clusters. The existence of small fifth jets in the data necessarily leads to a difference between simulation and data distributions. Qualitatively, additional clusters cause a worsening of the P_t-balancing, and hence a shift of the S variable away
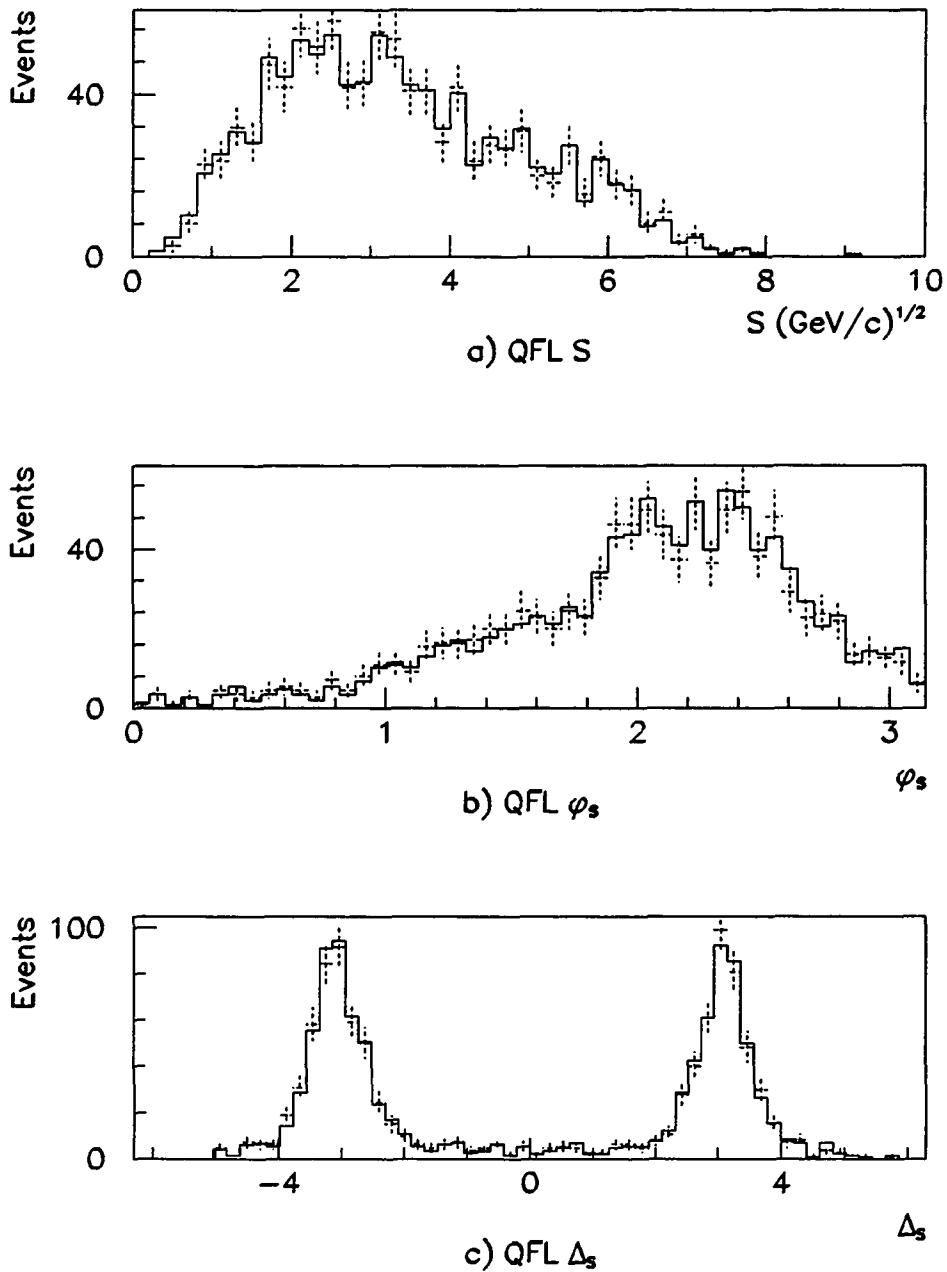
Figure 66.   Comparison of distributions for the variables a) S, b) ϕ_S and c) Δ_S with and without the Level 2 ξ cut. The cut distributions are overlaid on the uncut distributions.
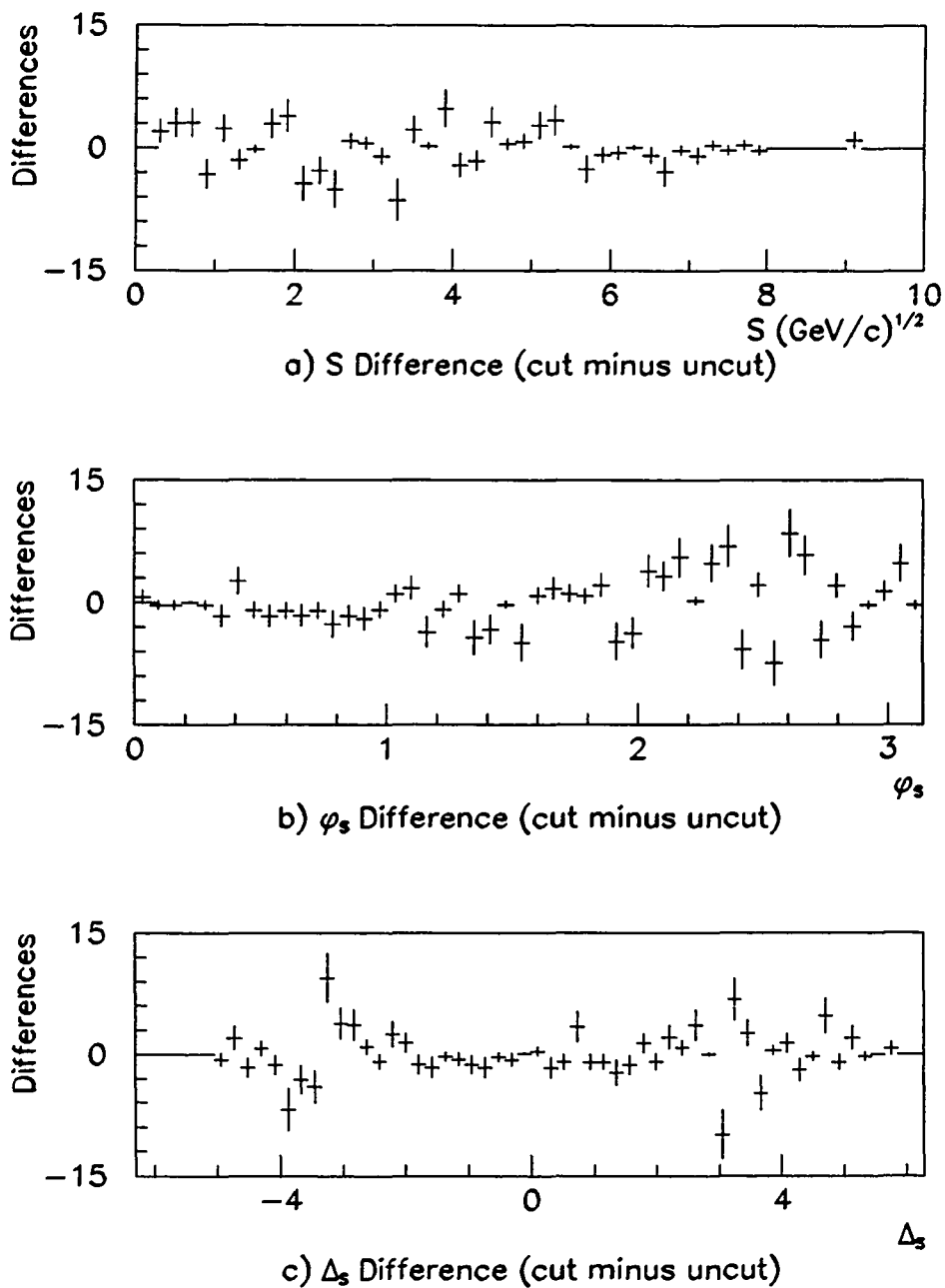
Figure 67. Differences between distributions for the variables a) S, b) ϕ_S and c) Δ_S before and after the Level 2 ξ cut.

from very low values (recall that events that balance well in P_t have small values of S). The effect on the angular variables ϕ_S and Δ_S is less clear. To investigate this, PAPAGENO has been used to generate five-jet events which are subsequently passed to the fast jet simulation. Due to the increased complexity of the five-jet process, theorists have not yet been able to calculate the corresponding full leading order matrix element. Therefore, events are generated using an approximate matrix element which includes only the gluon scattering terms. Since gluon scattering is the dominant process under the existing experimental conditions, this approximation is expected to be a fairly good one.

Results of the five-jet Monte Carlo study are shown in Figure 68, overlaid on the corresponding results for four-jet production. The same offline cuts have been applied in both cases. While the general agreement is good, a *depletion* in the signal region for the S variable is apparent for the five-jet case. Also, there is an *enhancement* in the five-jet signal regions for the ϕ_S and Δ_S variables. Therefore fifth jets in the data are a likely candidate for explaining the difference in the fitted values of $\mathcal{R}$ found using S, ϕ_S and Δ_S. Since the effects of fifth jets are in the opposite direction in the signal region for the S and the angular variables, the exclusion of fifth jets in the data should lead to a convergence in the values of $\mathcal{R}$. This reasoning has been tested by imposing a cut on the P_t of fifth jets. Denoting this quantity by $P_t^{(5)}$, three cuts have been made, namely $P_t^{(5)} < 25$, 20 and 15 GeV/c. The results are shown for the S, ϕ_S and Δ_S variables in Figures 69, 70 and 71 respectively.

The effect on the S distribution of cutting out more fifth jets is to increase the bins in the signal region ($0 < S < 2.5$). Conversely, the ϕ_S and Δ_S variables exhibit

5th Jet Effects (MC)
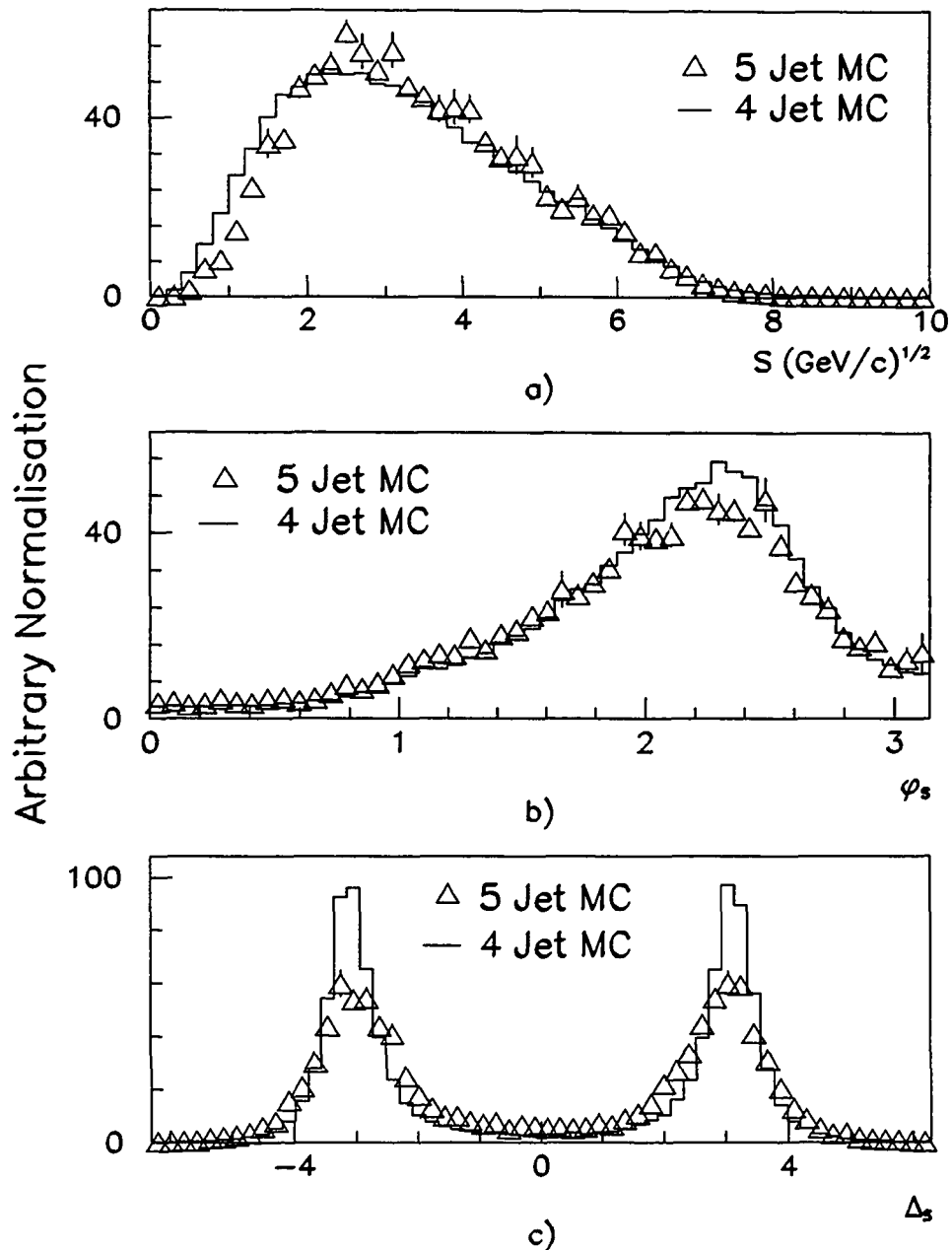
Figure 68. Comparison of the shapes of the three variables a) S, b) ϕ_S and c) Δ_S obtained using simulated five-jet events, overlaid on the results from simulated four-jet QCD double gluon emission.

a reduction of data entries in the signal regions ($|\phi_S| < 1$ and $\Delta_S \approx 0$ respectively).

Figure 72 shows the fitted values of $\mathcal{R}$ for all three variables as a function of cut on $P_t^{(5)}$ for a wider range of cuts. The fitted values of $\mathcal{R}$ for the three variables agree at a cut on $P_t^{(5)}$ of approximately 13 GeV/c. The conclusion from this behaviour is that the variation in the values of $\mathcal{R}$ obtained for the different variables with no explicit cut on fifth jets can be explained by the effects of an additional small P_t cluster in the data. The study of simulated five-jet events suggests that the value of $\mathcal{R}$ at which convergence is reached represents the best estimate of the double parton content of the data.

The method used in practice to find $\mathcal{R}$ is to fit both the S and Δ_S variables to straight lines as a function of fifth jet P_t cut, and determine at which point the lines intersect. The ϕ_S variable has been excluded as it has a significantly inferior signal finding resolution, and provides no useful additional information. The statistical error on $\mathcal{R}$ is calculated by performing a simultaneous log-likelihood fit to S and Δ_S, and finding the change in $\mathcal{R}$ necessary to increase the χ^2 parameter by 1 unit. This defines a robust procedure which will also be used in Chapter VII in the estimation of systematic errors. The result obtained with the structure function EHLQ1, with $Q = \langle P_t \rangle$ is $100 \cdot \mathcal{R} = 5.30 \pm 1.29$.

The determination of the double parton fraction based on a cut on the fifth jet in the data is a new technique, which makes use of the combined information available from P_t-balancing properties *and* angular correlations. Previous analyses by other groups have either ignored the effects of fifth jets, or have included cuts on these
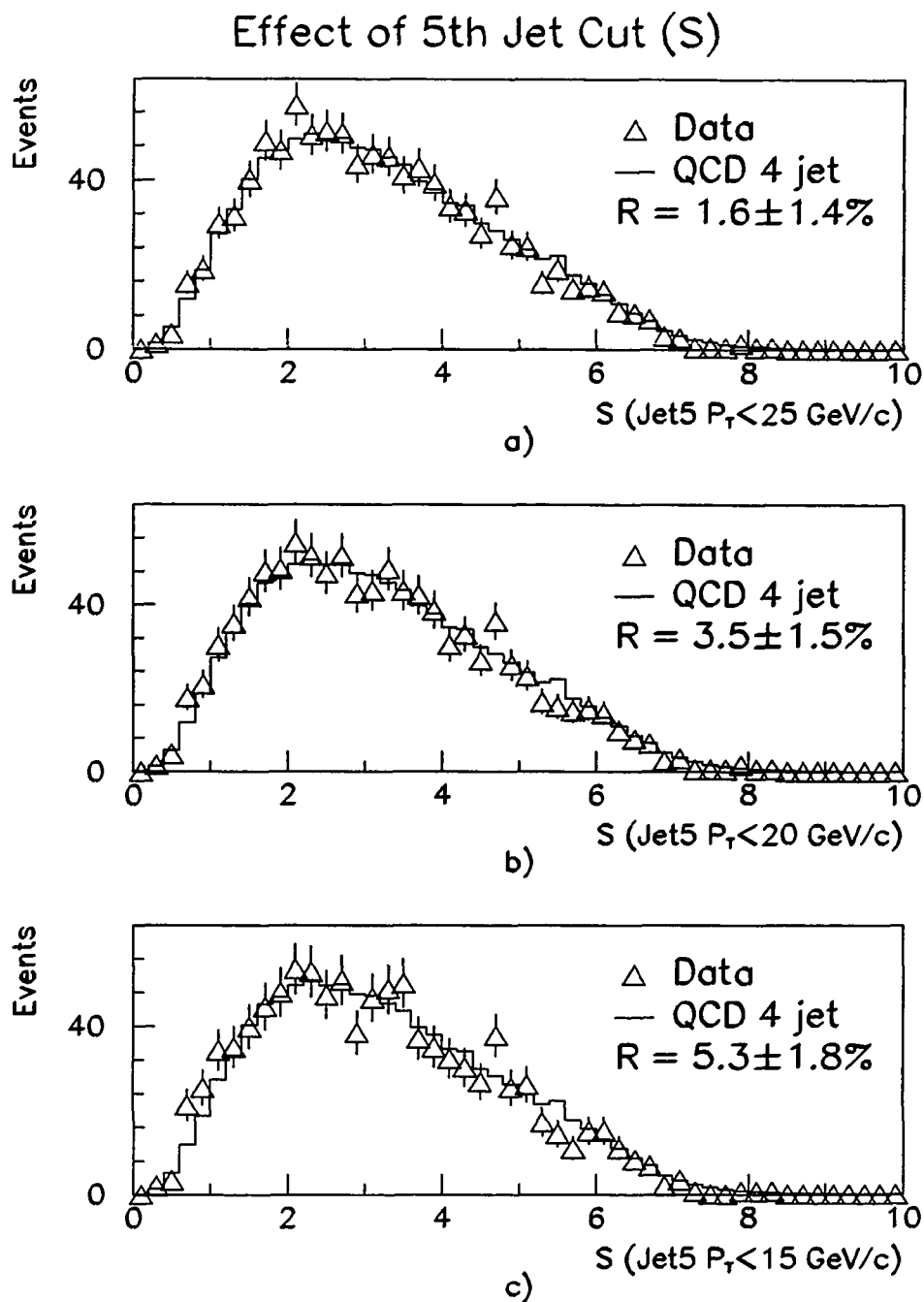
Figure 69. The S distribution obtained with data for three different cuts on $P_t^{(5)}$. The cuts are a) $P_t^{(5)} < 25$ GeV/c (default), b) $P_t^{(5)} < 20$ GeV/c and c) $P_t^{(5)} < 15$ GeV/c.
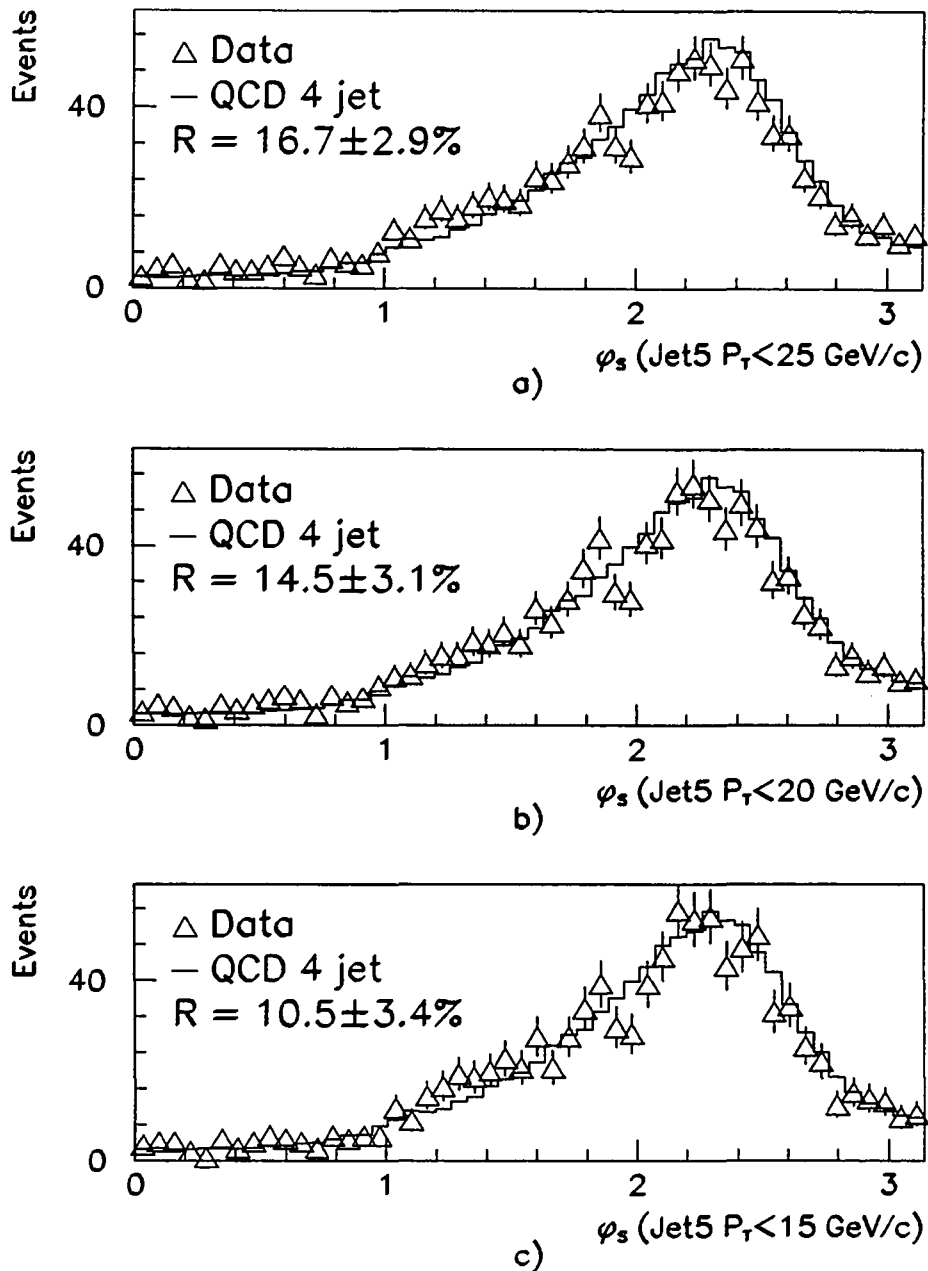
Figure 70. The ϕ_S distribution obtained with data for three different cuts on $P_t^{(5)}$. The cuts are a) $P_t^{(5)} < 25$ GeV/c (default), b) $P_t^{(5)} < 20$ GeV/c and c) $P_t^{(5)} < 15$ GeV/c.
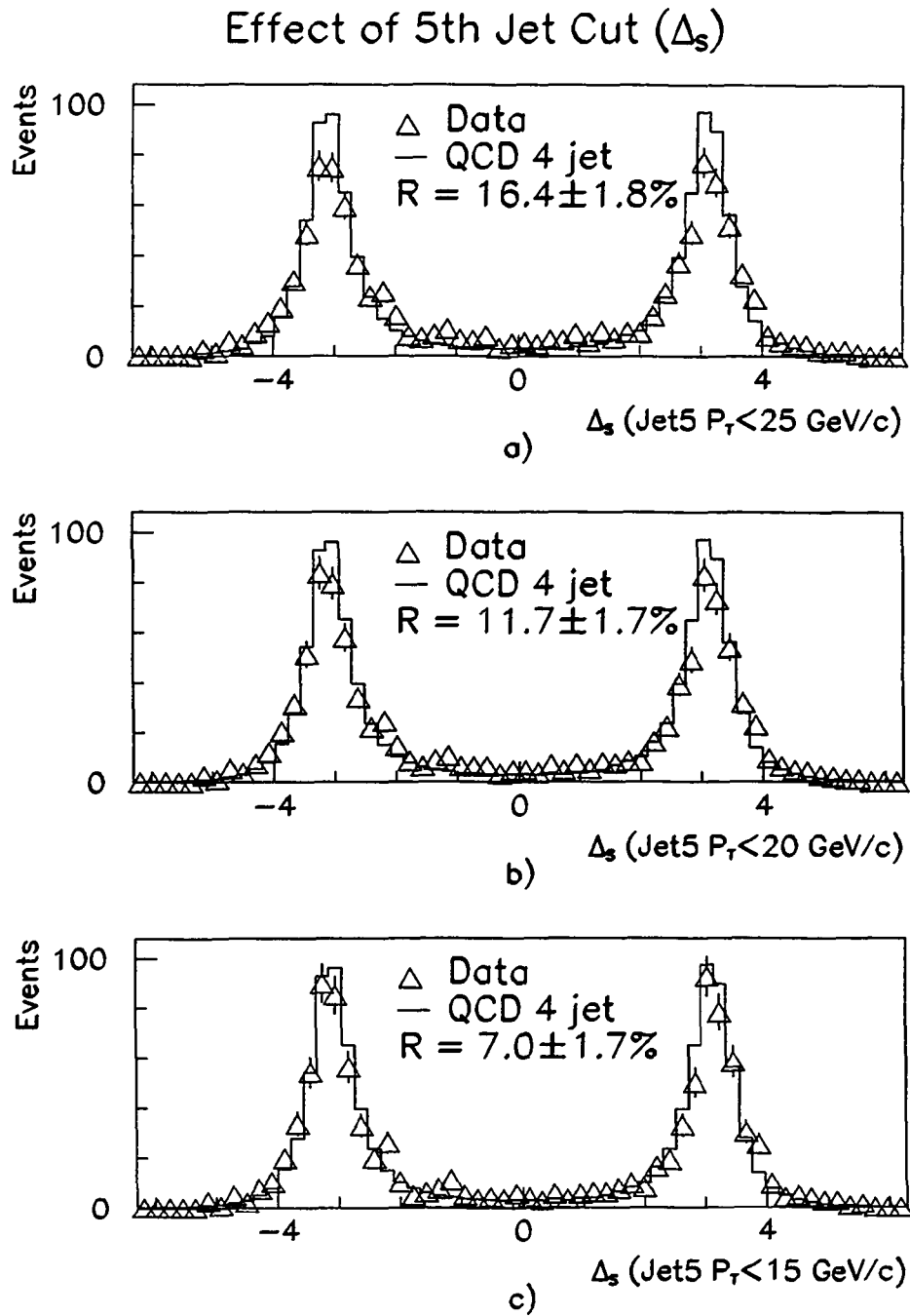
Figure 71. The Δ_S distribution obtained with data for three different cuts on $P_t^{(5)}$. The cuts are a) $P_t^{(5)} < 25$ GeV/c (default), b) $P_t^{(5)} < 20$ GeV/c and c) $P_t^{(5)} < 15$ GeV/c.

R vs 5th Jet P$_T$ Cut

R = 5.30%
Cut = 13.37 GeV/c
△ — △$_s$
✕ — S
+ — φ_s

R (%)

Jet 5 P$_T$ Cut (GeV/c)
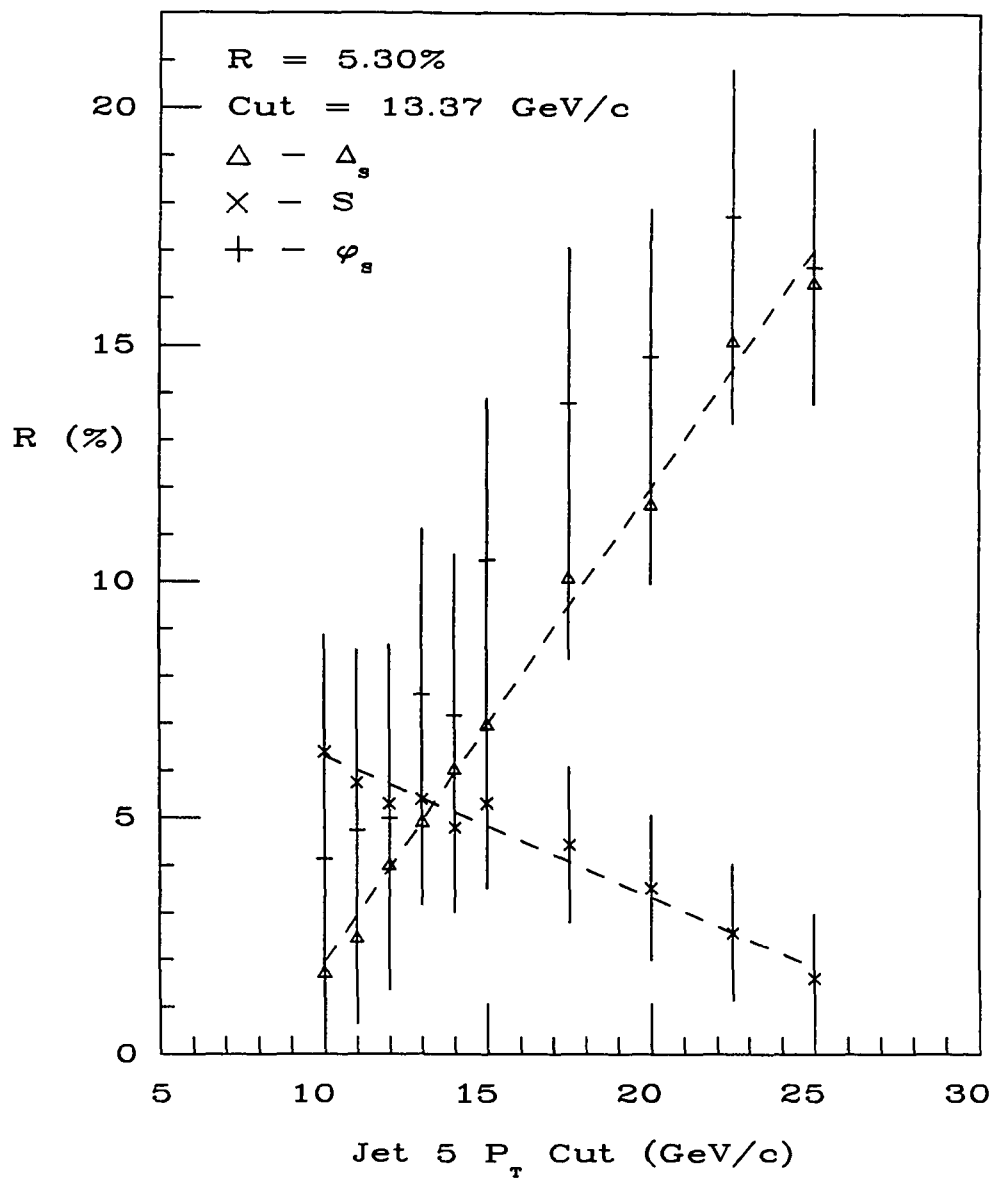
Figure 72. The double parton fraction $\mathcal{R}$ (%) as a function of the fifth jet P_t cut for the variables S, ϕ_S and Δ_S.

jets without thoroughly understanding their implications. This study indicates that a proper treatment of the effects of an additional jet in the data is the key to obtaining $\mathcal{R}$, given an exclusive four-jet Monte Carlo program. The use of only one variable to determine the double parton content may lead to a substantial mismeasurement.

The double parton signal is significant at the 4σ level, with statistical errors alone. This significance will be substantially reduced with the inclusion of systematic errors. Consequently, in Chapter VII limits are set on both the double parton cross section σ_{DP} and the effective cross section parameter, σ_{eff}. The latter will allow a comparison of results with the AFS and UA2 collaborations.

CHAPTER VII

LIMITS ON DOUBLE PARTON SCATTERING

The setting of limits on the double parton cross section σ_{DP} and the effective cross section σ_{eff} involves a careful determination of the acceptance of event cuts and the trigger. In addition, a complete evaluation of systematic errors must be performed. These issues are dealt with in detail in this chapter, and the significance of the results obtained is discussed. The insensitivity of σ_{eff} to the collision energy in the center-of-mass system allows a comparison of results with those of other collaborations.

A. Limit on σ_{DP}

The method used to evaluate an upper limit on the double parton scattering cross section σ_{DP} is based on the following equation,

$$N_{\mathrm{DP}} = \mathcal{L} \cdot \sigma_{\mathrm{DP}} \cdot \mathcal{A}_{\mathrm{DP}}^{\mathrm{cuts}} \cdot \mathcal{A}_{\mathrm{DP}}^{\mathrm{trig}}, \tag{74}$$

where N_{DP} is the observed number of events due to double parton scattering in the data, $\mathcal{L}$ is the integrated luminosity of the event sample, $\mathcal{A}_{\mathrm{DP}}^{\mathrm{cuts}}$ is the acceptance of the four-jet offline event cuts and $\mathcal{A}_{\mathrm{DP}}^{\mathrm{trig}}$ is the trigger acceptance for double parton events. Figure 73 shows the P_t spectrum of the smallest parton for Monte Carlo double parton events after all offline cuts have been applied. The kinematics of this process ensure that a parton generation cut of $P_t > 18$ GeV/c is fully efficient. Consequently the notation for the acceptance of the event cuts for double parton events will henceforth

DP Smallest Parton Pt Spectrum
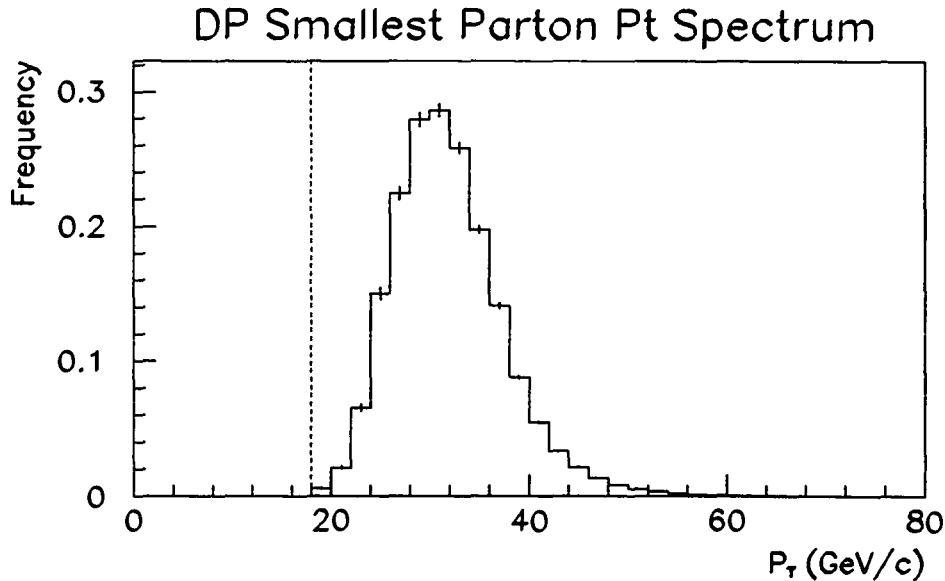
Figure 73. The P_t spectrum of the smallest generated parton for simulated double
parton events which pass all the four-jet cuts. The generation level for
partons ($P_t > 18$ GeV/c) is indicated by a dashed line.

be written as $\mathcal{A}_{DP}^{\geq 18}$ to represent the fact that this acceptance is determined for partons

having $P_t > 18$ GeV/c. Rewriting Equation 74 we obtain,

$$\sigma_{DP} = \frac{N_{DP}}{\mathcal{L} \cdot \mathcal{A}_{DP}^{\geq 18} \cdot \mathcal{A}_{DP}^{trig}}. \tag{75}$$

The luminosity of the event sample has been determined to be $\mathcal{L} = 324.9 \text{ nb}^{-1} \pm 6.8\%$

[91]. The remaining terms with their associated systematic errors are discussed fully

in the following sections.

1. Trigger Acceptance A_{DP}^{trig}

   The trigger acceptance for double parton events is dominated by the Level 2 ξ

cut, which required $\sum E_t - E_{t_1} - E_{t_2} > 40$ GeV, where E_{t_1} and E_{t_2} refer to the largest

and next largest E_t Level 2 clusters. This acceptance has been estimated using an unweighted sample of double parton events fragmented with the routine SETPRT and passed through the full QFL detector simulation. The CDF trigger Monte Carlo routine TRGSIM has been run on the output of QFL, and the usual four-jet cuts have been applied after jets have been clustered and corrected.

In order to have confidence in the results obtained from the double parton trigger simulation, both the simulated Level 2 $\sum E_t$ and cluster E_t have been checked using data. The Level 2 $\sum E_t$ has already been shown to be reliable by comparing four-jet data with a full simulation of double bremsstrahlung events (see Figure 42 of Chapter V, Section B2). Using the same data sets, a comparison of the Level 2 cluster E_t spectra for data and Monte Carlo has also been performed. The results are shown in Figure 74. Although the shapes of the spectra agree fairly well, the clusters produced by the simulation are systematically higher in E_t than those present in the data. This may be a result of the fact that noise in the plug and forward regions caused a slow turn-on of the trigger shoulder threshold during data-taking [96]. This would lead to the observed downward shift in the Level 2 cluster distributions in the data relative to the trigger simulation. The simulation does not correctly reproduce the subtle effects of noise. Figure 75 shows that much better agreement is obtained when the Monte Carlo distributions are shifted down by 2 GeV.

The agreement between the adjusted full trigger simulation and the four-jet data allows the double parton trigger acceptance due to the ξ cut to be estimated with confidence. Using the double parton and full detector simulations, the leading

Level 2 Cluster Comparison
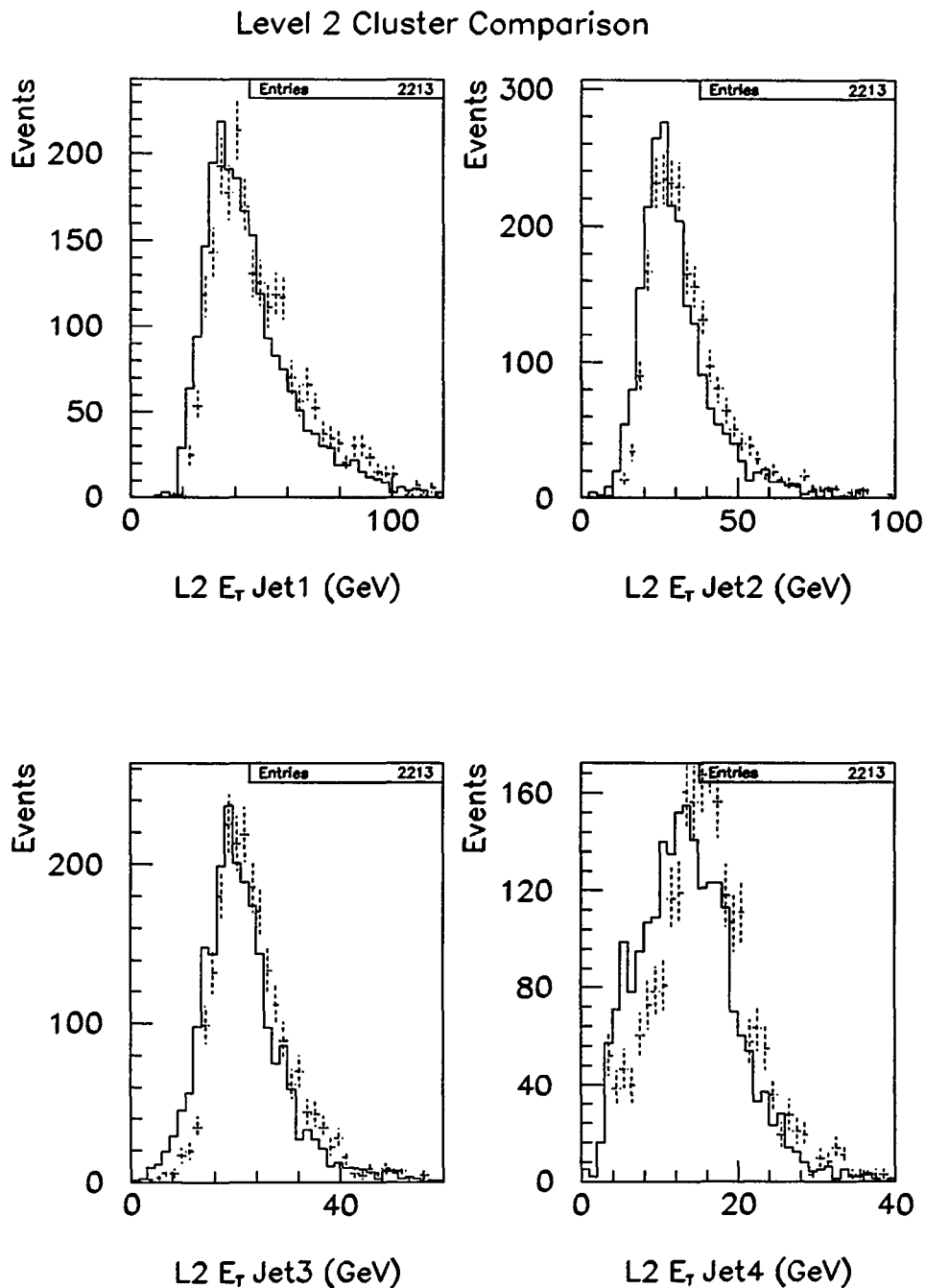
Figure 74. A comparison of the Level 2 cluster E_t spectra between four-jet data (solid) and simulated double bremsstrahlung events (dashed). The simulated data has been generated using PAPAGENO events (unweighted) and the full detector simulation.

Level 2 Cluster Comparison with 2 GeV Shift
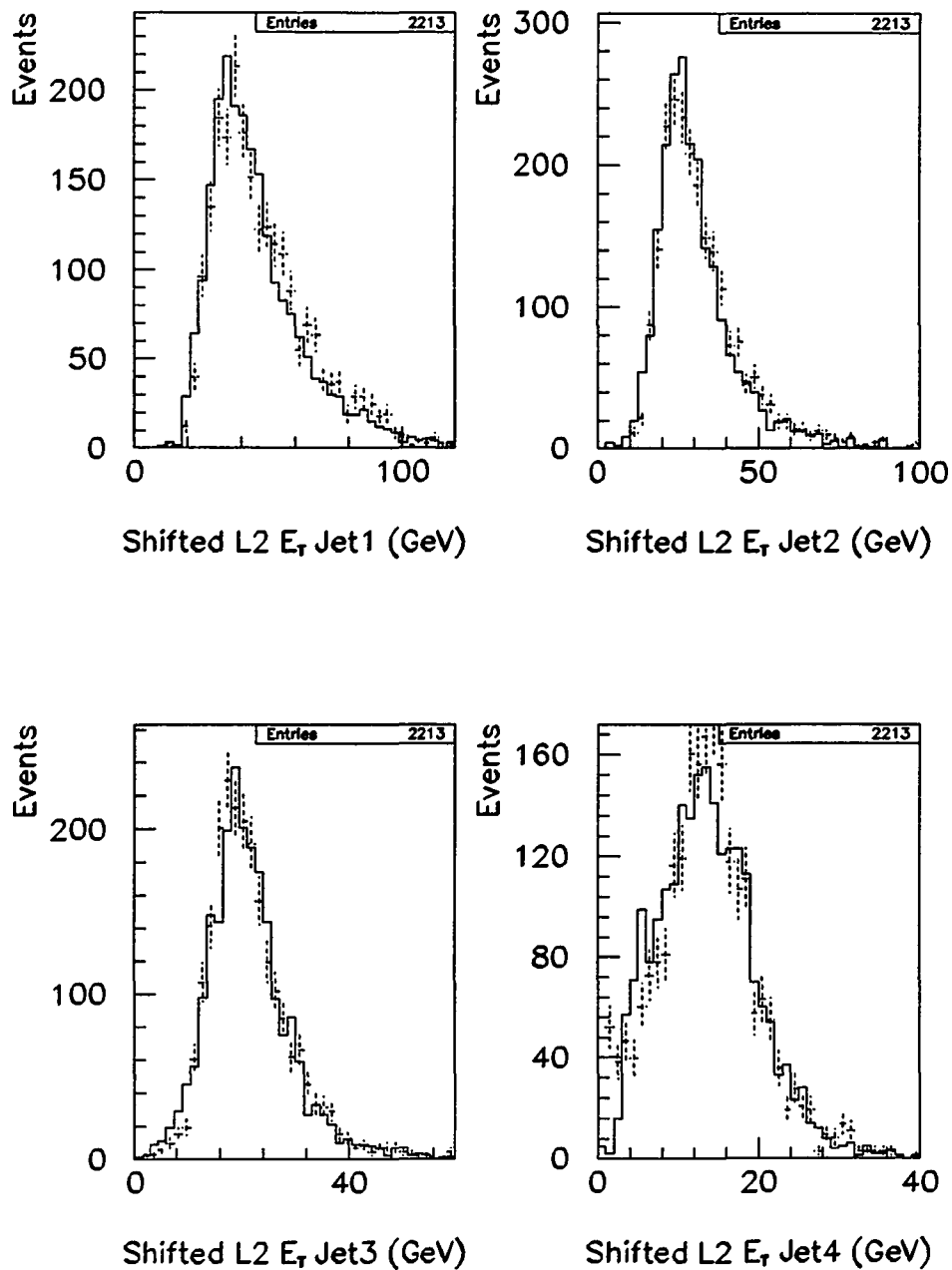
Figure 75. A comparison of the Level 2 cluster E_t spectra between four-jet data (solid) and simulated double bremsstrahlung events (dashed), where the simulated clusters have been shifted down by 2 GeV.

two Level 2 E_t clusters are shifted down by 2 GeV before being subtracted from the Level 2 $\sum E_t$ to form the ξ variable. The result can be seen in Figures 76 a) and b), where the cut E_t of 40 GeV is shown as a dashed line. The acceptance from this plot is found to be $515/591 = 0.87$. If the Level 2 cluster E_t shift is not performed, the acceptance drops to $453/591 = 0.77$ as shown in Figures 76 c) and d). The difference in results due to this shift is taken to be the systematic error inherent in the measurement, which amounts to 11.5%. The statistical error is 4%, which when added in quadrature with the systematic error yields a total error of 12%.

An independent check of the trigger acceptance of the ξ cut for double parton events has been performed using data taken with a special trigger. This trigger required $\sum E_t > 80$ GeV at Level 2, with no ξ requirement. Therefore the ξ distribution can be plotted after imposing the usual four-jet offline cuts, and the acceptance directly determined. Note that this assumes that the double parton and double bremsstrahlung processes have similar trigger acceptances. Figure 77 shows the results, before and after the online cut of 40 GeV. Although the statistics are fairly poor, the acceptance from this data is $30/37$, or 0.81, in good agreement with the result obtained from the simulation. The error on this measurement is 16.5% due to the limited statistics. Since this error is so large, the result from the Monte Carlo acceptance calculation is used for the purpose of establishing a limit.

The Level 2 $\sum E_t > 80$ trigger and the Level 3 trigger contribute less significantly to the total trigger acceptance. These acceptances have again been determined using the full double parton Monte Carlo simulation. Figure 78 shows the relevant

Level 2 ξ Acceptance

a) DP L2 Shifted ξ (GeV)

b) DP L2 Shifted ξ (GeV, cut)

c) DP L2 ξ (GeV)

d) DP L2 ξ (GeV, cut)
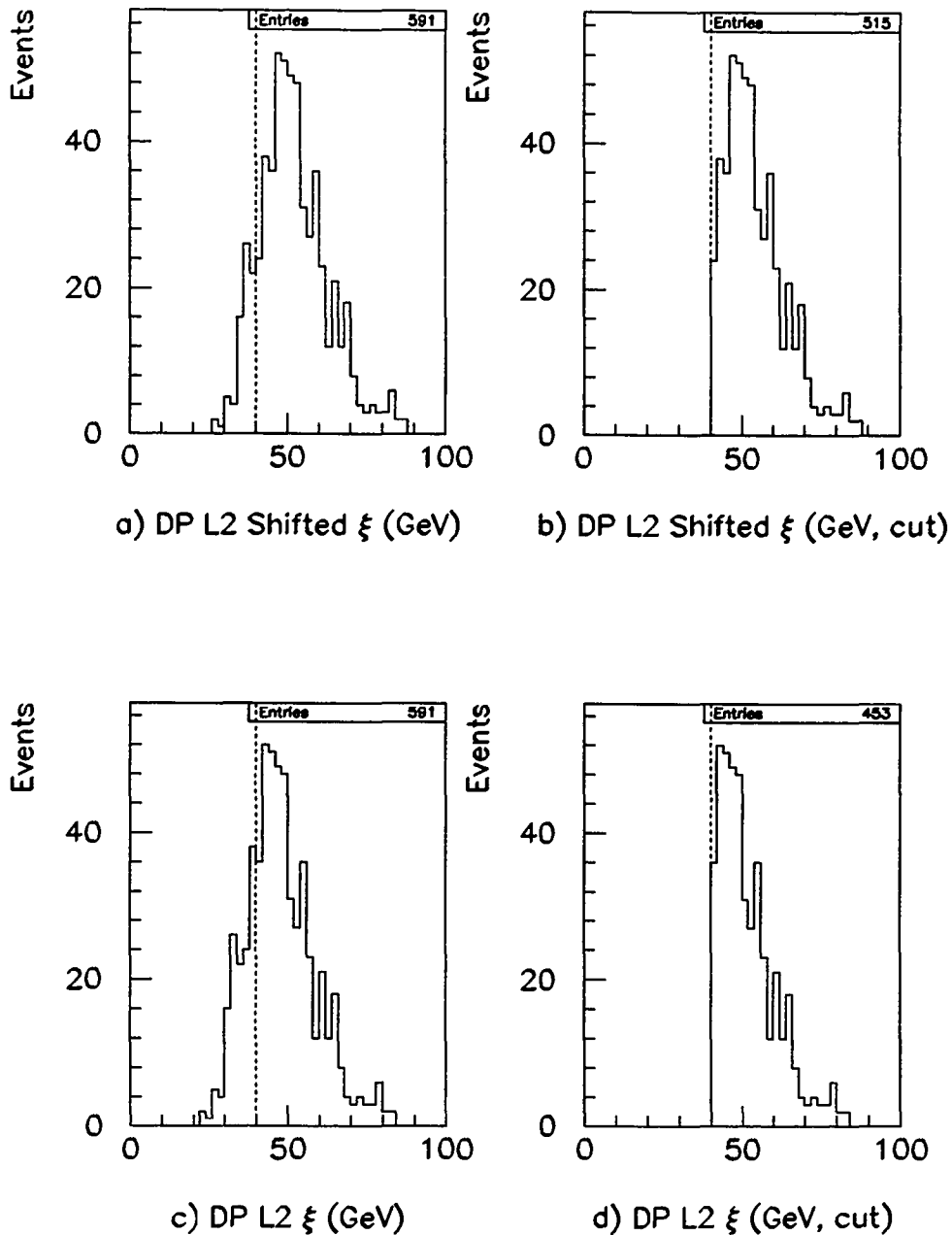
Figure 76. Acceptance of the Level 2 ξ cut for simulated double parton events. Shown are a) Level 2 ξ with Level 2 cluster E_t shifted by 2 GeV, b) same but with 40 GeV cut on ξ, c) Level 2 ξ with no shift, d) same but with 40 GeV cut on ξ.
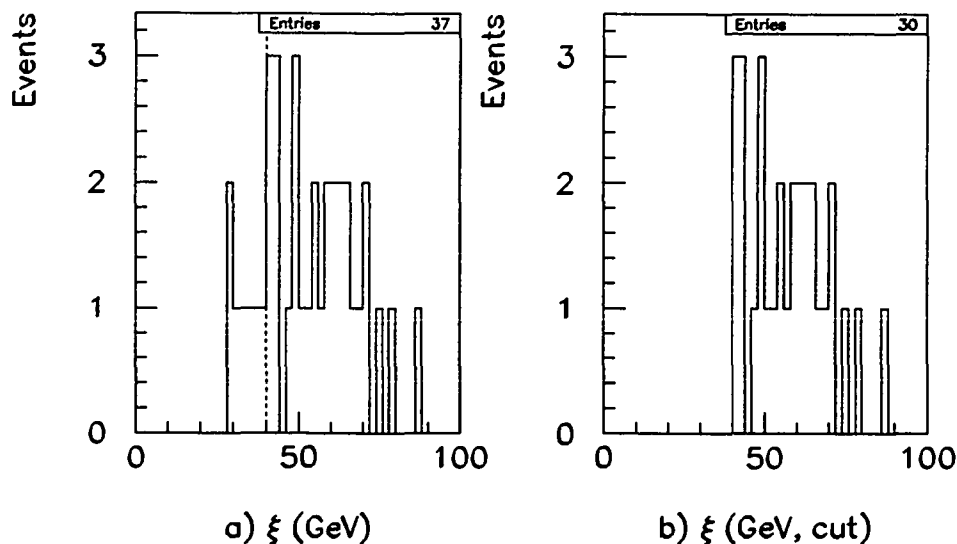
Figure 77. The ξ distribution obtained using a special run with the Level 2 trigger requirement $\sum E_t > 80$ GeV. Shown is ξ a) before and b) after the cut of $\xi > 40$ GeV.

simulated distributions before and after the trigger cuts. All offline cuts have been used when making these plots, and the Level 2 ξ cut has also been imposed to avoid double counting of acceptances. The combined acceptance of these two trigger cuts is 98%. Combining this result with that of the ξ cut yields a final value for the trigger acceptance:

$$\mathcal{A}_{DP}^{trig} = 0.85 \pm 0.10$$

2. Acceptance of Event Cuts $\mathcal{A}_{DP}^{\geq 18}$

The acceptance of the event cuts is obtained using simulated double parton events generated with $P_t > 18$ GeV/c. These events are passed to the fast jet sim-
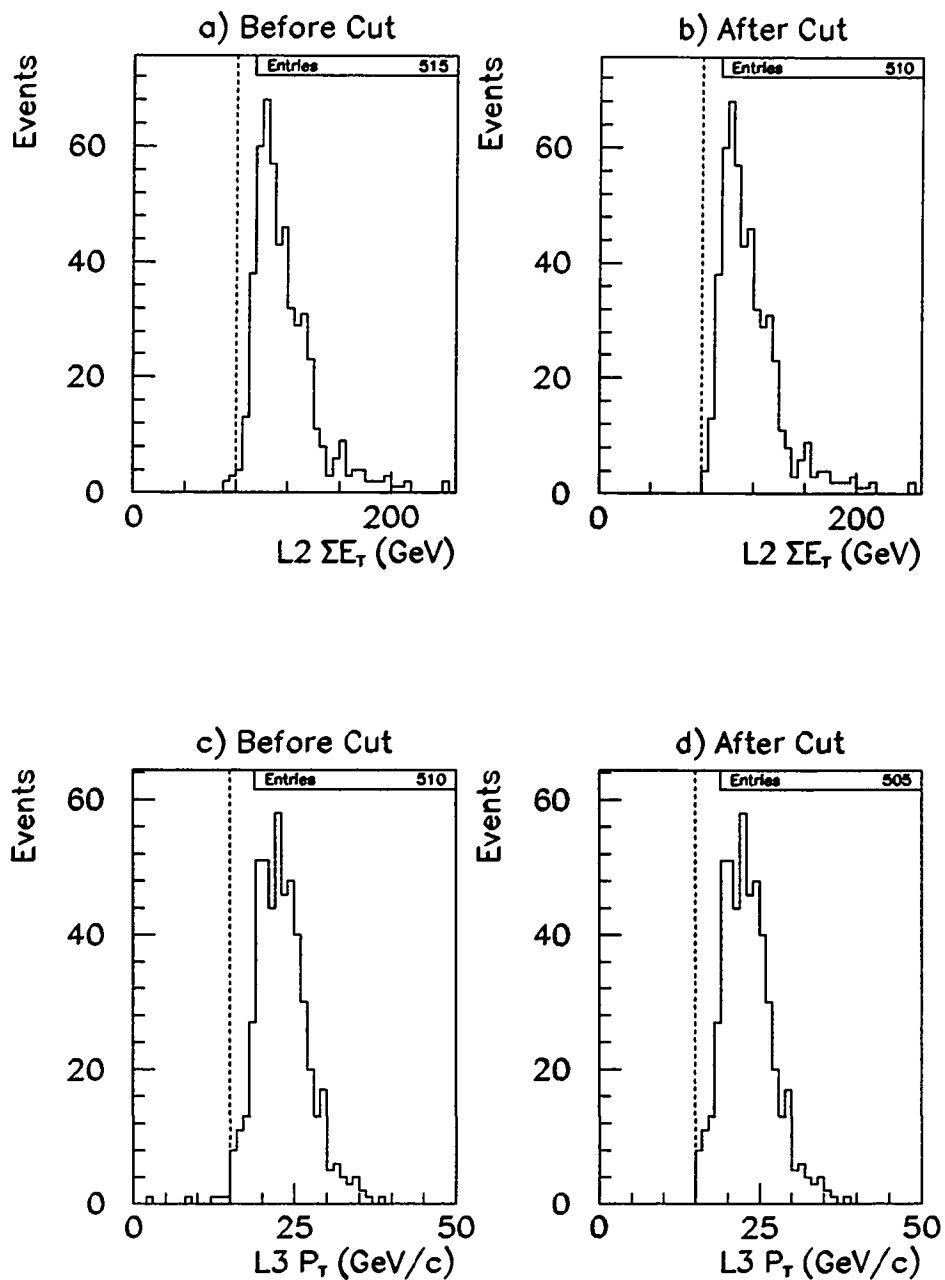
Figure 78. Double parton Level 2 $\sum E_t$ a) before and b) after the online cut of $\sum E_t > 80$ GeV, and Level 3 trigger acceptances c) before and d) after the online cut of $P_t > 15$ GeV/c. The full detector simulation has been used in conjunction with PAPAGENO.

ulation, and the same offline cuts used with the data are applied. Since the events are weighted according to their probability of occurrence, some care is needed in extracting $\mathcal{A}_{\mathrm{DP}}^{>18}$. The dijet cross section σ_{dijet} is given by the relation

$$\sigma_{\mathrm{dijet}} = w_1 + w_2 + \cdots + w_n, \tag{76}$$

where n dijet events have been generated and w_i is the weight of the ith event. Squaring Equation 76 we obtain

$$\sigma_{\mathrm{dijet}}^2 = [w_1 + w_2 + \cdots + w_n]^2 = w_1^2 + w_1 w_2 + w_2 w_1 + \cdots + w_n w_{n-1} + w_n^2. \tag{77}$$

Simulated double parton events are formed by merging together consecutive dijet events and combining their weights by multiplication to form the new event weight. Therefore, if n dijet events are generated and merged we can write,

$$W_{\mathrm{DP}} = w_1 w_2 + w_3 w_4 + \cdots + w_{n-1} w_n, \tag{78}$$

where W_{DP} is the sum of the weights of all double parton events. There are $n/2$ terms on the right hand side of Equation 78, and they are of the same size (on average) as the n^2 terms in Equation 77. We therefore can write,

$$W_{\mathrm{DP}} = \sigma_{\mathrm{dijet}}^2 \left(\frac{n/2}{n^2} \right) = \frac{\sigma_{\mathrm{dijet}}^2}{2n}. \tag{79}$$

The dijet cross section σ_{dijet} is calculated by the PAPAGENO program. The sum of event weights after all event cuts, denoted W_{DP}', may be determined by finding the area under any histogram formed from events passing the cuts. The acceptance $\mathcal{A}_{\mathrm{DP}}^{>18}$ is then given by,

$$\mathcal{A}_{\mathrm{DP}}^{>18} = \frac{W_{\mathrm{DP}}'}{W_{\mathrm{DP}}} = \frac{W_{\mathrm{DP}}' \cdot 2n}{\sigma_{\mathrm{dijet}}^2}. \tag{80}$$

As a consistency check, Equation 79 has been tested using a toy Monte Carlo program. Event weights are generated with a one-sided Gaussian distribution, with $\mu = 0$ and $\sigma = 1$. The event merging technique is used and the sum of the weights before and after merging is determined. The result obtained for a run of 3 million events (comparable to the number of events used in the PAPAGENO calculation) was:

$$\frac{(\text{Sum of weights})^2}{\text{Merged Sum} \times 2n} = 1.002. \tag{81}$$

Therefore the error specifically due to the event merging technique is negligible.

Results obtained for $\mathcal{A}_{DP}^{>18}$ with various structure functions and two different choices of Q^2 parameterization are shown in Table XI. The average value from these results, excluding those obtained with the structure functions EHLQ1 and DO2, is

$$\mathcal{A}_{DP}^{>18} = (6.18 \pm 0.85) \times 10^{-3}. \tag{82}$$

The excluded structure functions have been found to be inconsistent with existing data [97], and are used in this analysis solely to provide a conservative measure of theoretical uncertainty. The acceptance is fairly small since it necessarily includes an integral over a kinematic region of small acceptance, namely from $P_t = 18$ GeV/c to $P_t \simeq 25$ GeV/c. The acceptance approaches 100% only at higher values of P_t, as can be seen from Figure 73 of Section A (in this chapter).

3. Jet Separation Acceptance Correction

The fast jet simulation does not fully model the detailed fragmentation effects present in the data. These effects are treated globally, using an average jet position

Table XI. Values of $\mathcal{A}_{DP}^{\geq 18}$ obtained with various generating criteria.

Structure Fn.	Q	σ_{dijet} (nb)	$\mathcal{A}_{DP}^{\geq 18}(\%)$
EHLQ1	$\langle P_t \rangle$	39510 ± 72	0.608
EHLQ1	$\langle P_t/2 \rangle$	49280 ± 93	0.677
DO2	$\langle P_t \rangle$	46850 ± 83	0.531
DO2	$\langle P_t/2 \rangle$	59030 ± 110	0.620
MRS1	$\langle P_t \rangle$	27300 ± 78	0.725
MRS1	$\langle P_t/2 \rangle$	32350 ± 95	0.825
MRS2	$\langle P_t \rangle$	33980 ± 97	0.610
MRS2	$\langle P_t/2 \rangle$	41800 ± 123	0.704
MRS3	$\langle P_t \rangle$	30240 ± 85	0.560
MRS3	$\langle P_t/2 \rangle$	38190 ± 111	0.629
MART_1	$\langle P_t \rangle$	32700 ± 93	0.588
MART_1	$\langle P_t/2 \rangle$	41200 ± 120	0.654
MART_2	$\langle P_t \rangle$	38010 ± 108	0.534
MART_2	$\langle P_t/2 \rangle$	49800 ± 145	0.590
MART_3	$\langle P_t \rangle$	41180 ± 116	0.489
MART_3	$\langle P_t/2 \rangle$	55860 ± 162	0.526
MT_DIS1	$\langle P_t \rangle$	35260 ± 101	0.620
MT_DIS1	$\langle P_t/2 \rangle$	44820 ± 132	0.604

resolution. Occasionally, partons fragment in such a way as to produce an additional cluster close to the primary cluster. Therefore the jet separation cut ($\Delta R > 1.0$) may have a slightly different efficiency for real data than for the simulation. This effect has been observed in a previous analysis [98]. In addition, jets in the data are clustered

with a cone size of $R = 0.7$. Hence the jet separation is constrained to be $\Delta R > 0.7$. This is not the case for jets simulated with the fast jet Monte Carlo program. To check the acceptance of the jet separation cut with the fast jet simulation, the minimum jet separation before the cut has been examined. The full detector simulation (QFL) reproduces this distribution for four-jet double bremsstrahlung events with reasonable accuracy. Figure 79a) shows a comparison between ΔR for both QFL and data. Figure 79b) shows a comparison of ΔR before the separation cut using the fast jet simulation and QFL with simulated double parton events.

In agreement with expectations, the distribution of ΔR obtained with the fast jet simulation is shifted slightly towards higher separation values and also extends below 0.7. The acceptance of this cut determined using the full detector simulation is more reliable than that of the fast jet simulation, and hence a correction is applied to $\mathcal{A}_{DP}^{>18}$. Defining $\mathcal{A}^{sep}$ as the acceptance due to the separation cut $\Delta R > 1.0$ and using the results shown in Figure 79b) we obtain

$$\mathcal{A}_{QFL}^{sep} = 0.90, \tag{83}$$

$$\mathcal{A}_{fast}^{sep} = 0.86, \tag{84}$$

where $\mathcal{A}_{QFL}^{sep}$ and $\mathcal{A}_{fast}^{sep}$ are the acceptances due to the separation cut for events simulated with QFL and the fast jet simulation respectively. The correction to $\mathcal{A}_{DP}^{>18}$ is defined by the ratio $\mathcal{A}_{QFL}^{sep}/\mathcal{A}_{fast}^{sep}=0.90/0.86=1.05$. Thus the correction is small, but

should be included in the final result.

4. Determination of N_{DP}

The number of double parton events, N_{DP}, can be re-expressed using Equation 73,

$$\mathcal{R} = \frac{\text{Number of Double Parton Events}}{\text{Number of Double Bremsstrahlung Events}} = \frac{N_{\text{DP}}}{N_{\text{DB}}}, \qquad (85)$$

where N_{DB} is the number of double bremsstrahlung events in the data. The quantity $\mathcal{R}$ is determined by fitting the data to an admixture of double parton and double bremsstrahlung distributions. The number of double bremsstrahlung events (N_{DB}) can be equated with the number of four-jet events, since events due to other processes (including double parton scattering) form a very small fraction of the data. The number of double parton events found from the topological fits is taken to be the systematic error inherent in the measurement of N_{DB}.

The measurement of $\mathcal{R}$ is subject to systematic errors due to the theoretical uncertainty in event topology which can result in different variable shapes and consequently a change in the fitted fraction of double parton events. This uncertainty has been estimated by varying the structure function and Q^2 parameterizations used in both double bremsstrahlung and double parton event generation, and observing the change in $\mathcal{R}$. Such changes appear to affect the *rate* of both processes far more than they affect the event topology. Therefore, $\mathcal{R}$ remains fairly stable. Table XII shows results obtained with two different choices of structure functions and Q^2 parameterizations. The final value of $\mathcal{R}$ from these results is

$$100 \cdot \mathcal{R} = 5.29 \pm 1.30 \text{ (stat.)} \pm 0.30 \text{ (syst.)}, \qquad (86)$$
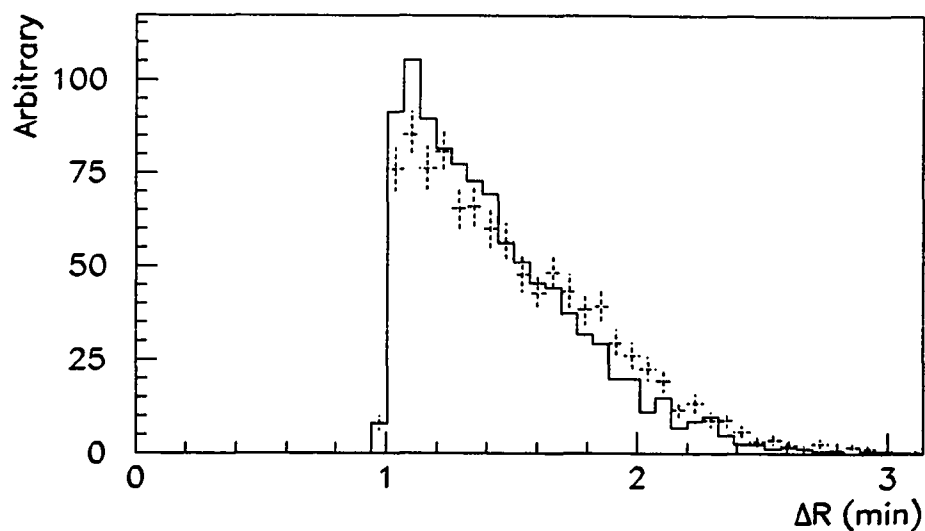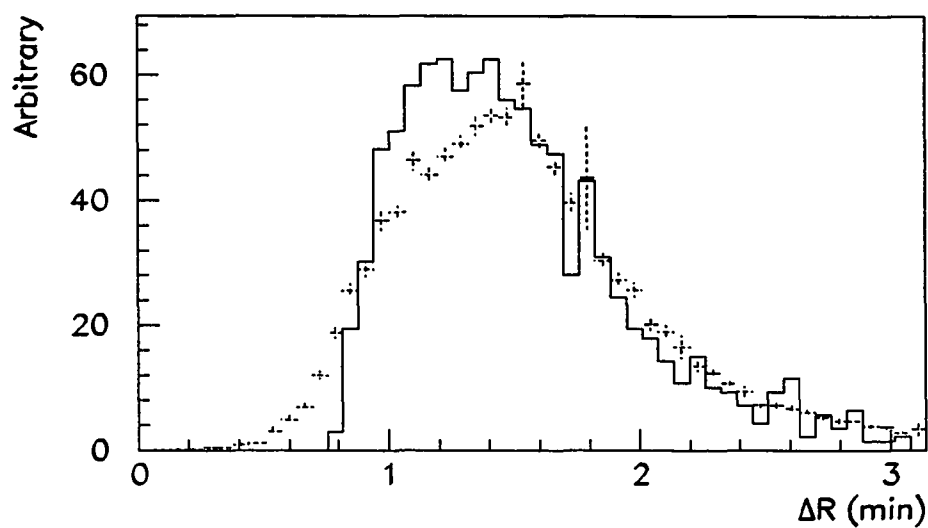
Figure 79. Comparison of minimum jet separation before the jet separation cut. Shown are a) data (dashed points) and full detector simulation (histogram) with events produced using the double bremsstrahlung Monte Carlo simulation, b) full detector simulation (histogram) and fast jet simulation (dashed points) with simulated double parton events.

Table XII. Results obtained for $\mathcal{R}$ with two different structure functions and Q^2 parameterizations.

Structure Fn.	Q	$\mathcal{R}$ (%)	Cut on $P_t^{(5)}$
EHLQ1	$\langle P_t \rangle$	5.30 ± 1.29	13.37
EHLQ1	$\langle P_t/2 \rangle$	5.65 ± 1.30	13.63
DO2	$\langle P_t \rangle$	4.91 ± 1.30	13.26
DO2	$\langle P_t/2 \rangle$	5.28 ± 1.30	13.42

where the quoted systematic error is the standard deviation of the four measurements in Table XII. Combining both systematic and statistical errors in quadrature results in a final error on $\mathcal{R}$ of 1.33. The determination of $\mathcal{R}$ also allows a systematic error to be assigned to N_{DB}, yielding the result

$$N_{\text{DB}} = 2213 \pm 2.1\% \text{ (stat.)} \pm 5.3\% \text{ (syst.)}. \tag{87}$$

5. Jet Energy Scale Uncertainty

A change in the jet energy scale results in a shift in both N_{DP} and $\mathcal{A}_{\text{DP}}^{\geq 18}$. However, these terms enter into the expression for σ_{DP} as a *ratio* (see Equation 75). Since both quantities vary in unison, the resulting change in the cross section is relatively small. The jet energy scale has been varied inside the jet correction routine in the following ways:

1. Absolute jet energy scale (ABS) increased and decreased by 5%, based on the results presented in an analysis of the central hadron calorimeter energy scale [87].

Table XIII. The effect of possible jet mismeasurement on N_{DB} and $\mathcal{A}_{\mathrm{DP}}^{\geq 18}$. The change in the ratio of these two terms is also tabulated.

	ABS ↑	REL ↑	OOC	ABS ↓	REL ↓	UE	Default
N_{DB} (Data)	2850	2323	3789	1642	2135	1762	2213
$\mathcal{A}_{\mathrm{DP}}^{\geq 18}$ (%)	0.938	0.655	1.329	0.385	0.569	0.438	0.608
$(N_{\mathrm{DB}}/\mathcal{A}_{\mathrm{DP}}^{\geq 18}) \times 10^{-5}$	3.04	3.55	2.85	4.26	3.75	4.02	3.64
% Deviation	-16.5	-2.5	-21.7	17.0	3.0	10.4	-

2. Relative jet energy scale (REL) increased and decreased by the statistical error inherent in its determination [83]. The region $0.2 <| \eta |< 0.8$ was not changed.

3. An out-of-cone (OOC) energy addition is performed.

4. An underlying event (UE) energy subtraction is performed.

Each of these modifications was performed separately, and the change in the ratio $N_{\mathrm{DB}}/\mathcal{A}_{\mathrm{DP}}^{\geq 18}$ determined. The results are shown in Table XIII. Adding the positive and negative shifts in quadrature, the systematic error on the cross section due to jet energy scale uncertainty is found to be +20.2% and −27.4% respectively. The error is not symmetric because the out-of-cone energy addition is significantly larger than the underlying event subtraction. In determining an upper limit on the cross section only the smaller (positive) error is relevant.

6. Error Due to the Use of an Approximate Matrix Element

The Kunszt-Stirling approximation to the exact leading order 2→4 parton matrix element [47] was used in the simulation of the four jet process. This simulation is used to generate the shapes of the three topological variables S, ϕ_S and Δ_S in

Approximate Matrix Element Comparison
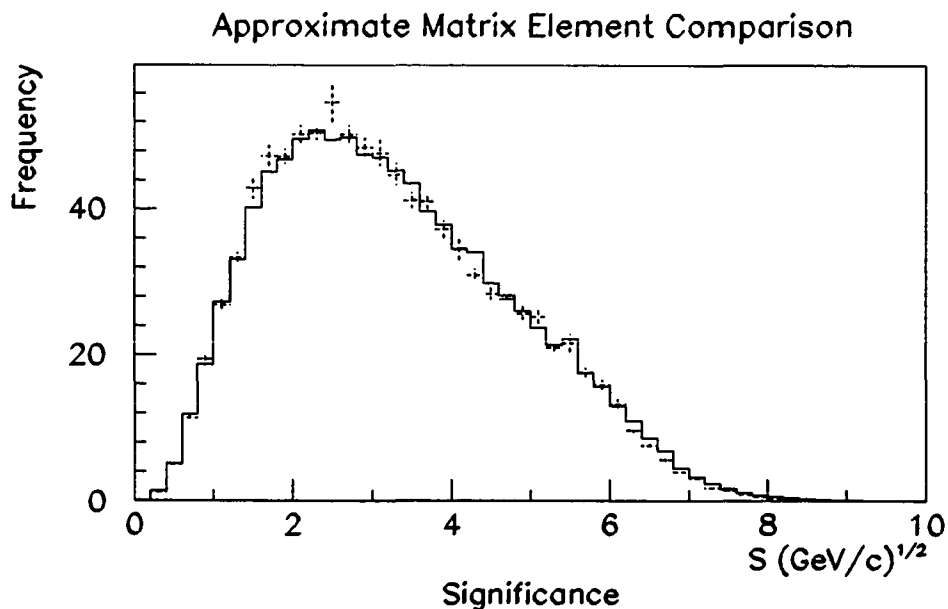
Figure 80. The S distribution obtained using the four-jet approximation by Maxwell, overlaid on S formed using the Kunszt-Stirling approximation.

order to extract $\mathcal{R}$ from the data. The systematic error arising from the use of an approximation was estimated by generating four jet events with a different approximate matrix element due to Maxwell [48] and observing the resulting change in $\mathcal{R}$. Figure 80 shows the S variable obtained using the two different approximations. The EHLQ1 set of structure functions, with $Q = \langle P_t \rangle$, was used in both cases. This figure shows that there is no appreciable change in the resulting topology of S. Therefore the systematic error due to the use of an approximate matrix element is considered negligible in comparison with the other sources of systematic error.

7. Uncertainty in Jet Resolution

The effect of jet resolution uncertainty on the acceptance of event cuts $\mathcal{A}_{DP}^{>18}$ has been tested by increasing and decreasing the default resolutions in the fast jet

Table XIV. The effect of changes in jet resolution on the acceptance $\mathcal{A}_{DP}^{\geq 18}$ for events produced with the EHLQ1 structure function and $Q = \langle P_t \rangle$.

Jet Resolution	$\mathcal{A}_{DP}^{\geq 18}$ (%)	% Change
Default	0.608	-
Up	0.620	+2.0
Down	0.604	-0.6

simulation by amounts given in Table X of Chapter V, Section C. The results are shown in Table XIV. Varying the jet resolution produces a very small change in the acceptance.

The jet resolution may also affect the topological distributions used to extract $\mathcal{R}$. To examine this possibility, the S and Δ_S variables have been formed using double parton and double bremsstrahlung events with higher and lower resolutions. A comparison of the double bremsstrahlung distributions shows no change resulting from the different resolutions, but the double parton distributions do change slightly for the S variable. The results obtained with the resolution increased and decreased, overlaid on the default results are shown in Figure 81. When used to fit the data in order to determine $\mathcal{R}$, these distributions result in a slight shift of the intersection point of S and Δ_S as a function of 5th jet P_t cut. The results are shown in Table XV. The variation in the results obtained is very small; the maximum change in $\mathcal{R}$ is 6%. In addition, $\mathcal{R}$ *decreases* in both instances when the jet resolution is increased or decreased. Therefore the systematic error associated with the effect of jet resolution

on the determination of $\mathcal{R}$ does not adversely affect either of the limits on double parton scattering.

8. Limit Calculation

Combining Equations 75 and 85 results in the relation

$$\sigma_{\mathrm{DP}}(P_t > 18 \text{ GeV}/c) = \frac{\mathcal{R} \cdot N_{\mathrm{DB}}}{\mathcal{L} \cdot \mathcal{A}_{\mathrm{DP}}^{\geq 18} \cdot \mathcal{A}_{\mathrm{DP}}^{\mathrm{trig}}}.$$
(88)

The following results have been obtained for the parameters in Equation 88,

- $100 \cdot \mathcal{R} = 5.29 \pm 1.30$ (stat.) ± 0.30 (syst.). Total error on $\mathcal{R}$ is 25.2%.

- $N_{\mathrm{DB}} = 2213 \pm 2.1\%$ (stat.) $\pm 5.1\%$ (syst.). Adding systematic and statistical errors in quadrature results in a total error of 5.5%.

- $\mathcal{L} = 324.9$ nb$^{-1} \pm 6.8\%$.

- $\mathcal{A}_{\mathrm{DP}}^{\geq 18} = (6.49 \pm 0.92) \times 10^{-3}$. This corresponds to an error of 14.2%. A factor of 1.05 has been applied to the acceptance quoted in Equation 82 in accordance with the result obtained in Section 3 of this chapter (jet separation correction).

- $\mathcal{A}_{\mathrm{DP}}^{\mathrm{trig}} = 0.85 \pm 0.10$. This represents an error of 11.8%.

- A systematic error of +20.2% (-27.4%) due to jet energy scale uncertainty.

- A systematic error of -6.3% due to the effect of jet resolution uncertainty on $\mathcal{R}$.

Adding all errors in quadrature yields a combined error of +38.2% (-42.9%). Inserting these numbers into Equation 88 we find

$$\sigma_{\mathrm{DP}} = 65.3 + 24.9 - 28.0 \text{ nb}.$$
(89)

The dominant contributions to the error on this result are from the determination of $\mathcal{R}$ and from the jet energy scale uncertainty. An upper limit on σ_{DP} is established
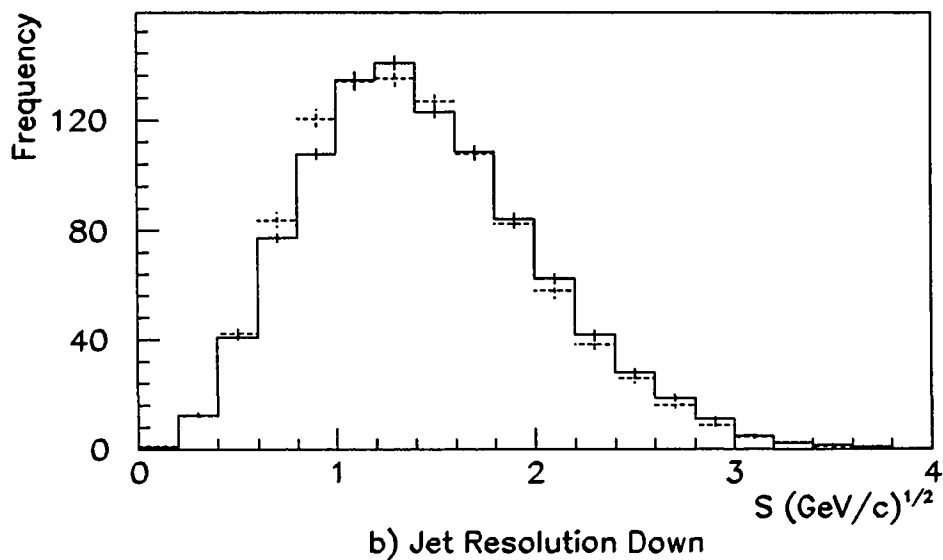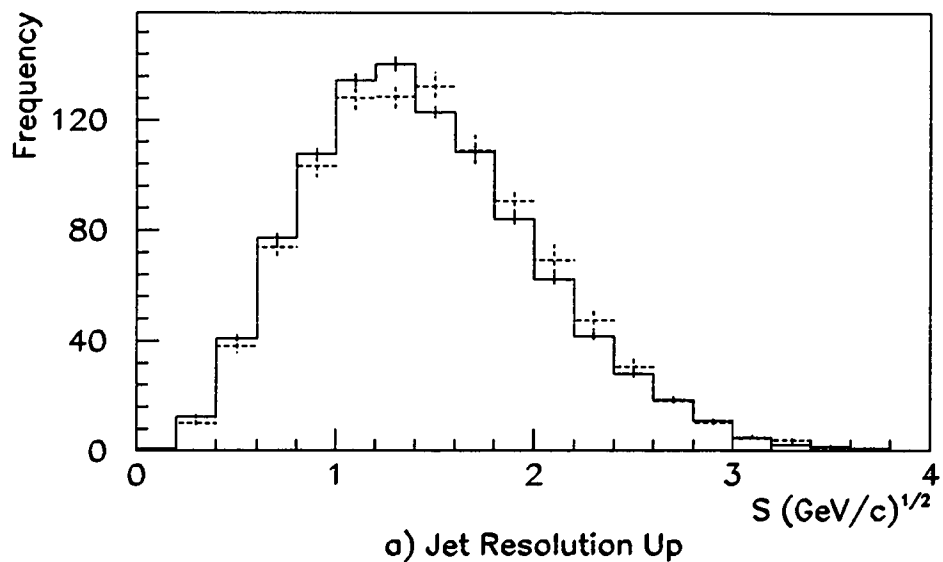
Figure 81. The effect of changes in jet resolution on the S variable, using simulated double parton events. Shown as dashed crosses are a) the results obtained with the jet resolution increased and b) with the jet resolution decreased. The default distribution is shown as a solid histogram in both cases.

Table XV. The effect of varying the jet resolution on the fitted value of $\mathcal{R}$. Also shown are the corresponding intersection values of $P_t^{(5)}$ for the S and Δ_S distributions.

Jet Resolution	$\mathcal{R}$	$P_t^{(5)}$ Cut
Default	5.30±1.29	13.37
Up	5.20±1.32	14.68
Down	4.97±1.27	14.73

following a standard prescription for dealing with limits in the presence of unphysical regions [99]. Gaussian errors are assumed, and the region $\sigma_{DP} < 0$ is excluded (this has a very small effect on the final result). At the 95% confidence level we find

$$\sigma_{DP} < 0.11 \ \mu b. \tag{90}$$

The UA2 collaboration has also set a limit on this cross section [60], they find $\sigma_{DP} < 0.82$ nb for partons having $P_t > 15$ GeV/c at the 95% confidence level. Since σ_{DP} is strongly dependent on the P_t cut and $\sqrt{s}$ of the experiment, a direct comparison between the two results is difficult. A meaningful comparison can however be made using the σ_{eff} parameter.

B. Limit on σ_{eff}

The σ_{eff} parameter permits a comparison of the CDF result with those of other experiments and also the extrapolation of results to other energy régimes, provided that parton correlations do not become appreciable. We have,

$$\sigma_{eff} = \frac{\sigma_{dijet}^2}{2 \cdot \sigma_{DP}} = \frac{\sigma_{dijet}^2 \cdot \mathcal{A}_{DP}^{\geq 18} \cdot \mathcal{A}_{DP}^{trig} \cdot \mathcal{L}}{2 \cdot N_{DB} \cdot \mathcal{R}}. \tag{91}$$

The only new parameter needed in addition to those already calculated in the previous section is σ_{dijet}, for partons having $P_t > 18$ GeV/c. The value used has been obtained from theory, using the PAPAGENO Monte Carlo program. An attempt has been made to extract the cross section from data, but the systematic error on the trigger acceptance is too large to be able to improve upon the result obtained from theory (see Appendix C). However, the magnitude of the result obtained with the data is close to the average of the results found using PAPAGENO with a variety of structure functions and Q^2 parameterizations.

The quantities $\mathcal{A}_{\text{DP}}^{\geq 18}$ and σ_{dijet} are both obtained from one run with a given set of Monte Carlo generation parameters (see Table XI). Taking the average value of all results, excluding those performed using the EHLQ1 and DO2 structure functions yields,

$$\sigma_{\text{dijet}}^2 \cdot \mathcal{A}_{\text{DP}}^{\geq 18} = 9.47 \pm 3.38 \ (\mu\text{b})^2. \tag{92}$$

This error dominates the uncertainty on σ_{eff}. Combining all errors in quadrature results in a total uncertainty on σ_{eff} of +54% (-51%). Inserting the measured values into Equation 91 gives the result,

$$\sigma_{\text{eff}} = \frac{1.05 \cdot 9.47 \times 10^{-12} \cdot 0.85 \cdot 324.9 \times 10^9}{2 \cdot 2213 \cdot 0.0529} = 11.7 \ {}^{+6.3}_{-5.9} \ \text{mb}. \tag{93}$$

In order to investigate the implications of this result for physics at the SSC, parton-level events have been generated using $E_{CM} = 20$ TeV and $\sigma_{\text{eff}} = 11.7$ mb. The cross sections for both double parton and double bremsstrahlung events as a function of the P_t of the smallest jet (P_{t_4}) and the total P_t of all jets can be seen in

Figure 82 a) and b) respectively. Events have been generated with $P_t > 10$ GeV/c.

Based on this study, one would expect to see a significant double parton signal at the

SSC for jets with $P_t < 60$ GeV/c. In fact, the double parton mechanism *dominates*

in the range $P_{t_4} < 40$ GeV/c. Note that Figure 82b) is included merely to indicate

the relative dependence of the respective cross sections on $\sum P_t$. The 10 GeV/c

minimum P_t translates to a minimum $\sum P_t$ of 40 GeV/c. In practice, a larger P_t cut

will probably be required in order to avoid a contamination of clusters due to the

underlying event under SSC conditions. Also note that the value taken for σ_{eff} is the

best-fit value from this analysis. The large errors on this result should be borne in

mind when considering the implications for physics at SSC/LHC energies.

The final limit on σ_{eff} is determined using a numerical technique [100]. This

method is used since the distribution of errors on σ_{eff} is not Gaussian, and also extends

into the unphysical region $\sigma_{\text{eff}} < 0$. The effective cross section σ_{eff} is expressed as a

ratio,

$$\sigma_{\text{eff}} = \frac{x}{y}, \tag{94}$$

where

$$x = \sigma_{\text{dijet}}^2 \cdot \mathcal{A}_{\text{DP}}^{>18} \cdot \mathcal{A}_{\text{DP}}^{\text{trig}} \cdot \mathcal{L} = 2.75 \pm 1.05 \text{ b}, \tag{95}$$

$$y = 2 \cdot \mathcal{R} \cdot N_{\text{DB}} = 234.14 + 76.70 - 89.33. \tag{96}$$

Since a conclusive signal cannot be claimed, only a *lower* limit may be set on σ_{eff}.

The relevant error on the y variable is the (smaller) positive error. A finely-binned

probability distribution is constructed using the quantity x/y, with the two variables
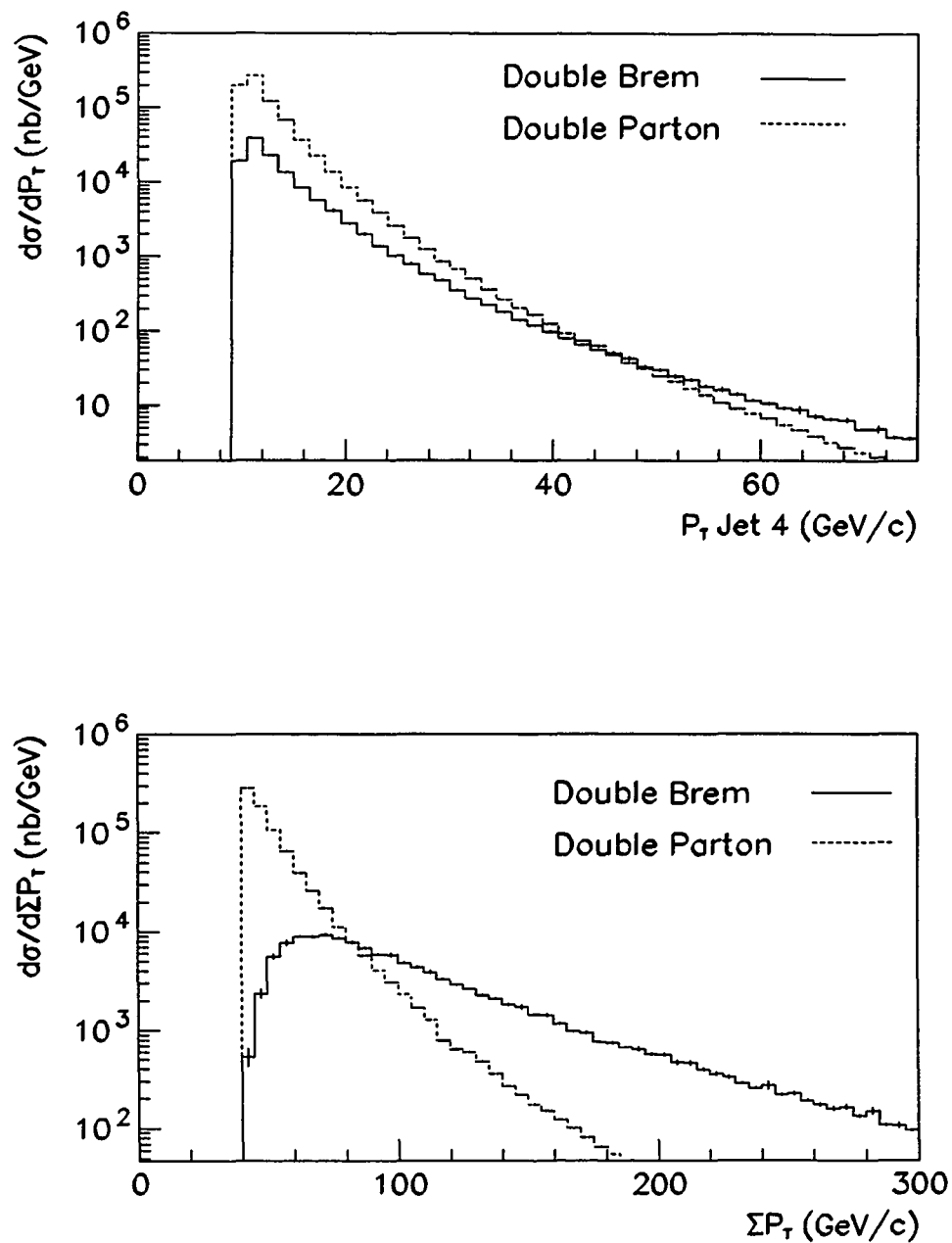
Figure 82. The double parton and double bremsstrahlung cross sections at $E_{CM} =$ 20 TeV as a function of a) the P_t of the smallest parton and b) the $\sum P_t$ of all four partons. Events were generated using structure function EHLQ1 with $Q = \langle P_t \rangle$.

x and y represented by Gaussian distributions. The mean and sigma for both variables are given in Equations 95 and 96. The 95% confidence level limit is then determined by finding the value of x/y ($=\sigma_{\text{eff}}$) which leaves 5% of the total area of the probability distribution on the lower (left hand) side of this value. Figure 83 shows the resulting distribution. The shaded region in this figure represents the range of values of σ_{eff} which are excluded at the 95% confidence level. An analogous procedure can also be followed using the reciprocal value, y/x. Now the value is found which leaves 5% of the area in the *upper* (right hand) side of the probability distribution. This is a useful consistency check of the limit. Using both methods, the result obtained is,

$$\sigma_{\text{eff}} > 4.2 \text{ mb (95\% C.L.)}. \tag{97}$$

At the 90% confidence level, the limit becomes,

$$\sigma_{\text{eff}} > 5.6 \text{ mb (90\% C.L.)}. \tag{98}$$

This result may be compared to the results of the AFS group and the UA2 collaboration. The AFS group claims to see a significant double parton signal, and measures $\sigma_{\text{eff}} = 5$ mb, with no quoted error [59]. The CDF limit excludes this result at the 90% confidence level, assuming that the two experiments are directly comparable. With an effective cross section of 5 mb the double parton signal should have been far more obvious (10% of the four-jet data).

The limit of the UA2 collaboration, $\sigma_{\text{eff}} > 8.3$ mb at the 95% confidence level [60] is compatible with the CDF result. UA2 use a theoretical estimation for the dijet cross section, with structure function DO1 and $Q = E_t^{\text{max}}$. Although this structure

Probability Distribution
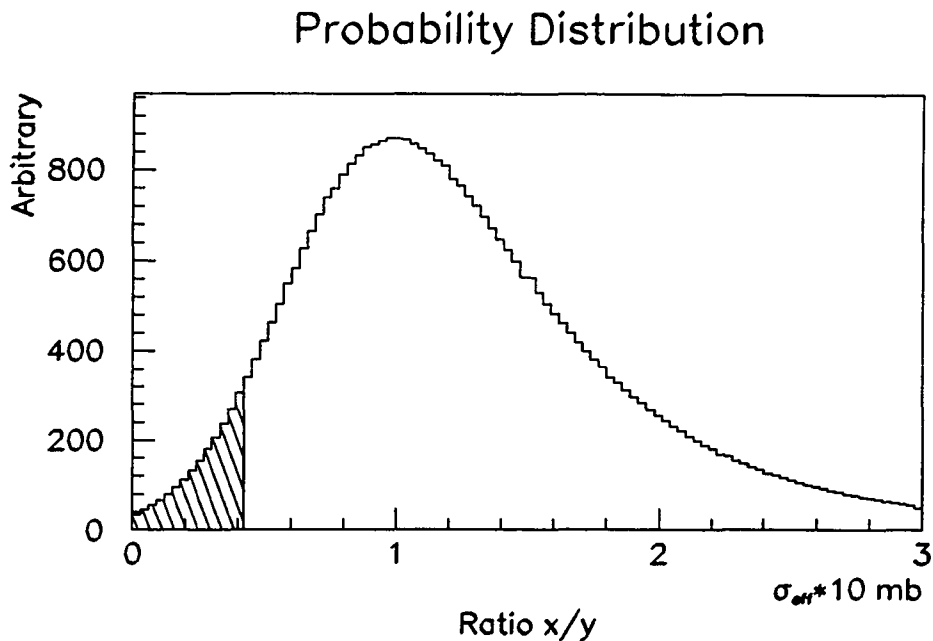
Figure 83. The probability distribution obtained for $\sigma_{\rm eff}$. The shaded region represents values of $\sigma_{\rm eff}$ excluded at the 95% confidence level.

function is currently not considered realistic, they estimate the theoretical error using results from the structure functions DO2, Gluck-Reya, MRSB1 and MRSB2 [101]. They exclusively use the S variable, and impose a cut of $P_t^{(5)} < 10$ GeV/c to reduce the effect of fifth jets.

To summarize, a robust procedure for determining the double parton content of four-jet data has been developed. The key to this procedure is the treatment of fifth jets, which are observed to bias the P_t-balancing and angular-type variables in *opposite* directions. The best fit to CDF data yields $\sigma_{\rm eff} = 11.7$ mb, with a large ($\sim$ 50%) error. A Monte Carlo study performed using this result suggests that double parton scattering will dominate conventional double bremsstrahlung production at

the SSC for jets having $P_t < 40$ GeV/c. The lower bounds on the effective cross section are $\sigma_{\text{eff}} > 4.2$ mb (95% C.L.) and $\sigma_{\text{eff}} > 5.6$ mb (90% C.L.), consistent with the results of the UA2 collaboration. The behaviour of the relative double parton to double bremsstrahlung cross sections suggests that the search for double parton scattering would benefit from the inclusion of lower P_t jets; jet properties are well understood by the CDF collaboration down to $P_t \sim 15$ GeV/c. This was not possible in this particular analysis due to complications introduced by the multijet trigger. The possibility of implementing such an improvement using data from the current (1992/93) run is being investigated.

CHAPTER VIII

SUMMARY AND CONCLUSIONS

The analysis presented in this dissertation has demonstrated that leading order QCD is consistent with CDF four-jet data, in a corrected (i.e. parton-level) P_t range from 25 GeV/c to approximately 120 GeV/c at $\sqrt{s} = 1.8$ TeV. No conclusive evidence for the double parton scattering process has been observed, despite the fairly large cross section predicted by the result of the AFS collaboration. A novel technique has been employed in treating the effects of fifth jets in the data. These jets are not explicitly modelled in the exclusive four-jet Monte Carlo calculation. Using this technique in conjunction with a careful evaluation of acceptances due to event cuts and the trigger, limits have been determined on σ_{DP} and σ_{eff}. These are,

$$\sigma_{DP} < 0.11 \ \mu b \ (95\% \ C.L.), \tag{99}$$

$$\sigma_{eff} > 4.2 \ mb \ (95\% \ C.L.), \tag{100}$$

$$\sigma_{eff} > 5.6 \ mb \ (90\% \ C.L.). \tag{101}$$

In addition, the best fit value obtained for the effective cross section, $\sigma_{eff} = 11.7^{+6.3}_{-5.9}$ mb has been used to estimate the resulting relative cross sections for the double parton and double bremsstrahlung processes at the SSC ($E_{CM} = 20$ TeV). The conclusion reached was that double parton scattering would dominate for a minimum jet P_t below 40 GeV/c, and should be observable up to a minimum jet P_t of approximately 60 GeV/c.

The special multijet trigger used during data-taking necessitated a cut of $P_t >$ 25 GeV/c on all jets after correction. Additionally, a cut of $\sum P_t > 140$ GeV/c was needed. These cuts resulted in a significant loss of sensitivity to a possible double parton signal. Ideally, the search for double parton scattering should include all jets with $P_t > 15$ GeV/c. Based on this analysis, a double parton signal should be clearly visible under these improved conditions. If not, the indication will be that our current picture of the proton as described in the parton model is incorrect.

REFERENCES

1   C. D. Anderson, Phys. Rev. **43**, 491 (1933).

2   E. Noether, *Nachr. Ges. Wiss. Gottingen*, 171 (1918).

3   S. Weinberg, Phys. Rev. Lett. **19**, 1264 (1967).

4   G. t'Hooft, Nucl. Phys. B **35**, 167 (1971).

5   P.W. Higgs, Phys. Rev. Lett. **13**, 508 (1964).

6   UA1 collaboration, G. Arnisson *et al.*, Phys. Lett. B **122**, 103 (1983).

7   UA1 collaboration, G. Arnisson *et al.*, Phys. Lett. B **126**, 398 (1983).

8   UA2 collaboration, M. Banner *et al.*, Phys. Lett. B **122**, 476 (1983).

9   UA2 collaboration, P. Bagnaia *et al.*, Phys. Lett. B **129**, 130 (1983).

10   N. Cabibbo, Phys. Rev. Lett. **10**, 531 (1963).

11   S. Glashow, J. Iliopoulos and L. Maiani, Phys. Rev. D **2**, 1285 (1970).

12   CDF collaboration, F. Abe *et al.*, A Limit on the Top Quark Mass From $p\bar{p}$ Collisions at $\sqrt{s} = 1.8$ TeV, submitted to Phys. Rev. D (1991).

13   L3 collaboration, B. Adeva *et al.*, Phys. Lett. B **231**, 509 (1989).

14   ALEPH collaboration, D. Decamp *et al.*, Phys. Lett. B **231**, 519 (1989).

15   OPAL collaboration, M. Akrawy *et al.*, Phys. Lett. B **231**, 530 (1989).

16   DELPHI collaboration, P. Aarnio *et al.*, Phys. Lett. B **231**, 539 (1989).

17   P. Dirac, in *The Principles of Quantum Mechanics*, Oxford University Press, Oxford, England, 1st edition (1930).

18   M. Gell-Mann, Phys. Lett. B **8**, 214 (1964).

19   V. Barger and R. Phillips, *Collider Physics*, Volume 71 of *Frontiers in Physics*, Addison-Wesley Publishing Company, New York (1987).

20   G. Altarelli and G. Parisi, Nucl. Phys. F **126**, 298 (1977).

21 D.W. Duke and J.F. Owens, Phys. Rev. D **30**, 49 (1984).

22 I.J.R. Aitchison and A.J.G. Hey, *Gauge Theories in Particle Physics*, 2nd edition, Adam Hilger, Bristol and Philadelphia (1989).

23 J.D. Bjorken and S.D. Drell, *Relativistic Quantum Mechanics*, McGraw-Hill, New York, (1964).

24 F. Halzen and A.D. Martin, *Quarks and Leptons: An Introductory Course in Modern Particle Physics*, John Wiley & Sons, New York, (1984).

25 H.D. Politzer, Phys. Rev. Lett. **30**, 1346 (1973).

26 D.J. Gross and F. Wilczek, Phys. Rev. Lett. **13**, 585 (1973).

27 B. Anderson *et al.*, Phys. Rep. **97**, 31 (1983).

28 T. Sjostrand, Comp. Phys. Comm. **27**, 243 (1982).

29 T. Sjostrand, Comp. Phys. Comm. **28**, 229 (1983).

30 T. Sjostrand, Comp. Phys. Comm. **39**, 347 (1986).

31 R.P. Feynman and R.D. Field, Nucl. Phys. B **136**, 1 (1978).

32 G. Hanson *et al.*, Phys. Lett. **35**, 1609 (1977).

33 JADE collaboration, W. Bartel *et al.*, Z. Phys. C **25**, 231 (1984).

34 TASSO collaboration, R. Brandelik *et al.*, Phys. Lett. B **97**, 453 (1980).

35 AMY collaboration, I.H. Park *et al.*, Phys. Rev. Lett. **62**, 1713 (1989).

36 S. Van de Meer, Stochastic Cooling Theory and Devices, *Proceedings of High Luminosity $p\bar{p}$ Collisions*, Berkeley, California (1978), p. 73.

37 D. Cline *et al.*, Search for New Phenomena Using Very High Energy pp and $p\bar{p}$ Colliding Beam Devices at Fermilab, *Proceedings of the 1976 Summer Study*, Batavia, Illinois (1976), p. 463.

38 UA2 collaboration, M. Banner *et al.*, Phys. Lett. B **118**, 203 (1982).

39 CDF collaboration, F. Abe *et al.*, Phys. Rev. Lett. **62**, 613 (1989).

40 R. Harris, *Two Jet Differential Cross Section and Structure Functions in pp̄ Collisions at √s = 1.8 TeV*, Ph.D. thesis, University of California at Berkeley, LBL-27246 (1989).

41 CDF collaboration, F. Abe *et al.*, Phys. Rev. Lett. **68**, 1104 (1992).

42 CDF collaboration, F. Abe *et al.*, Phys. Rev. D **45**, 1448 (1992).

43 E. Eichten, I. Hinchliffe, K. Lane and C. Quigg, Rev. Mod. Phys. **56**, 579 (1984).

44 R.D. Carlitz, *Parton Correlation Functions*, University of Pittsburgh Preprint PITT-88-05 (1989).

45 Z. Xu, D.H. Zhang and L. Chang, Nucl. Phys. B **291**, 392 (1987); J. Gunion and Z. Kunszt, Phys. Lett. B **159**, 167 (1985); S. Parke and T. Taylor, Nucl. Phys. B **269**, 410 (1986); Z. Kunszt, Nucl. Phys. B **271**, 333 (1986); J. Gunion and Z. Kunszt, Phys. Lett. B **176**, 163 and 477 (1986); J. Gunion and J. Kalinowski, Phys. Rev. D **34**, 2119 (1986); S. Parke and T. Taylor, Phys. Rev. D **35**, 313 (1987); F.A. Berends and W. Giele, Nucl. Phys. B **294**, 700 (1987); M. Mangano, S. Parke and Z. Xu., Nucl. Phys. B **298**, 673 (1988); M. Mangano and S. Parke, Nucl. Phys. B **299**, 190 (1987).

46 M.L. Mangano and S.J. Parke, *Multi-Parton Amplitudes in Gauge Theories*, FERMILAB-Pub-90/113-T (1990).

47 Z. Kunszt and W.J. Stirling, Phys. Rev. D **37**, 36 (1988).

48 C.J. Maxwell, Phys. Lett. B **192**, 190 (1987).

49 M. Mangano and S. Parke, Approximate Four Jet Cross Sections, *Proceedings of the 7th Topical Workshop on Proton-Antiproton Collider Physics*, Fermilab, Batavia, Illinois, edited by R. Raca, A. Tollestrup and J. Yoh (1988).

50 Z. Kunszt, Phys. Lett. B **145**, 132 (1984).

51 B. Humpert and R. Odorico, Phys. Lett. B **154**, 211 (1985).

52 N. Paver and D. Treleani, Phys. Lett. B **169**, 289 (1986).

53 N. Paver and D. Treleani, Nuovo Cimento A **70**, 215 (1982); bf A **73** 392 (1983).

54 D. Brown, *A Search for Double Parton Interactions in Proton-Antiproton Collisions at 1.8 TeV*, Ph.D. thesis, Harvard University (1989).

55 Yu. L. Dokshitzer, Zh. Eksp. Teor. Fiz. **73**, 1216 (1977).

56 L.V. Gribov, E.M. Levin and M.G. Ryskin, Phys. Rep. **100**, 1 (1983).

57 A.H. Mueller and J. Qiu, Nucl. Phys. B **268**, 427 (1986).

58 P. Sphicas, *Search for a High-Mass Resonance Decaying to Jets in Proton-Antiproton Collisions*, Ph.D. thesis, Massachusetts Institute of Technology (1988).

59 T Åkesson *et al.*, Z. Phys C **34**, 163 (1987).

60 UA2 collaboration, J. Alitti *et al.*, Phys. Lett. B **268**, 145 (1991).

61 CDF collaboration, F. Abe *et al.*, Nucl. Instrum. Methods A **271**, 387 (1988).

62 D. Perkins, *Introduction to High Energy Physics*, Addison-Wesley Publishing Company Inc., Reading, Massachusetts, 3rd edition (1987).

63 L. Balka *et al.*, Nucl. Instrum. Methods A **267**, 272 (1988).

64 S. Bertolucci *et al.*, Nucl. Instrum. Methods A **267**, 301 (1988).

65 Y. Fukui *et al.*, Nucl. Instrum. Methods A **267**, 280 (1988).

66 W. C. Carithers *et al.*, Performance and Calibration Studies of the CDF Endplug Calorimeter, *Proceedings of the Gas Sampling Calorimeter Workshop II*, Fermilab, Batavia, Illinois (1985).

67 G. Brandenburg *et al.*, Nucl. Instrum. Methods A **267**, 257 (1988).

68 S. Cihangir *et al.*, Nucl. Instrum. Methods A **267**, 249 (1988).

69 F. Bedeschi *et al.*, Nucl. Instrum. Methods A **268**, 50 (1988).

70 F. Snider *et al.*, Nucl. Instrum. Methods A **268**, 75 (1988).

71 G. Ascoli *et al.*, Nucl. Instrum. Methods A **268**, 33 (1988).

72 K. Byrum *et al.*, Nucl. Instrum. Methods A **268**, 46 (1988).

73 G. Drake *et al.*, Nucl. Instrum. Methods A **269**, 68 (1988).

74 E. Barsotti *et al.*, Nucl. Instrum. Methods A **269**, 82 (1988).

75 D. Amidei *et al.*, Nucl. Instrum. Methods A **269**, 51 (1988).

76 D. Brown and M.E.B. Franklin, CDF Internal Note 605 (1988).

77 G. Redlinger and Y.D. Tsay, CDF Internal Note 521 (1987).

78 J. Konigsberg *et al.*, *Testbeam 1990: Gas Calorimeter Absolute CARROT Calibration*, CDF Internal Note 1697 (1991).

79 T. Kamon *et al.*, *Forward-Central Dijet E_t Balancing and FHA Energy Scale*, CDF Internal Note 923 (1989).

80 D. Brown *et al.*, *Clustering Algorithms and Their Performance*, CDF Internal Note 605 (1988).

81 D. Brown, *A Study of Dijet P_t Balancing Using 1987 Data*, CDF Internal Note 835 (1987).

82 D. Brown and R. Carey, *Jet Corrections over the Full CDF η Range*, CDF Internal Note 755 (1987).

83 L. Keeble and B. Flaugher, *A New Jet Correction Function QDJSCO 2.0*, CDF Internal Note 1513 (1991).

84 F.E. Paige and S.D. Protopopescu, *Isajet: A Monte Carlo Event Generator for PP and $P\bar{P}$ Interactions*, BNL Theoretical Paper 37066 (1985).

85 D. Brown and S. Kannappan, *SETPRT, a Single Parton Fragmentation Module*, CDF Internal Note 873 (1989).

86 T. Hessing, S. Behrends, P. Tipton and B. Winer, *Monte Carlo Fragmentation Tuning for Jet Energy and Resolution Analysis*, CDF Internal Note 1131 (1990).

87 S. Behrends, *Central Calorimeter Response in Light of 1990 Test Beam Data*, CDF Internal Note 1286 (1990).

88 D. Brown, S. Kannapan and M. Shapiro, *QFL Version 2: Improvements and Checks*, CDF Internal Note 753 (1988).

89 A. Byon *et al.*, *The W and Z Underlying Event Analysis*, CDF Internal Note 1416 (1991).

90 S. White, *Reducing Luminosity Uncertainties*, CDF Internal Note 1031 (1989).

91 C. Grosso-Pilcher and S. White, *CDF Luminosity Calibration,* CDF Internal Note 1202 (1990).

92 I. Hinchliffe, private communication.

93 D. Brown, *A Very Fast Jet Monte Carlo,* CDF Internal Note 874 (1989).

94 R. Schwitters, *From Clusters to Jets,* CDF Internal Note 611 (1987).

95 L. Keeble, *QDJTMC Resolution Study,* CDF Internal Note 1656 (1992).

96 A. Roodman, private communication.

97 B. Flaugher, private communication.

98 Brian Winer, *The W Boson Transverse Momentum Spectrum in Proton-Antiproton Collisions at $\sqrt{s} = 1.8$ TeV,* Ph.D. thesis, Lawrence Berkeley Laboratory (1991).

99 Particle Data Group, Phys. Lett. B **239**, 1 (1990). The method for setting limits where there exists an unphysical region is explained in III.35.

100 Jim Mueller, private communication.

101 P. Lubrano, private communication.

Supplementary Sources Consulted

1 J. Huth and S. Behrends, *Statistics Issues for the Inclusive Jet E_t Paper,* CDF Internal Note 747 (1988).

APPENDIX A

PSEUDO-RAPIDITY AND JET SHAPE

Rapidity is defined by

$$y = \frac{1}{2} \ln \left(\frac{E + P_z}{E - P_z} \right) \tag{102},$$

where E is the energy of a particle, and P_z in the CDF co-ordinate system is its momentum component along the beam line. If a transformation is made to another frame moving with velocity β in the z direction then,

$$
\begin{aligned}
y' &= \ln \left(\frac{E' + P'_z}{\sqrt{P_t^2 + m^2}} \right) = \ln \left(\frac{\gamma(E - \beta P_z) + \gamma(P_z - \beta E)}{\sqrt{P_t^2 + m^2}} \right) \\
&= \ln \frac{(E + P_z)\gamma(1 - \beta)}{\sqrt{P_t^2 + m^2}} = y + \frac{1}{2} \ln \left(\frac{1 - \beta}{1 + \beta} \right),
\end{aligned}
\tag{103}
$$

where $\gamma^2 = 1/(1 - \beta^2)$, P_t is the transverse momentum of the particle (unaffected by the Lorentz boost) and m is its mass. The rapidity of the particle after the boost is offset from the initial rapidity by a *constant*. This is a useful property, since $p\bar{p}$ events are naturally boosted along the beam axis depending on the incident momenta of the partons that scatter.

Since rapidity depends on both mass and polar angle, this variable becomes impractical to use in the description of particles of different mass. Therefore the *pseudo-rapidity* η is used, defined as $\eta = -\ln \tan(\theta/2)$. This variable depends only on the polar angle θ. For high P_t particles of interest to CDF, pseudo-rapidity closely approximates rapidity. Expanding y in terms of η and $\alpha = \text{mass}/P_t$ we find,

$$
\begin{aligned}
y &= \frac{1}{2} \cdot \ln \left(\frac{\sqrt{\cosh^2 \eta + \alpha^2} + \sinh \eta}{\sqrt{\cosh^2 \eta + \alpha^2} - \sinh \eta} \right) \\
&\approx \eta - 0.5 \times \alpha^2 \tanh \eta + \mathcal{O}(\alpha^3).
\end{aligned}
\tag{104}
$$

If α is small, then $\eta \approx y$.

In η-ϕ space, jets are approximately circular. To see this, consider an arbitrary point specified by a momentum vector $\vec{P}$. Particles with small transverse momentum relative to this point (which represent the particles of a jet) can be modelled by adding a small perturbation transverse to the original vector,

$$d\vec{P} = \Delta\theta\hat{\Theta} + \sin\theta\Delta\phi\hat{\Phi}. \tag{105}$$

Holding the magnitude of the perturbation constant while varying the direction, we then have

$$\mid d\vec{P} \mid^2 = \Delta\theta^2 + \sin^2\theta\Delta\phi^2 = \text{const.} \tag{106}$$

For small $d\vec{P}$, $\sin\theta$ is a constant, as this is the angle of $\vec{P}$. Differentiating the expression for η gives,

$$\Delta\eta \approx -\Delta\theta/\sin\theta \tag{107}.$$

We now can write the η-ϕ locus of the points described by the perturbation $d\vec{P}$,

$$\Delta\eta^2 + \Delta\phi^2 \approx \Delta\theta^2/\sin^2\theta + \Delta\phi^2 = \mid d\vec{P} \mid^2 /\sin^2\theta = \text{const.} \tag{108}$$

Therefore, on average jets will have a circular P_t distribution in η-ϕ space.

APPENDIX B

LOG-LIKELIHOOD TEST RATIO

In this analysis, histogram bin contents are typically fairly low, especially in the

relevant regions where one might expect a double parton signal to appear. Evaluating

a χ^2 between fit and data based on Gaussian statistics is therefore not appropriate,

as fluctuations more accurately obey Poisson statistics. As a result, the form of the

χ^2 used is based on the log-likelihood test ratio [102], defined as

$$\lambda = \frac{\mathcal{L}(x \mid \theta_0)}{\mathcal{L}(x \mid \theta)}, \tag{109}$$

where $\mathcal{L}(x \mid \theta_0)$ is the likelihood of observing variable x given the parent distribution

denoted θ_0, and $\mathcal{L}(x \mid \theta)$ is the likelihood where all possible parent distributions are

allowed. The χ^2 parameter is defined as

$$\chi^2 = -2 \cdot \ln(\lambda). \tag{110}$$

For just one bin, we define,

$$n_q = \text{Number of events predicted by QCD}, \tag{111}$$

$$n_o = \text{Number of events observed}. \tag{112}$$

Now, the likelihood evaluated using Poisson statistics for $n = n_q$ is,

$$\mathcal{L}(x \mid \theta_0) = \frac{e^{-n_q} \cdot n_q^x}{x!} \tag{113}$$

and

$$\mathcal{L}(x \mid \theta) = \frac{e^{-n} \cdot n^x}{x!} \tag{114}$$

is the likelihood for $n \neq n_q$. Taking $n = x = n_o$ for one measurement, we then obtain

$$\lambda = \frac{e^{-n_q} \cdot n_q^{n_o}}{e^{-n_o} \cdot n_o^{n_o}},$$

(115)

and

$$\chi^2 = -2 \cdot [\ln(e^{-n_q + n_o \ln(n_q)}) - \ln(e^{-n_o + n_o \ln(n_o)})],$$

(116)

which simplifies, giving

$$\chi^2 = 2 \cdot [(n_q - n_o) + n_o \ln\left(\frac{n_o}{n_q}\right)].$$

(117)

The difference between the χ^2 parameter evaluated in this manner and that calculated using Gaussian statistics can best be seen with a simple example. Taking $n_o = 25$ and $n_q = 30$, the log-likelihood method yields a χ^2 of 0.884. For the Gaussian approximation, we have

$$\chi^2 = \frac{(30 - 25)^2}{30} = 0.833.$$

(118)

For many (m) bins, each with n_{qi} predicted and n_{oi} observed entries, the χ^2 parameter is given by,

$$\chi^2 = 2 \cdot \sum_{i=1}^{m} [(n_{qi} - n_{oi}) + n_{oi} \ln\left(\frac{n_{oi}}{n_{qi}}\right)].$$

(119)

APPENDIX C

EXPERIMENTAL DETERMINATION
OF THE DIJET CROSS SECTION

The dijet cross section for partons having $P_t > 18$ GeV/c has been measured using data taken with a special Level 2 trigger which required the $\sum E_t$ of all calorimeter towers to be above 40 GeV. This measurement is motivated by the desire to reduce the large error inherent in using a theoretical estimation of the cross section. Also, it will provide an independent check of the reliability of the fast jet simulation in estimating the acceptance of event cuts.

The dijet cross section σ_{dijet} is given by,

$$\sigma_{\text{dijet}} = \frac{N_{\text{dijet}}}{\mathcal{L} \cdot \mathcal{A}_{\text{dijet}}^{\text{trig}} \cdot \mathcal{A}_{\text{dijet}}^{\text{cuts}}}, \tag{120}$$

where N_{dijet} is the number of dijet events found in the data, $\mathcal{L}$ is the luminosity of the event sample, and $\mathcal{A}_{\text{dijet}}^{\text{trig}}$ and $\mathcal{A}_{\text{dijet}}^{\text{cuts}}$ are the acceptances of the trigger and event cuts respectively. A P_t cut of 25 GeV/c is made on all corrected jets, leaving 366 dijet events in the data. The fast jet Monte Carlo program is used to simulate dijet events in order to calculate the acceptance due to event cuts, and the full detector and trigger simulations are used to estimate the trigger acceptance. For the Monte Carlo sample generated with the fast detector simulation, the requirement $P_t > 25$ GeV/c ensures that no partons with $P_t < 18$ GeV/c remain in the sample. The parton generation P_t is therefore chosen as 18 GeV/c. To denote this cut, the term $\mathcal{A}_{\text{dijet}}^{\text{cuts}}$ in Equation 120

will henceforth be replaced by $\mathcal{A}_{\text{dijet}}^{>18}$. Event quality cuts imposed on both data and Monte Carlo samples are

1. $z_{\text{vertex}} < 60$ cm.

2. No double interactions observed in the VTPC.

3. Two (and only two) jets having $P_t > 25$ GeV/c, clustered with cone size $R = 0.7$.

4. $| \eta |< 3.5$

5. Jet separation $\Delta R > 1.0$.

The luminosity of the data sample has been determined to be $\mathcal{L} = 0.0846 \pm 6.8\%$ nb^{-1}. The data was accumulated during just one special run in 1989. The acceptances due to the trigger and event cuts have been determined using the Monte Carlo samples. Table XVI shows the results, and their variation with the jet energy scale. The method used to estimate this variation is identical to that presented in Chapter VII, Section A5.

In order to estimate the uncertainty on the dijet cross section, the structure function and Q^2 parameterization used in the evaluation of $\mathcal{A}_{\text{dijet}}^{\text{trig}}$ and $\mathcal{A}_{\text{dijet}}^{>18}$ has been varied, and the acceptances recalculated. The results are shown in Table XVII. To summarize the results obtained,

- $N_{\text{dijet}} = 366 \pm 5.2\%$.

- $\mathcal{L} = 0.0846$ nb$^{-1} \pm 6.8\%$.

- $\mathcal{A}_{\text{dijet}}^{\text{trig}} \cdot \mathcal{A}_{\text{dijet}}^{>18} = 0.108 \pm 0.006$.

- Jet energy scale uncertainty is +16.0%, -7.6%.

Table XVI. Results obtained for $\mathcal{A}_{\text{dijet}}^{\text{trig}}$, $\mathcal{A}_{\text{dijet}}^{>18}$ and N_{dijet} with variations in jet energy scale. Also shown is the corresponding value of σ_{dijet} obtained using these parameters.

Jet E-scale	N_{dijet}	$\mathcal{A}_{\text{dijet}}^{\text{trig}}$	$\mathcal{A}_{\text{dijet}}^{>18}$	σ_{dijet} (nb)	% Deviation
Default	366	0.773	0.1434	39042	–
Abs↑	416	0.695	0.1744	40583	+3.9
Abs↓	300	0.829	0.1163	36793	-5.8
Rel↑	374	0.756	0.1482	39372	+1.1
Rel↓	357	0.782	0.1392	38780	-1.5
OOC On	501	0.616	0.2133	45087	+15.5
UE On	310	0.822	0.1197	37255	-4.6

Table XVII. Results for the acceptances $\mathcal{A}_{\text{dijet}}^{\text{trig}}$ and $\mathcal{A}_{\text{dijet}}^{>18}$ for various choices of structure function and Q^2 parameterization.

Structure Fn.	Q	$\mathcal{A}_{\text{dijet}}^{\text{trig}}$	$\mathcal{A}_{\text{dijet}}^{>18}$
EHLQ1	$\langle P_t \rangle$	0.773	0.1434
EHLQ1	$\langle P_t/2 \rangle$	0.752	0.1492
DO2	$\langle P_t \rangle$	0.744	0.1336
DO2	$\langle P_t/2 \rangle$	0.767	0.1434

Combining these results, we obtain

$$\sigma_{\text{dijet}}^{\text{Data}} = 40.0 + 7.6 - 5.1 \ \mu\text{b},$$

(121)

and from theory we have

$$\sigma_{\text{dijet}}^{\text{Theory}} = 38.8 \pm 7.5 \ \mu\text{b}.$$

(122)

The value from theory ($\sigma_{\mathrm{dijet}}^{\mathrm{Theory}}$) has been taken from the average of the results shown in Table XI, excluding those obtained with the structure functions DO2 and EHLQ1.

The error on the cross section obtained using data is comparable to that obtained with theory. However, an additional systematic error must be added to the result obtained from the data due to an inconsistency between the shapes of the Level 2 $\sum E_t$ distributions obtained using data and full detector simulation. A comparison of these two distributions can be seen in Figure 84. This difference is most likely due to low E_t effects due to the underlying event or soft additional jets present in the data. At higher jet P_t the Level 2 $\sum E_t$ results are reproduced faithfully by the full detector simulation (see Figure 42). This discrepancy effectively rules out the possibility of using σ_{dijet} obtained from the data in the double parton result. However, the close agreement between the dijet cross sections obtained with data and theory is encouraging.
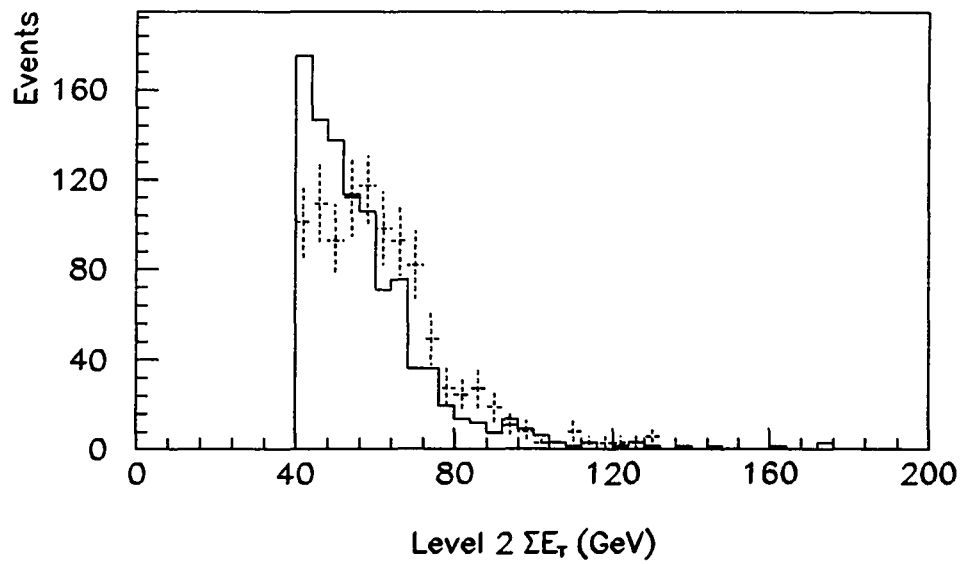
Figure 84. The Level 2 $\sum E_t$ obtained with data (solid) and theory combined with QFL and the full trigger simulation (dashed) for dijet events having $P_t > 25$ GeV/c.

APPENDIX D

THE CDF COLLABORATION

F. Abe,[11] D. Amidei,[14] C. Anway-Weiss,[3] G. Apollinari,[20] M. Atac,[6]

P. Auchincloss,[19] P. Azzi,[15] A. R. Baden,[8] N. Bacchetta,[15] W. Badgett,[14]

M. W. Bailey,[18] A. Bamberger,[6,a] P. de Barbaro,[19] A. Barbaro-Galtieri,[12]

V. E. Barnes,[18] B. A. Barnett,[10] G. Bauer,[13] T. Baumann,[8] F. Bedeschi,[17]

S. Behrends,[2] S. Belforte,[17] G. Bellettini,[17] J. Bellinger,[25] D. Benjamin,[24]

J. Benlloch,[6,a] J. Bensinger,[2] A. Beretvas,[6] J. P. Berge,[6] S. Bertolucci,[7]

K. Biery,[16,a] S. Bhadra,[9] M. Binkley,[6] D. Bisello,[15] R. Blair,[1] C. Blocker,[2]

A. Bodek,[19] V. Bolognesi,[17] A. W. Booth,[6] C. Boswell,[10] G. Brandenburg,[8]

D. Brown,[8] E. Buckley-Geer,[21] H. S. Budd,[19] G. Busetto,[15] A. Byon-Wagner,[6]

K. L. Byrum,[25] C. Campagnari,[6] M. Campbell,[14] A. Caner,[6] R. Carey,[8]

W. Carithers,[12] D. Carlsmith,[25] J. T. Carroll,[6] R. Cashmore,[6,a] A. Castro,[15]

F. Cervelli,[17] K. Chadwick,[6] J. Chapman,[14] G. Chiarelli,[7] W. Chinowsky,[12]

S. Cihangir,[6] A. G. Clark,[6] M. Cobal,[17] D. Connor,[16] M. Contreras,[4]

J. Cooper,[6] M. Cordelli,[7] D. Crane,[6] J. D. Cunningham,[2] C. Day,[6]

F. DeJongh,[6] S. Dell'Agnello,[17] M. Dell'Orso,[17] L. Demortier,[2] B. Denby,[6]

P. F. Derwent,[14] T. Devlin,[21] D. DiBitonto,[22] M. Dickson,[20] R. B. Drucker,[12]

K. Einsweiler,[12] J. E. Elias,[6] R. Ely,[12] S. Eno,[4] S. Errede,[9] A. Etchegoyen,[6,a]

B. Farhat,[13] B. Flaugher,[6] G. W. Foster,[6] M. Franklin,[8] J. Freeman,[6]

H. Frisch,[4] T. Fuess,[6] Y. Fukui,[11] A. F. Garfinkel,[18] A. Gauthier,[9]

S. Geer,[6] D. W. Gerdes,[4] P. Giannetti,[17] N. Giokaris,[20] P. Giromini,[7]

L. Gladney,[16] M. Gold,[12] K. Goulianos,[20] H. Grassmann,[15] G. M. Grieco,[17]

R. Grindley,[16,a] C. Grosso-Pilcher,[4] C. Haber,[12] S. R. Hahn,[6] R. Handler,[25]

K. Hara,[23] B. Harral,[16] R. M. Harris,[6] S. A. Hauger,[5] J. Hauser,[3]

C. Hawk,[21] T. Hessing,[22] R. Hollebeek,[16] L. Holloway,[9] S. Hong,[14] P. Hu,[21]

B. Hubbard,[12] B. T. Huffman,[18] R. Hughes,[16] P. Hurst,[8] J. Huth,[6] J. Hylen,[6]

M. Incagli,[17] T. Ino,[23] H. Iso,[23] H. Jensen,[6] C. P. Jessop,[8] R. P. Johnson,[6]

U. Joshi,[6] R. W. Kadel,[12] T. Kamon,[22] S. Kanda,[23] D. A. Kardelis,[9]

I. Karliner,[9] E. Kearns,[8] L. Keeble,[22] R. Kephart,[6] P. Kesten,[2] R. M. Keup,[9]

H. Keutelian,[6] D. Kim,[6] S. B. Kim,[14] S. H. Kim,[23] Y. K. Kim,[12] L. Kirsch,[2]

K. Kondo,[23] J. Konigsberg,[8] K. Kordas,[16,a] E. Kovacs,[6] M. Krasberg,[14]

S. E. Kuhlmann,[1] E. Kuns,[21] A. T. Laasanen,[18] S. Lammel,[3] J. I. Lamoureux,[25]

S. Leone,[17] J. D. Lewis,[6] W. Li,[1] P. Limon,[6] M. Lindgren,[3] T. M. Liss,[9]

N. Lockyer,[16] M. Loreti,[15] E. H. Low,[16] D. Lucchesi,[17] C. B. Luchini,[9]

P. Lukens,[6] P. Maas,[25] K. Maeshima,[6] M. Mangano,[17] J. P. Marriner,[6]

M. Mariotti,[17] R. Markeloff,[25] L. A. Markosky,[25] R. Mattingly,[2] P. McIntyre,[22]

A. Menzione,[17] E Meschi,[17] T. Meyer,[22] S. Mikamo,[11] M. Miller,[4]

T. Mimashi,[23] S. Miscetti,[7] M. Mishina,[11] S. Miyashita,[23] Y. Morita,[23]

S. Moulding,[2] J. Mueller,[21] A. Mukherjee,[6] T. Muller,[3] L. F. Nakae,[2]

I. Nakano,[23] C. Nelson,[6] C. Newman-Holmes,[6] J. S. T. Ng,[8] M. Ninomiya,[23]

L. Nodulman,[1] S. Ogawa,[23] R. Paoletti,[17] V. Papadimitriou,[6] A. Para,[6]

E. Pare,[8] S. Park,[6] J. Patrick,[6] G. Pauletta,[17] L. Pescara,[15] T. J. Phillips,[5]

F. Ptohos,[8] R. Plunkett,[6] L. Pondrom,[25] J. Proudfoot,[1] G. Punzi,[17]

D. Quarrie,[6] K. Ragan,[16,a] G. Redlinger,[4] J. Rhoades,[25] M. Roach,[24]

F. Rimondi,[6,a] L. Ristori,[17] W. J. Robertson,[5] T. Rodrigo,[6] T. Rohaly,[16]

A. Roodman,[4] W. K. Sakumoto,[19] A. Sansoni,[7] R. D. Sard,[9] A. Savoy-Navarro,[6] V. Scarpine,[9] P. Schlabach,[8] E. E. Schmidt,[6] O. Schneider,[12]

M. H. Schub,[18] R. Schwitters,[8] A. Scribano,[17] S. Segler,[6] Y. Seiya,[23]

G. Sganos,[16,a] M. Shapiro,[12] N. M. Shaw,[18] M. Sheaff,[25] M. Shochet,[4]

J. Siegrist,[12] P. Sinervo,[16,a] J. Skarha,[10] K. Sliwa,[24] A. Spies,[10] D. A. Smith,[17]

F. D. Snider,[10] L. Song,[6] T. Song,[14] M. Spahn,[12] P. Sphicas,[13] R. St. Denis,[8]

L. Stanco,[6,a] A. Stefanini,[17] G. Sullivan,[4] K. Sumorok,[13] R. L. Swartz, Jr.,[9]

M. Takano,[23] K. Takikawa,[23] S. Tarem,[2] F. Tartarelli,[17] S. Tether,[13]

D. Theriot,[6] M. Timko,[24] P. Tipton,[19] S. Tkaczyk,[6] A. Tollestrup,[6]

J. Tonnison,[18] W. Trischuk,[8] J. Tseng,[10] N. Turini,[17] Y. Tsay,[4]

F. Ukegawa,[23] D. Underwood,[1] S. Vejcik, III,[10] R. Vidal,[6] R. G. Wagner,[1]

R. L. Wagner,[6] N. Wainer,[6] J. Walsh,[16] G. Watts,[19] T. Watts,[21] R. Webb,[22]

C. Wendt,[25] H. Wenzel,[17] W. C. Wester, III,[12] T. Westhusing,[9] S. N. White,[20]

A. B. Wicklund,[1] E. Wicklund,[6] H. H. Williams,[16] B. L. Winer,[19] D. Wu,[14]

J. Wyss,[15] A. Yagil,[6] K. Yasuoka,[23] Y. Ye,[16,a] G. P. Yeh,[6] J. Yoh,[6]

M. Yokoyama,[23] J. C. Yun,[6] A. Zanetti,[17] F. Zetti,[17] S. Zhang,[14]

S. Zucchelli,[6,a]

[1] *Argonne National Laboratory, Argonne, Illinois 60439*

[2] *Brandeis University, Waltham, Massachusetts 02254*

[3] *University of California at Los Angeles, Los Angeles, California 90024*

(4) *University of Chicago, Chicago, Illinois 60637*

(5) *Duke University, Durham, North Carolina 27706*

(6) *Fermi National Accelerator Laboratory, Batavia, Illinois 60510*

(7) *Laboratori Nazionali di Frascati*

(8) *Harvard University, Cambridge, Massachusetts 02138*

(9) *University of Illinois, Urbana, Illinois 61801*

(10) *The Johns Hopkins University, Baltimore, Maryland 21218*

(11) *National Laboratory for High Energy Physics (KEK), Japan*

(12) *Lawrence Berkeley Laboratory, Berkeley, California 94720*

(13) *Massachusetts Institute of Technology, Cambridge, Massachusetts 02139*

(14) *University of Michigan, Ann Arbor, Michigan 48109*

(15) *Universita di Padova, Italy*

(16) *University of Pennsylvania, Philadelphia, Pennsylvania 19104*

(17) *University and Scuola Normale Superiore of Pisa, Italy*

(18) *Purdue University, West Lafayette, Indiana 47907*

(19) *University of Rochester, Rochester, New York 15627*

(20) *Rockefeller University, New York, New York 10021*

(21) *Rutgers University, Piscataway, New Jersey 08854*

(22) *Texas A&M University, College Station, Texas 77843*

(23) *University of Tsukuba, Tsukuba, Ibaraki 305, Japan*

(24) *Tufts University, Medford, Massachusetts 02155*

(25) *University of Wisconsin, Madison, Wisconsin 53706*

VITA

Louis Joseph Keeble ████████████████████████████████

██

where he was awarded the McQuail plate for academic achievement. From 1984–1987
he attended Bristol University where he was the joint recipient of the Rayleigh Fel-
lowship for the outstanding final year experimental project, entitled 'The Collapse of
Long-Chained Polymer Molecules'. Upon graduation with a B.Sc. (1st class honors)
in physics he accepted a position with the United Kingdom Atomic Energy Author-
ity in Winfrith, Dorset and performed experiments aimed at secondary oil recovery
from North Sea oil fields. In the summer of 1988 he accepted a Regents' Fellowship
at Texas A&M University and began working as part of the CDF collaboration in
experimental particle physics. In 1991 he was awarded the M.S. degree in physics.
His permanent mailing address is ████████████████████████
████████